Semiconductors, Vol. 35, No. 1, 2001, pp. 1–9. Translated from Fizika i Tekhnika Poluprovodnikov, Vol. 35, No. 1, 2001, pp. 3–10.
Original Russian Text Copyright © 2001 by Vikulin, Vikulina, Stafeev.

REVIEWS

Magnetotransistors

I. M. Vikulin, L. F. Vikulina, and V. I. Stafeev
Ukrainian Academy of Communications, 65021 Odessa, Ukraine

Submitted May 30, 2000; accepted for publication June 1, 2000

Abstract—Principles of the operation of transistors whose output current is controlled by an external magnetic field are generalized. The unijunction, bipolar, and field-effect magnetotransistors, and also their derivatives (magnetothyristors and magnetically controlled microcircuits) are considered. The most important applications are outlined. © *2001 MAIK "Nauka/Interperiodica".*

1. INTRODUCTION

Historically, photosensitive transistors (referred to as phototransistors) were the first type of transistor whose output current depended on external factors. Similarly, magnetosensitive transistors have come to be known as magnetotransistors. The output current of phototransistors depends on the incident luminous flux, whereas the output current in magnetotransistors is governed by the magnetic flux that passes through these devices. A distinguishing feature that is common to the above transistors and which governs their widespread application is the fact that both external actions are noncontact; i.e., the sources of the light and the magnetic field are electrically isolated from the responsive transistors. In the same manner as an optron can be formed from a light-emitting diode and a phototransistor, a source of magnetic flux and a magnetotransistor can be combined to form a magnetocouple. Both a permanent magnet and an electromagnet can be used as a source of magnetic flux. An interesting special feature of a magnetotransistor is the fact that its output current is also sensitive to luminous flux. Thus, double noncontact control of the output signal becomes possible (by magnetic flux and illuminance), which appreciably extends the transistor's capabilities.

2. UNIJUNCTION MAGNETOTRANSISTORS

Unijunction transistors (UJTs) operate on the basis of the base-resistance modulation by charge carriers injected from the emitter; as a result, the input current–voltage (*I*–*V*) characteristics are *S*-shaped (Fig. 1).

The larger the effective lifetime τ_E of injected charge carriers is in the base, the deeper they penetrate into the base and the smaller is the value of residual voltage V_0 to which the emitter voltage is reduced after switching the lower part of the base (see Fig. 1) from a high- to low-resistance state. When a UJT is put in a magnetic field, the injected charge carriers are affected by the Lorentz force [1, 2] which deflects them to the base sides (or in the opposite direction, depending on the alignment of the magnetic field and the UJT dimensions). Since the recombination rate for nonequilibrium charge carriers at the base sides is typically higher than that in the bulk, the above causes changes in τ_E and, correspondingly, in V_0 as well (Fig. 1). The dependence of V_0 on magnetic induction B can be used to develop a magnetic-field sensor that operates in the dc mode. However, the sensitivity of UJTs to a magnetic field in this mode is no higher than that of long-base magnetodiodes whose design and connection scheme are much simpler [3].

The use of the UJT-based oscillator as a magnetic-field sensor is of greater interest because, in practical electronics, the UJTs are mainly used as oscillators with a capacitance connected to the UJT's emitter and base (B_1). The total differential resistance of the UJT's input circuit can be represented as a combination of the active component [the positive (R^+) and negative (R^-) resistances of a system that consists of the emitter and base B_1] and the reactive component (the internal inductance L of a UJT) [4]. It has been shown previously [5] that L and R^- increase with increasing τ_E as long as the depth of the pulled-in injected carriers is no larger than the base length l_1. Since a magnetic field primarily affects τ_E, this field modifies the values of L and R^-, which results in variations in the amplitude and frequency of oscillations of the voltage at the UJT emitter [5–7]. The value of magnetosensitivity γ, defined as the ratio of alternating voltage V to the magnetic induction B and the supply current I

$$\gamma = V/IB, \tag{1}$$

may be as large as 2×10^3 V/(A T). Since $V \propto R^-$ and $R^- \propto \rho$ (ρ is resistivity of the base), it is necessary to use a high-resistivity semiconductor to enhance the magnetosensitivity. For this purpose, exclusion-type contacts to the Ge UJT base have been used. In this case, the exclusion phenomenon consists in the fact that an electric field in the UJT base exports the nonequilibrium minority carriers (holes) from the base through contact B_1; this makes it possible to decrease the concentration of equilibrium charge carriers in the base by an order of

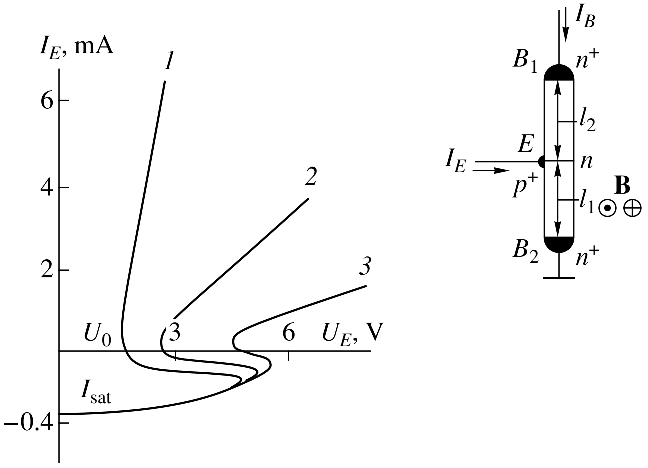

Fig. 1. Current–voltage characteristics of germanium unijunction transistors in a magnetic field with induction B = (*1*) 0, (*2*) 0.3, and (*3*) 0.6 T. Schematic representation of the device is shown in the inset.

magnitude, to increase ρ and R^-, and, correspondingly, to increase γ to the value of 10^4 V/(A T) [8, 9].

It is possible to use a UJT oscillator in the design of a magnetic-field sensor with a frequency-related output (i.e., with the dependence of oscillation frequency on a magnetic field). The frequency-based output makes it possible to appreciably simplify the interfacing of the sensor with a computer and to miniaturize the measuring devices.

3. SINGLE-COLLECTOR MAGNETOTRANSISTORS

The effect of a magnetic field on conventional vertical bipolar transistors (the emitter, base, and collector regions are arranged one after another in the direction from the surface to the semiconductor bulk) manifests itself by bending the trajectories of charge carriers injected from the emitter; this brings about an increase in the effective base length and a deviation of a fraction of the carriers from the collector [10]. The latter effect becomes more pronounced with the decreasing width of the emitter and collector, which ensures an increase in magnetosensitivity. The smallest emitter–collector overlap area governed by the diffusion length of impurities is attained for the lateral transistor design; therefore, this design ensures the highest magnetosensitivity. Figure 2b illustrates the structure of such a magnetotransistor; the dashed line delineates the space-charge region of the collector *p*–*n* junction. The charge carriers are deflected to the base surface in a magnetic field **B** directed perpendicularly to the plane of the drawing (⊕**B**), and their path to the collector decreases; for the opposite direction (⊙**B**), this path increases, which causes the current gain h_{21}^{B} and the current through the magnetotransistor to change.

The dependence of h_{21}^{B} on magnetic induction has been calculated [11] and the following formula has been derived:

$$h_{21}^{\mathrm{B}} = \alpha\{1 \pm \mu B\sqrt{(l+b)/A}\}. \tag{2}$$

Here, $A = kT/qE$, μ is the mobility, b is the emitter halfwidth, E is the electric-field strength in the base, and

$$\alpha = 1 - \frac{A^2}{2L^2} - \frac{2l+b}{2L^2}A \pm \frac{\mu B}{bL^2}$$
$$\times \sqrt{A^3}\left\{\frac{2}{3}\left[\sqrt{(l+b)^3} - \sqrt{l^3}\right] + \left[\sqrt{l+b} - \sqrt{l}\right]A\right\}.$$

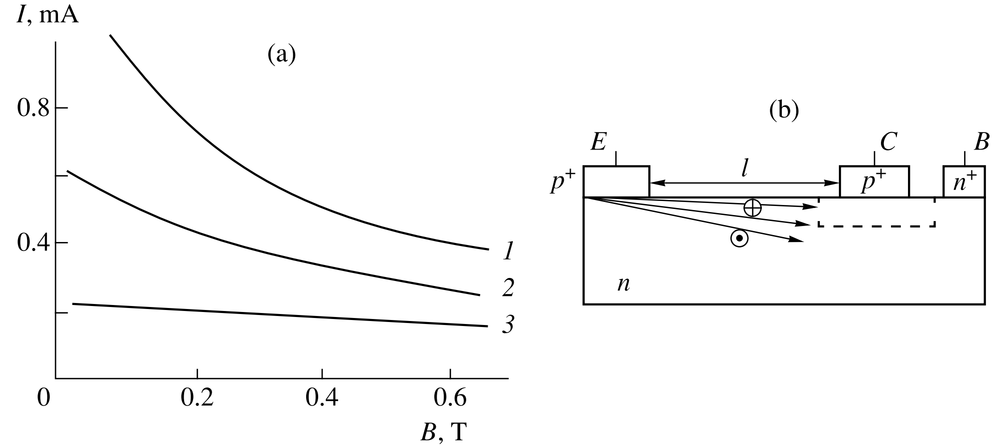

Fig. 2. (a) Dependence of current on magnetic induction and (b) the structure of a single-collector magnetotransistor. Curves in Fig. 2a correspond to the voltage V = (*1*) 25, (*2*) 20, and (*3*) 15 V; the magnetic-field direction is ⊙**B**. In Fig. 2b, the lines with arrows indicate the direction of charge-carrier motion: the upper line corresponds to a magnetic field **B** that is perpendicular to the plane of drawing (⊕); the lowest line is for the magnetic field **B** of opposite direction (⊙); and the middle line is for B = 0.

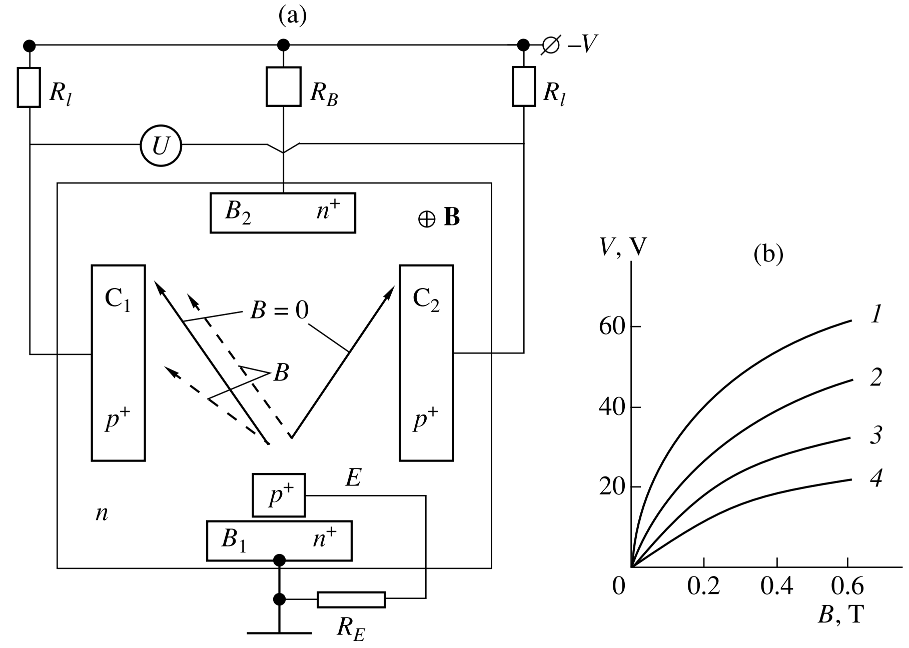

Fig. 3. (a) Schematic representation of a double-collector magnetotransistor and (b) the voltage between collectors as a function of magnetic induction at temperatures T = (*1*) –100, (*2*) –50, (*3*) 0, and (*4*) 60°C.

The positive and negative signs of the terms with μB correspond to opposite directions of the magnetic field ⊕**B** and ⊙**B**, respectively.

Formula (2) was experimentally verified using the n–p–n transistors based on p-Si with $\rho = 20$ kΩ cm. The areas of the emitter and collector are 0.6×0.6 mm^2, the distance between them is $l = 0.8$ mm, $L_p = 475$ µm, $E = 600$ V/cm, and $I_E = 1.5$ mA. For these values of the parameters, the term $A^2/2L^2$ and the rightmost term in the expression for α can be neglected. There is reasonably good agreement between the results of calculations of α using formula (2) and experimental data for the magnetic field ⊙**B**.

The highest magnetosensitivity is observed if a magnetotransistor is connected as a two-terminal device (the emitter–collector circuit) with a disconnected base. In this case, the current flowing through the transistor is given by $I = I^r_{\mathrm{CB}}/(1 - h^{\mathrm{B}}_{21})$. Under typical conditions, the reverse current of the collector p–n junction I^r_{CB} is small, the gain h^{B}_{21} is also small in microcurrent mode, and the magnetosensitivity is not high. Therefore, in order to increase I^r_{CB}, we have either to introduce shunting channels in the collector or to use an almost intrinsic semiconductor as the base. Figure 2a shows the dependences $I(B)$ for several voltages at the magnetotransistor for the two-terminal connection. As the current increases, the magnetosensitivity becomes higher, which can be explained by an increase in h^{B}_{21}. For a current of 0.6 mA, the magnetosensitivity is about 2×10^4 V/(A T).

4. DOUBLE-COLLECTOR MAGNETOTRANSISTORS

The design of a double-collector magnetotransistor with collectors located at both sides of the base is illustrated in Fig. 3. A double-collector magnetotransistor (e.g., of the p–n–p type) operates in the following way. In the absence of a magnetic field, the holes injected from the emitter are evenly divided between the collectors (solid lines in Fig. 3, $B = 0$), and their currents are identical. In a magnetic field ⊕**B** (the dashed lines), the charge-carrier flux deflects towards collector C_1; as a result, the current through collector C_1 increases, whereas that through collector C_2 decreases. In addition to carrier redistribution between collectors, the effect of base-length change also exists in a double-collector magnetotransistor. As can be seen from Fig. 3, this effect is based on the fact that the path of carriers arriving at collector C_1 decreases; i.e., the effective base length decreases, which results in an additional increase in current. In contrast, this effect causes an additional decrease in current for collector C_2 [8, 12]. For the opposite direction of a magnetic field ⊙**B**, the current of C_2 increases, whereas that of C_1 decreases.

Obviously, for $B = 0$, there is no potential difference V between collectors in a symmetric circuit ($V = 0$), whereas the voltage V increases with increasing magnetic induction B. Thus, the voltage V is a function of magnetic-field strength; the sign of V is indicative of the magnetic-field direction. As follows from the schematic in Fig. 3, the quantity V can be defined as

$$V = R_l(I_{C1} - I_{C2}) = R_l I_E(h_{21}^{B1} - h_{21}^{B2}), \qquad (3)$$

where h_{21}^{B1} and h_{21}^{B2} are the current gains for two halves of a double-collector magnetotransistor [13, 14].

Calculations show that, in weak magnetic fields ($\mu B \ll 1$),

$$h_{21}^{B1} - h_{21}^{B2} = \kappa^2(BE/4b\tau)[a^4 - (a-b)^4],$$

where $2a$ is the distance between collectors, $2b$ is the emitter width, τ is the lifetime of nonequilibrium charge carriers, and $\kappa = q/kT$.

It is worth noting that the Hall voltage V_H arises in a restricted base if the current of the majority of charge carriers flows between the base contacts B_1 and B_2 in a magnetic field. The Hall field deflects the injected charge carriers in the same direction as does the Lorentz force, which enhances the magnetosensitivity of a double-collector magnetotransistor.

For a horizontally extended emitter, the voltage $+V_H/2$ is applied to half of the emitter, whereas the voltage $-V_H/2$ is applied to the other half. These voltages are combined with the power-supply voltage applied to the emitter *p–n* junction, which results in a dissimilar injection of holes from two halves of the emitter and, correspondingly, in a difference between the collector currents. This effect can also serve as a basis for the operation of a double-collector magnetotransistor [15–29].

The linear dependence $V \propto I_E BE$ (3) is well verified for weak magnetic fields and low injection levels. In strong magnetic fields, the effective charge-carrier redistribution between collectors becomes less pronounced (all charge carriers arrive at the same collector); as a result, the magnetosensitivity becomes lower. As the injection level becomes higher, an increase in the injected-carrier concentration in the vicinity of the emitter causes a decrease in the resistance of this region and a decrease in E; as a result, the dependence $V = f(I_E)$ becomes weaker. Figure 3b shows the typical $V(B)$ dependences for a double-collector magnetotransistor at various temperatures. The transistors were made of silicon with $\rho = 200\ \Omega$ cm; they had $a = 75\ \mu$m, $b = 30\ \mu$m, and the collectors' length was 200 μm. A combination of the three aforementioned physical effects in the base of a double-collector magnetotransistor ensures the attainment of magnetosensitivity equal to 5×10^5 V/(A T), which is higher by a factor of 5–10 than the sensitivity of a single-collector magnetotransistor. Consequently, a double-collector magnetotransistor is not merely a combination of two single-collector magnetotransistors; thus, the former should be considered as a device in its own right. Furthermore, experimental double-collector magnetotransistors have also been made of germanium and indium antimonide.

Diffusion-related spreading of the injected-carrier flux directed to collectors also appreciably affects the sensitivity of a double-collector magnetotransistor. This results in a fraction of the injected charge carriers changing their trajectory in a magnetic field only in the region of one of the collectors and is not involved in the redistribution of charge carriers between the collectors; as a result, the magnetosensitivity becomes lower. The diffusion-caused spreading of the charge-carrier flux can be reduced by introducing a heavily doped region into the base between the collectors, forming a gradient of the band gap from the base center to the collectors, and using various shapes of the base contact B_1 and collectors. Such approaches make it possible to enhance the magnetosensitivity of a double-collector magnetotransistor by an order of magnitude.

A sensor based on a planar double-collector magnetotransistor (Fig. 3a) can only be used to measure a single component of a magnetic field. With the aim of measuring the two and three components of the magnetic-induction vector, magnetotransistor designs were developed with three collectors arranged on three sides of a cube-shaped base. Such magnetotransistors were employed in experimental samples of electronic compasses that did not include any moving components. Using these compasses, it is possible to develop systems that automatically control the direction of motion of any vehicle in the Earth's magnetic field. The high sensitivity of double-collector magnetotransistors enables them to respond to the motion of a permanent magnet located above these transistors. This effect has been used to develop pressure and motion sensors. An array with a circular arrangement of double-collector magnetotransistors has been used in rotation-angle sensors.

5. MAGNETOTHYRISTORS

Any thyristor may be represented as an equivalent circuit of two transistors. Consequently, a consideration of the magnetosensitive properties of thyristors is reduced to a consideration of the magnetosensitive properties of the constituent transistors. Using the conventional method [30, 31], we can easily show that the voltage of switching a thyristor controlled by the *p*-base is given by

$$V_{sw} = V_{CB}^{thr}\left[1 - h_{21}^{B1}\left(1 + \frac{I_c}{I_{av}}\right) - h_{21}^{B2}\right]^{1/C}, \qquad (4)$$

where V_{CB}^{thr} is the avalanche-breakdown voltage for the collector *p–n* junction, I_c is the control-electrode current, I_{sw} is the current at the point of switching, h_{21}^{B1} is the current gain for the *n–p–n* transistor, h_{21}^{B2} is the gain for the *p–n–p* transistor, and C is a constant equal to 2–6 for different materials. If the device is controlled

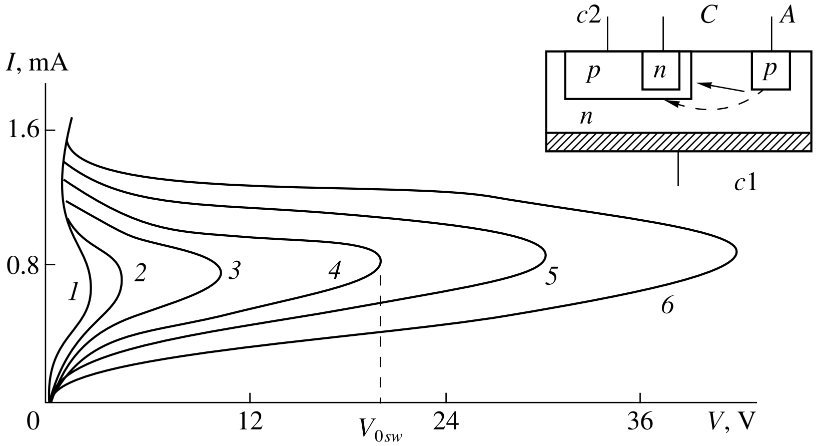

Fig. 4. Current–voltage characteristics of a thyristor in a magnetic field with induction B = (*1*) –1, (*2*) –0.8, (*3*) –0.4, (*4*) 0, (*5*) 0.4, and (*6*) 0.8 T. The structure of the device is shown in the inset.

via the *n*-base, the current amplification factors in (4) exchange places.

Using a magnetotransistor as one of the constituent transistors, we obtain a magnetothyristor structure whose switching voltage V_{sw} (4) is controlled by a magnetic field in accordance with the dependence $h_{21}^{\mathrm{B}}(B)$ (2). The structure of such a thyristor is shown in the insert in Fig. 4; either a contact c1 to the *n*-type base or a contact c2 to the *p*-type base can be used as the control electrode [32, 33]. A *p–n–p* constituent transistor whose emitter acts as an anode (A) is used here as a magnetotransistor. The processes in this transistor do not differ from the process of variation of h_{21}^{B} in a magnetotransistor in a magnetic field. For the magnetic-field direction ⊕**B**, the charge carriers injected from the anode are deflected from the collector, which results in a decrease in h_{21}^{B} and an increase in V_{sw}. In contrast, in the oppositely directed magnetic field, the charge carriers are deflected towards the collector, and V_{sw} decreases. The current through the control electrode governs the required value of $V_{0\mathrm{sw}}$ in the absence of a magnetic field. If electrode c1 is used to control the current, the magnetosensitivity is higher than in the case where the c2 electrode is used; this is caused in the former case, by a redistribution of the charge carriers injected from the anode between the *p*-collector and c1 occurring simultaneously with a variation in the effective base length. The magnetosensitivity γ related to variation in V_{sw} can be as high as 10^4 V/(A T) in a magnetic field.

It is possible to enhance the sensitivity of a magnetothyristor to a magnetic field with ⊕**B** polarity by using the magnetodiode effect. The circuit consisting of the anode and control electrode is the equivalent of a long-base diode connected in the forward direction. A transverse magnetic field enhances the resistance of this diode, which, for the diode fed by a constant voltage V_{A}, brings about a decrease in the corresponding current that represents the control current I_{c}. A decrease in I_{c} results in an additional increase in the switching voltage in a magnetic field ⊕**B**. In contrast, for the opposite polarity of the magnetic field, the magnetodiode effect (also reducing the value of I_{c}) reduces the importance of primary effects (an increase in the current gain); as a result the magnetosensitivity is lower. Figure 4 shows the *I–V* characteristics of a magnetothyristor made of *n*-Si with $\rho = 200\ \Omega$ cm, *p*-region spacing of 100 μm, and a wafer thickness of 200 μm. The control electrode is connected to the power supply with a constant voltage of $V_{\mathrm{A}} = 0.67$ V. Sensitivity to a magnetic field ⊕**B** upon variation in the switching voltage is 3×10^4 V/(A T), which exceeds the sensitivity of a magnetothyristor by a factor of 3–4 if the control circuit is fed from a current generator.

By analogy with a double-collector magnetotransistor, we can also introduce the term of a double-collector magnetothyristor. The latter differs from a double-collector magnetotransistor (Fig. 3) in design only by the fact that two additional *n*-emitters are introduced in the middle of the collector *p*-regions. In such a structure, there is an internal coupling between two thyristors. This coupling manifests itself in the fact that the deflection of injected charge carriers from one collector to the other (e.g., from C_2 to C_1) not only reduces the turn-on voltage of the first thyristor but also increases the turn-on voltage of the second thyristor. This enhances the interference immunity of the system if a magnetothyristor is used to switch the current by magnetic field from one circuit to another.

6. FIELD-EFFECT MAGNETOTRANSISTORS

The channel resistance of a field-effect transistor (FET) increases in a magnetic field as does the resistance of any semiconductor. Therefore, a FET can be used as a magnetoresistor [34]. However, a FET is more

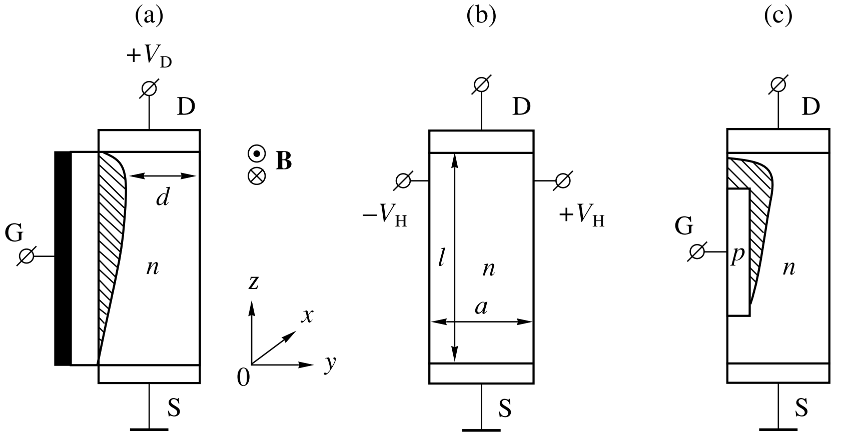

Fig. 5. (a) The structure of a MIS magnetotransistor, (b) its cross section in the $x0y$ plane, and (c) the structure of a field-effect magnetotransistor with *p–n* junction.

extensively used as a Hall-effect sensor. Since the voltage of a Hall-effect sensor is given by

$$V_H = IBR_H/d, \tag{5}$$

the sensor thickness d should be minimized in order to enhance the sensitivity of the device. However, there are lower limits to the thickness; these limits are related both to technological problems in preparing the thin samples and to the fact that, as the thickness decreases, scattering of charge carriers at the surface becomes more pronounced, which results in a decrease in their mobility. These difficulties can be surmounted to a large extent by using the field effect to reduce the effective sample thickness. If a FET is subjected to a transverse magnetic field, the Hall electric field comes into existence in the FET channel, as in any semiconductor sample with two nonrectifying contacts at its ends. The simplest field-effect magnetotransistor differs from the conventional FET only in that, in the former, there are additional lateral nonrectifying contacts to the channel; these contacts are intended for the measuring of the Hall voltage. Figures 5a and 5b illustrate the structure of an MIS magnetotransistor with an *n*-type channel. During operation in the channel-depletion mode, the channel thickness d is minimal in the vicinity of the drain (D). According to (5), the Hall voltage is largest where d is smallest. Therefore, it makes sense to form the Hall contacts near the drain. By increasing the magnitude of negative voltage at the gate, we can reduce d to very small values and, thus, increase V_H. As d decreases, the channel simultaneously recedes from the surface, which reduces the influence of the surface on the charge-carrier scattering. A field-effect magnetotransistor, with a *p–n* junction as the gate, operates in a similar way (Fig. 5c). A procedure for calculating the value of V_H for a field-effect magnetotransistor has been developed previously [2]. Formula (5) is used, with d being a function of V_G, V_D, and the coordinate z. For the saturation-mode operation of a field-effect magnetotransistor with the *p–n* junction (for the gate connected to the source, $V_G = 0$), the calculation yields

$$V_H = a\mu_H B \frac{V_{0G} k \sin\beta(1-2\cos\beta)}{e\sqrt{l-\left(1-\frac{27kz}{2l}\right)^2}}, \tag{6}$$

where

$$\beta = \frac{1}{3}\arccos\left(1-27k\frac{z}{2l}\right)+\frac{\pi}{3},$$

$$k = \frac{4}{9}\frac{V_D}{V_{0G}}\left(1-\frac{2}{3}\sqrt{\frac{V_D}{V_{0G}}}\right).$$

Calculations show that the values of Hall voltage for a field-effect magnetotransistor and a FET with a *p–n* junction are almost the same for channels with identical sizes and electrical parameters. For $I_D = 0.1$ mA, the experimentally determined sensitivity of Si-based magnetotransistors with the *p*-type channel is about 400 V/(A T), which is higher by a factor of 5–10 than the sensitivity of a Hall-effect sensor made of the same material.

By analogy with a field-effect magnetotransistor, a magnetic-field sensor based on two FETs has been developed; in this sensor, the semiconductor gate region that is common to both channels acts as a Hall-effect sensor. The channel resistances combined with load resistors form a bridge in whose diagonal a voltmeter is connected. In the absence of a magnetic field, the bridge is balanced, and the voltage measured by the voltmeter $V = 0$. In a magnetic field, with a current flowing through the gate contacts, the Hall voltage appears in the sensor, as in any semiconductor. Half of the voltage ($-V_H/2$) is applied to the left-hand channel and is blocking, whereas the other half ($+V_H/2$) is applied to the right-hand channel and is unblocking. As a result, the resistance of the left-hand channel increases, whereas that of the right-hand channel decreases, which causes a disbalance of the bridge, with the value of V increasing as the magnetic field increases.

In contrast with a single-channel field-effect magnetotransistor, transistors also act as amplifying components in a double-channel magnetotransistor; as a result, the magnetosensitivity of the latter increases by 1–2 orders of magnitude and attains the sensitivity of a double-collector magnetotransistor. Notwithstanding the fact that the technology of producing a two-channel field-effect transistor is more complicated (compared to that of a double-collector magnetotransistor), this device is promising for measuring the low magnetic fields because it features a lower level of intrinsic noise (as in all FETs) compared to that of bipolar transistors.

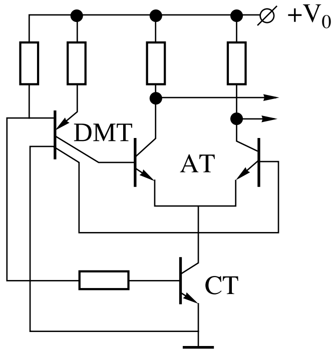

Fig. 6. Schematic diagram of an input circuit for an IC with a double-collector magnetotransistor. DMT stands for double-collector magnetotransistor; AT, for a differential amplifier composed of two transistors; and CT, for current-control transistor.

7. MAGNETICALLY CONTROLLED MICROCIRCUITS

Magnetosensitive components are mainly used in devices of two types: in measuring devices where the output signal is a function of magnetic induction and in switching devices where the output signal varies from “0” to “1” when the threshold value of magnetic-field induction B_{thr} is attained. The devices of both types are now produced as integrated circuits (ICs) [35–42] using the conventional silicon IC technology. Since an IC should operate in the conventional temperature range of –45–30°C, one of the most important tasks consists in ensuring that the IC operation is stable when the temperature varies; i.e., the output-signal amplitude should be made temperature-independent. One of the methods for solving this problem is considered here by the example of the IC whose schematic diagram is shown in Fig. 6.

The IC includes a double-collector magnetotransistor (DMT), a differential amplifier composed of two transistors (AT), and a current-control transistor (CT). As was noted above (see Fig. 3), the output voltage of a double-collector magnetotransistor decreases with increasing temperature, which results in a decrease in the output-signal amplitude if a simple amplifier is used. In order to compensate for this, a CT is introduced in the circuit; the input voltage to this transistor is derived from the interbase circuit of the double-collector magnetotransistor. This circuit (Fig. 3) is in fact a resistor and, as for any semiconductor resistance, can act as a thermally sensitive resistor. As the temperature increases, the resistance of the silicon resistor increases (as a result of a decrease in the charge-carrier mobility), which causes an increase in the voltage drop across this resistor; this voltage, in turn, is applied to the CT input. This leads to an increase in the current fed into the current-control transistor (CT) and into the transistors of the differential amplifier (AT) with increasing temperature. An increase in the current fed into any bipolar transistor (for low currents) brings about an increase in the gain [31]. Correspondingly, the gain of the differential amplifier increases, which compensates for a decrease in the amplifier’s input signal V_{in}; as a consequence, the output signal of the amplifier is temperature-independent and is governed only by the value of B. Thus, one can almost completely compensate the temperature-induced instability of the output signal [35, 40].

In conventional ICs, the circuit components are separated by the insulation regions, with these components being connected via the connector strips formed at the crystal surface. These regions and strips appreciably increase the IC dimensions and complicate the technology. In connection with this, research in functional microelectronics have recently been directed towards the development of devices whose neighboring components have bulk coupling. Examples of such ICs are the ICs in which the neighboring transistors have common regions; i.e., for example, the collector region of one transistor serves as the base for another transistor, so that the signal is conveyed from one transistor to the other by the direct transport of injected charge carriers. Such a bulk connection is used in the design of a number of magnetosensitive devices. As can be seen from Fig. 6, the collector regions of the double-collector magnetotransistor and the base regions of the CT have the same type of conduction. This formed the basis for the design of a magnetosensitive device in which the collector region of the double-collector magnetotransistor simultaneously serves as the base region of the corresponding CT.

In order to enhance the magnetosensitivity, several magnetosensitive components can be combined in a single IC. Such a combination is exemplified by a bridge formed from four single-collector magnetotransistors, with the current increasing in a magnetic field for one pair of oppositely arranged magnetotransistors and decreasing for the other pair. In such an IC, common regions of two neighboring magnetotransistors can also be used (the emitters of two magnetotransistors can be held in common, the emitter of one magnetotransistor can serve as the collector for another magnetotransistor, etc.). A similar bridge can be formed from two double-collector magnetotransistors with opposite types of conduction.

If it is necessary to obtain an alternating signal, which is a function of a constant magnetic field, a double-collector magnetotransistor is used, with the interbase region and emitter of this transistor serving simultaneously as a UJT and being connected according to the scheme of a UJT oscillator. The emitter performs an alternating injection of charge carriers into the base; these carriers are redistributed between the collectors in the same manner as in a conventional double-collector magnetotransistor that operates in the dc mode (Fig. 3). An alternating injection also gives rise to the output ac voltage (proportional to B) between the collectors. In this case, the magnetosensitive-device structure combines a double-collector magnetotransistor and a UJT with the base and emitter common to both transistors [38, 43]. The above-considered approach to the design of magnetically controlled ICs is the most promising because, in this case, the total size of the semiconductor chip and the number of interconnections between the IC components are reduced, the technology for producing an IC is simplified, and the IC cost is lowered.

It is also possible to assign optical couplers to semiconductor ICs; these couplers are devices composed of an input light-emitting diode and an output photodetector, which are optically coupled and electrically isolated [39]. As the input current changes, the luminous flux incident on the photodetector changes as well. This causes the output signal to change. If a component that is sensitive to a magnetic field is used as a photodetector, it is possible to obtain an optical coupler whose output signal can be controlled by both illumination and the external magnetic field. Experimentally, this statement has been verified using optical couplers of two types. In the first of these, phototransistors were used as photodetectors, whereas, in the second, photothyristors were used. The optical couplers have been made of commercial couplers of the AOU102 and AOU103 types [41]. It is shown that a magnetic field with an induction of 0.4 T brings about the same change in the negative-resistance portion of the I–V characteristic of a photothyristor as does the radiation of a light-emitting diode at a current of 8 mA (the maximum current is 20 mA). The dual noncontact control of the output parameter of an optical coupler makes it possible to appreciably expand the functional capabilities of this device.

8. CONCLUSION

It is worth noting that, notwithstanding the large number of developed magnetosensitive devices, these devices do not duplicate each other; rather, each of them has certain advantages that can be realized in specific applied circuits. Thus, a unijunction transistor makes it possible to use the smallest number of components to develop a magnetic-field sensor with an alternating output signal; a bipolar transistor has the smallest size and the smallest number of lead-outs; a double-collector magnetotransistor features the highest magnetosensitivity; a magnetothyristor is preferable as a magnetically controlled switch for large currents; and a field-effect magnetotransistor has the lowest level of internal noise and is used to measure the low-amplitude magnetic signals.

Magnetosensitive devices are widely used in modern measuring techniques and automation. On the basis of these devices, electronic compasses, magnetic-tape readers, sensors of various parameters (pressure, displacement, rotational speed, etc.), noncontact switches, dc collectorless motors, the systems of electronic starters for automobiles, and many other devices have been made. This ensures the further development and improvement of these devices.

REFERENCES

1. V. I. Stafeev and É. I. Karakushan, *Magnetodiodes* (Nauka, Moscow, 1975).
2. I. M. Vikulin, L. F. Vikulina, and V. I. Stafeev, *Galvanomagnetic Devices* (Radio i Svyaz’, Moscow, 1983).
3. G. A. Egiazaryan and V. I. Stafeev, *Magnetodiodes, Magnetotransistors, and Their Application* (Radio i Svyaz’, Moscow, 1987).
4. S. A. Garyainov and Yu. S. Tikhodeev, *Physical Models of Semiconductor Devices with Negative Resistance* (Radio i Svyaz’, Moscow, 1997).
5. I. M. Vikulin, L. F. Vikulina, M. A. Glauberman, and Yu. A. Zaporozhchenko, Radiotekh. Élektron. (Moscow) **24**, 1709 (1972).
6. I. M. Vikulin, L. F. Vikulina, M. A. Glauberman, and Yu. A. Zaporozhchenko, Radiotekh. Élektron. (Moscow) **31**, 2552 (1979).
7. I. M. Vikulin, L. F. Vikulina, M. A. Glauberman, and Yu. A. Zaporozhchenko, Radiotekh. Élektron. (Moscow) **25**, 2384 (1973).
8. I. M. Vikulin, L. F. Vikulina, M. A. Glauberman, and Yu. A. Zaporozhchenko, Radiotekh. Élektron. (Moscow) **26**, 2123 (1974).
9. I. M. Vikulin, L. F. Vikulina, M. A. Glauberman, and Yu. A. Zaporozhchenko, Fiz. Tekh. Poluprovodn. (Leningrad) **7**, 2363 (1973) [Sov. Phys. Semicond. **7**, 1573 (1973)].
10. I. M. Vikulin, M. A. Glauberman, L. F. Vikulina, and N. A. Kanshcheva, Fiz. Tekh. Poluprovodn. (Leningrad) **9**, 1534 (1975) [Sov. Phys. Semicond. **9**, 1011 (1975)].
11. L. F. Vikulina and É. Kladieva, Radiotekh. Élektron. (Moscow) **30**, 1668 (1985).
12. I. M. Vikulin, M. A. Glauberman, L. F. Vikulina, and Yu. A. Zaporozhchenko, Fiz. Tekh. Poluprovodn. (Leningrad) **8**, 580 (1974) [Sov. Phys. Semicond. **8**, 369 (1974)].
13. L. F. Vikulina and V. V. Kozel, Radiotekh. Élektron. (Moscow) **30**, 824 (1985).

14. I. M. Vikulin, L. F. Vikulina, and M. A. Glauberman, Prib. Tekh. Éksp., No. 5, 181 (1974).
15. D. M. Kozlov, G. I. Rekalova, I. M. Mitnikova, *et al.*, Fiz. Tekh. Poluprovodn. (Leningrad) **11**, 568 (1977) [Sov. Phys. Semicond. **11**, 327 (1977)].
16. I. M. Mitnikova, D. M. Kozlov, and G. I. Rekalova, Fiz. Tekh. Poluprovodn. (Leningrad) **12**, 48 (1978) [Sov. Phys. Semicond. **12**, 26 (1978)].
17. H. P. Baltes and R. S. Popovic, Proc. IEEE **74**, 1107 (1986).
18. V. Zieren and B. P. Duyndam, IEEE Trans. Electron Devices **ED-19**, 83 (1982).
19. R. S. Popovic and H. P. Baltes, Sens. Actuators **4**, 155 (1983).
20. V. Zieren and S. Middelboek, Sens. Actuators **2**, 251 (1982).
21. G. I. Rekalova, D. M. Kozlov, and T. V. Persiyanov, IEEE Trans. Magn. **MAG-17**, 3373 (1981).
22. Ch. S. Roumenin, Sens. Actuators **6**, 19 (1984).
23. V. Zieren, S. Kordic, and S. Middelhoek, IEEE Electron Device Lett. **EDL-3**, 394 (1982).
24. A. W. Vinal and N. A. Masnari, IEEE Electron Device Lett. **EDL-3**, 396 (1982).
25. I. M. Vikulin, N. A. Kanishcheva, and M. A. Glauberman, Fiz. Tekh. Poluprovodn. (Leningrad) **11**, 587 (1977) [Sov. Phys. Semicond. **11**, 340 (1977)].
26. I. M. Vikulin, M. A. Glauberman, and N. A. Kanishcheva, Fiz. Tekh. Poluprovodn. (Leningrad) **10**, 785 (1976) [Sov. Phys. Semicond. **10**, 467 (1976)].
27. I. M. Vikulin, M. A. Glauberman, and N. A. Kanishcheva, Fiz. Tekh. Poluprovodn. (Leningrad) **11**, 1609 (1977) [Sov. Phys. Semicond. **11**, 947 (1977)].
28. I. M. Vikulin, M. A. Glauberman, and N. A. Kanishcheva, Fiz. Tekh. Poluprovodn. (Leningrad) **15**, 399 (1981) [Sov. Phys. Semicond. **15**, 229 (1981)].
29. I. M. Vikulin, M. A. Glauberman, N. A. Kanishcheva, *et al.*, Fiz. Tekh. Poluprovodn. (Leningrad) **15**, 479 (1981) [Sov. Phys. Semicond. **15**, 274 (1981)].
30. V. A. Kuz'min, *Low- and High-Power Thyristors* (Sov. Radio, Moscow, 1971).
31. I. M. Vikulin and V. I. Stafeev, *Physics of Semiconductor Devices* (Radio i Svyaz', Moscow, 1990).
32. I. M. Vikulin, Yu. A. Zaporozhchenko, V. V. Garshenin, and Yu. F. Kuptsov, Fiz. Tekh. Poluprovodn. (Leningrad) **9**, 2360 (1975) [Sov. Phys. Semicond. **9**, 1522 (1975)].
33. I. M. Vikulin, M. A. Glauberman, and N. A. Kanishcheva, Fiz. Tekh. Poluprovodn. (Leningrad) **12**, 1609 (1978) [Sov. Phys. Semicond. **12**, 950 (1978)].
34. V. V. Alekseev and I. M. Vikulin, Prib. Tekh. Éksp., No. 2, 165 (1984).
35. A. N. Marchenko, in *Magnetically Controlled Integrated Circuits* (1986), Ser. 2, Vol. 3, p. 72.
36. M. Oppengeimer, Electronics **44** (16), 46 (1971).
37. O. K. Khomeriki, *Semiconductor Magnetic-Field Transducers* (Énergiya, Moscow, 1986).
38. I. M. Vikulin, L. F. Vikulina, M. A. Glauberman, and N. A. Kanishcheva, Prib. Tekh. Éksp., No. 3, 250 (1981).
39. Yu. R. Nosov, *Optoelectronics* (Radio i Svyaz', Moscow, 1989).
40. L. F. Vikulina, Tekh. Konstr. Élektron. Apparat., No. 3, 52 (1998).
41. L. F. Vikulina, Prib. Tekh. Éksp., No. 6, 100 (1999).
42. L. F. Vikulina, Prib. Tekh. Éksp., No. 2, 145 (2000).
43. L. F. Vikulina and M. A. Glauberman, *Physics of Temperature and Magnetic-Field Sensors* (Mayak, Odessa, 2000).

Translated by A. Spitsyn

Semiconductors, Vol. 35, No. 1, 2001, pp. 10–13. Translated from Fizika i Tekhnika Poluprovodnikov, Vol. 35, No. 1, 2001, pp. 11–14.
Original Russian Text Copyright © 2001 by Selishchev.

ATOMIC STRUCTURE AND NONELECTRONIC PROPERTIES OF SEMICONDUCTORS

Kinetics of Production of Oxygen-Containing Quenched-in Donors in Silicon and Their Nonuniform Distribution: An Analytical Solution

P. A. Selishchev

Faculty of Physics, Shevchenko National University, Vladimirskaya ul. 64, Kiev, 252017 Ukraine

Submitted June 17, 1999; accepted for publication June 1, 2000

Abstract—The kinetics of production of oxygen-containing quenched-in donors in silicon, when atomically dissolved oxygen intensely forms the bound states (complexes), is considered. An analytical time-dependent homogeneous solution of the corresponding nonlinear kinetic equations is obtained. The uniform distribution of oxygen atoms and their complexes is shown to become unstable for certain parameters of the problem owing to their interaction, and a spatially periodic distribution is developed with a period in the range of 10–1000 Å. *© 2001 MAIK "Nauka/Interperiodica".*

Technologically, modern microelectronics is based on one of the chief semiconductor materials, i.e., single-crystalline silicon. Electrical, mechanical, and technological properties of crystalline silicon are to a large extent determined by the content of its main accompanying impurity, namely, oxygen. The presence of oxygen governs the kinetics of production of quenched-in donors and microdefects, the lifetime of charge carriers, and the efficiency of gettering. By virtue of specific properties of oxygen in silicon, which differ from those of other background and doping impurities, it serves as a catalyst for various physical and technological processes. The role of oxygen becomes especially prominent during various thermal treatments.

In spite of active investigations over the last 45 years [1, 2], the problems associated with oxygen-containing silicon remain very topical, the central one among them most likely being the kinetics of production of oxygen-containing complexes related to the precipitation of oxygen and the formation of quenched-in donors.

It has been established [2, 3] that various oxygen-containing complexes exhibit donor properties, and a number of models describing the kinetics of their formation have been proposed. In study [3] and in subsequent models [2], a system of four nonlinear equations was analyzed for uniform concentrations of complexes composed of one, two, three, and four oxygen atoms. It was assumed that the complexes containing more than four oxygen atoms lose their donor properties. The nonlinear kinetic equations for the concentration of oxygen and its complexes suggested first in [3] have been solved either in the quasi-steady approximation or numerically. The models proposed explain many experimental facts; however, at least nine types of electrically active oxygen-containing complexes [2] have already been found by now. Furthermore, the experimentally measured concentration of quenched-in donors formed at 350–500°C was by several orders of magnitude higher than that predicted by the theory. For their formation at 350–400°C, the diffusivity of oxygen in silicon must be considerably higher than the actual diffusivity.

The theoretical approach proposed in this study makes it possible to overcome these difficulties. First, a homogeneous but time-dependent solution to the equations of kinetics was obtained analytically for an arbitrary number of various types of oxygen-containing complexes. This enabled us to trace the dynamics of the process as a whole (i.e., in relation to parameters of the problem) both with and without the quasi-steady approximation, thereby defining its domain of applicability.

Second, investigating the stability for a uniform distribution of oxygen in silicon shows that, in the low-temperature region (by virtue of elastic interaction between the oxygen atoms and their complexes), this distribution can be unstable with respect to establishing a uniform spatially periodic distribution. Actually it is known that oxygen in the silicon-crystal lattice can form various interstitial configurations, for example, in the form of a Si–O–Si quasi-molecule or in the form of free interstitial atoms (a metastable configuration); however, they are not bonded to the lattice and, thus, are more mobile. By virtue of the anisotropy for certain directions in the crystal, single-type defects are attracted. If the temperature of the sample under irradiation is below a certain threshold value, this attraction is found to dominate over the diffusion. Therefore, in the case of even an infinitesimal inhomogeneity appearing, for example, as a result of fluctuations, the mobile complexes move in such a way as to support the structure formed.

Thus, the distribution of oxygen in silicon depends on a previous thermal treatment and can be substantially nonuniform even before the annealing. Its local concentration can considerably exceed the concentration averaged over the volume and be sufficient for the formation of more complicated complexes (quenched-in donors) on increasing temperature.

Since the diffusivity of oxygen is activation-controlled, it increases abruptly in the course of annealing a silicon sample. If the temperature of the sample is below the threshold value (in the opposite case, the oxygen distribution becomes uniform), nonuniformity of the oxygen distribution in silicon increases; the oxygen complexes, including electrically active ones, begin to form where the concentration of oxygen is higher.

The dependence of the formation of quenched-in donors on a preliminary thermal treatment is experimentally confirmed [1, 2]. A number of facts were experimentally established with respect to nonuniform distribution of intrinsic and impurity defects and their complexes in silicon [4, 5] and of the microclusters of oxygen-containing quenched-in donors [6, 7]. The manifestations of elastic fields induced by the spatially periodic variation of the density of the interstitial impurity–defect clusters in silicon were investigated previously [8]. The quasi-periodic distribution of boron in silicon initiated by the ion implantation of boron was observed in [9, 10].

The development of nonuniform distribution and precipitation of oxygen proceed simultaneously and are controlled by its diffusion. Therefore, these processes can be induced not only by annealing but also by any other external action that stimulates the diffusion and gives rise to a nonequilibrium state for which the association of oxygen-containing complexes dominates over their decomposition. Such an action can be, for example, irradiation.

BASIC EQUATIONS

We consider a crystalline oxygen-containing sample of silicon. It is reasonable to assume that it is the transition of oxygen into its metastable interstitial configuration which, being mobile, favors an increase in the oxygen diffusivity. In addition, a higher effective diffusivity is obtained for oxygen if we take into account its diffusion by means of complexes that are formed by oxygen with defects and do not have common bonds with the crystal lattice [2], for example, the complexes with a doubly negatively charged vacancy (migration energy is 0.18 eV) and a singly negatively charged interstitial atom (migration energy is assumed to be 0.4 eV) [2, 11].

The oxygen atoms, which are mobile due to a certain mechanism, (their concentration is denoted by a variable n_1) form the low-mobility complexes, which can contain 2, 3, …, i oxygen atoms (their concentration is n_2, n_3, …, and n_i, respectively). For describing the accumulation of the oxygen-containing complexes when the association processes dominate over those of decomposition, we have the well-known set of equations:

$$\frac{\partial n_1}{\partial t} = -\gamma_{1,2} n_1^2 - \operatorname{div} J + K, \tag{1}$$

$$\frac{\partial n_i}{\partial t} = -\gamma_{i,i+1} n_i n_1 + \gamma_{i-1,i} n_{i-1} n_1. \tag{2}$$

Here, $i = 2, 3, \ldots$;

$$J = -D\left(\nabla n_1 - \frac{n_1 F}{T}\right) \tag{3}$$

is the diffusion flux of the mobile oxygen atoms;

$$F(r) = -\sum_{i=1} \int \nabla V_{1,i}(r-r') n_i(r') dr' \tag{4}$$

is the force acting on oxygen atoms, which are at the point r, and originating from other oxygen atoms and their complexes located at the point r'; and $V_{1,i}(r-r')$ are the corresponding interaction potentials, whose origin can be different. However, in what follows, we assume for definiteness sake that the interaction occurs by means of elastic fields; T is the temperature of a crystal expressed in energy units. The quantity

$$K = K^* + \mu_v N n_v + \mu_i N n_1$$

describes an increase in the concentration of mobile oxygen. This increase is summed from the excitation rate of a metastable interstitial configuration and the rates of formation of complexes: vacancy–(oxygen atom) and (interstitial atom)–(oxygen atom); N is the oxygen concentration; here, n_v and n_i are the concentrations of intrinsic vacancies and interstitial atoms; μ_v and μ_i are proportional to the vacancy diffusivity (D_v) and the interstitial-atom diffusivity (D_i), respectively. The value of K may be small, but, due to the high diffusivity of mobile oxygen [12], its flux can be considerable. The parameters $\gamma_{i,i+1}$ are proportional to the diffusivity $D = D(T)$ and, therefore, depend on temperature.

As a rule, it is the effective oxygen diffusivity that is determined in experiments [2]. If we use its value in Eq. (1), the value of K should be set to zero, while the total concentration of atomically dissolved oxygen is represented by the quantity n_1.

Ignoring the phenomena near the surface, we investigate the cyclic boundary conditions.

UNIFORM DISTRIBUTION

In the case of uniform distribution of oxygen and its complexes, $J = 0$ and Eqs. (1) and (2) are transformed into a set of ordinary differential equations that has a unique homogeneous solution. The quantity $n_1(t)$ can be obtained by direct integration of Eq. (1):

$$n_1(t) = n_{\mathrm{st}}\frac{1 + C\exp(-\zeta t)}{1 - C\exp(-\zeta t)}, \quad (5)$$

where $n_{\mathrm{st}} = \sqrt{K/\gamma_{1,2}}$ is the time-independent solution to Eq. (1), to which the solution for arbitrary initial conditions steadily tends with time;

$$\begin{gathered} C = (n_0/n_{\mathrm{st}} - 1)/(n_0/n_{\mathrm{st}} + 1), \\ \zeta = 2\sqrt{K\gamma_{1,2}}, \quad n_0 = n_1(t = 0). \end{gathered} \quad (6)$$

Using the substitution

$$t \longrightarrow y = \int_0^t n_1(\tau)d\tau,$$

we reduce the set of Eqs. (1) and (2) to the following set of linear inhomogeneous linking equations with constant coefficients:

$$\frac{dn_i}{dy} - \gamma_{i,i+1}n_i = \gamma_{i-1}n_{i-1}, \quad i = 2, 3, \ldots . \quad (7)$$

Solving Eqs. (7) and passing again to the variable t, we obtain

$$n_i(t) = n_1(t)\left(\prod_{l=1}^{i-1}(-\gamma_{l,l+1})\right)\sum_{m=1}^{i}\frac{\left[\frac{n_1(t)}{n_0}\right]^p}{\prod\limits_{\substack{j=1 \\ j\neq m}}^{i}(\gamma_{m,m+1} - \gamma_{j,j+1})},$$

$$p \equiv \frac{\gamma_{m,m+1} - \gamma_{1,2}}{\gamma_{1,2}}. \quad (8)$$

The solution given by (5) and (8) corresponds to the following initial state: $n_1(t = 0) = n_0$, $n_i(t = 0) = 0$ for $i \geq 2$. It was obtained under the assumption that $\gamma_{m,m+1} \neq \gamma_{j,j+1}$ for $m \neq j$. In the steady-state case,

$$n_i(t) = n_i^{\mathrm{st}} = \gamma_{1,2}n_{\mathrm{st}}/\gamma_{i,i+1}.$$

For $K \longrightarrow 0$, $n_1(t) \longrightarrow n_0/(n_0\gamma_{1,2}t + 1)$, and $n_1(t) < n_0$ for $t > 0$.

If $\gamma_{i,i+1} \gg \gamma_{1,2}$ for every $i > 1$, the first term in (8) is much greater than the following ones and the latter can be neglected. In this case, $n_i(t) \approx \gamma_{1,2}n_1(t)/\gamma_{i,i+1}$ and $n_i(t)/n_m(t) \approx \gamma_{m,m+1}/\gamma_{i,i+1}$.

When the phenomenon is considered within the time interval Δt, during which the concentrations of oxygen and its complexes vary insignificantly with time (i.e., for $|\Delta n_1|/n_1 = \gamma_{1,2}n_1\Delta t \ll 1$), we obtain the approximate quasi-stationary solution valid for a time not exceeding the value of Δt.

Knowledge of a homogeneous time-dependent solution given by (5) and (8) to Eqs. (1) and (2) makes it possible both to trace the variation with time in concentrations of complexes containing an arbitrary number of oxygen atoms in the mode of active formation of precipitates and to determine more accurately which of them are electrically active by comparing the experimental time dynamics of the modified electrical properties of a crystal with the corresponding theoretical calculations.

STABILITY OF UNIFORM QUASI-STEADY DISTRIBUTION AND FORMATION OF SPATIALLY PERIODIC DISTRIBUTION

In order to investigate the stability of a quasi-stationary homogeneous solution, we consider the evolution of its small perturbations $\delta n_1(r, t)$ and $\delta n_i(r, t)$. We assume that, in Eqs. (1) and (2), $n_1(r, t) = n_1 + \delta n_1(r, t)$ and $n_i(r, t) = n_i + \delta n_i(r, t)$, where n_1 and n_i are the uniform stationary (quasi-stationary) concentrations. Retaining only linear terms, taking into account that $n_1(t) \approx n_0 \gg n_i$ for $i > 1$, and, therefore, neglecting the interaction with complexes, we obtain the linearized equations for $\delta n_1(r, t)$ and $\delta n_i(r, t)$:

$$\begin{gathered} \frac{\partial\delta n_1}{\partial t} = -2\gamma_{1,2}n_1\delta n_1 - D\Delta\delta n_1 - \frac{D}{T} \\ \times \operatorname{div}[n_1(r)\int\nabla_r V(r - r')\delta n_1(r')]dr', \end{gathered} \quad (9)$$

$$\begin{gathered} \frac{\partial\delta n_i}{\delta t} = -\gamma_{i,i+1}n_i\delta n_1 - \gamma_{i,i+1}n_1\delta n_i \\ + \gamma_{i-1,i}n_{i-1}\delta n_1 + \gamma_{i-1,i}n_1\delta n_i. \end{gathered} \quad (10)$$

The solution to set (9) and (10) has the form

$$\delta n_1(r, t), \quad \delta n_i(r, t) \simeq \exp(\lambda t + ikr).$$

The variance equation for the damping constant λ is as follows:

$$\begin{gathered} \{\lambda + D[\gamma + k^2 + \alpha k^2 V(k)/V_0]\} \\ \times \prod_{i=2}(\lambda + \gamma_{i,i+1}n_0) = 0, \end{gathered} \quad (11)$$

where

$$\begin{gathered} \alpha = n_0V_0/T, \quad \gamma = 2\gamma_{1,2}/D, \\ V(k) = \int V(r)\exp(-ikr)dr. \end{gathered}$$

A value of λ depends on problem parameters and, for some of them ($\alpha = \alpha_c$), a value of Reλ reverses its sign. This occurs for a certain direction and a certain value of the wave vector $k = k_c$. Thereafter, we assume that the wave vector has precisely this direction. The potential $V(k)$ can be expressed in terms of the Green function of a perfect crystal [13]. Retaining the first and second terms, which describe the long-range attraction and the short-range repulsion, we have

$$V(k) = V_0(-1 + Bk^2), \tag{12}$$

where $V_0 = -V(k = 0)$ is the function of elastic moduli and of a variation in a crystal volume as a result of introducing an oxygen atom in the matrix; the coefficient B is of the order of the square of several periods of the crystal lattice.

When the interaction between oxygen atoms exceeds a certain threshold value and dominates over the influence of diffusion, the uniform state becomes unstable. An accidental increase in oxygen concentration in a certain plane leads to the fact that the oxygen atoms tend to be arranged in the same plane, owing to the anisotropy of interaction. Thus, alternating planes are formed: enriched with and depleted of oxygen. They are perpendicular to k_c. A further increase in α leads to the appearance of unstable modes with different k, and the nonuniform distribution becomes more complicated, for example, quasi-periodic or three-dimensional.

We obtain the bifurcation threshold values of α and k from Eq. (11) assuming that

$$\mathrm{Re}[\lambda(\alpha_c, k_c)] = \lambda(\alpha_c, k_c) = 0, \quad \left.\frac{d\lambda}{dt}\right|_{k = k_c} = 0,$$

$$\alpha_c = 1 + 2\sqrt{\gamma n_0 B}(\sqrt{\gamma n_0 B} + \sqrt{\gamma n_0 B + 1}), \tag{13}$$

$$k_c^2 = \frac{\alpha_c - 1}{2\alpha_c B}. \tag{14}$$

The period of the nonuniform distribution for $\alpha = \alpha_c$ is $2\pi/k_c$.

From the analysis of the data obtained, it follows that the threshold value $\alpha = \alpha_c$ increases with oxygen concentration or with the rate of formation of its mobile complexes. The numerical estimates show that a value $\alpha_c - 1$ is on the order of 10^{-3}–10^{-4}. In this case, the period of the nonuniform distribution of oxygen and its complexes can vary nonmonotonically, its characteristic variations with parameters of the problem being from 10 to 1000 Å.

The time of establishing the spatially periodic distribution in this model is governed by the diffusion of oxygen and depends on temperature. Consequently, the spatially nonuniform state can be observed in a certain temperature range. If the crystal temperature is higher than the threshold temperature, the nonuniform state does not develop, but if the temperature is too low, the time of its development becomes large.

The results obtained can serve as a justification for the assumption made by the authors of [4, 7, 14] about the role of the nonuniform distribution of oxygen in the appearance of quenched-in donors observed at low temperatures. Since at temperatures that are low but sufficient for diffusion, the nonuniform distribution of the oxygen-containing complexes is obtained, the formation of more complicated complexes with the electric activity (quenched-in donors) proceeds primarily where the local oxygen concentration is highest.

REFERENCES

1. C. S. Fuller, J. A. Ditzenberg, and N. B. Hannay, Phys. Rev. **96** (3), 833 (1954).
2. V. M. Babich, N. I. Bletskan, and E. F. Venger, *Oxygen in Single Crystals of Silicon* (Interpres, Kiev, 1997).
3. W. Kaiser, H. L. Frish, and H. Reiss, Phys. Rev. **112** (5), 1546 (1958).
4. I. V. Antonova, A. Misyuk, V. P. Popov, and S. S. Shaĭmeev, Fiz. Tekh. Poluprovodn. (St. Petersburg) **31** (8), 998 (1997) [Semiconductors **31**, 852 (1997)].
5. P. A. Pavlov, V. I. Pashkov, and T. Yu. Chigirinskaya, Pis'ma Zh. Tekh. Fiz. **15** (4), 57 (1989) [Sov. Tech. Phys. Lett. **15**, 561 (1989)].
6. N. T. Bagraev, N. A. Vitovskiĭ, L. S. Vlasenko, *et al.*, Fiz. Tekh. Poluprovodn. (Leningrad) **17** (11), 1979 (1983) [Sov. Phys. Semicond. **17**, 1263 (1983)].
7. A. N. Kabaldin, V. B. Neĭmash, V. M. Tsmots', and L. I. Shpinar, Ukr. Fiz. Zh. **40** (10), 1079 (1995).
8. I. I. Kolkovskiĭ and V. V. Luk'yanitsa, Fiz. Tekh. Poluprovodn. (St. Petersburg) **31** (4), 405 (1997) [Semiconductors **31**, 340 (1997)].
9. M. A. Myasnikov, V. I. Obodnikov, V. G. Seryapin, *et al.*, Fiz. Tekh. Poluprovodn. (St. Petersburg) **31** (3), 338 (1997) [Semiconductors **31**, 279 (1997)].
10. M. G. Stepanov, A. B. Potapov, and G. G. Malinetskiĭ, Preprint No. 69, Inst. Prikl. Mat. RAN (Keldysh Institute of Applied Mathematics, Russian Academy of Sciences, 1997).
11. I. D. Konozenko, A. K. Semenyuk, and V. I. Khivrich, *Radiation Effects in Silicon* (Naukova Dumka, Kiev, 1974).
12. L. I. Murin and V. P. Markevich, Fiz. Tekh. Poluprovodn. (Leningrad) **22** (7), 1327 (1988) [Sov. Phys. Semicond. **22**, 840 (1988)].
13. M. A. Krivoglaz, *Diffuse Scattering of X-rays and Neutrons by Fluctuation Nonuniformities in Nonideal Crystals* (Naukova Dumka, Kiev, 1983).
14. D. I. Brinkevich, V. P. Markevich, L. I. Murin, and V. V. Petrov, Fiz. Tekh. Poluprovodn. (St. Petersburg) **26** (4), 628 (1992) [Sov. Phys. Semicond. **26**, 383 (1992)].

Translated by V. Bukhanov

Semiconductors, Vol. 35, No. 1, 2001, pp. 106–111. Translated from Fizika i Tekhnika Poluprovodnikov, Vol. 35, No. 1, 2001, pp. 105–109.
Original Russian Text Copyright © 2001 by Karavaev, Chernyshov.

LOW-DIMENSIONAL SYSTEMS

Resonance Tunneling of X-Electrons in AlAs/GaAs(111) Structures: Pseudopotential Calculations and Models

G. F. Karavaev and V. N. Chernyshov

Siberian Physicotechnical Institute at Tomsk State University, Siberian Division, Russian Academy of Sciences,
Novosobornaya pl. 1, Tomsk, 634050 Russia

e-mail: kanc@spti.tsu.ru

Submitted February 22, 2000; accepted for publication June 21, 2000

Abstract—The *X*-electron resonance tunneling in AlAs/GaAs(111) heterostructures with AlAs electrodes was considered. Calculations of the model with potential discontinuities at the boundaries were carried out using the scattering matrix method. The complex band structure was calculated by the empirical pseudopotential method. Resonance peaks in the transmission coefficients, related to *X*-states in AlAs and *L*-states in GaAs, were found. A model describing these processes is suggested. *© 2001 MAIK “Nauka/Interperiodica”.*

An intensive study of various nanostructures, interesting due to their optical and electrical properties, has been carried out in recent years. Most of the studies deal with GaAs/AlAs(001) heterostructures having AlAs layers embedded in the GaAs crystal. The electronic properties of such structures are related to the Γ-valley electrons, but the so-called Γ*X*-mixing of electrons at the heterojunction interfaces is also important.

In this study, we focus our attention on structures with (111)-plane interfaces. There are experimental studies dedicated to heterostructures grown on the GaAs substrates with such interfaces (see [1–8], for instance). It is shown in [1–8], that under certain conditions of the growing process, high-quality structures having a fairly large peak-to-valley ratio in the current–voltage characteristic can be manufactured. A resonance tunneling in the double-barrier GaAs/AlAs(111) structure was considered theoretically in [9], where ΓΓ, Γ*L* and *LL* transfer channels were analyzed. Resonance properties of such structures are governed mainly by the tunneling of the Γ-electrons from the GaAs conduction-band minimum. The AlAs conduction-band bottom is known to include three nonequivalent *X* valleys; therefore, they have an essential role to play in the tunneling processes. However, the Γ-valley electrons in GaAs cannot pass into *X* valleys crossing the (111) interface without scattering at phonons or defects, which essentially complicates the description of the tunneling process.

A different situation occurs in AlAs/GaAs(111) structures with thin GaAs layers incorporated in the AlAs crystal. The resonance properties of the structure are determined in this case by *X*-electron tunneling from the AlAs conduction-band minimum. Estimations show that, for a GaAs layer thickness of less than ten monolayers, the resonance Γ states are higher in energy than *X* valleys in AlAs and, therefore, the *X* electrons make the main contribution to the electronic properties of such heterostructures. Substituting the GaAs layer with the $Al_xGa_{1-x}As$ solid solution and choosing the solid-solution composition, we can obtain a situation where the Γ-electrons in it do not influence the heterostructure properties. A similar effect can also be obtained with hydrostatic compression.

We now consider an AlAs/GaAs heterostructure with the (111) plane interfaces having AlAs as electrodes. Scattering of *X* electrons by such heterointerfaces occurs when a nonvanishing wave vector component $k_\parallel$ parallel to the boundary exists. For a given structure, six points with coordinates $k_\parallel = (2\pi/3a)(\pm1, \pm, \mp2)$ (a is the lattice constant) exist in the surface Brillouin zone; the *X* valleys are situated and the *L* valleys exist for the same $k_\parallel$ in their neighborhood. For a given $k_\parallel$, the *X* valleys have wave-vector components $k_\perp = (2\pi/3a)(\mp1, \mp1, \mp1)$ normal to the interface plane, and the *L* valleys have $k_\perp = (2\pi/3a)(\pm1, \pm1, \pm1)$. The wave-vector component $k_\parallel$ is conserved when passing across the heterointerface, while the $k_\perp$ component is not conserved. Therefore, the *XL* scattering at the (111) heterointerface is possible for a given $k_\parallel$. Since the *L*-state energy in GaAs E_L(GaAs) is close to 0.29 eV, and the *X*-state energy in AlAs E_X(AlAs) is close to 0.21 eV (energy is measured from the GaAs conduction-band bottom), the *XL*-mixing of electronic states upon scattering at the heterointerface is important. In such structures, the *X* wells and *L* barriers exist in AlAs and in GaAs, conversely, the *L* wells and *X* barriers exist.

We studied *XX*, *XL*, and *LL* mixing in a AlAs/GaAs(111) structure using a model of the crystal potential with a discontinuity at the heterointerface. In such a model, general solutions to the Schrödinger equation and their normal derivatives are sewed at the interface plane. The so-called complex band-structure problem is solved in order to construct general solutions in every layer. For the AlAs/GaAs $(3\sqrt{3}\,a)$/AlAs $(3\sqrt{3}\,a)$/GaAs $(3\sqrt{3}\,a)$/AlAs heterostructure (the thickness of a layer is given in the parentheses) we calculated the transmission coefficient P_{XX} (the first and second subscripts designate, respectively, the incident and passing wave types) for valleys with $k_{\|} = (2\pi/3a)(1, 1, -2)$. Obviously, a similar result will be obtained for other valleys. Heteroboundaries coincided with the As-layer planes. Calculation was carried out by the scattering-matrix technique [10]; the complex band structure was determined using the empiric pseudopotential approach. A detailed description of the calculation method is given elsewhere [11, 12]. Parameters of the pseudopotentials [13] were determined from the conditions for best fit of calculated and experimentally obtained energy gaps. Reciprocal lattice vectors satisfying the condition $(k_0 + b_1)^2 \le 10(2\pi/a)^2$, where k_0 is equal to k_X or k_L, were exactly taken into account in the wave function expansion; in addition, about 250 plane waves were taken into account using the Levdin perturbation theory. We have shown that consideration of such a large number of plane waves is necessary to preserve the unitarity of the scattering matrix.

The GaAs(111) complex band structure is illustrated in Fig. 1. For a chosen $k_{\|}$, the X valley of the $X(0, 0, -1)$ type exists for $k_X = k_\perp = (2\pi/3a)(-1, -1, -1)$; the L valley of the $L(1/2, 1/2, -1/2)$ type exists for $k_L = k_\perp = (2\pi/6a)(1, 1, 1)$. Solid lines in Fig. 1 represent the energy dependences for real $k_\perp$. The variation range of real $k_\perp$ is equal to the reciprocal-space period in direction (111), i.e., $2\sqrt{3}\,\pi/a$. Dotted lines in Fig. 1 depict the dependences for complex $k_\perp$ with $\mathrm{Re}k_\perp = k_X$ or k_L. Apart from data on real wave vectors, there are a lot of $k_\perp(E)$ dependences with large $\mathrm{Im}k_\perp(E)$ within the chosen energy range, which are not presented in Fig. 1. The complex band structure of AlAs(111) has similar features. All branches of the complex band structure (about 30) were taken into account to construct the general solution to the Schrödinger equation.

The transmission coefficients P_{XX} are shown in Fig. 2. First two peaks correspond to the X resonances in the AlAs X well. An intricate structure near the energy of 0.42 eV is related to L resonances in the GaAs L-wells and appears due to the XL interaction at heteroboundaries. We note that the XL interaction is fairly weak and features a pronounced dependence on the heteroboundary type. Thus, the transmission coefficient for the AlAs/GaAs system with a single heteroboundary is equal to approximately 0.04 (for energy near 0.42 eV) if the Ga atomic plane in GaAs is nearer to the heteroboundary (*ga*-type) than the Al plane in AlAs. In the opposite case (the *al*-type heteroboundary), this coefficient is three orders of magnitude smaller. In the structure considered, the order of heteroboundaries is the following: *al–ga–al–ga*. It is this dependence on the heteroboundary type that gives rise to the essential distinction of peak heights near the energy of 0.42 eV. Changing the system dimensions, we found that the first peak of the transmission coefficient in the vicinity of the above energy (of smaller height) is related to the right-hand GaAs L well, whereas the second (larger) peak is related to the left-hand one. The qualitative explanation of this behavior is as follows. An electron reaching the right-hand GaAs L well “leaves the field” rather easily violating sharp resonance conditions, since the transmission coeffi-

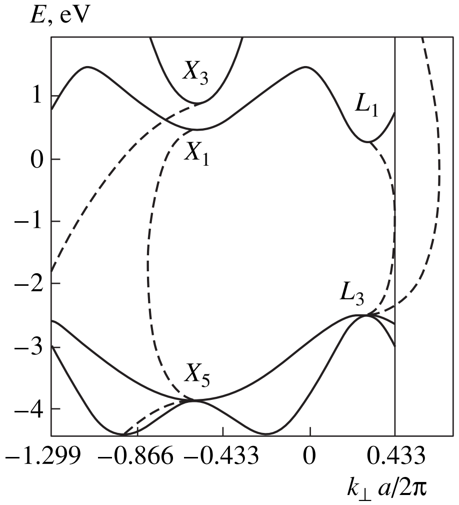

Fig. 1. Complex band structure of GaAs(111) for $k_{\|} = (2\pi/3a)(1, 1, -2)$. Solid lines represent the real-$k_\perp$ dependence of the energy and dashed lines represent the complex-$k_\perp$ dependence of the energy for $\mathrm{Re}k_\perp = k_X$ (or k_L).

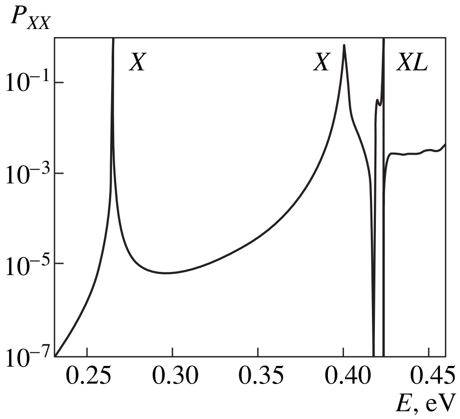

Fig. 2. Transmission coefficients P_{XX} for the AlAs/GaAs $(3\sqrt{3}\,a)$/AlAs$(3\sqrt{3}\,a)$/GaAs$(3\sqrt{3}\,a)$/AlAs heterostructure. Types of resonance peaks are shown.

Table 1. Energy values (in eV) at the X and L points for AlAs and GaAs

	X_1	X_3	X_5	L_1	L_3^{v}	L_3^{c}
AlAs	0.20823	1.18303	–4.24294	0.86169	–2.88137	3.06542
GaAs	0.46877	0.90684	–3.84209	0.29084	–2.45145	3.36002

cient for the rightmost (*al*-type) GaAs/AlAs heteroboundary is about 0.04. A different situation occurs for electrons in the left-hand GaAs L well, where an electron is confined between the first (*al*-type) and third (also *al*-type) heteroboundaries, with the transmission coefficients being of three orders of magnitude smaller.

Analysis of the results of pseudopotential-based calculation data shows that, within the energy range necessary for the description of the electron scattering with the participation of X and L states of AlAs and GaAs, it is sufficient to consider only the interaction of the states in the X_1, X_3, and L_1 valleys. What is more, qualitatively correct results can be obtained in the two-valley approximation with the X_1 and L_1 valleys involved. Consideration of X_3 states is necessary to satisfy the conditions of the obtained scatting matrices more exactly.

Table 2. Values of the momentum-operator matrix elements (in atomic units) for AlAs and GaAs

	AlAs	GaAs
$\langle X_1\|p_z\|X_3\rangle$	0.10793i	0.11399i
$\langle X_1\|p_x\|X_{5x}\rangle$	0.49409i	0.49235i
$\langle X_3\|p_x\|X_{5y}\rangle$	0.52922i	0.52863i
$\langle L_1\|p_x\|L_{31}^{\mathrm{v}}\rangle$	0.42154i	0.42011i
$\langle L_1\|p_x\|L_{32}^{\mathrm{v}}\rangle$	0.24338i	0.24254i
$\langle L_1\|p_x\|L_{31}^{\mathrm{c}}\rangle$	0.00581i	0.00910i
$\langle L_1\|p_x\|L_{32}^{\mathrm{c}}\rangle$	−0.00335i	−0.00525i
$\langle L_{31}^{\mathrm{v}}\|p_x\|L_{31}^{\mathrm{c}}\rangle$	0.26767i	0.26246i
$\langle L_{31}^{\mathrm{v}}\|p_x\|L_{32}^{\mathrm{c}}\rangle$	−0.34219i	−0.34272i
$\langle L_{32}^{\mathrm{v}}\|p_x\|L_{31}^{\mathrm{c}}\rangle$	0.34219i	0.34272i
$\langle L_{32}^{\mathrm{v}}\|p_x\|L_{32}^{\mathrm{c}}\rangle$	0.12746i	0.133263i
$\langle L_{31}^{\mathrm{v}}\|p_z\|L_{31}^{\mathrm{c}}\rangle$	−0.32502i	−0.33112i
$\langle L_{32}^{\mathrm{v}}\|p_z\|L_{32}^{\mathrm{c}}\rangle$	−0.46523i	−0.46038i

Thus, one may hope to construct, within the framework of the method of envelope wave functions, a three-valley model, which adequately reproduces the results of the exact calculation of the electron transmission. A variant of the *kp* Hamiltonian, ensuring more or less correct results for the complex band structure, is necessary to construct a model. Sewing conditions for the envelope functions consistent with the exact calculation are also necessary.

In order to construct the model, we expand wave functions for any layer near points k_0 as

$$\psi_{k_0k} = \exp[i(k-k_0)r]\sum_m D_m(k)|K_{0m}\rangle, \qquad (1)$$

where k_0 equals k_X or k_L, and $|K_{0m}\rangle$ are the Bloch functions at the point k_0.

The expansion coefficients $D_m(k)$ and $k_\perp$ can be found from the following set of equations which has to be solved for fixed E and $k_\parallel$:

$$\sum_m D_m(k)\{[E_m(k_0) + (k-k_0)^2 - E]\delta_{nm} + 2(k-k_0)p_{nm}\} = 0. \qquad (2)$$

Here, $p_{nm} = \langle K_{0n}|p|K_{0m}\rangle$ is the matrix element of the momentum operator and $E_m(k_0)$ is the energy at the point k_0. Hereafter, we use the atomic units. Thus, solving Eq. (2), we determine the complex band structure, i.e. the dependences $k_{\perp j}(E, k_\parallel)$ and $D_m(E, k_\parallel, k_{\perp j})$ relations, where j is a number of the solution.

Our studies showed that, when constructing the *kp* Hamiltonian in the vicinity of the $X(0, 0, –1)$ point in the energy range of interest, we may restrict ourselves to the consideration of the X_1 and X_3 conduction-band valleys and the X_5 valence-band valley. We note that a consideration of the X_5 valleys is necessary to obtain a correct $k_{\perp j}(E, k_\parallel)$ dependence, but their contribution into the wave function is insignificant. We took into account in (1) and (2) the L_1 conduction-band valley and the L_3^v valence-band and L_3^c conduction-band valleys in the neighborhood of the $L(1/2, 1/2, –1/2)$ point. The corresponding wave functions have a major contribution from the L_1 valleys with small corrections due to the L_3 states. The quadratic dispersion law is valid here in a wide energy range, yielding accurately

Table 3. Values of the t_{ij} matrix elements in atomic units

i	j					
	1	2	3	4	5	6
1	–0.0257	0.0452	0.0170	0.0146	–0.0131	0.0067
2	0.0286	–0.0223	–0.0139	0.0024	0.0351	0.0113
3	0.0128	–0.0472	0.0018	0.0396	0.0744	0.0085
4	–0.0089	–0.0100	0.0035	0.0754	–0.1680	0.0446
5	0.0022	–0.0024	0.0066	–0.0031	0.0178	0.0086
6	0.0092	0.0194	–0.0058	–0.0358	0.1515	0.0033

the branches of the complex band structure shown in Fig. 1, which begin from the L_1 lower conduction band level.

The energies $E_m(k_0)$ and the matrix elements of momentum operator were found using pseudowave functions obtained as a result of the exact pseudopotential calculation. The values of these quantities are listed in Tables 1 and 2. The momentum-matrix elements are given for $X(0, 0 –1)$ and $L(1/2, 1/2, 1/2)$ valleys. The X_{5x} and X_{5y} wave functions of the degenerate X_5 state have, respectively, a symmetry of x and y coordinates; the L_{31} and L_{32} wave functions for the degenerate L_3 levels have, respectively, the symmetries $(1/\sqrt{2})(x - y)$ and $(1/\sqrt{6})(x + y - 2z)$. The momentum-matrix elements that are not listed in Table 2 are either zero or can be easily determined on the grounds of symmetry. The momentum-matrix elements for other X and L valleys can be obtained using the relevant symmetry elements from the group T_d^2.

A general solution for the given E and $k_{\|}$ can be derived as a superposition of solutions related to the L and X points. We introduce the notation $\chi_j = k_{\perp j} - k_{0\perp}$ and the following numeration of the complex band structure branches. Let $\chi_1 = -\chi_4$ ($\mathrm{Re}\chi_1 > 0$, or $\mathrm{Im}\chi_1 > 0$) correspond to branches beginning from the level X_1 of the conduction band, let $\chi_3 = -\chi_6$ ($\mathrm{Re}\chi_3 > 0$, or $\mathrm{Im}\chi_3 > 0$) correspond to branches beginning from the level X_3 and let $\chi_2 = -\chi_5$ ($\mathrm{Re}\chi_2 > 0$, or $\mathrm{Im}\chi_2 > 0$) correspond to branches beginning from the level L_1 of the conduction band. Then the general solution for the fixed value of $k_{\|}$ can be represented as

$$\Psi_E = \sum_{j=1}^{6} C(\chi_j, E)\Psi_j, \tag{3}$$

where $C(\chi_j E)$ are arbitrary coefficients, and $\Psi_j = \Psi_{k_0 k_j}$ are particular solutions found previously. Using this procedure, we can first find general solutions both to the left and to the right of the heteroboundary and also the conditions for sewing at the heteroboundary including twelve different coefficients $C(\chi_j, E)$ (six for each side).

Substituting (1) into (3), we can rewrite the general solution (3) as

$$\Psi_E = F_{X_1}|X_1\rangle + F_{X_3}|X_3\rangle + F_{L_1}|L_1\rangle, \tag{4}$$

where the envelope functions F are defined by the relations

$$\begin{aligned}
F_{X_1} = {} & C(\chi_1)D_{X_1}(\chi_1)\exp(i\chi_1 z) \\
& + C(-\chi_1)D_{X_1}(-\chi_1)\exp(-i\chi_1 z) \\
& + C(\chi_3)D_{X_1}(\chi_3)\exp(i\chi_3 z) \\
& + C(-\chi_3)D_{X_1}(-\chi_3)\exp(-i\chi_3 z), \\
F_{L_1} = {} & C(\chi_2)D_{L_1}(\chi_2)\exp(i\chi_2 z) \\
& + C(-\chi_2)D_{L_1}(-\chi_2)\exp(-i\chi_2 z), \\
F_{X_3} = {} & C(\chi_1)D_{X_3}(\chi_1)\exp(i\chi_1 z) \\
& + C(-\chi_1)D_{X_3}(-\chi_1)\exp(-i\chi_1 z) \\
& + C(\chi_3)D_{X_3}(\chi_3)\exp(i\chi_3 z) \\
& + C(-\chi_3)D_{X_3}(-\chi_3)\exp(-i\chi_3 z).
\end{aligned} \tag{5}$$

The z-axis is here directed along the (111) direction. We note that the terms related to the envelope functions $|X_5\rangle$ and $|L_3\rangle$ are omitted in (5). As was mentioned above, their contribution to the wave functions is negligible. Derivatives of the envelope functions are given by

$$\begin{aligned}
F'_{X_1} = {} & i\chi_1[C(\chi_1)D_{X_1}(\chi_1)\exp(i\chi_1 z) \\
& - C(-\chi_1)D_{X_1}(-\chi_1)\exp(-i\chi_1 z)] \\
& + i\chi_3[C(\chi_3)D_{X_1}(\chi_3)\exp(i\chi_3 z) \\
& - C(-\chi_3)D_{X_1}(-\chi_3)\exp(-i\chi_3 z)], \\
F'_{L_1} = {} & i\chi_2[C(\chi_2)D_{L_1}(\chi_2)\exp(i\chi_2 z) \\
& - C(-\chi_2)D_{L_1}(-\chi_2)\exp(-i\chi_2 z)],
\end{aligned} \tag{6}$$

$$\begin{aligned} F'_{X_3} = {} & i\chi_1[C(\chi_1)D_{X_3}(\chi_1)\exp(i\chi_1 z) \\ & - C(-\chi_1)D_{X_3}(-\chi_1)\exp(-i\chi_1 z)] \\ & + i\chi_3[C(\chi_3)D_{X_3}(\chi_3)\exp(i\chi_3 z) \\ & - C(-\chi_3)D_{X_3}(-\chi_3)\exp(-i\chi_3 z)]. \end{aligned}$$

For the fixed z corresponding to a certain position of the heteroboundary, six relations (5) and (6) can be represented in the matrix form as

$$\mathbf{F} = \mathbf{\Phi C}, \quad (7)$$

where $\mathbf{F}$ is a vector with F_{X_1}, F_{L_1}, F_{X_3}, F'_{X_1}, F'_{L_1}, and F'_{X_3} components; $\mathbf{C}$ is a vector with components $C(\chi_1)$, $C(\chi_2)$, $C(\chi_3)$, $C(-\chi_1)$, $C(-\chi_2)$, and $C(-\chi_3)$; and $\mathbf{\Phi}$ is a 6×6 matrix, whose elements are determined from the relations (5) and (6).

Relation (7) can be written for both of the materials forming the heterostructure. The subscripts "1" and "2" stand, respectively, for the material on the left (AlAs in our case) and on the right (GaAs); thus, we have

$$\mathbf{F}_1 = \mathbf{\Phi}_2\mathbf{C}_1, \quad \mathbf{F}_2 = \mathbf{\Phi}_2\mathbf{C}_2. \quad (8)$$

A relation between the $\mathbf{C}_1$ and $\mathbf{C}_2$ coefficients (conditions for sewing on the heteroboundary) can be written as

$$\mathbf{C}_1 = \mathbf{J}\mathbf{C}_2, \quad (9)$$

where $\mathbf{J}$ is the so-called sewing matrix for a given heteroboundary; its elements are calculated in the pseudopotential approximation. Notice, that, in the three-valley approximation, $\mathbf{J}^{-1}$ coincides very closely with the sewing matrix at the next GaAs/AlAs boundary (we chose an even number of monolayers between these heteroboundaries), which is a clear indication of the three-valley approximation validity.

The sewing conditions for the envelope functions and their derivatives follow from (8) and (9) and have the form

$$\mathbf{F}_1 = \mathbf{T}\mathbf{F}_2, \quad (10)$$

where $\mathbf{T}$ is a 6×6 matrix:

$$\mathbf{T} = \mathbf{\Phi}_1\mathbf{J}\mathbf{\Phi}_2^{-1}. \quad (11)$$

Calculation of the $\mathbf{T}$ matrix elements showed their weak energy dependence. Therefore, energy-averaged values can be used for the $\mathbf{T}$ matrix elements. It is convenient to represent the results in the symmetric form as

$$\mathbf{T}_1\mathbf{F}_1 = \mathbf{T}_2\mathbf{F}_2, \quad (12)$$

where $\mathbf{T} = \mathbf{T}_1^{-1}\mathbf{T}_2$. Matrix elements of T_k ($k = 1, 2$) have the form:

$$(T_k)_{ij} = \delta_{ij} + (-1)^k t_{ij}, \quad (k = 1, 2). \quad (13)$$

Values of t_{ij} are given in Table 3. Notice, that the matrix elements of $\mathbf{T}$ in the off-diagonal blocks (t_{ij} for $i = 1, 2, 3$; $j = 4, 5, 6$; $i = 4, 5, 6$; and $j = 1, 2, 3$) depend on a choice of wave vector dimension and, therefore, they cannot be compared with dimensionless t_{ij} in the diagonal blocks of this matrix. The nonvanishing of t_{ij} is due to the difference between the complex band structures for AlAs and GaAs and to the wave-function overlap in the boundary plane. By analyzing the data in Table 3, we may draw the qualitative conclusion that the *XL* interaction is mainly due to the mixing of derivatives of the *L* and *X* envelope functions in the boundary plane. When using the sewing conditions for the envelope functions, it is well to bear in mind that they were derived in the atomic units ($\hbar = 1$, $m_0 = 1/2$, where m_0 is the electron mass). The $|X_1\rangle$, $|X_2\rangle$, and $|L_1\rangle$ functions for both materials have to be real. The presented t_{ij} values are related to the AlAs/GaAs boundary with AlAs being on the left (the "*al*" boundary in our notation). For heteroboundaries removed from it by an even number of monolayers, the sewing conditions remain the same. For the heteroboundaries removed from it by an odd number of monolayers, the sign before F_{L_1} and F'_{L_1} for both materials has to be changed in the formula (12) in order to obtain the boundary conditions, which is rather obvious.

In order to verify the model, we calculated the transmission coefficients for the above-mentioned structure using the sewing condition (12) and obtained a nearly perfect agreement with the pseudopotential calculation data. This permits us to conclude that the fairly simple model developed is adequate. We anticipate that the obtained sewing conditions for envelope functions will be used for the calculation of various physical characteristics of heterostructures: tunneling times, current–voltage characteristics, etc.

ACKNOWLEDGMENTS

This study was supported in part by the program of the Russian Ministry of Science "Surface atomic structures" (project no. 5.12.99) and the Russian Foundation for Basic Research (project no. 00-02-17996).

REFERENCES

1. S. de Gironncoli, S. Baroni, and R. Resta, Phys. Rev. Lett. **62**, 2853 (1989).
2. M. Livingstone, I. Galbraith, and B. S. Wherrett, Nuovo Cimento **17**, 1595 (1995).
3. L. Cong, E. Williamson, and M. J. Nathan, J. Electron. Mater. **25**, 305 (1996).

4. B. J. García, C. Fontaine, W. W. Ruhle, *et al.*, Microelectron. J. **26**, 777 (1995).
5. A. Chin and K. Lee, Appl. Phys. Lett. **68**, 3437 (1996).
6. R. K. Hayden, T. Takamasu, N. Miura, *et al.*, Tech. Rep. ISSP, No. 3148, 1 (1996).
7. T. Watanabe, T. Yamamoto, P. O. Vassaro, *et al.*, Microelectron. J. **27**, 411 (1996).
8. G. Wang, P. Trong, R. Melliti, *et al.*, Phys. Status Solidi A **164**, 117 (1997).
9. G. F. Karavaev and S. N. Grinyaev, Izv. Vyssh. Uchebn. Zaved. Fiz., No. 9, 91 (1998).
10. D. Y. Ko and J. S. Inkson, Phys. Rev. B **38**, 9945 (1988).
11. S. N. Grinyaev and V. N. Chernyshov, Fiz. Tekh. Poluprovodn. (St. Petersburg) **26**, 2057 (1992) [Sov. Phys. Semicond. **26**, 1157 (1992)].
12. G. F. Karavaev, S. N. Grinyaev, and V. N. Chernyshov, Izv. Vyssh. Uchebn. Zaved. Fiz., No. 9, 64 (1992).
13. V. A. Chaldyshev and S. N. Grinyaev, Izv. Vyssh. Uchebn. Zaved. Fiz., No. 3, 38 (1983).

Translated by S. Ktitorov

Semiconductors, Vol. 35, No. 1, 2001, pp. 112–116. Translated from Fizika i Tekhnika Poluprovodnikov, Vol. 35, No. 1, 2001, pp. 110–114.
Original Russian Text Copyright © 2001 by Berashevich, Danilyuk, Kholod, Borisenko.

LOW-DIMENSIONAL SYSTEMS

Charge-Carrier Transport in Nanometer-Sized Periodic Si/CaF$_2$ Structures with Participation of Traps

Yu. A. Berashevich*, A. L. Danilyuk, A. N. Kholod, and V. E. Borisenko
Belarussian State University of Information Science and Radio Engineering, ul. Brovki 17, Minsk, 220013 Belarus
** e-mail: julia@nano.bsuir.edu.by*

Submitted April 28, 2000; accepted for publication June 22, 2000

Abstract—A model is proposed for carrier transport in Si/CaF$_2$ nanometer periodic structures with the participation of traps in insulators. Simulation of the current–voltage characteristics of such structures showed that trap participation enhances the total carrier transport by 2–3 orders of magnitude and causes nonmonotonicity of current–voltage characteristics. The carrier transport depends on the energy level corresponding to traps, the number of states in a trap at the carrier trajectory, its deviation from a rectilinear one, insulator thickness, and potential barrier height. *© 2001 MAIK “Nauka/Interperiodica”.*

INTRODUCTION

Nanometer structures forming a system of quantum wells (QWs) are attracting increasing interest due to their prospective application as a basis of solid-state devices employing quantum-size effects [1].

From the viewpoint of compatibility with the well-developed silicon technology, it seems profitable to study periodic structures based on Si/CaF$_2$ [2–4]. These are produced by molecular-beam epitaxy on single-crystal silicon substrates [5]. Alternating nanometer-sized insulator and semiconductor layers form a periodic structure where each period includes Si and CaF$_2$ layers. It is of great interest to study mechanisms of carrier transport via QWs formed in such structures in the context of their outlook for optoelectronics and nanoelectronics.

The experiments [6–8] showed that the carrier transport through the Si/CaF$_2$ periodic structures implies a nonuniform distribution of electrons and holes over structure periods, a region of negative differential resistance (NDR) in the current–voltage characteristic, charging effects (including a nonzero potential at a zero current), nonlinear temperature dependences of current, etc. Each effect is undeniably related to the contribution of certain carrier transport mechanisms. The most probable is the tunnel transport and transport over trap states assisted by carrier “heating” and avalanche multiplication, and charge accumulation in QWs.

However, from the viewpoint of model concepts, only the tunnel transport was adequately described [6].

To develop this model, we analyzed electron and hole transport through the Si/CaF$_2$ periodic structure over trap states in the insulator. Such transport was considered simultaneously with the classical tunneling described by the Wentzel–Kramers–Brillouin (WKB) approximation. The generalized model and numerical analysis are considered in this paper.

THE MODEL

The Si/CaF$_2$ periodic structure forms a system of QWs, where the wide-gap insulator CaF$_2$ and silicon play the role of a barrier and a potential well, respectively. The energy diagram of such a structure with an external bias and the considered electron and hole transport mechanisms are shown in Fig. 1. In the absence of an external bias, the potential barrier shape is assumed to be rectangular.

The model includes the following groups of electron processes: (i) carrier injection from the contact via tunneling through the insulator barrier and traps in the barrier, (ii) carrier tunneling through potential barriers and their simultaneous transport over trap levels in the insulator barrier, (iii) electron and hole recombination in the semiconductor, and (iv) carrier drain to the contact via tunneling and with the participation of traps.

Electron and hole tunneling through the insulator barrier is assumed to be elastic. The tunneling probability is determined in the quasi-classical WKB approximation [9].

Along with carrier tunneling through potential barriers, we consider carrier transport over trap levels in insulator layers.

Trap levels are assumed to be produced by the Schottky structural defects, i.e., empty sites caused by CaF$_2$ molecule dissociation. These defects in polar crystals can be double and single [10]. Double Schottky defects are neighboring vacancies of opposite polarity, arising due to Ca and F atom transition into interstices followed by vacancy diffusion to sinks. Double defects form traps for electrons and holes. Single defects, i.e., vacancies of the same type, form traps only for electrons or only for holes. The carrier transport with the participation of traps proceeds in the relay-race mode. It is also assumed that a fraction of the carriers in silicon layers is involved in radiative and nonradiative recombination.

To determine the current through the structure, we write a set including continuity equations for electron and hole fluxes, the one-dimensional Poisson equation, and an equation describing the distribution of the external applied voltage V_{bias} between the structure contacts and periods:

$$\begin{cases} \dfrac{dn_i}{dt} = g_i^{\text{trap}}(n_{i-1}, n_i) - g_{i+1}^{\text{trap}}(n_i, n_{i+1}) \\ \quad + g_i^{\text{tun}}(n_{i-1}, n_i) - g_{i+1}^{\text{tun}}(n_i, n_{i+1}) - \gamma_i n_i p_i, & (1) \\ \dfrac{dp_i}{dt} = g_{i+1}^{\text{trap}}(p_{i+1}, p_i) - g_i^{\text{trap}}(p_i, p_{i-1}) \\ \quad + g_{i+1}^{\text{tun}}(p_{i+1}, p_i) - g_i^{\text{tun}}(p_i, p_{i-1}) - \gamma_i n_i p_i, & (2) \\ \dfrac{d}{dx}\left(\varepsilon_i \dfrac{d\varphi_i}{dx}\right) = -\dfrac{q(n_i - p_i)}{\varepsilon_0}, & (3) \\ V_{\text{bias}} = \sum_1^n \varphi_i + \varphi_{k1} + \varphi_{k2}. \end{cases}$$

Here $i = 1, \ldots, n$ is the structure period index (n is the number of periods), $n_i(p_i)$ is the electron (hole) concentration in the ith semiconductor layer, g_i^{trap} is the rate of carrier transport through the ith insulator layer with the participation of traps, g_i^{tun} is the rate of tunnel carrier transport through the ith insulator layer, γ_i is the coefficient of electron and hole recombination in the ith semiconductor layer, ε_0 is the permittivity of free space, ε_i is the piecewise continuous function consisting of the relative permittivities of semiconductor and insulator materials in the ith period, q is the elementary charge, φ_i is the potential drop at the ith period, and φ_{k1} and φ_{k2} are potential drops at the emitter and collector, respectively.

The rates of electron and hole tunnel transition through the potential barrier are given by (see [6])

$$g_{i(n)}^{\text{tun}} = \frac{\sqrt{m_{yn} m_{zn}}}{2\pi^2 \hbar^3 d_{\text{Si}}} \int_0^{E_{\text{F}}} [F_{i(C)}(E) - F_{i(C)}(E + q\varphi_{Di})] dE \times \int_0^E D_{i(n)}^{\text{tun}}(E - E_\perp, m_{xn}) dE_\perp, \quad (4)$$

$$g_{i(p)}^{\text{tun}} = \frac{\sqrt{m_{yp} m_{zp}}}{2\pi^2 \hbar^3 d_{\text{Si}}} \int_{E_{\text{F}}}^0 [F_{i(V)}(E) - F_{i(V)}(E + q\varphi_{Di})] dE \times \int_0^E D_{i(p)}^{\text{tun}}(E - E_\perp, m_{xp}) dE_\perp, \quad (5)$$

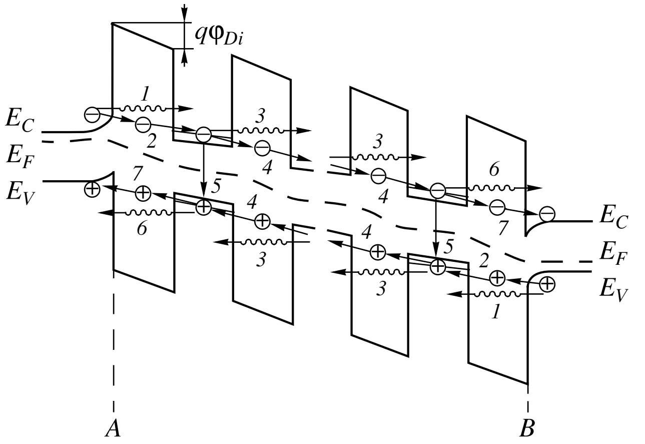

Fig. 1. Energy diagram of the Si/CaF$_2$ structure and electron and hole behavior in it: (*1*) tunneling from the emitting contact, (*2*) emission from the emitting contact into traps in the insulator, (*3*) tunneling through the insulator barrier, (*4*) transport through the trap level in insulator, (*5*) recombination, (*6*) carrier tunneling to the collector contact, and (*7*) transport from insulator traps to the collector contact; *A* is the electron emitter (hole collector) and *B* is the electron collector (hole emitter).

where $m_{xn(p)}$, $m_{yn(p)}$, and $m_{zn(p)}$ are the effective masses of electrons (n) and holes (p) in the silicon well; the tunneling direction is along the axis x; directions z and y lie in the plane of layers; $D_{in(p)}^{\text{tun}}$ is the barrier tunnel penetrability for electrons (holes); $\hbar$ is the Planck constant; d_{Si} is the silicon layer thickness, E is the maximum electron energy in the injecting electrode; $F_{iC(V)}(E)$ is the Fermi–Dirac distribution function for electrons (holes); and φ_{Di} is the potential drop across the ith insulator layer.

The tunneling probability in terms of the WKB approximation [9] is given by

$$D_{in(p)}^{\text{tun}} = \exp\left(-\frac{2}{\hbar}\int_{x_1}^{x_2}\left\{2m_{xn(p)}\left[U_{in(p)} - \left(\frac{q^3\varphi_i}{4\pi\varepsilon_0\varepsilon_D d_D}\right)^{1/2} - E + E_\perp\right]\right\}^{1/2} dx\right), \quad (6)$$

where x_1 and x_2 are classical turning points, $U_{in(p)}$ is the potential barrier height for electrons (n) and holes (p), and d_D is the insulator layer thickness.

The rates of electron and hole tunneling transitions over trap states when the carrier energy reaches the trap level energy are written as (see [11-12])

$$g_{in(p)}^{\text{trap}} = \frac{a^2\sqrt{m_{yn(p)} m_{zn(p)}}}{4\pi^2 \hbar d_D m_{xn(p)}}$$

$$\times \int_{0}^{E_F} [F_{iC(V)}(E) - F_{iC(V)}(E + q\varphi_{Di})]dE \quad (7)$$

$$\times \int_{E_F - q\varphi_{Di}}^{E} ED^{\text{trap}}_{in(p)}(E - E_\perp)dE_\perp,$$

where a is the distance between trap states. The coefficient of carrier tunnel passage over trap levels in an insulator is given by (see [11,12])

$$D^{\text{trap}}_{in(p)} = G\sum_{m=0}^{\infty}(p_m)\frac{m!}{d_D^m}\alpha^{-m}_{in(p)}, \quad (8)$$

where

$$p_m = \frac{(N_D a^2 d_D)^m}{m!}\exp(-N_D a^2 d_D)$$

is the probability of m traps being arranged along the carrier trajectory through insulator with the defect concentration N_D,

$$\alpha^{-1}_{in(p)} = [2m_{xn(p)}(U_{in(p)} - E + E_\perp)/\hbar^2]^{-0.5}$$

is the characteristic attenuation length of an electron (hole) state (of energy E) in a uniform barrier, G is the contribution to the coefficient of tunnel passage of levels broadened due to charging effects, scattering, and deviation of trap level trajectories from the rectilinear.

Parameters employed to simulate carrier transport in Si/CaF$_2$ layered structures

Parameter	Value
CaF$_2$ layer thickness	1–2.5 nm
Si layer thickness	1–2.5 nm
Number of periods	20
Potential barrier height for electrons [13]	3.3 eV
Potential barrier height for holes [13]	7.6 eV
Effective electron mass in the silicon QW plane [5]	$0.35m_0$
Effective hole mass in the silicon QW plane [5]	$0.35m_0$
Effective mass for electron tunneling [14]	$0.42m_0$
Effective mass for hole tunneling [14]	$0.42m_0$
Recombination coefficient for electrons and holes in a semiconductor	10^{-22} m^{-3} s^{-1}
Carrier density at contacts	10^{22} m^{-3}
Relative dielectric constant of CaF$_2$ [6]	5
Relative dielectric constant of Si [6]	7.5
Energy position of the trap level relative to the Fermi energy in the silicon layer [7]	0.60–0.63 eV
Number of states along the carrier trajectory over the trap level	2–4

The number of states along the carrier trajectory over the trap level is related to the barrier thickness, distance between trap states, and the trajectory deviation from the rectilinear one as (see [11])

$$m = \frac{d_D}{a}\left(1 + \frac{\theta^2}{2}\right), \quad (9)$$

where θ is the angle (in radians) characterizing the trajectory sinuosity.

The current density through the structure is given by (see [6])

$$J(V) = J_{i(n)}(\varphi_{Di}) + J_{i(p)}(\varphi_{Di}) - \sum_{i=1}^{n}[q\gamma_i n_i(\varphi_{Di})p_i(\varphi_{Di})d_{\text{Si}}]. \quad (10)$$

Here, $J_{i(n)}(\varphi_{Di})$ and $J_{i(p)}(\varphi_{Di})$ are the densities of nonrecombinative components of electron and hole currents in the ith semiconductor layer

$$J_{in(p)}(\varphi_{Di}) = qn_i(p_i)d_{\text{Si}}(g^{\text{tun}}_{in(p)} + g^{\text{trap}}_{in(p)})/N_{C(V)}, \quad (11)$$

where $N_{C(V)}$ is the effective density of states in the conduction (valence) band.

The developed model was used to analyze the current–voltage (*I–V*) characteristic of the 20-period Si/CaF$_2$ structure at room temperature on the assumption that the insulator and semiconductor layer thicknesses, recombination coefficient, and potential barrier heights for electrons and holes are identical for all the structure periods. The carrier transitions were considered at energies close to the Fermi energy of emitting contacts and quasi-Fermi levels in QWs.

THE RESULTS OF CALCULATION AND DISCUSSION

The *I–V* characteristic of the Si/CaF$_2$ periodic structure was calculated taking into account the following factors: the number of states along the carrier trajectory over trap levels, the number of defect levels, the existence of trapping centers in an insulator for one or both types of carrier, CaF$_2$ and Si layer thicknesses, deviation from a rectilinear trajectory in the trap center vicinity, and the barrier height.

The parameters used in the calculations are listed in the table. When the insulator and semiconductor thicknesses were not varied parameters, they were taken as 2.0 and 1.5 nm, respectively.

The *I–V* characteristics of the structure were calculated separately for both tunneling and trap carrier-transport mechanisms. In the entire applied voltage range, the “trap” current contribution was established to substantially exceed the tunneling current (by two–three orders of magnitude). In both cases, the dependence of the current on the external voltage is exponential and monotonic due to the different potential barriers for electron transitions by the tunneling and trap-

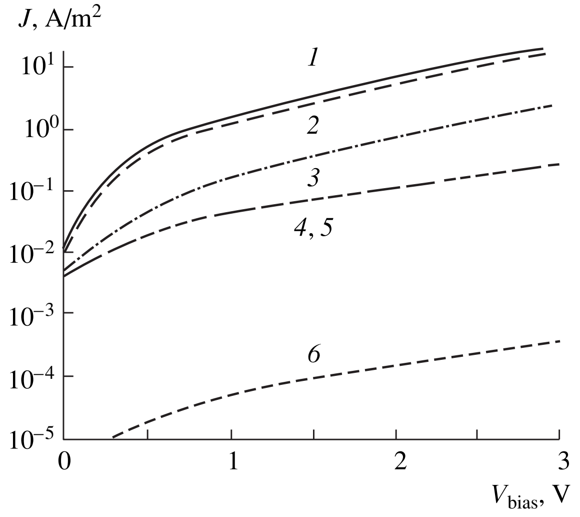

Fig. 2. Impact of traps on the *I–V* characteristic of the 20-period Si/CaF$_2$ structure for carrier transport over traps (*1*) with the participation of two trap types, (*2*) with the participation of only electron traps, and (*3*) with participation of only hole traps; tunneling transport: (*4*) total tunneling current, (*5*) contribution of electrons, and (*6*) contribution of holes. Carrier transport through traps of energy at the level of the conduction-band bottom and the valence-band top is assumed for electrons and holes, respectively.

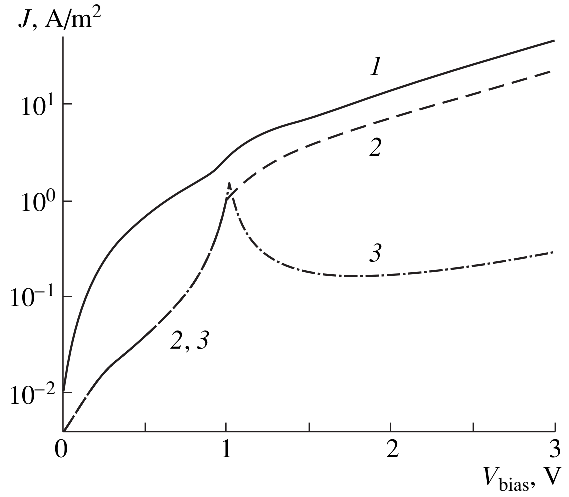

Fig. 3. Impact of the trap level energy position on the *I–V* characteristic of the 20-period Si/CaF$_2$ structure for carrier transport (*1*) over two types of traps for electrons (holes) with a higher (lower) energy relative to the conduction-band bottom (the valence-band top) by 0.02 eV and with an energy equal to the conduction-band bottom (the valence-band top), (*2*) only over traps for electrons (holes) with an energy higher (lower) relative to the conduction-band bottom (the valence-band top) by 0.02 eV, and (*3*) over traps for the energy level arrangement analogous to curve *1* on the assumption of the absence of carrier scattering.

related mechanisms. In the case of transport over trap levels, the barrier is discretized into a few narrower barriers. The *I–V* characteristics for the described case are plotted in Fig. 2 (curves *1*, *4*). Since the insulator can contain single and double Schottky defects, we studied the impact of defect type on trap-related transport in the Si/CaF$_2$ periodic structure. Figure 2 also shows the calculated *I–V* characteristics for the cases when the insulator contains only electron or only hole traps (curves *2*, *3*). The trap energy level coincided with the QW bottom. Thus, the current is higher in the insulator containing only electron traps by an order of magnitude. Analogous ratios were observed for the electron and hole components of the tunneling current: the former is higher by two–three orders of magnitude (Fig. 2, curves *5*, *6*). This is caused by different potential barrier heights for electrons (3.3 eV) and holes (7.6 eV).

If the carrier transport over two trap levels with different energies is taken into account, the *I–V* characteristic exhibits steps and becomes nonmonotonic (see Fig. 3). This effect is related to coinciding trap positions and carrier energies in the QW. Adding the carrier transport over trap levels to the total flux causes a current spike at a certain potential. Neglect of scattering processes causes a resonance in the structure when the carrier energy in the QW coincides with the trap level position (curve *3*). In this case, the *I–V* characteristic exhibits a resonance peak. The consideration of carrier scattering in the QW leads to the energy-state and resonance broadening, and to the absence of a current drop portion in the *I–V* characteristic (curves *1*, *2*). The number of current spikes is controlled by the number of levels in the insulator with an energy exceeding the conduction-band bottom energy of nanometer-scale silicon.

The trap current, as the tunneling one, was shown to depend exponentially on the potential-barrier height. However, the current tunneling component decreases by three orders of magnitude as the barrier height grows from 3 to 5 eV, while the trap component decreases only by an order of magnitude. This occurs because the potential barrier height at the trap transport affects only the characteristic attenuation distance of an electron wave with energy E in the uniform potential barrier.

Since the defect concentration depends on the conditions of Si/CaF$_2$ structure formation, the impact of the number m of states in the trap on carrier trajectories over the trap level was studied. The current density was shown to grow by three orders of magnitude as m decreases from 4 to 2 due to the barrier transparency increase at the carrier transport over the trap states.

An analysis of the impact of the structure size showed different dependences of current components on Si and CaF$_2$ layer thickness (see Fig. 4). As the Si layer thickness increases from 1 to 2.5 nm, the tunneling and trap-related currents vary insignificantly (curves *2*, *4*). An analogous CaF$_2$ thickness growth exponentially reduces the trap-related and tunneling currents by five and seven orders of magnitude (curves *1*, *3*).

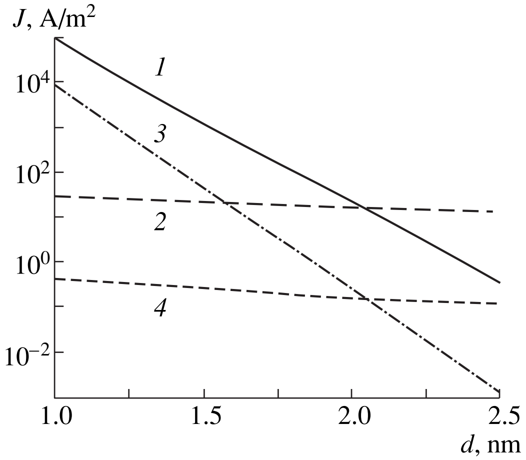

Fig. 4. Impact of CaF_2 and Si thicknesses on the *I–V* characteristic of the Si/CaF_2 20-period structure at an external bias of 3 V: (*1*, *2*) the current through traps and the (*3*, *4*) tunneling current versus CaF_2 and Si thicknesses, respectively.

An increased deviation of the carrier trajectory over the trap level from a rectilinear one (angle θ increase from 0° to 45°) decreases the current by 30–45 times due to an increase in the number of states in traps along the trajectory, as well as in the trajectory length itself.

CONCLUSION

The proposed model of simultaneous carrier transport by tunneling and over traps in Si/CaF_2 nanometer periodic structures and the corresponding calculations showed that the trap states increase the total transported charge by two–three orders of magnitude. Furthermore, the *I–V* characteristic qualitative shape depends on the trap level energy and concentration, and the deviation of the carrier trajectory over trap levels from a rectilinear one. In some cases, the consideration of charge transport over trap levels leads to nonmonotonic *I–V* characteristics when levels in the well and insulator coincide as the external bias voltage grows. It is important to take these trends into account when designing nanoelectronic and optoelectronic devices based on QWs not only in Si/CaF_2 structures, but also in those close (in electronic properties) to Si/SiO_2 structures where transport through the trap should also play a significant role.

ACKNOWLEDGMENTS

This study was performed within project T99-102 supported by the Foundation for Basic Research of the Republic of Belarus and the International Program “Nanoelectronics.”

REFERENCES

1. C. G. Smith, Rep. Prog. Phys. **59**, 235 (1996).
2. L. Vervoort, F. Bassani, I. Michalcescu, *et al.*, Phys. Status Solidi **190**, 123 (1995).
3. F. Bassani, L. Vervoort, I. Michalcescu, *et al.*, J. Appl. Phys. **79**, 4066 (1996).
4. F. Arnaud d’Avitaya, L. Vervoort, F. Bassani, *et al.*, Europhys. Lett. **31**, 25 (1995).
5. A. G. Cullis, L. T. Canham, and P. D. J. Calcott, J. Appl. Phys. **82**, 909 (1997).
6. V. E. Borisenko, A. L. Danilyuk, and A. N. Kholod, Mikroélektronika **27**, 170 (1998).
7. V. Ioannou-Sougleridis, V. Tsakiri, A. G. Nassiopoulou, F. Bassani, S. Menard, and F. Arnaud d’Avitaya, *European Projects: Silicon Modules for Integrated Light Engineering* (Marseille, 1999), p. 133.
8. S. Menard, F. Bassani, M. Liniger, F. Arnaud d’Avitaya, A. N. Kholod, and V. E. Borisenko, *Physics Chemistry and Application of Nanostructures* (Minsk, 1999), p. 23.
9. C. B. Duke, *Tunneling in Solids* (Academic, New York, 1969), Solid Physics Supplement 10, p. 390.
10. *Electron Processes and Defects in Ionic Crystals. Collection of Scientific Works*, Ed. by I. Tale (Latv. Gos. Univ., Riga, 1985).
11. V. Ya. Kirpichenkov, Zh. Éksp. Teor. Fiz. **113**, 1522 (1998) [JETP **86**, 833 (1998)].
12. I. M. Lifshits and V. Ya. Kirpichenkov, Zh. Éksp. Teor. Fiz. **77**, 989 (1979) [Sov. Phys. JETP **50**, 499 (1979)].
13. M. T. Cuberes, A. Bauer, H. J. Wen, *et al.*, J. Vac. Sci. Technol. B **12**, 2646 (1994).
14. C. Svensson and I. Lundström, J. Appl. Phys. **44**, 4657 (1973).

Translated by A. Kazantsev

Semiconductors, Vol. 35, No. 1, 2001, pp. 117–121. Translated from Fizika i Tekhnika Poluprovodnikov, Vol. 35, No. 1, 2001, pp. 115–119.
Original Russian Text Copyright © 2001 by Sadygov, Burbaev, Kurbatov.

PHYSICS OF SEMICONDUCTOR DEVICES

An Avalanche Photodiode with Metal–Insulator–Semiconductor Properties

Z. Ya. Sadygov*, T. M. Burbaev, and V. A. Kurbatov****

** Joint Institute for Nuclear Research, Dubna, Moscow oblast, 141980 Russia*

*** Lebedev Institute of Physics, Russian Academy of Sciences, Leninskiĭ pr. 53, Moscow, 117924 Russia*

e-mail: burbaev@sci.lebedev.ru

Submitted June 13, 2000; accepted for publication June 16, 2000

Abstract—A new design of the avalanche photodetector combining the avalanche photodiode and MIS structure properties was tested. The noise and high-frequency properties of the device were studied. The device exhibited a noise factor of less than 10 at a high multiplication factor ($M > 1000$) even with hole injection. This is indicative of a drastic change in the effective ratio of the coefficients of impact ionization by electrons and holes in favor of the latter. Measurements of the photosensitivity distribution over a photodetector area for $M = 8000$ showed a high uniformity. *© 2001 MAIK “Nauka/Interperiodica”.*

INTRODUCTION

The use of the silicon-based metal–insulator–semiconductor (MIS) structure as an avalanche photodiode was first proposed in [1]. However, the structures developed there did not maintain a dc mode and operated in the pulsed mode of electric bias, exhibiting very high gains [2] unattainable for ordinary avalanche photodiodes (APD). Further studies [3] also detected drastically improved noise characteristics of these structures compared to APD noise. The need to operate in a bias pulsed mode was avoided by using a wide-gap semiconductor with a great number of deep donor states as a MIS structure insulator (see [4–6]). In this case, carriers accumulated during a “one-electron” process at the interface flow out through a high-resistivity layer of a wide-gap semiconductor. A major disadvantage of such structures is the poor reproducibility of wide-gap layer “doping,” as well as their sensitivity to the following high-temperature treatment necessary to form receiving areas and to produce contact coatings for oxides with oxygen vacancies.

In this study, we examine the characteristics of an avalanche photosensitive MIS structure [7–9] where carriers flow out tangentially from the interface to an outer electrode along the silicon–insulator interface when operating in the dc bias mode.

DEVICE DESIGN AND OPERATION

The device is intermediate between conventional APDs and photosensitive MIS structures intended for avalanche mode operation. This planar photodiode design with a lightly doped collector whose photosensitive area is covered with an insulator layer and a semitransparent metal coating connected to a collector electrode (see Fig. 1). As for operation, it is a MIS device where the diode structure maintains the carrier drain away from the semiconductor–insulator interface to the outer electrode connected to a metal coating of the insulator. This enables the MIS structure to operate in the avalanche mode at a continuous bias mode. A thin collector layer in the operating mode is totally depleted and decreases the energy of carriers arriving at the insulator–semiconductor interface.

The design shown in Fig. 1 is intended to detect near ultraviolet and short-wavelength visible light [8] absorbed in the silicon surface region; therefore, the device has an n-type base. The probabilities of impact ionization by carriers of opposite sign differ greatly in ordinary silicon APDs. Therefore, the type of carriers injected into the field region is crucial, since it controls the noise factor [10]. In MIS structures, this can be important at relatively low multiplication factors when screening the field by the charge accumulated at the interface is still not efficient. However, as will be evident from the obtained data, the type of carriers initiating an avalanche is not important at high gains.

To identify the main features of the device operation, we assume that one-electron pulses are separated in time, so that the time of the one-electron process of development–decay including the spreading of accumulated charge is much shorter than the time between photon absorption events in the same local region. We assume also that light is absorbed in the base region, which corresponds to the measuring conditions, and simplifies consideration. In this case, holes are the carriers initiating the avalanche process.

Figure 2 displays the energy-band diagram of the device in the operating mode. As is evident, the main difference from conventional APDs is that the field extends to the entire collector region (the p-region in this case) totally depleted in the operating mode.

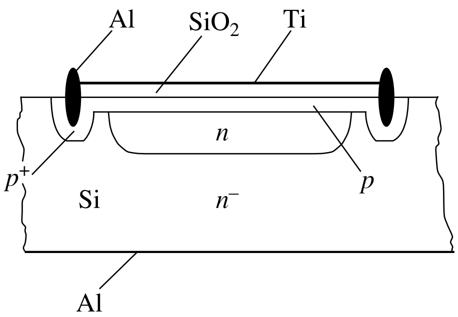

Fig. 1. Structure of the MI–*p*–*n* photodiode.

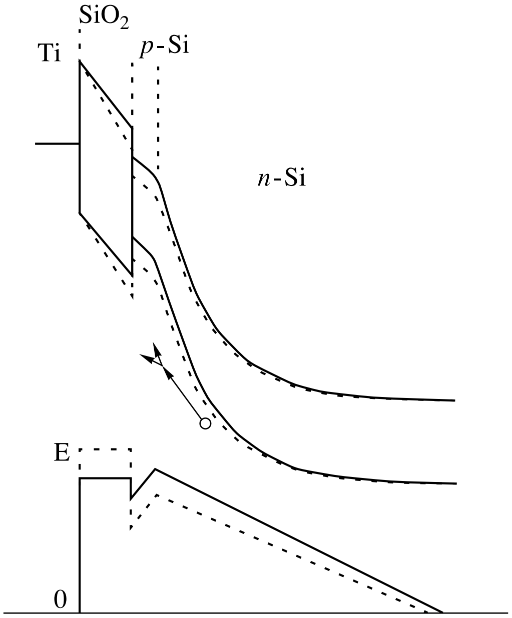

Fig. 2. Energy-band diagram of the MI–*p*–*n* structure. The dashed line represents the potential and electric field distribution in the local region of photocarrier accumulation.

Photocarriers are multiplied in the strongest field region, and holes fall into the potential well at the semiconductor–insulator interface. In contrast to simple MIS structures, the multiplication (strongest field) region is somewhat separated from the interface; therefore, carriers approach the interface with lower energies, which extends the device service life.

Photocarrier accumulation at the interface lowers the potential, and, hence, weakens the field in the local region of the one-electron process, which eventually terminates the multiplication. A potential change in the region of photocarrier accumulation rives rise to a pulling field over the interface, which shifts photocarriers to the outer electrode; thus, the normal field component is restored. Efficient self-quenching of the one-electron avalanche process requires a charge-relaxation time much longer than the time of avalanche development–attenuation. On the other hand, the charge-relaxation time controls the domain of photoresponse linearity, which is stable while the local regions of accumulated charge occupy merely a small part of the photosensitive area in the mode of steady photon flux. This is the difference between the considered device and the APDs operating in the Geiger mode and losing sensitivity for the voltage restoration time in the whole diode after each pulse.

Hereinafter, when describing the device operation, we use the terms “avalanche” and “avalanche process”, though these conventionally mean self-extinguishing multiplication processes in an unchanged field lower than the breakdown one. In the considered case, attenuation proceeds in a varied field whose initial value, according to estimates, far exceeds the breakdown field. Since the processes of impact ionization by various carriers are separated in time and occur under different electric fields, the ratio between coefficients of impact ionization by electrons and holes changes in favor of carriers initiating the avalanche. Therefore, the effective ratio of these coefficients, determining the noise factor and process-development time [10, 11] is much better than for APDs.

EXPERIMENTAL DATA

Tests of photodiodes showed that they require “forming” since the device parameters vary in time if the current is flowing. The forming changes their mode; i.e., the operating voltage increases for a given current (or multiplication factor), and the noise parameters are substantially improved. Results of forming partially diminish even within few hours; however, a fraction of a charge remains in the insulator for a few months.

The forming seems to introduce a charge into the insulator. This changes the interface potential and somewhat levels off its fluctuations, since the number and energy of carriers coming to the interface in any local region increase as the field strengthens in this region. As a result, the field as a whole weakens in the semiconductor region and strengthens in the insulator one. To restore the operating mode after forming, the supply voltage should be increased. This is not a serious operational problem, since the supply current can be easily stabilized.

Such behavior of the tested devices is similar to that of simple MIS structures operating in the avalanche mode at a pulsed bias [3]. However, the impact of high-energy carriers on an insulator, leading to irreversible changes in device parameters, is substantially reduced in the considered diode due to partial cooling of carriers in the *p* layer.

The dark generation current i_0, i.e., the ratio of the dark current to the multiplication factor, was unchanged ($i_0 \sim(4–5) \times 10^{-10}$ A) at operating modes (at high M) after forming. This means that the average frequency of noise pulses is about $\sim 3 \times 10^9$ s^{-1}; i.e., a direct measurement of the amplitude distribution requires a temporal resolution no worse than 10^{-10} s.

We studied photodiode noise properties using a conventional technique for low-signal radio engineering; i.e., a dc signal was measured after square-law detection of noise, which made it possible to restrict our measurements to a relatively narrow frequency range (3 MHz in the considered case). We omit other measurement details described elsewhere [3, 6] and consider the basic results.

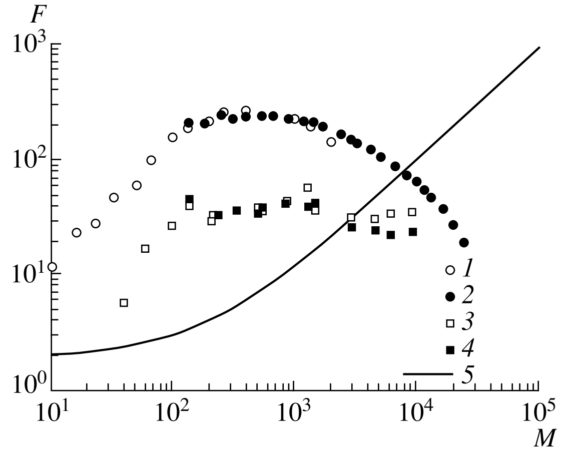

Fig. 3. Dependences of the noise factor of the avalanche process on the multiplicative factor for the A07 diode, measured (*1*, *2*) before and (*3*, *4*) after forming, for the noise caused by radiation with $\lambda = 0.7$ μm (*1*, *3*) and the dark-current noise (*2*, *4*). Curve *5* was calculated by the McIntyre formula for the case of electron injection at $k = 0.01$.

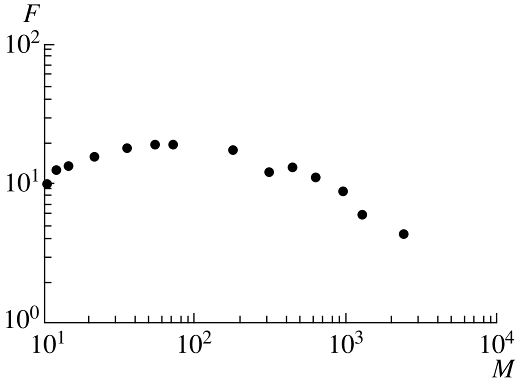

Fig. 4. Dependence of the noise factor of the avalanche process on the multiplication factor for the A08 diode.

NOISE FACTOR

Figure 3 displays the measured noise factors for one of the tested diodes (A07) and illustrates the results of forming. The first run was carried out with no special forming, except for that occurring during the measurements themselves. The second run was performed after forming for two hours at a current of 8 μA.

The noise factor was measured using 0.7-μm radiation absorbed mostly in the electroneutral region. In this case, holes are injected into the diode active region, which is extremely adverse to the signal-to-noise ratio, as is evident from the data acquired at relatively low M. At the same time, the noise factors measured at the highest M are lower than those calculated according to the McIntyre theory for electron injection and for very small $k = 0.01$.

Figure 3 also shows the noise factors determined on the assumption that the entire dark current is caused by the initiating current i_0 amplification. The values of F determined for thermal and optical generation coincide in the region $M > 100$. This means that the dark generation controlling the diode threshold parameters in this range occurs in volume (as the optical one at $\lambda = 0.7$ μm), and its rate depends on the substrate material quality and diode technology. We note that we have also obtained similar values of i_0 for conventional MIS structures [3].

Another device (A08) exhibited substantially better noise characteristics. After primary forming, it was operated at $M > 10^4$ with $F \sim 3$. However, its noise characteristics were impaired in the course of operation, which manifested itself in irregular bursts of low-frequency noise that appeared at high M. After 100-h operation, the highest M, at which no noise spikes were yet observed, was about 3×10^3 with $F \approx 5$ (see Fig. 4).

It is remarkable that such parameters in the McIntyre theory correspond to the ratio of impact ionization coefficients $k \approx 1.5 \times 10^{-3}$ in favor of holes. This means that the self-screening mechanism in this case changes this ratio approximately by four orders of magnitude. For low M, a rather high noise level corresponding to $k = 1$ is observed and is efficiently suppressed beginning from smaller M than in diode A07.

SPEED OF RESPONSE

Figure 5 displays the measured amplitude–frequency characteristic (AFC) of the noise current reduced to the unit band for the A08 diode operating at $M = 5000$ and current $I_0 = 7$ μA.

Beginning from frequencies of hundreds kilohertz, the dependence gradually slopes down according to $I_N \sim f^{-0.2}$, while at frequencies above 100 MHz the slope $I_N \sim f^{-1}$ is related to the RC limiting. The MIS diode capacitance (40 pF) and load resistance (25 Ω) (the measuring receiver input and a load from the noise current source for lowering the standing wave coefficient in a transmitting line) yield $RC = 10^{-9}$ s. This time corresponds to the boundary (–3 dB) frequency of 160 MHz. To ascertain that the weak frequency dependence in the range 0.1–100 MHz is not caused by the measuring technique, the noise AFC was measured for a silicon APD operating at $M = 240$, $I_0 = 1.8$ μA, and $F = 4.2$ in the same measuring channel. These data are also plotted in Fig. 5. As it follows from the values of F and M,

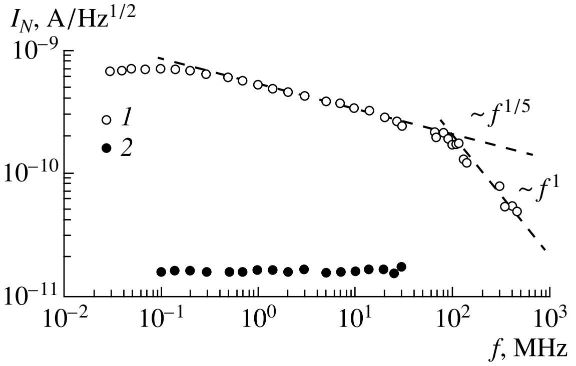

Fig. 5. Amplitude–frequency dependence of the noise current for (*1*) the A08 diode at $M = 5000$ and (*2*) the silicon APD at $M = 240$.

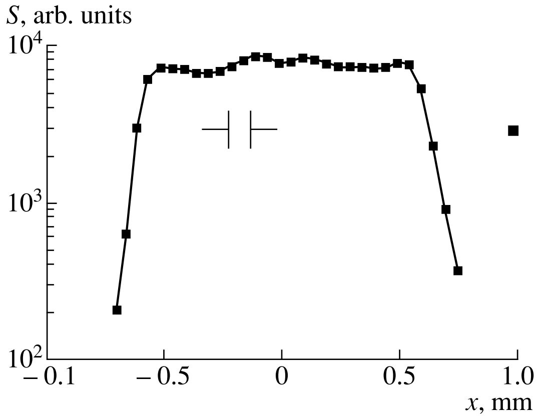

Fig. 6. Coordinate dependence of the A08 diode photosensitivity at $M = 8000$.

this diode is characterized by $k \approx 0.02$ which is a very good parameter for APDs.

The fact that the frequency dependence exponent in the range 0.1–100 MHz is (within a good accuracy) an integer fraction (1/5) is of no basic importance, since our previous measurement of MIS structures and heterojunction diodes yielded both weaker and stronger dependences in this frequency range. This dependence can be controlled not only by the temporal characteristics of one-electron pulses, but probably also by the amplitude dependence of pulse shape, which calls for corresponding direct measurements.

However, it is quite probable that this frequency falloff is caused by a distributed resistance of the semitransparent metal coating and a distributed capacitance of the structure.

We failed to separate the band limitation caused by the finite length of one-electron pulses against the background of the frequency dependence related to *RC*. However, we can state that the related cutoff frequency is substantially higher than $f_{\max}^{(RC)} = 160$ MHz.

As is known, the APD high-frequency properties are characterized by the gain–bandwidth product, which is approximately constant for specific APD types (Si, Ge) [11]. Silicon APDs are characterized by the best value of this parameter, $\Delta f \times M = 340$ GHz [12]. For MIS-type avalanche structures this product depends on operating mode [13]. Nevertheless, it makes sense to compare this value achieved in the operating mode to that for APDs. Though the obtained results do not allow the calculation of the product $\Delta f \times M$ for the tested device, they make it possible to estimate its minimum. For example, assuming that $\Delta f_{MIS} \geq 2\Delta f_{RC}$, we obtain $\Delta f \times M \geq 1500$ GHz, which far exceeds the corresponding value in APDs.

GAIN DISTRIBUTION OVER THE PHOTOSENSITIVE AREA

One of the APD disadvantages is its nonuniform photosensitivity distribution over the photoresponsive area, which becomes more pronounced with increasing multiplication factor. A negative feedback mechanism in MIS avalanche photodetectors substantially levels off the gain distribution over the interface plane and allows operation at much larger photoresponsive areas than in APDs. At the same time, there exists a certain problem related to the semitransparent metal electrode resistance becoming comparable to the structure dynamic resistance at the operating point and reducing the signal current at sufficiently large photoresponsive areas. This attenuation depends on the proximity of the avalanche process to the massive metal electrode, which causes a corresponding nonuniformity in the photosensitivity.

To diminish this effect, the device photoresponsive area of 1.1×1.1 mm^2 in total was divided into four sectors. Figure 6 displays the measured coordinate dependence of photosensitivity at $M \approx 8000$. The measurements were carried out using an optical probe with a cross section of 70×70 μm (the cross section of the light-emitting area image of the light-emitting diode at the highest magnification of an MBS-2 microscope objective).

The nonuniformity found in the sensitivity over the area does not exceed 30%. The typical distribution shape, i.e., the lowered sensitivity in central regions of separate sectors, is indicative of the impact of semitransparent-coating resistance. The appreciable photosensitivity beyond the receiving area edge is caused by scattered radiation in the optical system.

CONCLUSION

A new type of avalanche photodetector was studied, which combines photodiode technology and performance with the high gain and photosensitivity parameters of avalanche MIS structures.

It is shown that the type of carriers initiating the avalanche process at high multiplication factors does not have a profound impact on the noise factor in structures with a negative feedback (such as the MIS).

Further studies in this area should be focused on increasing the oxide stability to high-energy carriers by optimizing the semiconductor structure in order to lower the energy of carriers coming to the interface or by using a more stable insulator coating instead of oxide.

ACKNOWLEDGMENTS

This study was carried out at the Lebedev Physical Institute and Lebedev Center of Physical Research and was supported by the Ministry of Science and Technology within the Programs “Scientific Instrument Making” (contract No. 28/5, Dec. 21, 1998) and “Potential Devices and Technologies of Microelectronics and Nanoelectronics” (No. 02.04.1.1.16.É.1.), as well as by the Russian Foundation for Basic Research (project no. 99-02-16675) and Federal Program of Support for Leading Scientific Schools (project no. 96-15-96341).

REFERENCES

1. N. I. Gol’braĭkh, A. F. Plotnikov, and V. É. Shubin, Kvantovaya Élektron. (Moscow) **2**, 2624 (1975).
2. S. V. Bogdanov, A. B. Kravchenko, A. F. Plotnikov, and V. E. Shubin, Phys. Status Solidi A **93**, 361 (1986).
3. T. M. Burbaev, V. V. Kravchenko, V. A. Kurbatov, and V. É. Shubin, Kratk. Soobshch. Fiz., No. 4, 19 (1990).
4. A. G. Gasanov, V. M. Golovin, Z. Ya. Sadygov, and N. Yu. Yusipov, Pis’ma Zh. Tekh. Fiz. **14**, 706 (1988) [Sov. Tech. Phys. Lett. **14**, 313 (1988)].
5. T. M. Burbaev and V. A. Kurbatov, Kratk. Soobshch. Fiz., Nos. 11–12, 38 (1994).
6. A. P. Boltaev, T. M. Burbaev, G. A. Kalyuzhnaya, *et al.*, Fiz. Tekh. Poluprovodn. (St. Petersburg) **29**, 1220 (1995) [Semiconductors **29**, 630 (1995)].
7. Z. Ya. Sadygov, RF Patent No. 2086047 (1996).
8. N. Bacchetta, D. Bisello, Z. Sadygov, *et al.*, Nucl. Instrum. Methods Phys. Res. A **387** (1–2), 225 (1997).
9. Z. Ya. Sadygov, M. K. Suleĭmanov, and T. Yu. Bokova, Pis’ma Zh. Tekh. Fiz. **26** (7), 75 (2000) [Tech. Phys. Lett. **26**, 305 (2000)].
10. R. McIntyre, IEEE Trans. Electron Devices **ED-13** (1), 164 (1966).
11. R. B. Emmons, J. Appl. Phys. **38**, 3705 (1967).
12. T. Kaneda, H. Takanashi, H. Matsumoto, and T. Yamoka, J. Appl. Phys. **47**, 4960 (1976).
13. T. M. Burbaev, V. A. Kurbatov, N. E. Kurochkin, and V. A. Kholodnov, Fiz. Tekh. Poluprovodn. (St. Petersburg) **34**, 1010 (2000) [Semiconductors **34**, 971 (2000)].

Translated by A. Kazantsev

Semiconductors, Vol. 35, No. 1, 2001, pp. 122–123. Translated from Fizika i Tekhnika Poluprovodnikov, Vol. 35, No. 1, 2001, p. 120.
Original Russian Text Copyright © 2001 by Editorial Board.

PERSONALIA

Vladimir Mikhaĭlovich Arutyunyan (dedicated to his 60th birthday)

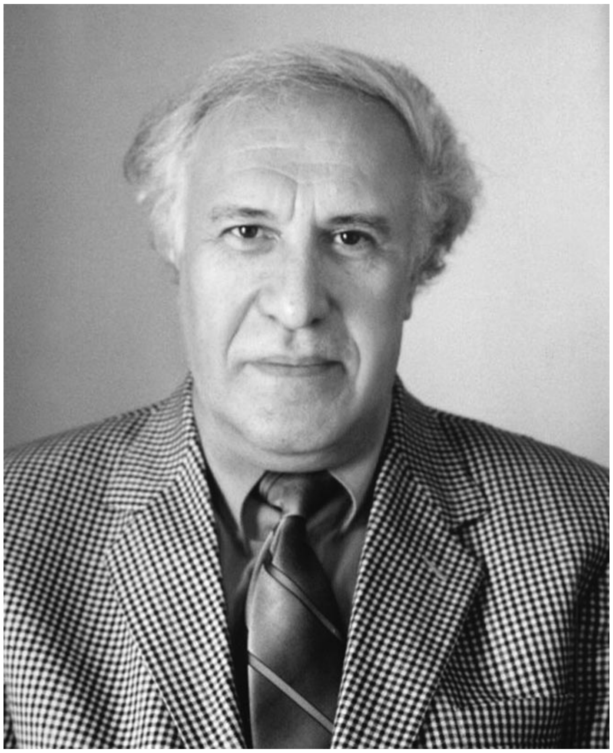

In August 2000, Professor Vladimir Mikhaĭlovich Arutyunyan celebrated his 60th birthday. He is a prominent scientist in the field of physics and technology of semiconductors, a full member of the National Academy of Sciences of Armenia, and the head of the Department of the Physics of Semiconductors and Insulators at Yerevan State University.

The entire scientific and administrative activity of V.M. Arutyunyan is closely related to origination and development of the semiconductor physics and semiconductor microelectronics in Armenia. He is the author of a number of monographs and reviews.

V.M. Arutyunyan has developed a generalized theory of generation–recombination- and injection-related phenomena in semiconductor structures with a complex band structure. He has suggested new mechanisms for the formation of portions with negative *S*-type differential resistance in current–voltage characteristics and for a number of other anomalous effects under the conditions of double injection and impact ionization. V.M. Arutyunyan contributed significantly to the theory of high-field and concentration-related phenomena in microwave devices such as Gunn-effect diodes and transit-time microwave diodes. In collaboration with his colleagues and followers, V.M. Arutyunyan conducted a large series of experimental and theoretical studies devoted to the physics of compensated, graded-gap, magnetosensitive, and ion-sensitive semiconductors; photodetectors in the ultraviolet and infrared regions of the spectrum; solar cells; superconducting systems; porous silicon; and so on.

He suggested new devices and technologies that were patented in the USSR, the USA, and the Russian Federation. V.M. Arutyunyan contributed significantly to solving the problems of photoelectrochemical conversion of solar energy and to the physics of processes occurring at the semiconductor–electrolyte and semiconductor–gas interfaces. Many of the studies started by V.M. Arutyunyan are now continued in collaboration with scientists from Russia, USA, Germany, France, and Sweden.

1063-7826/01/3501-0122$21.00 © 2001 MAIK “Nauka/Interperiodica”

Thanks to the fruitful activities of V.M. Arutyunyan, the Department of Semiconductor Physics (and the corresponding research laboratory) of Yerevan State University became one of the major scientific centers.

Professor Arutyunyan devotes much attention to the training of young scientists. There are many candidates and doctors of science among his followers. He is the Editor-in-Chief of the journal “Izvestiya NAN Armenii. Fizika,” whose English version is published in USA. V.M. Arutyunyan celebrated his birthday in the prime of his life.

In wishing V.M. Arutyunyan many happy returns of the day, his colleagues and friends also wish him many more years of creative activity and scientific achievements in the honorable effort of training young scientists.

**Colleagues, friends,
and the editorial staff
of this journal.**

Translated by A. Spitsyn

Semiconductors, Vol. 35, No. 1, 2001, pp. 14–19. Translated from Fizika i Tekhnika Poluprovodnikov, Vol. 35, No. 1, 2001, pp. 15–20.
Original Russian Text Copyright © 2001 by Bland, Thomas, Virchenko, Kuz'min, Tkachenko.

ATOMIC STRUCTURE AND NONELECTRONIC PROPERTIES OF SEMICONDUCTORS

Mössbauer-Effect Study of Off-Center Atoms in IV–VI Semiconductors

J. Bland*, M. F. Thomas*, V. A. Virchenko, V. S. Kuz'min**, and T. M. Tkachenko****

** Department of Physics, Oliver Lodge Laboratory, The University of Liverpool, Oxford Street, 69 7ZE Liverpool, UK*

*** Institute of Solid-State and Semiconductor Physics, Belarussian Academy of Sciences,*
ul. Brovki 17, Minsk, 220072 Belarus

e-mail: lttt@ifttp.bas-net.by

Submitted April 28, 2000; accepted for publication May 24, 2000

Abstract—PbTeSnSe and GeSnTe compound semiconductors were studied by ^{119}Sn Mössbauer spectroscopy in the temperature range from 5 to 240 K. Analysis of temperature dependences of the quadrupole splitting of Mössbauer spectra measured during a cooling–heating cycle confirmed the presence of off-center atoms in these materials. *© 2001 MAIK “Nauka/Interperiodica”.*

1. BRIEF REVIEW OF PUBLICATIONS

An off-center atom is an atom in a crystal lattice that is able to move from one regular site to another as the temperature changes. The off-center atom is modeled by an atom in a double-well asymmetric potential, unlike an ordinary atom, which is located in a single-well potential [1, 2]. The off-center site occupation manifests itself in anomalous temperature dependences of crystal properties, for example, thermal conductivity and heat capacity [3–5]. To date, these anomalies have been observed and thoroughly studied for alkali-halide crystals [6] and oxides [7, 8]. Such investigations are of interest because the presence of a small amount of off-center atoms can either induce or suppress phase transitions in an entire crystal [9, 10]. Recently, off-center behavior of certain atoms in semiconductor materials has been observed [11–16].

Until the 1990s, investigations of off-center atoms concerned only small atoms that are substituted for larger atoms in crystal lattices. However, it was demonstrated [17–19] that large Pb and Sn atoms occupy off-center positions in IV–VI semiconductors. Such materials are of practical importance because they undergo ferroelectric phase transitions.

The identification of off-center site occupation by Sn atoms in PbTeSnSe and GeSnTe [19] is of particular interest from the standpoint of Mössbauer spectroscopy, since this allows one to perform direct Mössbauer-effect measurements of the ^{119}Sn isotope. The effect of off-center impurities on integral physical characteristics of complex systems is difficult to resolve from many other extraneous effects. In this connection, Mössbauer spectroscopy offers advantages over other investigation techniques. Mössbauer spectroscopy is an important method for structural investigations, which is particularly sensitive to local atom arrangement and changes in it [20, 21]. Therefore, Mössbauer spectroscopy competes to a large extent with the extended X-ray absorption fine structure (EXAFS) technique, which is also used in studies of off-center atoms [11–13, 17–19].

Baltrunas [22] studied PbTeSnSe and GeSnTe by Mössbauer spectroscopy to determine room-temperature dependence of Mössbauer parameters on composition. Nikolaev *et al.* [23] found that quadrupole splitting in PbSnTe increased as temperature decreased from 300 to 77 K.

Virchenko [24] attempted to use ^{57}Fe Mössbauer spectroscopy with the aim of revealing the off-center behavior of apical oxygen atoms in the YBaCuO high-temperature superconductor. However, determining the quadrupole splitting in this system involves severe difficulties because of the presence of four overlapping doublets in the Mössbauer spectrum of Fe.

Thus, since the discovery of off-center atoms in 1965, they continue to attract interest because of their dramatic impact on the physical properties of crystals.

In this study, ^{119}Sn Mössbauer spectroscopy was used for the first time to provide experimental evidence for off-center behavior of Pb, Sn, and Ge atoms in PbTeSnSe and GeSnTe.

2. EXPERIMENTAL

To study the thermal behavior of the off-center atoms, we used the following IV–VI semiconductor alloys: $(PbTe)_{1-x}(SnSe)_x$ with $x = 0.2$ and 0.8 and $Ge_{1-x}Sn_xTe$ with $x = 0.2$ and 0.8, because three types of

1063-7826/01/3501-0014$21.00 © 2001 MAIK “Nauka/Interperiodica”

off-center atoms were identified in these solid solutions of various compositions [17, 18].

Four samples were studied. $Pb_{0.8}Te_{0.8}Sn_{0.2}Se_{0.2}$ (sample 1) undergoes a low-temperature phase transition. At the same time, since the Sn content is 20%, we can consider Sn atoms off center [17, 18]. Pb atoms are off center in $Pb_{0.2}Te_{0.2}Sn_{0.8}Se_{0.8}$ (sample 2) [17, 18]; Sn atoms, in $Ge_{0.8}Sn_{0.2}Te$ (sample 3) [19]; and Ge atoms, in $Ge_{0.2}Sn_{0.8}Te$ (sample 4) [14–16].

The polycrystalline samples were prepared by fusing the components taken in appropriate amounts. The prepared solid solutions were homogenized by 120-h annealing, and then the samples were cooled slowly to room temperature. A certain amount of ^{119}Sn isotope was introduced into the samples. Phase analysis showed that, at room temperature, samples 1 and 4 had the cubic NaCl structure, sample 2 showed the presence of cubic and orthorhombic phases, and sample 3 had a rhombohedral structure.

Mössbauer measurements were performed in the conventional transmission geometry with the use of a constant-acceleration spectrometer and a $Ca^{119m}SnO_3$ source at the Oliver Lodge Laboratory of the University of Liverpool, UK. A nominal line width of a standard absorber of (^{119}Sn) 0.4 mg/cm^2 in thickness was 0.92 mm/s. All Mössbauer samples were thin enough to apply the thin-absorber approximation [21]. For all samples, the measurements were performed during cooling–heating cycles in the temperature range from 240 to 5 K with a step of 20 K. The spectra were processed with the FfitA and FCFCORE-3 programs.

3. RESULTS AND DISCUSSION

Figure 1 shows the Mössbauer spectra of all the samples measured at 200 K.

In the entire temperature range used, the spectrum of sample 1 consists of only one subspectrum related to the cubic structure with random distribution of Sn atoms over the Sn–Pb sublattice. The line width is 0.90 mm/s. The isomer shift is 3.6 mm/s relative to $CaSnO_3$. For this sample, the variation of the isomer shift with temperature was thoroughly studied (Table 1). A moderate increase in the isomer shift with decreasing temperature is obviously due to the quadratic Doppler effect and is consistent with the theoretical value for Sn: 3.5×10^4 mm/(s K) [21]. The values of the isomer shift measured during heating slightly exceed those measured during cooling, but these differences are insignificant. Table 1 also lists values of the quadrupole splitting measured during the cooling–heating cycle. The temperature dependence of the quadrupole splitting is anomalous (Fig. 2).

In the entire temperature range used, the spectrum of sample 2 consists of two subspectra: subspectrum 2(1), associated with the orthorhombic phase (isomer shift is 3.4 mm/s relative to $CaSnO_3$), and subspectrum 2(2), related to the cubic phase (isomer shift is 3.6 mm/s). The quadrupole splitting of subspectrum 2(1) (orthorhombic phase) has a rather weak temperature dependence (Table 2). The quadrupole splitting of subspectrum 2(2) (cubic phase) shows a stronger dependence on temperature (Fig. 3). For both the subspectra, line widths were taken to be 1.06 mm/s; the broadening in excess of this value was attributed to the quadrupole splitting, irrespective of the actual cause.

A weak subspectrum with an isomer shift of about 0 mm/s and quadrupole splitting of (0.75 ± 0.05) mm/s is observed in the spectra of samples 3 and 4. Baltrunas [22] observed no such subspectrum for this semiconductor. Such values of the isomer shift and the quadrupole splitting are characteristic of tetravalent Sn in a distorted octahedron. The appearance of this subspectrum is probably related to oxidation of the sample. However, it is possible that Sn in GeSnTe resides not only in the Ge sublattice, where Te atoms are its nearest neighbors, but also in the Te sublattice, where the first coordination shell is composed of Sn and Ge atoms randomly distributed over the lattice.

For the second weak subspectrum in the 200-K spectra of samples 3 and 4, the isomer shift is (3.45 ± 0.05) mm/s. The quadrupole splitting for this subspectrum increases from 0 to 1.50 mm/s as the temperature decreases from 240 to 5 K. This increase is attributable to a certain low-temperature phase transition. It is well known that the transition from the NaCl to GeS structure is observed in PbTe at a pressure of 50 kbar [19]. As a result, the coordination number for Pb atoms changes from 6 to 3 + 3, and the unit-cell volume considerably decreases. An analogous effect was found for Sn in GeTe. In our case, we presume that GeSnTe undergoes a similar phase transition as the temperature

Table 1. Isomer shift and quadrupole splitting of ^{119}Sn spectrum of $Pb_{0.8}Sn_{0.2}Te_{0.8}Se_{0.2}$ measured during cooling–heating cycle

T, K	Cooling		Heating	
	isomer shift, mm/s	quadrupole splitting, mm/s	isomer shift, mm/s	quadrupole splitting, mm/s
200	3.61	0.17	3.61	0.16
180	3.62	0.20	3.63	0.22
160	3.64	0.20	3.65	0.24
140	3.64	0.21	3.66	0.23
120	3.65	0.22	3.66	0.27
100	3.65	0.26	3.66	0.28
80	3.66	0.29	3.68	0.31
60	3.67	0.36	3.67	0.33
40	3.68	0.37	3.68	0.38
20	3.68	0.38	3.68	0.40
5	3.69	0.40	3.69	0.40

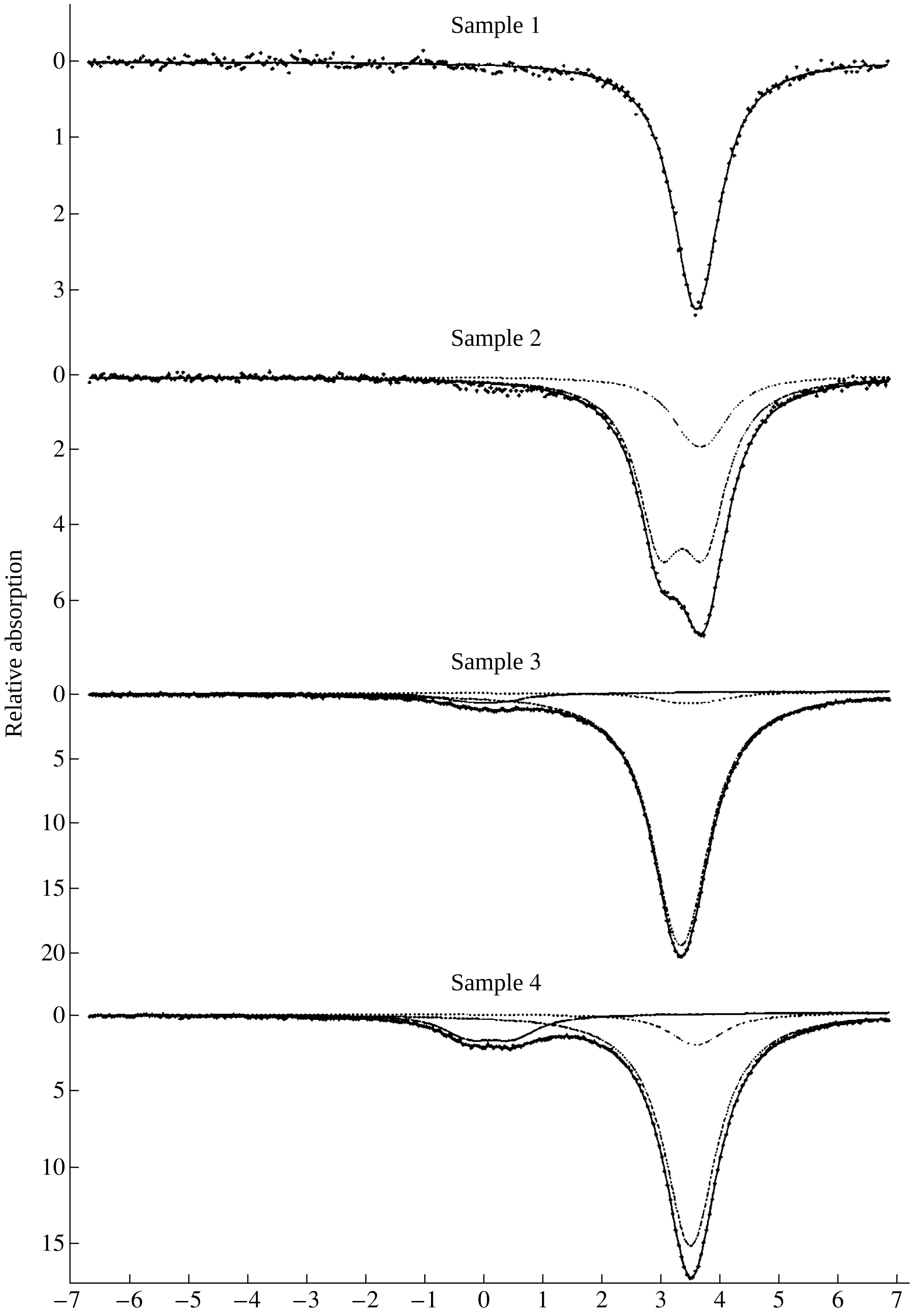

Fig. 1. Mössbauer spectra measured at 200 K for sample 1 (3 variables, $\chi^2 = 0.94$), sample 2 (6 variables, $\chi^2 = 1.28$) sample 3 (9 variables, $\chi^2 = 1.07$), and sample 4 (9 variables, $\chi^2 = 1.11$).

decreases. Such change in the local environment of Sn can lead to an increase in the electric-field gradient at Sn and the quadrupole splitting observed. We also cannot exclude from consideration specific features of the spectrum processing and line broadening owing to the possible increase in the number of various distances between atoms in the first coordination shell. Under the assumption that there are off-center displacements of Sn atoms, this number increases with decreasing temperature.

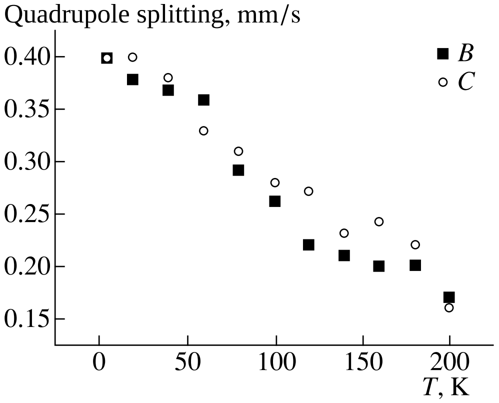

Fig. 2. Temperature dependence of the quadrupole splitting of Sn in sample 1. *B* denotes cooling; and *C*, heating.

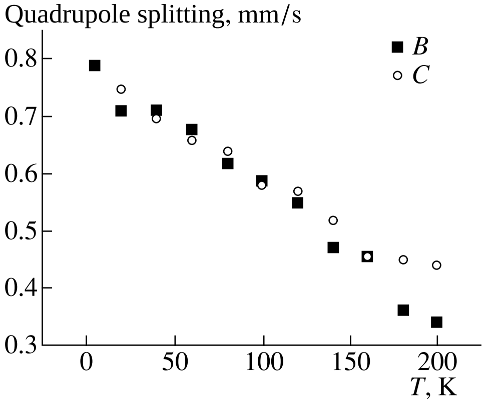

Fig. 3. Temperature dependence of the quadrupole splitting of Sn in sample 2. *B* denotes cooling; and *C*, heating.

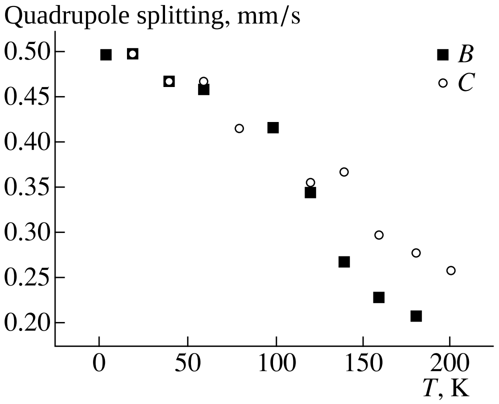

Fig. 4. Temperature dependence of the quadrupole splitting of Sn in sample 3. *B* denotes cooling; and *C*, heating.

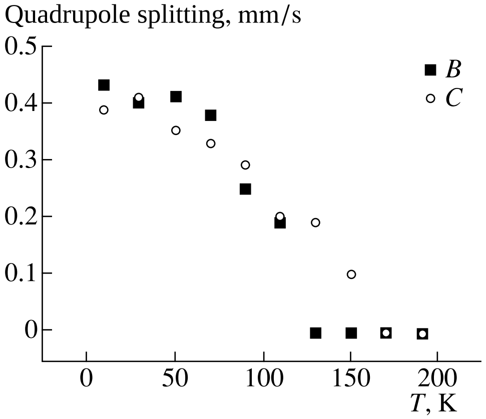

Fig. 5. Temperature dependence of the quadrupole splitting of Sn in sample 4. *B* denotes cooling; and *C*, heating.

The isomer shift of the second low-intensity subspectrum virtually coincides with those of the most intense subspectra related to the main rhombohedral phase in sample 3 and the major cubic phase in sample 4. Temperature dependences of the quadrupole splitting for the main subspectra in the spectra of samples 3 and 4 are shown in Figs. 4 and 5, respectively.

As the temperature increases, the off-center atoms shift from their equilibrium sites in the semiconductor lattice. As a result, local environments of the resonance atoms change. In terms of a point-charge model, the electric-field gradient produced by a single nearest neighboring atom at a resonance Sn atom is proportional to $1/R^3$, where R is the distance between the atoms. The electric-field gradient at the Sn atom is the vector sum of electric-field gradients produced by all nearest neighbors. More distant coordination shells have only an insignificant effect on the electric-field gradient because of this dependence on distance. At the same time, even small changes in R in the nearest neighbor environment have a dramatic impact on the electric-field gradient at Sn. The electric-field gradient is proportional to the experimental value of the quadrupole splitting. Assuming there is a double-well potential, the temperature dependence of the off-center displacement shows a hysteresis behavior [4]. Therefore, we should expect an anomalous temperature dependence of the quadrupole splitting measured during the cooling–heating cycle. In samples 1 and 3, the Mössbauer Sn atoms themselves are off center. In samples 2 and 4, Pb and Ge atoms, respectively, occupy off-center sites, which also influences the local field at the resonance Sn atoms.

In sample 2, the off-center Pb atoms are not nearest neighbors to Sn atoms. In addition, Sn and Pb occupy crystallographically nonequivalent sites in the cubic and orthorhombic lattices, which results in the two subspectra in the Mössbauer spectra of Sn. Therefore, the off-center displacements of Pb atoms have only a slight effect on the quadrupole splitting of the ^{119}Sn spectra (Fig. 3). In sample 3, Sn atoms occupy at least three crystallographically nonequivalent sites, which also obscures the effect (Fig. 4).

Table 2. Quadrupole splitting of ^{119}Sn spectra of samples 2, 3, and 4 measured during cooling–heating cycle

T, K	2(1)		2(2)		3		4	
	Quadrupole splitting, mm/s		Quadrupole splitting, mm/s		Quadrupole splitting, mm/s		Quadrupole splitting, mm/s	
	cooling	heating	cooling	heating	cooling	heating	cooling	heating
240							0	0
220							0	0
200	0.74	0.77	0.34	0.44	0	0.26	0	0.1
180	0.73	0.78	0.36	0.45	0.21	0.28	0	0.19
160	0.76	0.76	0.46	0.46	0.23	0.30	0.19	0.20
140	0.74	0.77	0.47	0.52	0.27	0.37	0.25	0.29
0	0.76	0.78	0.55	0.57	0.35	0.36	0.38	0.33
100	0.76	0.79	0.59	0.58	0.47		0.41	0.35
80	0.77	0.79	0.62	0.64		0.42	0.40	0.41
60	0.79	0.79	0.68	0.66	0.46	0.47	0.43	
40	0.79	0.80	0.71	0.70	0.47	0.47		
20	0.80	0.80	0.71	0.75	0.50	0.50		
5	0.81		0.79		0.50			

It is well known that a very small magnitude of quadrupole splitting corresponds to high symmetry of the environment of the resonance atom. Therefore, for sample 1, in which Sn atoms reside only in the cubic Pb–Sn sublattice, the magnitude of quadrupole splitting is small at temperatures around 200 K. Even small variations of interatomic distances with temperature drastically affect the symmetry of the environment of Sn, which has a profound effect on values of the quadrupole splitting. The quadrupole splitting for this sample measured during the cooling–heating cycle shows a rather pronounced temperature hysteresis. A similar effect is observed for sample 4, which also has a cubic structure (Fig. 5) in which the off-center Ge atoms are the nearest neighbors of Sn atoms. The temperature dependence of the quadrupole splitting measured for this sample during the cooling–heating cycle is also anomalous.

4. CONCLUSION

The direct experimental evidence for off-center atoms in $(PbTe)_{1-x}(SnSe)_x$ with $x = 0.2$ and 0.8 and $Ge_{1-x}Sn_xTe$ with $x = 0.2$ and 0.8 was obtained by ^{119}Sn Mössbauer spectroscopy. The temperature dependence of the quadrupole splitting in these systems measured during the cooling–heating cycles are anomalous. The well-pronounced temperature hysteresis is observed for the quadrupole splitting in $Pb_{0.8}Sn_{0.2}Te_{0.8}Se_{0.2}$ and $Ge_{0.2}Sn_{0.8}Te$, which indicates that Sn and Ge atoms occupy off-center sites in these semiconductors.

REFERENCES

1. A. M. Stoneham, *Theory of Defects in Solids: The Electronic Structure of Defects in Insulators and Semiconductors* (Clarendon Press, Oxford, 1975; Mir, Moscow, 1978), Vol. 2.
2. A. P. Saĭko, V. E. Gusakov, and V. S. Kuz'min, Dokl. Akad. Nauk Belarusi **37**, 93 (1993).
3. A. P. Saĭko, V. E. Gusakov, and V. S. Kuz'min, Pis'ma Zh. Éksp. Teor. Fiz. **56**, 425 (1992) [JETP Lett. **56**, 411 (1992)].
4. A. P. Saĭko, V. E. Gusakov, and V. S. Kuz'min, Pis'ma Zh. Éksp. Teor. Fiz. **57**, 108 (1993) [JETP Lett. **57**, 116 (1993)].
5. A. P. Saiko, V. E. Gusakov, and V. S. Kuz'min, Physica C (Amsterdam) **235–240**, 1239 (1994).
6. V. Naraynamurti and R. O. Pohl, Rev. Mod. Phys. **42**, 677 (1970).
7. Y. Yacoby and S. Just, Solid State Commun. **15**, 715 (1974).
8. Y. Yacoby, W. B. Holzapfel, and D. Bauerle, Solid State Commun. **23**, 947 (1977).
9. B. E. Vugmeĭster and M. D. Glinchuk, Zh. Éksp. Teor. Fiz. **79**, 947 (1980) [Sov. Phys. JETP **52**, 482 (1980)].
10. B. E. Vugmeĭster and M. D. Glinchuk, Usp. Fiz. Nauk **146**, 459 (1985) [Sov. Phys. Usp. **28**, 589 (1985)].
11. A. I. Lebedev and I. A. Sluchinskaya, J. Alloys Compd. **203**, 51 (1994).
12. A. I. Lebedev, I. A. Sluchinskaya, V. N. Demin, and I. H. Munro, Izv. Akad. Nauk, Ser. Fiz. **60**, 46 (1996).
13. A. I. Lebedev and I. A. Sluchinskaya, Fiz. Tverd. Tela (St. Petersburg) **34**, 1491 (1992) [Sov. Phys. Solid State **34**, 793 (1992)].

14. Q. T. Islam and B. A. Bunker, Phys. Rev. Lett. **59**, 2701 (1987).
15. B. A. Bunker, Q. T. Islam, and W. F. Pong, Physica B (Amsterdam) **158**, 578 (1989).
16. B. A. Bunker, Z. Wang, and Q. T. Islam, Ferroelectrics **120**, 23 (1991).
17. A. I. Lebedev and I. A. Sluchinskaya, Ferroelectrics **143**, 91 (1993).
18. A. I. Lebedev and I. A. Sluchinskaya, Ferroelectrics **157**, 275 (1994).
19. A. I. Lebedev, I. A. Sluchinskaya, V. N. Demin, and I. H. Munro, Pis’ma Zh. Éksp. Teor. Fiz. **63**, 600 (1996) [JETP Lett. **63**, 635 (1996)].
20. G. Schatz, A. Weidinger, and J. A. Gardner, *Nuclear Condensed Matter Physics (Nuclear Methods Applications)* (Wiley, New York, 1996).
21. *Chemical Applications of Mössbauer Spectroscopy*, Ed. by V. I. Goldanskii and R. H. Herber (Academic, New York, 1962; Mir, Moscow, 1970).
22. D. Baltrunas, Phys. Status Solidi B **204**, 811 (1997).
23. I. N. Nikolaev, V. P. Potapov, A. P. Shotov, and E. E. Yurkevich, Pis’ma Zh. Éksp. Teor. Fiz. **25**, 185 (1977) [JETP Lett. **25**, 168 (1977)].
24. V. A. Virchenko, V. S. Kuz’min, T. M. Tkachenko, and A. V. Shablovskii, J. Magn. Magn. Mater. **183**, 78 (1998).

Translated by N. Izyumskaya

Semiconductors, Vol. 35, No. 1, 2001, pp. 20–23. Translated from Fizika i Tekhnika Poluprovodnikov, Vol. 35, No. 1, 2001, pp. 21–24.
Original Russian Text Copyright © 2001 by Demidov, Karzanov, Lobanov, Markov, Sdobnyakov.

ATOMIC STRUCTURE AND NONELECTRONIC PROPERTIES OF SEMICONDUCTORS

A Long-Range Influence of the Argon-Ion Irradiation on the Silicon Nitride Layers Formed by the Ion Implantation

E. S. Demidov*, V. V. Karzanov, D. A. Lobanov, K. A. Markov, and V. V. Sdobnyakov
Nizhni Novgorod State University, pr. Gagarina 23, Nizhni Novgorod, 603600 Russia
** e-mail: ett@phys.unn.runnet.ru*

Submitted May 25, 2000; accepted for publication May 31, 2000

Abstract—The effect of stimulating synthesis reactions for the Si_3N_4 phase in nitrogen-enriched silicon layers under the influence of argon-ion implantation into the rear side of silicon wafers was investigated. Dependences of variations in the IR absorption and the resistivity of the synthesized layers on argon-implantation dose were obtained. The morphology of a wafer surface after argon implantation with various doses was investigated by atomic-force microscopy. The effect is attributed to the action of shock waves arising owing to microbursts of argon blisters. *© 2001 MAIK “Nauka/Interperiodica”.*

1. INTRODUCTION

It was found [1] that IR absorption was enhanced in the region of 1150 cm^{-1} as a result of argon-ion irradiation of Czochralski silicon samples (i.e., with a dissolved-oxygen concentration close to the limiting one) with doses exceeding 10^{16} cm^{-2}. This means that, under the action of irradiation, a quantity of the optically active oxygen (i.e., the number of Si–O bonds) increased. Thus, it was shown that the ion bombardment could stimulate the processes of formation of chemical bonds beyond the stopping range of implanted ions.

Hence, the idea arose of investigating the possibility of stimulating the reaction of synthesizing a heterogeneous phase in silicon enriched with a chemically active impurity using ion implantation. As a system under investigation, the silicon layers enriched with ion-implanted nitrogen were chosen. Investigations [2, 3] showed that insulating characteristics of the ion-implantation synthesized Si_xN_y layers preliminary formed on the working side of the wafers were significantly improved as a result of the rear-side argon-ion treatment. In this paper, we report the results of a complex investigation of optical and electrical characteristics of the Si_xN_y synthesized layers as functions of an argon-implantation dose. The state of the silicon-wafer surface bombarded by argon ions was examined by atomic-force microscopy (AFM).

2. EXPERIMENTAL PROCEDURE

In this study, we investigated silicon wafers of the brands BKÉ-100b (crucibleless-grown *n*-Si with a resistivity of 100 Ω cm), BKD-2000 (crucibleless-grown *p*-Si with a resistivity of 2000 Ω cm), and KÉM-0.005 (*n*-Si: As with a resistivity of 0.005 Ω cm). All the samples were treated using a standard chemical and mechanical procedure; wafer thickness amounted to 0.6 mm. In the experiment, we implanted nitrogen ions into wafers preliminarily heated to a temperature of 400°C. The ion energies were $E_N = 150$ keV for forming the Si_xN_y buried layers and $E_N = 40$ keV for forming the surface layers. The implantation dose amounted to $\Phi_N = (1–5) \times 10^{17}$ cm^{-2}, and the ion-flux density was $j_N \le 10^{14}$ cm^{-2} s^{-1}. Thereafter, the rear sides of the wafers were irradiated with argon ions with the following parameters: $E_{Ar} = 40$ keV, $j_{Ar} \le 10^{14}$ cm^{-2} s^{-1}, an argon implantation dose Φ_{Ar} was varied from 10^{15} cm^{-2} to 3×10^{17} cm^{-2}, and a target was heated to $T = 500$°C. Such a choice of the wafer temperature was made because the effect of enhancement of the Si_3N_4-phase fraction in the Si_xN_y layers was detected [2, 3] precisely at $T \ge 500$°C.

The modifications in Si_xN_y layers were detected by two methods: IR transmission spectra in the range of 700–1000 cm^{-1} and the current–voltage (*I*–*V*) characteristics of the Si_xN_y–Si structures being compared before and after argon-ion irradiation. The IR spectra were recorded using a Bruker-113IFS spectrometer. The choice of high-resistivity samples BKÉ-100 and BKD-2000 for measuring the IR spectra was due to the desire to reduce the effect of absorption by the majority carriers. The *I*–*V* characteristics were measured using the two-contact technique, and the low-resistivity samples KÉM-0.005 were used to assess the resistivity of the nitride layer; such a choice was made for decreasing the contribution from a substrate and from barrier effects to the total resistance of the structure. As a contact material, we used the eutectic alloy In–Ga with a contact-area diameter of 5 mm.

The surface morphology of the ion-bombarded silicon wafers was studied by AFM using a TopoMetrix TMX 2100 Accurex scanning probe microscope in the contact mode. For measurements, we used a silicon-nitride cantilever with a pyramidal probe.

3. RESULTS AND THEIR DISCUSSION

In Fig. 1, we show the transmission spectra for a BKÉ-100 silicon sample irradiated from the working side with nitrogen ions with an energy of 150 keV and a dose $\Phi_N = 5 \times 10^{17}$ cm^{-2} before and after the argon-ion implantation (curves *1* and *2*, respectively). For comparison, we show the IR spectrum for a unirradiated silicon sample (line *3*). Even after nitrogen implantation, a significant minimum of transmission appears in the region of 800–900 cm^{-1}, which corresponds to the absorption by the Si_3N_4 amorphous phase [4]. As a result of additional irradiation of the sample from the rear side with argon ions with $\Phi_{Ar} = 3 \times 10^{17}$ cm^{-2}, an enhancement in absorption occurs in the indicated frequency region, which corresponds to an increase in the number of the Si–N bonds.

In Fig. 2, we display the differential IR spectra of the BKÉ-100 silicon sample. Line *1* shows the spectrum of the sample after irradiation with nitrogen and argon with respect to the spectrum of the sample irradiated only with nitrogen. In the region of interest, the absorption coefficient increased from 45 to 49%.

In Fig. 2, we also show the results of certain check experiments. Since argon was implanted at $T = 500°C$, it remains to be clarified whether or not the modifications observed in the spectra are the consequence of elevated temperature. Line *2* shows the spectrum of a sample annealed after nitrogen implantation at a temperature of 500°C with respect to the spectrum of a sample irradiated with nitrogen without annealing. In this case, the enhancement is seen to be much weaker than in the former case.

To estimate the contribution of the “argon” layer to the IR spectra of the structures under investigation, we construct the difference spectra for a pure silicon and an argon-implanted silicon (Fig. 2, line *3*). As can be seen from the plot, the modifications introduced by argon are negligible.

Thus, we may conclude that the observed enhancement in the absorption by silicon nitride is exactly associated with the process of the argon-ion irradiation.

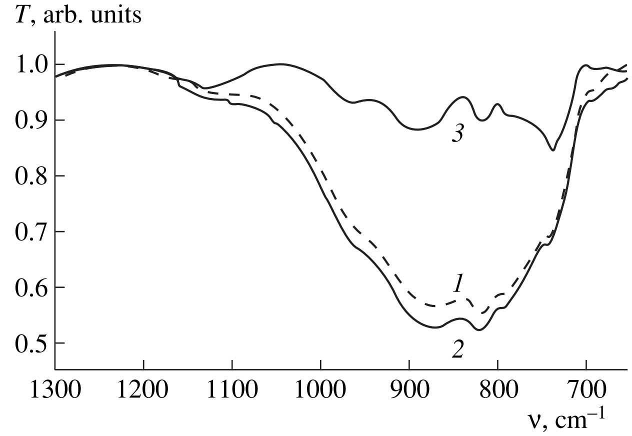

Fig. 1. IR transmission spectra of a nitrogen-implanted silicon sample: (*1*) after nitrogen implantation from the working side; (*2*) after argon irradiation from the rear side; and (*3*) the spectrum of an unirradiated sample.

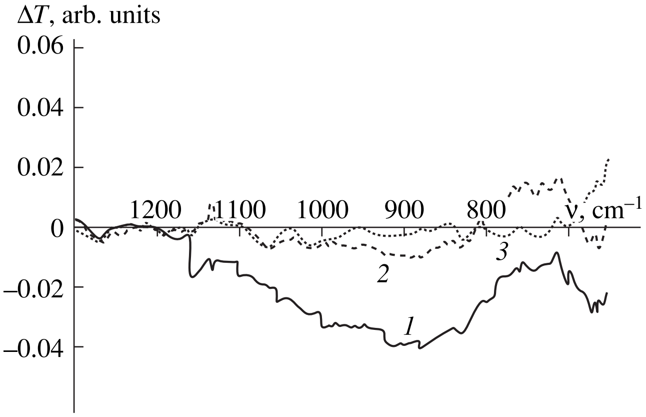

Fig. 2. Differential IR spectra of silicon samples: (*1*) the spectrum of the sample after nitrogen implantation and additional argon irradiation with respect to the spectrum of the sample irradiated only by nitrogen; (*2*) spectrum of the sample after nitrogen implantation and annealing at $T = 500°C$ with respect to the spectrum of the sample irradiated with nitrogen and unannealed; (*3*) the spectrum of the sample after the irradiation with argon with respect to the spectrum of unirradiated silicon.

We experimentally studied the dose dependence of the effects observed. In Fig. 3, the modification in the IR absorption at $\nu = 860$ cm^{-1} is shown as a function of an argon-irradiation dose for a fixed implanted-nitrogen dose $\Phi_N = 5 \times 10^{17}$ cm^{-2}. As can be seen from Fig. 3, argon irradiation with doses lower than $\Phi_{Ar} = 10^{16}$ cm^{-2} does not significantly affect the absorption coefficient of the Si_xN_y–Si structure. In the dose range from 10^{16} to 10^{17} cm^{-2}, we observe an abrupt change in the absorption after which (for a dose $\Phi_{Ar} \sim 10^{17}$ cm^{-2} and higher) the stabilization occurs. A similar dose dependence for the argon implantation was obtained [1] in the case of stimulating the optical activity of oxygen in silicon by ion irradiation.

The results of the influence of argon irradiation with $\Phi_{Ar} = 3 \times 10^{17}$ cm^{-2} on electrical properties of structures were reported recently [3]. In the study cited, an enhancement in resistivity of a nitride layer was observed [3], while a qualitative shape of *I*–*V* characteristics corresponded to the theory of a current flow in an insulator [5]. As the investigations showed, the effect of improving insulating properties of a Si_xN_y layer was also of the threshold character. A marked rise in the resistivity of a silicon-nitride synthesized layer begins also after exceeding an argon dose of $\Phi_{Ar} = 10^{16}$ cm^{-2}

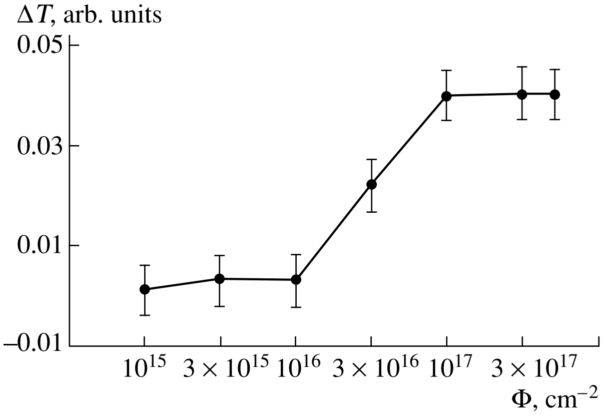

Fig. 3. Enhancement of the IR absorption of nitrogen-implanted silicon ($\Phi_N = 5 \times 10^{17}$ cm^{-2}, E = 150 keV) as a function of an argon-irradiation dose.

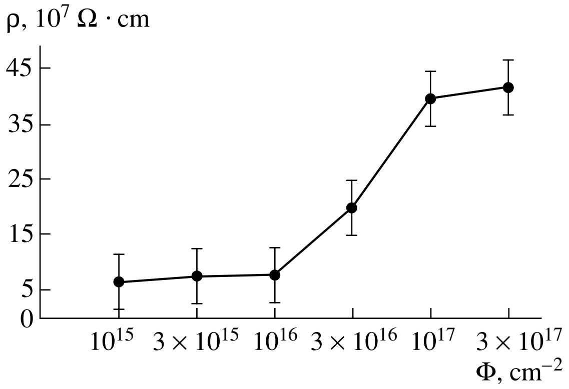

Fig. 4. Enhancement of resistivity of the nitrogen-implanted silicon layer ($\Phi_N = 10^{17}$ cm^{-2}, E = 40 keV) as a function of an argon-irradiation dose.

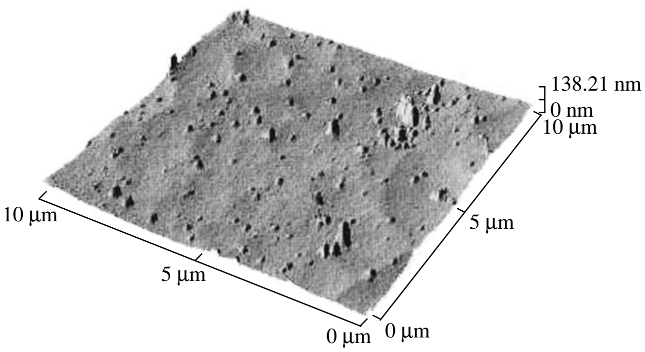

Fig. 5. Microscopic image of the silicon-wafer surface implanted with argon ions with a dose of $\Phi = 3 \times 10^{16}$ cm^{-2}.

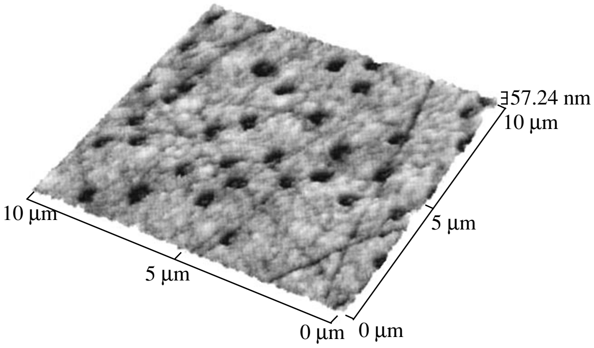

Fig. 6. Microscopic image of the silicon-wafer surface implanted with argon ions with a dose $\Phi = 3 \times 10^{17}$ cm^{-2}.

(Fig. 4). The identical shape of the dependences for the absorption coefficient and the electrical resistance on a dose of implanted argon and their threshold character imply that the origin of the effects observed is associated with processes occurring in the stopping range of argon ions at the rear side of a wafer during ion irradiation.

The surface topography was investigated at the rear side of wafers by the AFM for various doses of argon-ion irradiation. These investigations showed that the topography of a silicon-wafer surface irradiated with argon ions with doses of $\Phi \le 10^{15}$ cm^{-2} remained virtually unchanged.

As the argon-implantation dose increases to $\Phi = 10^{16}$ cm^{-2}, individual blisters begin to appear on the surface; their sizes are about 150 nm and the density is 2×10^8 cm^{-2}. On further increasing the implantation dose (Fig. 5), an increase in size and density of the blisters is observed to 200–230 nm and 3.5×10^8 cm^{-2}, respectively. The surface profile becomes more and more irregular; at some scans, the coalescence of blisters is observed. With the following increase in the dose, the coalescence proceeds more and more actively; as a result, the surface density of blisters is reduced approximately by an order of magnitude (to ~10^7 cm^{-2}). Some of the blisters attain a size of 300 nm.

When the wafers are irradiated with argon ions with $\Phi = 10^{17}$ cm^{-2}, the surface topography is drastically modified. Circular-shaped craters with irregular edges of 500 nm in diameter and 100–150 nm deep appear on the sample surface. Upon further increase of the argon-implantation dose, we observe the development of a “spongy” structure in the surface layer (Fig. 6).

In our opinion, the following processes take place during the argon irradiation of silicon wafers. Argon implanted in the silicon matrix with a relatively low dose (up to ~3×10^{15} cm^{-2}) shows no chemical activity and remains mobile. With attaining a reasonably high dose (about $\Phi \sim 10^{16}$ cm^{-2}), redundant argon is accumulated in blisters concentrating presumably around microdefects formed during the growth of the ingot. Upon further increasing the dose ($\Phi \sim 10^{16}$ cm^{-2} and higher), individual argon blisters begin to coalesce. With an increase in the dose, the coalescence proceeds progressively more actively, as a result of which blister sizes increase and their density decreases. However, mechanical stresses in silicon hamper an unlimited growth of blisters and set their critical values both in sizes and in density. With a further increase in the implantation dose (up to $\Phi_{Ar} = 10^{17}$ cm^{-2}), the coalescence of blisters gives way to flaking, as a result of which craters are observed on the surface.

The fact that the blisters and craters are not deep in the crystal but on its surface is caused by an approximate equality between values of the mean projected range for argon ions ($\bar{R}_p = 41 \pm 18.1$ nm) and the thickness of the sputtered silicon layer (about 35 nm) for $\Phi_{Ar} = 10^{17}$ cm^{-2} and $E_{Ar} = 40$ keV [6]. For a dose $\Phi_{Ar} = 10^{17}$ cm^{-2}, the crystal surface falls into the region of the argon-distribution peak, in which case the highest density of blisters is attained.

Thus, as already mentioned, the reason for the appearance of a crater on the irradiated surface is a burst of argon blisters during irradiation for doses of $10^{16} < \Phi_{Ar} < 10^{17}$ cm^{-2}. During the burst of blisters, the shock waves are formed with a differential pressure of $P \sim 10^9$ Pa (i.e., on the order of the ultimate strength for silicon). Propagating deep into the crystal, these waves induce considerable modifications in the defect–impurity system of the silicon crystal. One such modification is the stimulated reaction of synthesizing the Si_3N_4 phase in Si_xN_y layers with a high density of defects.

Here, it is worth mentioning study [7], in which the production of Si_3N_4-based ceramics is described as follows. Molecular nitrogen was let into a container with silicon powder. Thereafter, it was compressed to a pressure of 10^7 Pa. When the entire system was heated above 300°C, the synthesis of silicon nitride took place; i.e., high pressure and temperature lead to the promotion of a chemical reaction between silicon and nitrogen. This process is similar to that described by us; the difference consists in the fact that, in our case, the reaction of synthesis arose under the dynamic action of shock waves, rather than under static conditions.

CONCLUSION

On the basis of the results obtained, the following conclusions can be made.

(i) The argon-beam treatment of the rear side of a silicon wafer stimulates the synthesis of a Si_3N_4 insulator phase in the Si_xN_y layer formed on the front side of the crystal and thus improves its insulating properties.

(ii) The effects under investigation manifest themselves in the argon-implantation dose range of 10^{16} cm^{-2} $< \Phi_{Ar} < 10^{17}$ cm^{-2}.

(iii) According to the model proposed, the modifications observed in the Si_xN_y layers are caused by the nucleation, growth, and bursting of blisters on the surface of the samples irradiated with argon, as a result of which arise shock waves responsible for the stimulation of silicon nitride synthesis near the working surface.

ACKNOWLEDGMENTS

We thank Corresponding Member of the RAS M.F. Churbanov for his useful participation in discussing certain results of this study and also G.A. Maksimov, D.O. Filatov, V.K. Vasil’ev, and V.L. Shargel’ for their help in carrying out the experiments.

This study was supported by the Ministry of Education of the Russian Federation program “Higher School Investigations in the Field of Production Technologies” (2000), project no. 01.12.01.15

REFERENCES

1. P. V. Pavlov, E. S. Demidov, and V. V. Karzanov, Vysokochist. Veshchestva, No. 3, 31 (1993).
2. P. V. Pavlov, K. A. Markov, V. V. Karzanov, and E. S. Demidov, Vysokochist. Veshchestva, No. 2, 56 (1995).
3. E. S. Demidov, K. A. Markov, and V. V. Karzanov, Fiz. Tekh. Poluprovodn. (St. Petersburg) **34**, 170 (2000) [Semiconductors **34**, 163 (2000)].
4. Yu. A. Volgin and I. N. Ukhanov, Opt. Spektrosk. **38** (4), 727 (1975) [Opt. Spectrosc. **38**, 412 (1975)].
5. M. Lampert and P. Mark, *Current Injection in Solids* (Academic, New York, 1970; Mir, Moscow, 1973).
6. A. F. Burenkov, F. F. Komarov, M. A. Kumakhov, and M. M. Temkin, *Tables of Parameters of Spatial Distribution of Ion-Implanted Impurities* (Belarus. Gos. Univ., Minsk, 1980), p. 114.
7. O. Yamada, in *The Chemistry of Synthesis by Combustion*, Ed. by M. Koizumi (Mir, Moscow, 1998), translated from Japanese.

Translated by V. Bukhanov

Semiconductors, Vol. 35, No. 1, 2001, pp. 24–32. Translated from Fizika i Tekhnika Poluprovodnikov, Vol. 35, No. 1, 2001, pp. 25–33.
Original Russian Text Copyright © 2001 by Morozova, Karetnikov, Blinov, Gavrishchuk.

A Study of Luminescence Centers Related to Copper and Oxygen in ZnSe

N. K. Morozova*, I. A. Karetnikov*, V. V. Blinov*, and E. M. Gavrishchuk**

** Moscow Power Institute, ul. Krasnokazarmennaya 17, Moscow, 111250 Russia*
e-mail: MorozovaNK@mpei.ru
*** Institute of High-Purity Substances, Russian Academy of Sciences, ul. Tropinina 49, Nizhni Novgorod, 603600 Russia*

Submitted May 15, 2000; accepted for publication May 17, 2000

Abstract—The effects of deviation from stoichiometry and the copper and oxygen concentrations on cathodoluminescence spectra were studied in ZnSe condensates obtained by chemical vapor deposition and doped with Cu during growth. The results were supplemented with the study of the microstructure and microcomposition using scanning electron microscopy, measurements of electrical conductivity, and calculations of the equilibrium between the native point defects. It is shown that three types of Cu-related centers are always accompanied with self-activated centers that include oxygen at the Se lattice site (O_{Se}). The paired centers *SA*(I)–Cu(I), *SAL*(II)–Cu(II), and III–Cu(III) are typical of all II–VI compounds. All observed I–III Cu-containing centers are associative. Models of emission centers are suggested. A change of the emission type I–III is related to the recharging of the same group of defects that include O_{Se}, Zn(Cu), and V_{Zn}. New phenomena that occurred in the region of I–III bands and were related to the profound purification of the material were observed. *© 2001 MAIK "Nauka/Interperiodica".*

INTRODUCTION

The type of centers formed by Cu in a ZnSe lattice and their manifestation in the luminescence spectra have been repeatedly discussed [1–8]. There are three main emission bands that can be attributed to the doping of II–VI compounds with copper. For ZnSe, the Cu–*R* (640 nm) and Cu–*G* (510 nm) bands are best known [1–4, 6, 7]. The third band has been studied in detail for ZnS; this band is responsible for the green emission (~510 nm) of ZnS:Cu luminophors [6, 7, 9, 10]. For ZnSe, this band should peak at ~730 nm. It has been shown recently [11] that, in studying the emission from the Cu-related centers in ZnSe, it is necessary to take into account the self-activated accompanying emission related to oxygen rather than to copper. As far back as 1968, Stringfellow and Bube [1] pointed out that, in ZnSe:Cu, self-activated emission always accompanies the Cu–*R* band; the centers responsible for this emission have almost the same structure as those responsible for the Cu–*R* band.

Recent studies [12–14] of high-purity ZnSe crystals, which were intentionally doped only with copper and which contained oxygen as a background impurity, suggested that the self-activated emission accompanying the Cu-related bands is not connected with the well-studied "self-activated" $SA^{\text{III–VII}}$ emission band that owes its origin to activation by impurities belonging to the III–VII Groups. For clarity in the following presentation, we denote the bands that emerge owing to activation by oxygen of various II–VI compounds as *SA*(I), *SAL*(II), and III, whereas the similar Cu-related bands are denoted as Cu(I), Cu(II), and Cu(III).

The interpretation of the Cu-related emission centers in II–VI compounds is contradictory. In particular, the green Cu–*G* emission in ZnSe at low temperatures [1] is related to the electronic configuration Cu $3d^8$; however, this band has also been attributed [2] to transitions from the shallow donor level to the acceptor level in a complex of copper with a certain accompanying impurity *X* (the {Cu–*X*} center). Recently, it was suggested [15] that the emission band in ZnSe in the vicinity of Cu–*G* at 4.2 K was related to V_{Se}; however, according to the data reported in [13, 16, 17], selenium vacancies are responsible for the infrared (IR) emission in the range of 820–960 nm.

According to [1, 2], the emission band Cu–*R* in ZnSe:Cu is caused by the transition of electrons from the conduction band to the level of the isolated Cu_{Zn} center. It was also suggested [5] that the Cu–*R* emission band peaked at 642 nm at 300 K is not related to copper at all and does not differ from the self-activated ZnSe luminescence; in fact, this band is often dominant in presumably pure crystals and is retained in the crystals thoroughly freed from copper. Moreover, the methods of optically detected magnetic resonance (ODMR) and electron spin resonance (ESR) do not support the involvement of copper in the Cu–*R*-center formation [18].

In addition to this, it was assumed [3, 8] that copper could form isolated centers at the lattice ($Cu_{Zn}^{\times(/)}$) and interstitial ($Cu_i^{\times(\bullet)}$) sites in ZnSe. The corresponding associations $\{Cu_{Zn}^{\times}-Cu_i^{(\bullet)}\}$ and $\{Cu_{Zn}^{/}-D_{Zn}^{(\bullet)}\}$ act as acceptors in the donor–acceptor pairs and are responsible for the Cu–*G* and Cu–*R* bands, respectively.[1]

FORMULATION OF THE PROBLEM, SAMPLES, AND METHODS

Oxygen is an unavoidable background impurity in ZnSe, and its limiting concentration may be as high as ~10^{20} cm^{-3} if the methods for purification are conventional. Awareness of this problem has become more and more widespread in the relevant publications. We attempted to study the effect of doping ZnSe with copper while having regard for the presence of oxygen. In order to solve the formulated problem, we used chemical vapor deposition (CVD) to grow the samples [19]. This technology makes it possible to obtain fairly pure ZnSe, dope it controllably with Cu during growth while varying the excess of Zn or Se with respect to the stoichiometric composition, and introduce various amounts of oxygen. This implied that it was possible to form various types of Cu-related centers or complexes.

During the growth of ZnSe (from gaseous H_2Se and Zn precursors), copper was introduced in combination with zinc in the vapor phase [11]. Using this technology at 700°C, we deposited a number of polycrystalline ZnSe condensates. We now consider the results obtained for representative samples.

Condensate *A* had an increased concentration of oxygen [O] ~ 10^{20} cm^{-3} in the main part (Fig. 1). The deviation from stoichiometry varied along the length, so that, in the middle portion (l = 7–20 cm), a slight excess of Zn was observed. The concentration of copper [Cu] in the main portion of condensates *A* and *B* was ~10^{16} cm^{-3}. As [Cu] increased, we observed an increase in the resistivity that varied along the length from 2×10^9 to 1×10^{11} Ω cm. Condensate *B* with a lower concentration of oxygen (2×10^{18} cm^{-3}) was grown with an excess of Se compared to condensate *A* by increasing the ratio between H_2Se and Zn to 1.7. Condensate *C* was grown using the same setup without intentional doping with copper; in this case, 0.9 vol % of oxygen was added to the gaseous phase, with the ratio between H_2Se and Zn being maintained at 1.2. The concentration of other impurities in the ZnSe condensates was no higher than 10^{15}–10^{16} cm^{-3} [14].

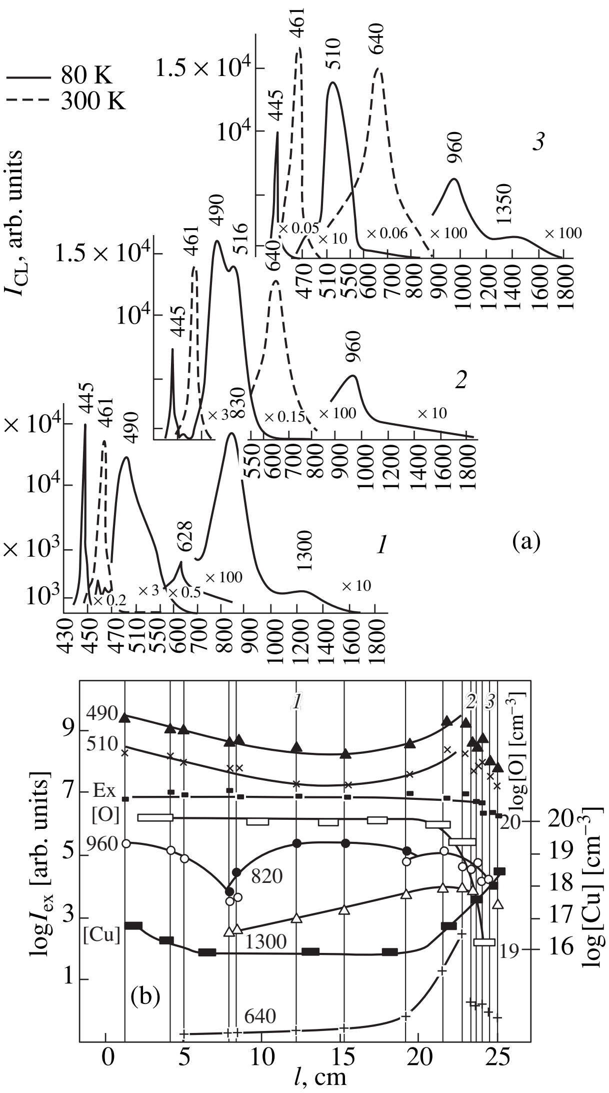

Fig. 1. (a) Cathodoluminescence spectra of condensate *A* and (b) variations of cathodoluminescence-band intensities and also of [O] and [Cu] over the length. For clarity's sake, the band intensities are multiplied by the coefficients as follows: $I_{490.510} \times 10^2$ (80 K), $I_{820.960} \times 1$ (80 K), $I_{1300} \times 10^{-1}$ (80 K), and $I_{640(SA)} \times 10^4$ (300 K). All the intensities are calculated from the area under the curves, except for the excitonic band $I_{ex} \times 10^2$ (80 K) whose intensity corresponds to the peak. The spectra are represented for typical freshly cleaved portions of condensate *A*: spectra *1* are for l = 12 cm; spectra *2*, for l = 22 cm; and spectra *3*, for l = 25 cm.

We studied the cathodoluminescence spectra stepwise along the length of freshly cleaved condensates. The method has been described in detail elsewhere [14, 20, 21]. The structure and microhomogeneity of the crystallites were studied using a scanning electron microscope (SEM). Resistivity was measured using probe contacts. The total concentration of oxygen was determined by a kinetic method using gas chromatography [22], and that of copper was determined by precision spectral analysis.

---

[1] It is generally accepted that the two charge states of copper at the lattice sites are denoted as Cu_{Zn}^{1+} ($3d^{10}$) and Cu_{Zn}^{2+} ($3d^9$) in relation to the nearest neighboring surroundings, or, to put it differently, $Cu_{Zn}^{/}$ ($3d^{10}$) and $Cu_{Zn}^{\times}$ ($3d^9$) are the nearest-neighbor surroundings with reference to the matrix lattice. The designations $^{/}$, $^{\bullet}$, and $^{\times}$ are identical to $^{-}$, $^{+}$, and ^{0}.

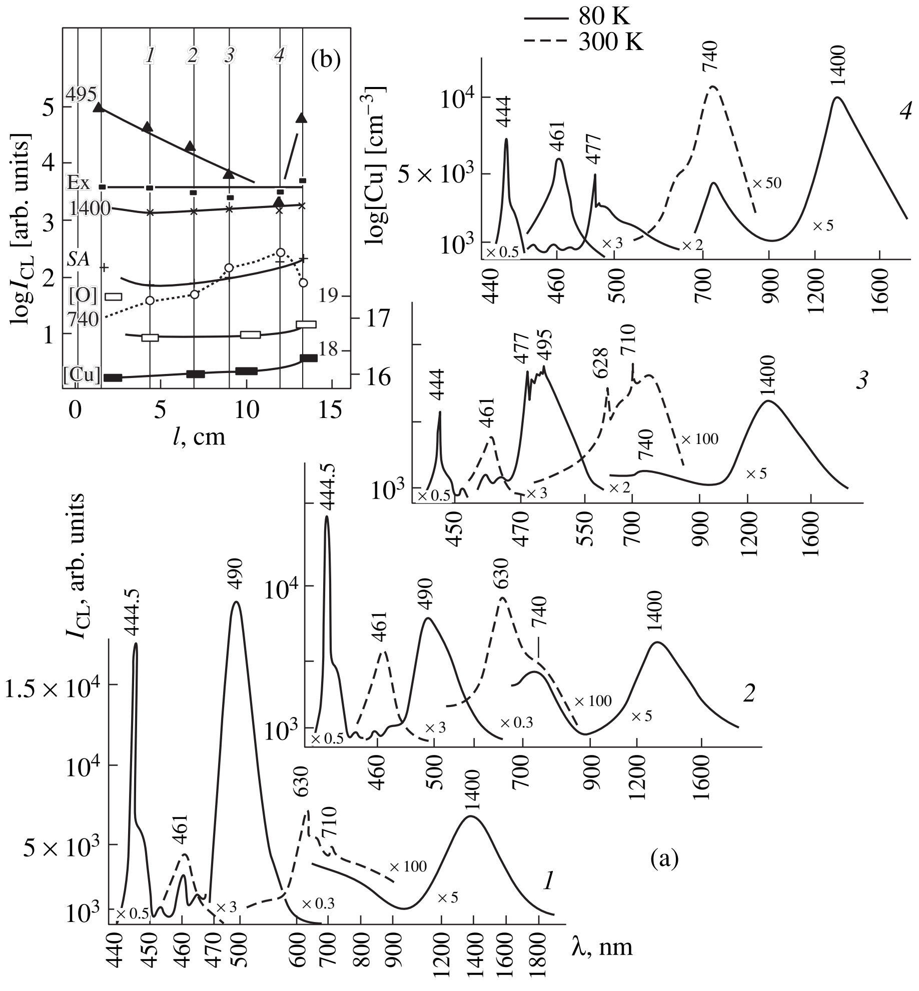

Fig. 2. (a) Cathodoluminescence spectra of condensate *B* and (b) variations of the band intensities also of [O] and [Cu] over the length. The intensities are evaluated from the peaks and correspond to 80 K for the bands at 495 and 1400 nm and to 300 K for excitonic band (Ex) and for bands *SA*-630 and *SA*-740 nm. Designations for the spectra *1*, *2*, *3*, and *4* in (a) correspond to the same designations as in (b).

EXPERIMENT

Typical cathodoluminescence spectra of condensate *A* are shown in Fig. 1a. The spectra feature an excitonic band with a peak at 445 nm and a half-width of 16–18 meV at 80 K and a peak at 461 nm and a half-width of ~40–44 meV at 300 K. The intensity I_{ex} of the excitonic band and its spectral position and half-width remain almost unchanged over the length of the condensate, which is indicative of structural homogeneity of the condensate over its length. The general shape of cathodoluminescence spectra is typical of the ZnSe samples with nearly stoichiometric composition [14].

The green emission copper-related band Cu–*G* is distinct at 80 K in the cathodoluminescence spectra of ZnSe:Cu condensate *A* with [O] ~ 10^{20} cm^{-3} over its entire length. For the freshly cleaved samples, the copper-related Cu–*G* band has a peak at ~510 nm at 80 K (Fig. 1a, spectrum *3*), which is close to the position of the zero-phonon component (508 nm, according to [2]). It is characteristic that the intensity of the green-emission band decreases as the Cu concentration increases to 10^{18} cm^{-3} when oxygen concentration [O] decreases from 10^{20} to ~10^{19} cm^{-3} in the end part of the condensate (Fig. 1b). For condensate *B* with a reduced oxygen concentration ([O] ~ 10^{18} cm^{-3}), the green-emission band Cu–*G* in the cathodoluminescence is not characteristic at all of the main part of the condensate for the same value of [Cu] (Fig. 2). The obtained data indicate that the intensity of the Cu–*G* band depends on the concentration of oxygen (along with numerous other observations). Apparently, the complex {Cu–*X*} responsible [2] for the Cu–*G* band in ZnSe includes oxygen as impurity *X*.

The latter inference is supported by the similar behavior of the accompanying self-activated band peaking at 490–495 nm and related to the presence of oxygen at the ZnSe lattice sites [14]. The band peaking

Comparison of emission bands corresponding to self-activated oxygen- and copper-containing centers in II–VI compounds

Compound		ZnS	ZnSe	CdS
$E_g^{80\ \mathrm{K}}$, eV		3.826	2.814	2.575
characteristic of the center	charge state			
SA(I)	$\mathrm{I}^{/(\times)}$	445 (415)	628 (605)	635 (594)
$\{\mathrm{O}_\mathrm{S}^{*} \cdot A_i^{\bullet} \cdot V_A^{//}\}^{/}$		$E_A = 0.69$ (0.59)	$E_A = 0.61$ (0.55)	$E_A = 0.38$ (0.27)
Excess of metal				
Cu(I)				
$\{\mathrm{O}_\mathrm{S}^{*} \cdot \mathrm{Cu}_i^{\bullet} \cdot V_A^{//}\}^{/}$		450	640	640
$3d^{10}$		$E_A = 0.7$	$E_A = 0.65$	$E_A = 0.36$
SAL(II)	$\mathrm{II}^{r(\cdot)}$			
$\{\mathrm{O}_\mathrm{S}^{*} \cdot A_i^{\bullet\bullet} \cdot V_A^{//}\}^{\times}$		355–370	477	520–545
Stoichiometry		$E_A = {\sim}0.3$	$E_A = 0.15$	
Cu(II)				
$\{\mathrm{O}_\mathrm{S}^{*} \cdot \mathrm{Cu}_i^{\bullet\bullet} \cdot V_A^{//}\}^{\times}$		380	508	~530–540
$3d^{9}$		$E_A = 0.37$	$E_A = 0.24$	
III	$\mathrm{III}^{\cdot(\cdot\cdot)}$			
$\{\mathrm{O}_\mathrm{S}^{*} \cdot A_i^{\bullet\bullet} \cdot V_A^{/}\}^{\bullet}$		510	735	730
Excess of metalloid		$E_A = 1.1$	$E_A = 0.87$	$E_A = 0.54$
Cu(III)				
$\{\mathrm{O}_\mathrm{S}^{*} \cdot \mathrm{Cu}_i^{\bullet\bullet} \cdot V_A^{/}\}^{\bullet}$		520	740	730
$3d^{9}$		$E_A = 1.13$	$E_A = 0.87$	$E_A = 0.5$

Note: Numbers in the third, fourth, and fifth columns indicate the wavelength of the peak of zero-phonon emission band (in nm) at 80 K for the corresponding center and compound; the position of the emission-center acceptor level E_A (in eV) is measured from the top of the valence band. For *SA*(I), the data correspond to two components of the doublet: the short-wavelength one (in brackets) and the long-wavelength one.

at 490–495 nm is similar to the self-activated *SAL* emission band in ZnSe and has been studied in detail recently [12, 14]. The Cu–*G* band appears in the spectra of the ZnSe:Cu condensate in combination with band *SAL*; these bands have nearly the same spectral position and behavior (Fig. 1b). As [Cu] increases over the condensate-*A* length, the contribution of the Cu–*G* band increases compared to the band peaked at 490 nm (Fig. 1a). The observations of the simultaneous presence of self-activated luminescence and the emission related to copper-containing centers have been also reported in previous publications for all II–VI compounds. These data are systematized in the table for three compounds. It has been repeatedly noted that the parameters of the deep acceptor recombination levels of Cu and those of centers owing their existence to activation with oxygen are nearly the same (see table).

In previous publications, the origination of self-activated or Cu–*G* and Cu–*R* centers has been related most often to a variation in the copper concentration. Thus, according to [24], for [Cu] < 3×10^{15} cm^{-3} at 300 K, a band peaked at 610 nm and related to self-activated *SA* centers should be observed; as [Cu] increases to ~2×10^{16} cm^{-3}, the Cu–*R* band peaked at 645 nm appears. The low-temperature Cu–*G* 535 nm band becomes distinct if [Cu] ≥ 4×10^{17} cm^{-3}. Our experiments showed that the above inferences are partially justified only for condensate *B* with a lowered concentration of oxygen. For condensate *A* with [O] ~ 10^{20} cm^{-3} and [Cu] ≈ 10^{16} cm^{-3}, the green- and orange-emission bands are clearly recognized for the entire length. These results show that the intensity of Cu-related bands depends not only on [Cu] but also on [O].

The orange emission band Cu–*R* virtually does not manifest itself in the spectra of the condensates studied

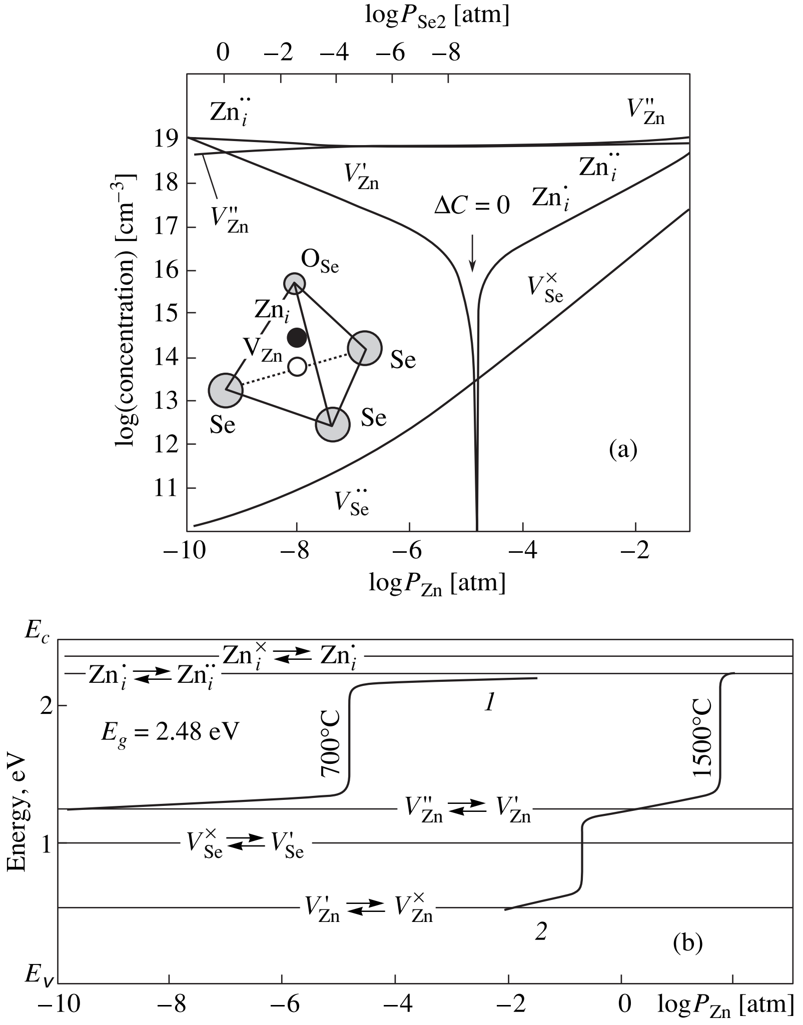

Fig. 3. (a) Equilibrium between native point defects in ZnSe at 700°C recalculated for low temperature conditions; $\Delta C = 0$ represents the stoichiometric point. (b) Shift of the Fermi level (at 300 K) within the homogeneity domain of ZnSe. Curve *1* corresponds to Fig. 3a; curve *2* is drawn for comparison and corresponds to the equilibrium temperature close to the melting point (1500°C) [21]. A structural unit of sphalerite lattice (tetrahedral environment of a cationic site) is shown in the insert in (a).

at 80 K (Figs. 1, 2a). This is especially true of condensate *B* with a lowered concentration [O]. At room temperature, the Cu–*R* band peaked at 640 nm gives way to a green emission band in the spectra (Fig. 1a). It is very difficult to differentiate between the above band and the *SA* cathodoluminescence band peaking at ~630 nm and caused by activation with oxygen.

DISCUSSION OF THE RESULTS

The behavior of the orange emission self-activated *SA*(I) band in ZnSe has been studied in detail in [12, 13, 21]; it was shown that the complex responsible for this band includes oxygen at the lattice site, the zinc vacancy $V_{Zn}^{//}$, and $Zn_i^{\bullet}$. Oxygen at the lattice site (O_S) is neutral as an isoelectronic center, or else we may assume that oxygen in this center has a negative effective charge O_S^{*} (see table). Since this *SA*(I) luminescence is originated and enhanced if Zn is in excess, this luminescence was related to Zn in early experiments with ZnS [25]. The above band is thermally stable; it is distinguishable up to 300–400 K for all compounds included in the table, both undoped and doped with Cu. The spectral position of the band remains unchanged if the temperature and the excitation intensity vary [1, 13, 26].

According to the data of numerous studies [6, 7, 12–14, 27], oxygen included in the *SA*(I) center is located at the lattice site. In order to characterize the nearest neighbors of the oxygen center O_S at the lattice site, we show a structural unit (an elementary tetrahedron) in Fig. 3a. If the oxygen atom is located at the lattice site (O_{Se}), the Zn atom should be displaced from the lattice site to O_{Se} according to calculations reported in [27, 28]. The effect of the isoelectronic center results in a decrease in the distance between the interacting particles by 40–50% [27, 28], which can be thought of as the formation of Zn_i and V_{Zn} to the first approximation [27]. The ODMR and ESR methods verify the presence of a zinc vacancy in the structure of the orange emission center [18, 29].

However, the above center cannot be formally identified with a donor–acceptor (DA) pair or an *A* center whose origination is presumably due only to the Coulomb interaction. The *A* center is destroyed in the course of thermal treatment in zinc vapors, whereas the close Frenkel pairs (formed, e.g., by irradiation) are annealed out even at 150 K [18, 29]. In contrast to the above centers (as was mentioned above), the orange luminescence of ZnSe is not only enhanced with an excess of Zn but also persists to 300–400 K. Evidently, the cause of this is oxygen that stabilizes the center (Fig. 3a).

The charge state of the center should depend on the surrounding accommodating lattice: on the charge state and the type and concentration of the native point defects that influence the Fermi level [12]. We may assume that the displacement of Zn from the lattice site gives rise to the $\mathrm{O}_{\mathrm{S}}^{*}$-center environment ($V_{\mathrm{Zn}}$ and Zn_i) that can acquire a charge depending on the type and number of charge carriers in the crystal (Fig. 3b). If zinc is in excess, the vacancy and interstitial zinc may be charged as $V_{\mathrm{Zn}}^{//}$ and $\mathrm{Zn}_i^{\bullet}$. In this charge state, these defects can also be involved in a complex. In this case, the complex $\{\mathrm{O}_{\mathrm{S}}^{*} \cdot \mathrm{Zn}_i^{\bullet} \cdot V_{\mathrm{Zn}}^{//}\}^{/}$ is negatively charged; it is also possible that these centers give rise to a DA pair $\{\mathrm{O}_{\mathrm{S}}^{*} \cdot \mathrm{Zn}_i^{\bullet} \cdot V_{\mathrm{Zn}}^{//}\}^{/} - \mathrm{Zn}_i^{\bullet}$ by attaching an additional Zn atom.

The model of DA recombination is consistent with the doublet structure (see table) and the behavior of the short- and long-wavelength components of the *SA* band [13, 20]. The energy difference between the doublet bands is close to the ionization energy for interstitial Zn. The short-wavelength component of the doublet becomes more intense with decreasing [Zn] as a result of annealing in Se vapors [13]. The intensity of this component also increases with temperature, whereas the long-wavelength component is gradually quenched as the temperature is raised to 300 K [13, 30].

We now dwell on the role of copper in the formation of I–III centers. Assumptions that Cu is of no concern are inexact. Since the structure of the *SA* center has become clearer by now (Fig. 3a; see table), it is obvious that copper can be incorporated into this center in the place of Zn. It has been noted previously [1] that the doping of ZnSe with copper introduces acceptor levels in the band gap; these levels lie 0.05–0.1 eV deeper than those of the *SA* centers, so that the Cu–*R* band is invariably shifted somewhat to longer wavelengths compared to the *SA* band. Copper replacing zinc at the lattice sites ($\mathrm{Cu}_{\mathrm{Zn}}$) can play the same role as $\mathrm{Zn}_{\mathrm{Zn}}$, because Cu and Zn are neighbors in the periodic table of elements and, thus, have almost the same size and electronegativity, the charge states of +1 and +2, etc. Therefore, the role of Cu in the formation of the same centers should not be underestimated. In addition, $\mathrm{Cu}_{\mathrm{Zn}}$ favors the introduction of oxygen; i.e., it is conducive to complex formation. Obviously, the role of Cu is less important if there is an excess of Zn, which constitutes the condition for the formation of *SA* bands; apparently, this is why the involvement of Cu in the formation of the Cu–*R* (*SA*) band has been doubted [5]. It has been shown [6] that the role of Cu becomes more important in the formation of *SA* centers at dislocations in ZnS. The behavior of an isolated Cu ion at the lattice site of oxygen-free II–VI crystals has not been studied and seems to be an artificial problem.

Studies of condensates *A* and *B* verified the profound effect of deviation from stoichiometry on the type of centers formed (I, II, or III). In fact, the emergence of the Cu–*G* or Cu–*R* cathodoluminescence bands depends not only on [Cu] and [O]. Thus, as we noted above, the intensity of the *SA* band increases only if there is an excess of Zn. This special feature is also distinguishable for the condensates. For example, special features of the growth of condensate *A* suggest that a certain enhancement of zinc deposition occurs in the middle part of this condensate. This is corroborated by variations in the intensity of the IR bands peaked at 820 and 960 nm (Fig. 1b).[2] In a number of publications [13, 30], it has been noted that, as the concentration of excess zinc in ZnSe increases, the intensity of the band peaked at 820 nm ($V_{\mathrm{Se}}^{\times}$) increases compared to that peaked at 960 nm ($V_{\mathrm{Se}}^{\bullet}$). As the concentration [Zn] decreases (which occurs at the end parts of condensate *A*), the band peaked at 820 nm is replaced by the band peaked at 960 nm.

An increase in the intensity of the band peaked at 820 nm in the middle part (~10 cm) of condensate *A* accounts for an increase in the intensity of the Cu–*R* band with [Cu] being kept constant and for a decrease in the intensity of the Cu–*G* band peaked at 490 nm (Fig. 1b). This represents one of the numerous observations indicating that the intensities of the Cu–G(II) and Cu–*R*(I) bands are also related to variations in the crystal's stoichiometry. An insufficient amount of excess Zn_i in the studied condensates *A* and *B*, whose composition is nearly stoichiometric, retards the formation of Cu–*R*(I) and *SA*(I) centers [12, 14]. The role of excess zinc consists primarily in determining the charge state of the center. For a deficit of Zn, the *SA*(I) center ceases to exist (because its charge state changes), and the center transforms into *SAL*(II) (see table). The conditions for the emergence of the band peaked at 495 nm imply that ZnSe has the stoichiometric composition or has a slight excess of selenium [14]. In this case, the charge state of dominant defects corresponds to $V_{\mathrm{Zn}}^{//}$ and $\mathrm{Zn}_i^{\bullet\bullet}$ (Fig. 3b); in general, the complex can be represented as $\{\mathrm{O}_{\mathrm{S}}^{*} \cdot \mathrm{Zn}_i^{\bullet\bullet} \cdot V_{\mathrm{Zn}}^{//}\}^{\times}$ or $\mathrm{II}^{\times(\bullet)}$ (see table). The band *SAL* is quenched at 150–200 K and shifts with the coefficient close to $\Delta E_g/\Delta T$. The latter is due to the fact that the acceptor level of the *SAL* center is comparatively shallow in the band gap [1, 8].

---

[2] According to [16, 17], the bands peaked at 820 and 960 nm are related to V_{Se}. The two luminescence bands are caused by transitions from an excited state and from the conduction band to the ground level $V_{\mathrm{Se}}^{\times(\bullet)}$. The short-wavelength band is related to an intracenter transition, whereas the long-wavelength band is associated with a transition from the conduction band to the ground level of V_{Se} [17]. Both charge states $V_{\mathrm{Se}}^{\times(\bullet)}$ of selenium vacancies can be observed if the Fermi level position is close to that of the ground level of the F^{+} center, and an increase in the number of the charged $V_{\mathrm{Se}}^{\bullet}$ centers enhances the probability of transitions $E_c \longrightarrow E(V_{\mathrm{Se}}^{\bullet})$ compared to the intracenter transitions.

The band III. Figure 2 illustrates the variations in the cathodoluminescence spectra in the middle part of condensate *B* grown with an excess of Se. An excess in Se was accomplished by increasing the ratio H_2Se/Zn during the growth. Curves *1–4* corresponding to an increase in the excess of Se reveal the band peaked at ~740 nm. This band arises only in the middle part of condensate *B* (in the zone enriched with Se) and becomes more intense as the excess of Se increases. In this situation, in the part of the condensate where an increase in [Se] is observed, the intensities of the *SAL* and *SA* bands decrease.[3] We believe that we observe band III that has been inadequately studied in ZnSe [13, 21]. Band III is not typical of condensate *A* obtained with an additional introduction of Zn (in the course of doping with Cu).

Obviously, the origination of band III is related to an appreciable excess of metalloid in the crystals, in which case the Fermi level descends to the level of prevalent native acceptors $V_{\mathrm{Zn}}^{/}$. Figure 3b illustrates variations of the Fermi level in the entire domain of existence of ZnSe at 700 and 1500°C [21]. As can be seen, the defects $V_{\mathrm{Zn}}^{//}$ become dominant for a large excess of Se and at temperatures higher than 1000°C. We may assume that the lattice governs the recharging of the center, which can be described by the model $\{\mathrm{O}_{\mathrm{S}}^{*} \cdot A_i^{\bullet\bullet} \cdot V_{\mathrm{Zn}}^{/}\}$; i.e., the charge state of the center is transformed into the last of the feasible states ($\mathrm{III}^{\bullet(\bullet\bullet)}$). An analysis of the published data shows that center III comes into existence for all II–VI compounds if there is an appreciable excess of metalloid (see table). According to these data, the bands III and Cu(III) are thermally stable, persist up to 300 K, and do not shift with temperature. It has been repeatedly pointed out that this type of emission depends on [O], for example, in ZnS [6, 25] and CdS [31].

The model of center III suggested by us differs from that proposed in [6, 10], where a doubly positively charged metalloid vacancy was considered as a recombination center. However, the latter model [10] necessitates the preferential formation of vacancies $V_{\mathrm{VI}}^{\bullet\bullet}$ in II–VI compounds if there is an appreciable excess pressure of metalloid vapor; in particular, the sulfur vacancies $V_{\mathrm{S}}^{\bullet\bullet}$ are expected in ZnS for an excess sulfur-vapor pressure of ~100 atm [10].

Thus, all three main bands I–III arising as a result of doping both with oxygen and with copper are related to a deviation from stoichiometry. The role of Cu and its charge states when the center is recharged and there is a deviation from stoichiometry can be perceived from the table. The existence of band *SA*(I) [or band Cu(I) in the presence of copper] requires the presence of a donor or (in pure crystals) an excess of Zn. Bands *SAL*(II) or Cu(II) (in the presence of copper) are formed under the conditions that are close to stoichiometric or for a slight excess of metalloid. Band III is formed if there is an appreciable excess of metalloid, with the Fermi level descending and the concentration of native acceptors $V_{\mathrm{Zn}}^{/}$ increasing (Fig. 3).

If the samples are thoroughly purified, all three oxygen-related bands observed for the purest parts (differing in their deviation from stoichiometry) of the condensates demonstrate certain common specific features; i.e., a very narrow line appears on the short-wavelength side. This line is peaked at 710, 628, and 477 nm for bands III, *SA*, and *SAL* (Figs. 1–3).

In order to verify the role of oxygen in the formation of cathodoluminescence bands I–III in ZnSe, we grew condensate *C* with ~0.9 vol % of oxygen added to the vapor phase. Copper was not intentionally introduced, and, according to our analysis, its concentration in the condensate was comparable to the concentrations of other background impurities (~10^{15} cm^{-3}). The cathodoluminescence spectra measured at 80 K stepwise over the length of condensate *C* were similar to those for condensate *A*. Oxygen was mainly removed from the sample by precipitating as ZnO in the initial part of the condensate (in the range of 0–5 cm over the length) because ZnO is a higher temperature compound than ZnSe. ZnO was not detected in the excitonic spectra measured (in the region 370 nm) for the cleavages of the entire central part of condensate *C* (l = 9–22 cm). The oxygen concentration measured over the entire length of condensate *C* was no higher than ~4×10^{19} cm^{-3}.

The cathodoluminescemce spectra measured at 300 K are unusual for this material that is purer (due to the fact that it was not doped with copper) (see Fig. 4). Thus, the *SA* band whose contour is conventionally bell-shaped at room temperature (Fig. 1a) is now resolved into narrow lines (Fig. 4). These lines become somewhat more intense with increasing degree of the contaminants' removal and prevail in the spectra for cleavages of the purest central part of condensate *C*. These lines are peaked at 628 nm in the vicinity of band *SA*(I) and at 710 nm in the region of band III. The half-width of both lines is ~40 meV, the same as for the excitonic band. However, the intensity of these lines is lower by almost two orders of magnitude than that of the excitonic band (Fig. 4).

---

[3] It is worth noting that, if there is an excess of Se, the intensity of the IR band peaked at ~1400 nm increases by 1–2 orders of magnitude.

Previously, similar lines have been also observed for the low-temperature band II for the purest starting part of the ZnSe CVD condensate [14]. These lines peaked at 477 nm for band *SAL*(II) and at 508 nm for band Cu(II) and had a half-width of 20–25 meV at 80 K and an intensity of 5×10^3 arbitrary units, which is comparable to the parameters of the excitonic band peaked at 444 nm.

Similar narrow lines were observed for thoroughly purified CdTe and ZnTe compounds [32] and became known as the "*Z*-center" lines. The three possible charge states of oxygen-related center, as suggested by us, are consistent with those described in [32]: $Z^{-/0}$, $Z^{0/+}$, and $Z^{+/+2}$. In [32], the lines of the *Z* centers are related to an exciton bound by (localized at) an isolectronic oxygen-containing center in ZnTe. It has been pointed out that it is preferable to detect the *Z* centers at structural defects (dislocations) [33] for low concentration of the impurity responsible for the phenomenon under consideration. In materials that are insufficiently pure, the oxygen-related isoelectronic center can be surrounded by the Cottrell impurity cloud because this center has a short-range deformation potential. A thorough removal of foreign impurities resulted in the suppression of electron–phonon interaction [32] and in the emergence of a narrow line related to the isoelectronic center; judging from its spectral position, this line may be associated with the zero-phonon component.

We observe these phenomena in ZnSe, where, according to the published data, an oxygen-related isoelectronic center should not bound an exciton [34]. Nevertheless, the phenomenon is observed for oxygen- and copper-related centers I–III (and only for these). The positions of the *Z*-center bands observed in CdTe [35] are also close to those of I–III oxygen-containing centers in CdTe [36].

We verified the relation of the narrow lines to the oxygen-containing centers by studying another type of ZnSe crystal that was grown from the melt with an excess of selenium and was ultimately saturated with oxygen to a concentration as high as 3×10^{20} cm^{-3}. In this case, we also detected narrow lines that were peaked at 628 and 710 nm and had a half-width of ~40 meV both at 80 and at 300 K; these lines did not shift with temperature. The intensities of these lines are almost the same as of those shown in Fig. 4. The absence of spectral shift with temperature was also observed for broader *SA* bands [11–14] as was pointed out above; i.e., a narrow line constitutes the basis of the complex rather than represents a new line. The origin of the phenomenon is still not completely understood.

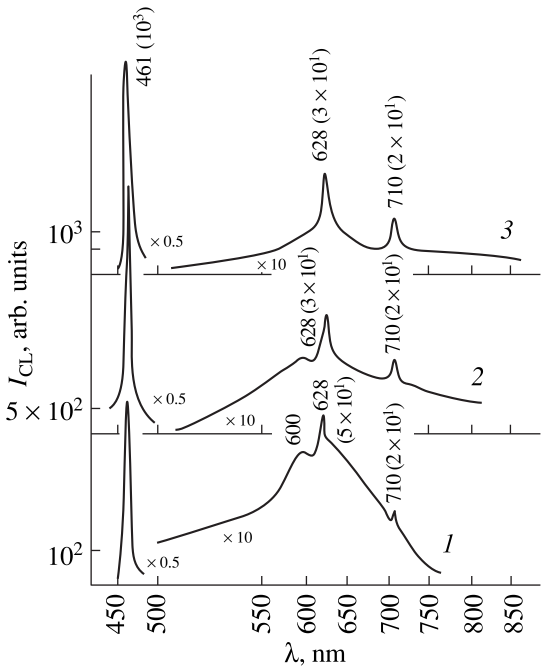

Fig. 4. Cathodoluminescence spectra for cleavages of the central part of condensate *C*; the spectra were measured at 300 K. Spectra *1*, *2*, and *3* correspond to the condensates of low, medium, and high purity.

CONCLUSION

Summing up, we can note the following:

(1) All the observed I–III copper-related centers are associative, and, in contrast with concepts persisting at present in a number of publications, their levels, that are located in the ZnSe band gap and are responsible for the emission bands Cu–*G* and Cu–*R*, are related to complexes rather than to isolated Cu_{Zn} centers. Oxygen is a constituent of the complexes. The centers similar to oxygen-containing self-activated centers are responsible for typical copper-related emission bands in ZnSe.

(2) Self-activated O-containing centers always accompany the three types of Cu-containing centers. In the structure of such centers, Cu_{Zn} plays the same role as Zn_{Zn}. The paired centers responsible for the cathodoluminescence bands *SA*(I)–Cu(I), *SAL*(II)–Cu(II), and III–Cu(III) are typical of all II–VI compounds that have been studied previously.

(3) In fact, all centers I–III are related to an isolated oxygen atom at the lattice site because the O_S center cannot exist without the considered imperfect surroundings. On the other hand, the O_S^* isoelectronic center is a complex.

(4) Within the homogeneity domain of ZnSe (for comparatively low temperatures of growing the compound), only three charge states are possible for the oxygen-containing center, which is consistent with the concepts of the *Z* centers. The change in the emission type I–III is related to the recharging of the same group of native point defects that include oxygen O_S^*, Zn_i(Cu), and V_{Zn}.

(5) The main bands originating from doping with oxygen and copper depend on the stoichiometry of ZnSe crystals: for an excess of Zn, bands I are dominant; for crystals close to stoichiometry, bands II are prevalent; and, for the samples having an appreciable excess of metalloid, bands III are dominant.

(6) The emission spectrum of centers I–III can characterize the overall purity of the crystal: a high degree of purification to the total concentration of impurities of no higher than 10^{17} cm^{-3} is accompanied with the emergence of narrow lines against the background of broad bands.

REFERENCES

1. G. B. Stringfellow and R. H. Bube, Phys. Rev. **14** (3), 903 (1968).
2. M. Godlewski, W. E. Lamb, and B. C. Cavenett, Solid State Commun. **39**, 595 (1981).
3. V. I. Sokolova, T. P. Surkova, M. V. Chukichev, and Vu Zoan M'en, Fiz. Tverd. Tela (Leningrad) **26**, 3681 (1984) [Sov. Phys. Solid State **26**, 2215 (1984)].
4. E. D. Wheeler, Jack L. Boone, J. F. Farmer, and H. R. Chandrasekhar, J. Phys. Chem. Solids **58** (1), 79 (1997).
5. V. D. Ryjikov, V. Havrushin, A. Klazlauskaz, *et al.*, J. Lumin. **52** (1–4), 71 (1992).
6. A. M. Gurvich, Author's Abstract of Doctoral Dissertation (Tartu, 1970).
7. *Physics and Chemistry of II–VI Compounds*, Ed. by M. Aven and J. S. Prener (North-Holland, Amsterdam, 1967; Mir, Moscow, 1970).
8. G. N. Ivanova, V. A. Kasiyan, D. D. Nedeoglo, and S. V. Oprya, Fiz. Tekh. Poluprovodn. (St. Petersburg) **32** (2), 171 (1998) [Semiconductors **32**, 154 (1998)].
9. N. P. Golubeva and M. V. Fok, Zh. Prikl. Spektrosk. **35**, 551 (1981).
10. *Physics and Chemistry of II–VI Compounds*, Ed. by A. N. Georgobiani (Nauka, Moscow, 1986).
11. N. K. Morozova, I. A. Karetnikova, V. V. Blinov, *et al.*, in *Proceedings of the XXX International Scientific and Technical Workshop "Noise- and Degradation-Related Processes in Semiconductor Devices"* (Mosk. Énerg. Inst., Moscow, 2000), p. 204.
12. N. K. Morozova, I. A. Karetnikov, and E. M. Gavrishchuk, Neorg. Mater. **35**, 917 (1999).
13. L. D. Nazarova, Author's Abstract of Candidate's Dissertation (Moscow, 1995).
14. N. K. Morozova, E. M. Gavrishchuk, O. R. Golovanova, *et al.*, Zh. Prikl. Spektrosk. **63**, 731 (1996).
15. I. A. Gorn, V. N. Martynov, E. S. Volkova, and V. I. Grinev, Fiz. Tekh. Poluprovodn. (Leningrad) **24**, 538 (1990) [Sov. Phys. Semicond. **24**, 336 (1990)].
16. F. J. Bryant and P. S. Manning, J. Phys. C **5**, 1914 (1972).
17. A. P. Okonechnikov, Author's Abstract of Doctoral Dissertation (Yekaterinburg, 1996).
18. K. M. Lee, L. S. Dang, and G. D. Watkins, Inst. Phys. Conf. Ser. **59**, 353 (1981).
19. G. G. Devyatykh, E. M. Gavrishchuk, and Yu. A. Dadanov, Vysokochist. Veshchestva **2**, 174 (1990).
20. N. K. Morozova, A. V. Morozov, I. A. Karetnikov, *et al.*, Fiz. Tekh. Poluprovodn. (St. Petersburg) **28**, 1699 (1994) [Semiconductors **28**, 944 (1994)].
21. N. K. Morozova, V. A. Kuznetsov, V. D. Ryzhikov, *et al.*, *Zinc Selenide: Growth and Optical Properties* (Nauka, Moscow, 1992).
22. V. S. Zimogorskiĭ, N. K. Morozova, N. A. Yashtulov, and V. V. Blinov, in *Proceedings of the XXX International Scientific and Technical Workshop "Noise- and Degradation-Related Processes in Semiconductor Devices"* (Mosk. Énerg. Inst., Moscow, 2000), p. 211.
23. N. K. Morozova, V. A. Kuznetsov, *et al.*, *Zink Sulfide: Growth and Optical Properties* (Nauka, Moscow, 1987).
24. V. I. Gavrilenko, A. M. Grekhov, D. V. Korbutyak, and V. G. Litovchenko, *Optical Properties of Semiconductors. A Handbook* (Naukova Dumka, Kiev, 1987), p. 432.
25. É. P. Pol'skikh, Author's Abstract of Candidate's Dissertation (Moscow, 1974).
26. L. P. Gal'chinetskiĭ, I. A. Karetnikov, V. E. Mashchenko, *et al.*, Zh. Prikl. Spektrosk. **58**, 488 (1993).
27. F. N. Dmitriev, V. D. Ryzhikov, and L. P. Gal'chinetskiĭ, *Thermodynamics of Isovalent Doping of Crystalline II–VI Semiconductor Compounds* (Nauchn.-Issled. Inst. Monokristallov, Kharkov, 1990).
28. É. D. Aluker, D. Yu. Lusis, and S. A. Chernov, *Electronic Excitations and Radioluminescence in Alkali-Halide Crystals* (Znanie, Riga, 1979).
29. G. D. Watkins, in *Radiation Effects in Semiconductors*, Ed. by N. B. Urli and J. W. Corbett (Inst. of Physics, London, 1977).
30. O. V. Vakulenko, V. N. Kravchenko, V. D. Ryzhikov, *et al.*, Fiz. Tekh. Poluprovodn. (St. Petersburg) **31**, 1211 (1997) [Semiconductors **31**, 1041 (1997)].
31. N. K. Morozova, A. V. Morozov, V. G. Galstyan, *et al.*, Neorg. Mater. **30**, 731 (1994).
32. A. V. Kvit, S. A. Medvedev, Yu. V. Klevkov, *et al.*, Fiz. Tverd. Tela (St. Petersburg) **40**, 1010 (1998) [Phys. Solid State **40**, 924 (1998)].
33. A. Gukasyan, A. Kvit, Y. Klevkov, and S. Oktyabrsky, Solid State Commun. **97**, 897 (1996).
34. G. S. Iseler and A. J. Strauss, J. Lumin. **3**, 1 (1970).
35. A. V. Kvit, Yu. V. Klevkov, S. R. Oktyabrsky, and B. G. Zhurkin, Semicond. Sci. Technol. **9**, 1805 (1994).
36. N. K. Morozova, I. A. Karetnikov, V. V. Blinov, *et al.*, Zh. Prikl. Spektrosk. **67** (1), 96 (2000).

Translated by A. Spitsyn

Semiconductors, Vol. 35, No. 1, 2001, pp. 33–39. Translated from Fizika i Tekhnika Poluprovodnikov, Vol. 35, No. 1, 2001, pp. 34–39.
Original Russian Text Copyright © 2001 by Bogoboyashchiĭ.

ELECTRONIC AND OPTICAL PROPERTIES OF SEMICONDUCTORS

The Concentration Dependence of Acceptor-State Radii in p-$Hg_{0.78}Cd_{0.22}Te$ Crystals

V. V. Bogoboyashchiĭ

Kremenchuk State Polytechnical Institute, Kremenchuk, 39614 Ukraine

Submitted April 4, 2000; accepted for publication May 24, 2000

Abstract—Hopping conduction in undoped p-$Hg_{0.78}Cd_{0.22}Te$ crystals containing native double-charged acceptors (Hg vacancies) with concentrations of 10^{16}–10^{18} cm^{-3} was studied. Electrical conduction with a variable hopping range is dominant in the entire concentration range at temperatures below 6–16 K. The measured parameters of this conduction were used to calculate the acceptor-state radius as a function of vacancy concentration N_A. It is shown that, for $N_A < 4 \times 10^{17}$ cm^{-3}, the low-temperature conduction occurs via the vacancy states whose radius is independent of N_A. For $N_A > 5 \times 10^{17}$ cm^{-3}, the hopping conduction is governed by the states of uncontrolled shallow-level impurity acceptors. The radius of the state for these defects increases with increasing N_A owing to an increase in the effective permittivity of the medium. *© 2001 MAIK “Nauka/Interperiodica”.*

1. INTRODUCTION

The behavior of atomic wave functions Ψ in the vicinity of a metal–insulator transition is very important for gaining insight into the phenomenon of such a transition [1–3]. In particular, it is of interest to study the variation in the radius a of the impurity state in semiconductor crystals as the characteristic parameter approaches the threshold value [1–3] and also to study the influence of screening on the localization of states in the impurity band [4].

In this respect, the Mott transition is better understood; with this transition, the localized and delocalized band states exist simultaneously and are separated by the mobility threshold E_c, whereas the Fermi energy of electrons F may vary gradually. Here, the radius a of the localized state increases as its energy approaches E_c and becomes infinite for $F = E_c$ [1–3]. The behavior of wave functions of impurities in the subthreshold concentration range immediately prior to the emergence of the first states localized according to Anderson has been studied to a lesser extent.

For studying the impurity states in lightly doped semiconductors, the phenomenon of hopping conduction (ε_3 conductivity with a constant activation energy or conductivity with a variable hopping range) has been used with good results; the characteristics of such conduction are directly defined by the parameters of the impurity-related wave function. However, in the region of the intermediate doping level, the so-called ε_2 conductivity is often dominant; this conductivity is related to the existence of delocalized, negatively charged donor states (or positively charged acceptor states) [1, 2]. Because of this, direct experimental data on the behavior of the radius a of an impurity state in the vicinity of the Anderson transition are scarce.

In this paper, we report the results of studying the concentration dependence of resistivity ρ of undoped p-$Hg_{0.78}Cd_{0.22}Te$ crystals with extrinsic conduction induced by native acceptors (mercury vacancies V_{Hg}).

2. FORMULATION OF THE PROBLEM

Crystals of $Hg_{1-x}Cd_xTe$ solid solutions possess a number of properties that make their study extremely attractive from the standpoint of the fundamental physics of semiconductors [4]. In the case under consideration, interest in this material was caused by the following circumstances.

According to [5, 6], there is no ε_2 conduction in p-$Hg_{0.8}Cd_{0.2}Te$ crystals that contain a high concentration of mercury vacancies ($N_A \sim 10^{17}$ cm^{-3}); rather, high-temperature hopping conduction with a variable hopping range obeying the Mott law is observed. In this case, the temperature dependence of resistivity $\rho(T)$ is given by

$$\rho = \rho_0 \exp(T_0/T)^{1/4}. \qquad (1)$$

The parameter T_0 in (1) is governed by the radius a of the state of mercury vacancies whose concentration can be controlled within a wide range in $Hg_{0.8}Cd_{0.2}Te$ without affecting the donor concentration N_D [6]. This situation is very convenient for studying the dependence $a(N_A)$.

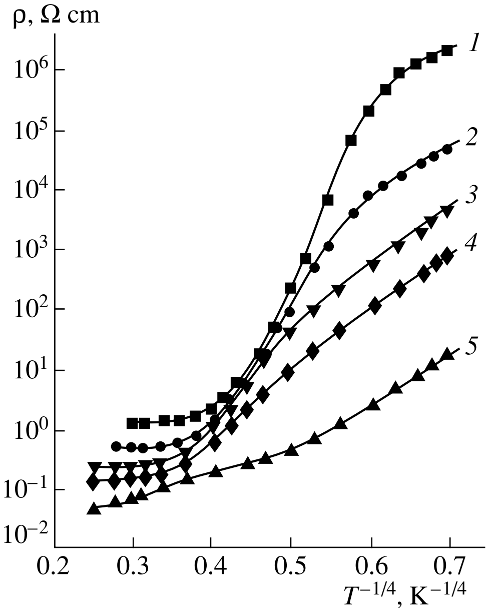

Fig. 1. Temperature dependences of resistivity for undoped p-$Hg_{0.78}Cd_{0.22}Te$ crystals that are saturated with tellurium and have a low concentration of mercury vacancies N_A = (*1*) 1.1×10^{16}, (*2*) 5.3×10^{16}, (*3*) 1.0×10^{17}, (*4*) 2.8×10^{17}, and (*5*) 4.2×10^{17} cm^{-3}.

The value of the parameter T_0 in the Mott law (1) is also controlled by the density of acceptor states $g(F)$ in the vicinity of the Fermi level at $T = 0$. According to [2], the relation between a, T_0, and $g(F)$ is written as

$$a = \left[\frac{21.2}{k_B T_0 g(F)}\right]^{1/3}. \qquad (2)$$

Since the undoped p-$Hg_{0.8}Cd_{0.2}Te$ crystals with a high concentration of V_{Hg} are compensated only slightly [6], it may be assumed that the following expression can be used to estimate $g(F)$ away from the Mott transition:

$$g(F) \approx \frac{\varepsilon N_D}{e^2 N_A^{1/3}}. \qquad (3)$$

This formula was derived in [2] for the case under consideration. Thus, the radius of the V_{Hg} state can be calculated using (2) and (3) if the values of T_0, N_A, and N_D are determined from experiments.

As is known, the concentration of active vacancies N_A in the narrow-gap p-$Hg_{0.8}Cd_{0.2}Te$ crystals under the conditions of slight compensation can be easily determined from the concentration of free holes at $T = 77$ K.

In the crystals under consideration, the donor concentration N_D can be evaluated by the following method. If the measurements are performed for batches of samples cut from the same single-crystal wafer, the value of N_D in each batch would vary insignificantly from sample to sample and can be considered constant. However, the radius of the isolated-acceptor state can be calculated theoretically. Thus, by measuring T_0 in the samples with a fairly low concentration of V_{Hg} and using formulas (2) and (3), we can determine the value of N_D that is characteristic of the given batch of samples.

When calculating the radius of the isolated-acceptor state, it should be taken into account that, in diamond-like semiconductors with a degenerate valence band, the wave function Ψ of an isolated acceptor is characterized by two spatial parameters [2]. One of these (a_h) describes the decay of the Ψ amplitude in the vicinity of an acceptor, whereas the second (a_l) accounts for the decay away from the acceptor. For a singly charged shallow-level acceptor, the values of a_h and a_l have been calculated by the effective-mass method in [7] and [2], respectively. In the effective-mass approximation for the light and heavy holes ($m_{lh} \ll m_{hh}$), we have

$$a_h = \frac{\hbar}{\sqrt{2m_{hh}E_A}}, \quad a_l = \frac{\hbar}{\sqrt{2m_{lh}E_A}}, \qquad (4)$$

where E_A is the ionization energy for a simple acceptor.

The condition $m_{lh} \ll m_{hh}$ is satisfied readily for $Hg_{0.8}Cd_{0.2}Te$; however, in this material, the Hg vacancy is a doubly charged acceptor, which requires that certain corrections be introduced in formulas (4). These corrections are fairly obvious: the form of relations (4) should be retained, but E_A should be replaced by the binding energy (per hole) in the acceptor neutral state. Thus, we obtain

$$a_{h2} = \frac{\hbar}{\sqrt{m_{hh}(E_{A1} + E_{A2})}}, \quad a_{l2} = \frac{\hbar}{\sqrt{m_{lh}(E_{A1} + E_{A2})}}, \qquad (5)$$

where E_{A1} and E_{A2} are the ionization potentials for the Hg vacancy. A variational calculation performed by the Rietz method substantiated this statement to an accuracy of 1%.

It is reasonable to assume that, for low concentrations of V_{Hg}, the role of a in (2) will be played by a_{l2} because the mean hopping range under the conditions of validity of the Mott law (1) is fairly large in the experiment ($\sim N_D^{-1/3}$).

3. EXPERIMENT

For the experiment, we chose several single-crystal wafers of undoped n-$Hg_{1-x}Cd_xTe$ ($x = 0.220 \pm 0.005$); these wafers were cut from different ingots that contained $n = (3 \pm 1) \times 10^{14}$ cm^{-3} of impurity-induced electrons.

The selected wafers were subjected for a week to homogenizing annealing in Hg vapors at a temperature

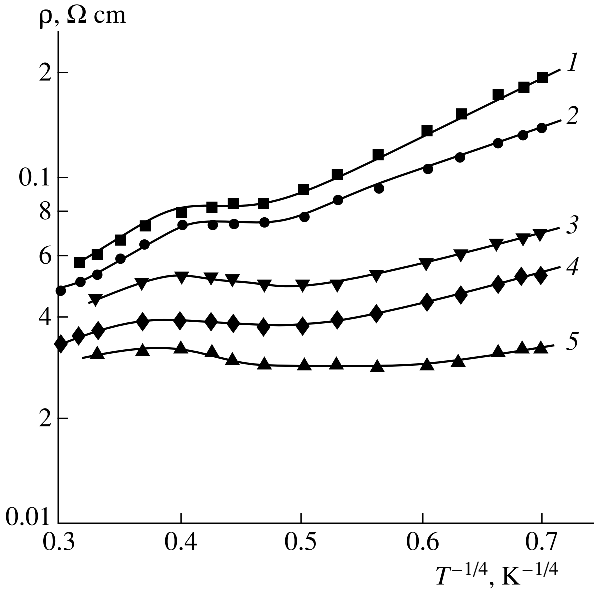

Fig. 2. Temperature dependences on resistivity for undoped p-$Hg_{0.78}Cd_{0.22}Te$ crystals that are saturated with tellurium and have a high concentration of mercury vacancies N_A = (*1*) 5.9×10^{17}, (*2*) 6.7×10^{17}, (*3*) 7.0×10^{17}, (*4*) 1.0×10^{18}, and (*5*) 1.1×10^{18} cm^{-3}.

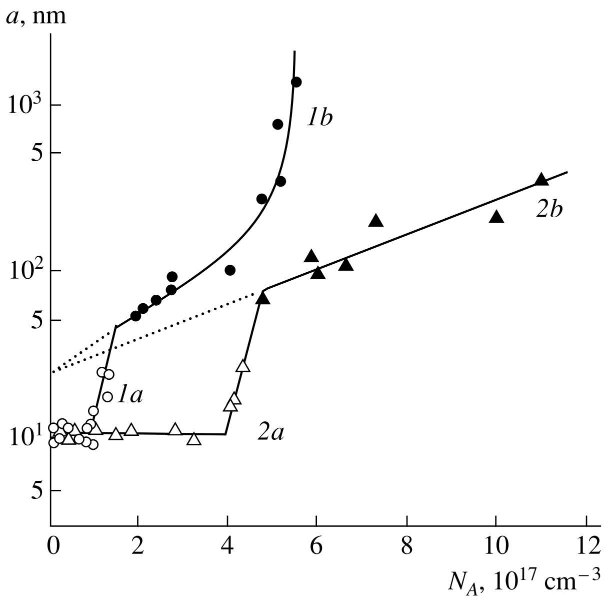

Fig. 3. Concentration dependence of the acceptor-state effective radius for undoped p-$Hg_{0.78}Cd_{0.22}Te$ crystals. Curves *1a* and *1b* correspond to the crystals saturated with mercury, and the curves *2a* and *2b* are for the crystals saturated with tellurium.

of T_a = 600°C, with the vapor pressure being 10 atm. Further, the wafers were cut into the samples with a surface area of $1.2 \times 0.3 \times 0.1$ cm^3 and a thickness of 0.1 cm. Some of the samples were subjected first to a 24-h annealing at T_a = 600°C under an Hg vapor pressure of 2.5 atm and then to an annealing in saturated Te_2 vapors at temperatures from 240 to 490°C. The remaining samples were annealed in almost saturated Hg vapors at various temperatures (from 420 to 505°C). The duration of the last annealing stage was sufficient for establishing the macrouniform distribution of vacancies in the sample.

As a result, we obtained a series of p-$Hg_{0.78}Cd_{0.22}Te$ crystals with a concentration of electrically active Hg vacancies of 10^{16}–10^{18} cm^{-3}. The samples annealed in the Te_2 vapors had a heterophase structure and contained $\sim 3 \times 10^{18}$ cm^{-3} of excess Te in the form of inclusions of the second phase 2–3 nm in size. The samples annealed in Hg vapors had a homophase structure.

The concentration of Hg vacancies in the samples was determined from the results of the Hall measurements of the free-hole concentration at 77 K in a magnetic field B = 1 T; the data [8, 9] concerning the field dependence of the Hall coefficient and the concentration dependence of the average ionization degree for the vacancies were taken into account.

Figures 1 and 2 show the results of measuring the dependence $\rho(T)$ in the temperature range of 4.2–250 K for a number of crystals saturated with Te. The dependence $\rho(T)$ for the samples saturated with Hg is similar; however, in these samples, the activation energy for the ε_1 conductivity caused by free holes in the valence band is lower.

As follows from Fig. 1, for a relatively low concentration of V_{Hg} ($N_A < 3 \times 10^{17}$ cm^{-3}), the region of hopping conduction described by (1) is directly adjacent to the region of the freezing-out of the ε_1 conduction. For $N_A > 5 \times 10^{17}$ cm^{-3}, the freezing-out of the ε_1 conduction is almost unobserved, so that conduction over the impurity band is dominant in the entire range of extrinsic conduction (Fig. 2). In the crystals with $N_A > 6 \times 10^{17}$ cm^{-3}, the impurity conduction is evidently metallic at intermediate temperatures. At lower temperatures, the conductivity becomes activation-controlled again and is still described by the Mott law (1). The temperature corresponding to the onset of activation depends on N_A; it decreases from 16 to 7 K as N_A increases from 5×10^{17} to 1.1×10^{18} cm^{-3}. The minimal value of metallic conductivity is 10–15 Ω cm, which is quite consistent with the Mott theory [1] for doped semiconductors.

In the samples saturated with Te, the temperature of transition to the Mott law (1) is relatively high and increases from 11 to 15 K as N_A increases from 4×10^{16} to 4×10^{17} cm^{-3}. By contrast, this temperature decreases as N_A increases further. In the crystals saturated with Hg, the critical temperature is 4–5 K lower. The value of the parameter T_0 depends heavily on the concentration of native acceptors. For a low concentration of V_{Hg},

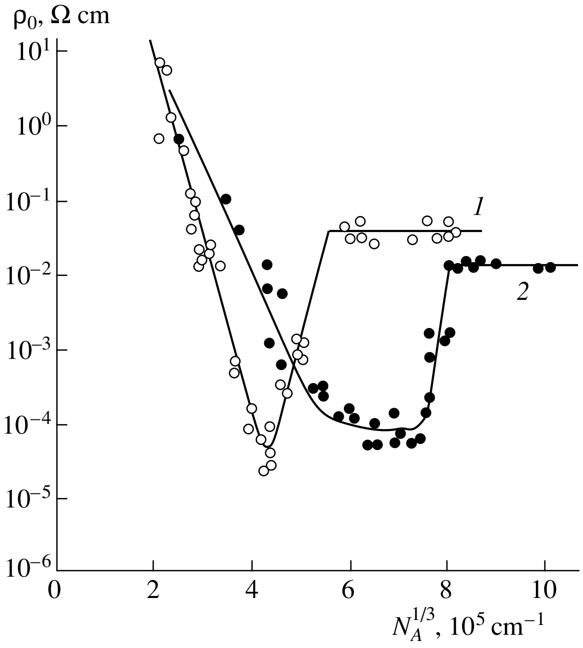

Fig. 4. Concentration dependence of the pre-exponential factor in the expression for hopping conductivity in undoped p-$Hg_{0.78}Cd_{0.22}Te$ crystals. Curve *1* corresponds to the crystals saturated with mercury, curve *2* is for the crystals saturated with tellurium.

T_0 on average first increases somewhat with increasing N_A but then, starting with a certain concentration of V_{Hg}, decreases rapidly by several orders of magnitude. Nevertheless, in the entire range of concentrations used, the value of T_0 remains finite and easily measurable.

Figure 3 (curves *1a*, *2a*) shows the concentration dependence of the effective radius a of the vacancy state; this dependence was plotted on the basis of the results of measuring the values of T_0 and N_A and using expressions (2)–(5). In calculations, it was assumed that $E_{A2} = 2E_{A1}$ and that $E_{A1} = 18.5$ meV for the crystals saturated with Te, and $E_{A1} = 15.5$ meV for the samples saturated with Hg [9]. It can be seen that, for a low concentration of vacancies, the parameters of the acceptor states do not depend in the least on N_A. However, as N_A increases, the behavior of a drastically changes starting with a certain value of N_A: the value of a rapidly increases by five to six times in a narrow range of concentrations. The concentration of vacancies at the inflection point depends on the conditions of sample preparation and is $\sim 1 \times 10^{17}$ cm^{-3} for the crystals saturated with mercury and $\sim 4 \times 10^{17}$ cm^{-3} for the samples with a heterophase structure saturated with tellurium.

As N_A increases further, the value of a continues to increase; this increase in a is in general significantly steeper in the samples saturated with mercury. At first, the increase in a is slow, but then the rate of increase becomes drastically higher and, ultimately, infinite. In the samples saturated with Hg, this occurs for $N_A \approx 5.5 \times 10^{17}$ cm^{-3}. In the sample saturated with Te, the unlimited increase in a was not observed, probably due to an insufficiently high concentration of vacancies in the samples.

The pre-exponential factor ρ_0 in formula (1) depends exponentially on the vacancy concentration for small N_A and decreases rapidly with increasing N_A. After the critical point is reached, this factor increases drastically by two orders of magnitude and then becomes independent of N_A (Fig. 4).

4. DISCUSSION OF THE RESULTS

The majority of the observed special features of low-temperature electrical conduction in undoped p-$Hg_{0.8}Cd_{0.2}Te$ crystals that contain Hg vacancies can be explained by taking into account the multicharge state of native acceptors and the actual content and type of uncontrolled impurities in the material studied. In fact, judging from the results of measurements of T_0, the initial n-$Hg_{0.8}Cd_{0.2}Te$ are compensated to a large extent (the compensation factor being $K \approx 0.9$); i.e., the concentration of acceptor impurities in these crystals is comparable to N_D. This inference agrees satisfactorily with the results of the measurements of the electron and hole mobilities. Some of the impurity-related acceptors N_{A1}^* (most likely, half of the total amount) are shallow-level singly charged centers whose ionization potential E_A is two times smaller than the first ionization potential E_{A1} of native acceptors. Because of this, the impurity-related acceptors, in spite of their low concentration, would profoundly affect the position of the Fermi level for electrons at low temperatures.

For the sake of illustrating the above statement, Fig. 5 schematically shows the structure of the lower part of the p-$Hg_{0.8}Cd_{0.2}Te$ acceptor band at $T = 0$ in the one-electron approximation as applied to the situation in which $N_{A1} \approx N_D$ and the concentration of vacancies in the crystal is not high, so that the energy of interaction between vacancies and charged donors is not too high. It can be seen that the Fermi level is now located much lower than in the absence of impurity-related acceptors ($F < F_0$). If, in addition, $E_{A1} < F$, the value of F can be easily calculated using the theory [2], neglecting the negatively charged complexes of vacancies with donors, and assuming that all impurity-related acceptors are ionized; thus, we obtain

$$F = E_{A1} - \frac{e^2}{\varepsilon}\left[\frac{4\pi N_A}{3\ln(N_D/N_{A1}^*)}\right]^{1/3}. \qquad (6)$$

For the sake of comparison, we point out that, in the absence of impurity-related acceptors, the Fermi energy for electrons would be given by [2]

$$F_0 \approx E_{A1} - 0.61\frac{e^2}{\varepsilon}\left[\frac{4\pi N_A}{3}\right]^{1/3}. \qquad (7)$$

In the range of low V_{Hg} concentrations, the Fermi level F at $T = 0$ is located well above the level E_A of the impurity-related acceptors; therefore, the latter are completely ionized and are not involved in the charge transport. On the other hand, for $N_A < 4 \times 10^{17}$ cm^{-3}, the value of overlap integral for the vacancy states is small; therefore, the energy of these states should be independent of N_A. Under these conditions, the effective radius of the V_{Hg} state should be independent of N_A as well. It is this behavior of a that can be perceived from Fig. 3.

As the concentration of V_{Hg} increases, the Fermi level F descends according to (6), eventually attains the value of $F \approx E_A$, and, thus, finds itself within the band of impurity-related acceptors. Obviously, after the Fermi level has become located within this band, hopping conduction would now proceed preferentially over the states of the impurity-related acceptor whose size and spectral density are appreciably larger. As a result, the effective acceptor-state radius determined from the data on hopping conductivity should decrease drastically by several times. Under these conditions, the preexponential factor ρ_0 should also experience an abrupt change; after that, ρ_0 becomes independent of N_A, which is completely consistent with experimental data (Fig. 4).

It is reasonable to presume that the experimentally observed abrupt changes in a and ρ_0 are caused by exactly the above effects. This presumption is supported, for example, by the following estimates. We assume that $N_A^* = 0.5N_D$ and take into account that $E_{A1} = 15.5$ meV for the crystals saturated with Hg and $E_{A1} = 18.5$ meV for the crystals saturated with Te [9]. In this case, the concentrations of Hg vacancies $N_A \approx 10^{17}$ cm^{-3} in the crystals saturated with Hg and $N_A \approx 4 \times 10^{17}$ cm^{-3} in the samples saturated with Te correspond to $F \approx 8$ meV, which is close to the experimental value of the ionization energy for copper $E_A \approx 7.5$ meV [10].

In connection with this, the effective radius of the acceptor state in the crystals with a high concentration of vacancies (in the region where ρ_0 is constant in Fig. 4) was calculated in a somewhat different manner. The density of states in the vicinity of F was assumed to be equal

$$g(F) \approx \frac{\varepsilon N_A^*}{e^2 N_D^{1/3}}, \qquad (8)$$

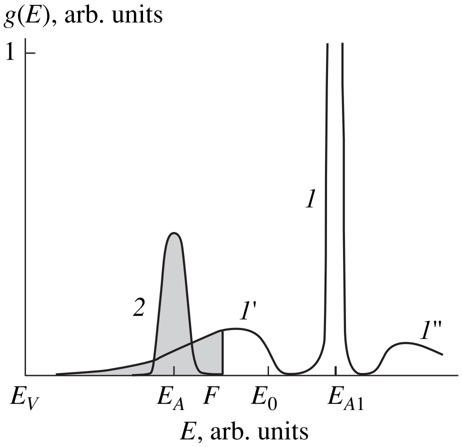

Fig. 5. Schematic representation of the acceptor-band structure in p-$Hg_{0.78}Cd_{0.22}Te$ crystals. Contour *1* corresponds to the main peak of the lowest band for the Hg-vacancy states; contour *1*' corresponds to the Hg-vacancy states split off by the charged-donor field; contour *1*" corresponds to the Hg-vacancy states split off by the field of singly charged acceptors; and contour *2* delineates the band of states of singly charged impurity-related acceptors. The area corresponding to the states occupied by electrons at $T = 0$ is shaded.

because the average distance between the impurity-related acceptors and donors, which controls the width of the impurity acceptor band, is equal to $N_D^{-1/3}$ by an order of magnitude. In calculations, it was still assumed that $N_A^* = 0.5N_D$.

The results of calculations are shown in Fig. 3 (curves *1b*, *2b*). It can be seen that, in this concentration range, the value of a gradually increases with N_A; in the limit of $N_A = 0$, a tends to $a \approx 25$ nm for both Hg- and Te-saturated samples. In fact, this value of a coincides with that for the radius a_l of the state of an isolated impurity-related acceptor; in the material under consideration, this radius, according to (4), is equal to 26 nm if it is assumed that $E_A \approx 7.5$ meV [10].

It is the author's opinion that the gradual increase in the radius a for the impurity-related acceptors (see Fig. 3) is caused by the influence of neutral vacancies on the effective permittivity of the crystal. In fact, the volume of the state of a singly charged acceptor in $Hg_{0.78}Cd_{0.22}Te$ is 15–20 times larger than that of the V_{Hg} state. Therefore, even for $N_A \approx 1 \times 10^{17}$ cm^{-3}, ~10 vacancies, neutral at low temperatures, are found within the sphere of radius a_l around the impurity center. Polarizability of neutral vacancies is high ($\alpha \propto a_{h2}^3$). Because of this, for such large values of N_A, these vacancies should induce a large increase in the effective static permittivity ε_0 of the crystal and, correspondingly, in a_l.

If this assumption is valid, the results obtained indicate that the polarizability of a vacancy in Hg-saturated

p-$Hg_{0.78}Cd_{0.22}Te$ crystals is ~1.5 times larger than the polarizability of a vacancy in the samples saturated with Te. It is quite consistent with experimental evidence for the ionization energy of a vacancy to be appreciably higher in Te-enriched crystals [9]. An anomalous increase in the radius of the state of impurity-related centers for the vacancy concentration of $N_A \approx 5.5 \times 10^{17}$ cm^{-3} is indicative of an anomaly in the static permittivity of Hg-saturated p-$Hg_{0.78}Cd_{0.22}Te$ crystals with such a concentration of vacancies. Using this assumption and the Clausius–Mossotti formula, we find that the polarizability of V_{Hg} is equal to $\alpha \approx 3/[4\pi(\varepsilon_0 + 2)N_A^{\infty}] \approx 2.2 \times 10^{-20}$ cm^3; this amounts to $\sim 2.5 a_{h2}^3$ for $Hg_{0.78}Cd_{0.22}Te$, which is quite a reasonable value.

At the same time, we have $N_A a_h^3 \ll 1$; therefore, there are almost no vacancies in a sphere with radius a_h. Correspondingly, the permittivity in this case should remain unchanged; i.e., the vacancies should not appreciably affect the ionization energy of shallow-level impurity-related acceptors.

It is worth noting that the suggested mechanism responsible for an increase in the characteristic size of an impurity-related acceptor state is consistent with the observed constancy of the vacancy-state size, because $N_A a_{l2}^3 < 1$ for $N_A < 4 \times 10^{17}$ cm^{-3}.

Finally, taking into account the impurity-related acceptors, we can easily interpret the emergence of a portion with metallic conductivity in the resistivity–temperature curve at intermediate temperatures for the crystals with $N_A > 6 \times 10^{17}$ cm^{-3} (see Fig. 2). In such crystals, the free-hole concentration is governed by Hg vacancies, whereas the low-temperature conductivity is controlled by the impurity-related acceptors. However, according to [9], for $N_A > 6 \times 10^{17}$ cm^{-3} and T =77 K, the vacancy band merges with the valence band as a result of the screening of the vacancy potential by free holes. It is clear that, in these conditions, the impurity-related acceptor states are delocalized as well.

As the temperature is lowered, the free-hole concentration decreases, and the impurity states leave the valence band. As a result, conduction over these state should become activation-controlled.

Thus, the results reported here support with reasonable assurance the suggested explanation for the mechanism of a drastic change in the effective value of a. In contrast, it is difficult to relate the behavior of a to the proximity of the metal–insulator transition in the acceptor band. In fact, as shown recently [10] for p-$Hg_{0.78}Cd_{0.22}Te$ crystals, the condition for the metal–insulator transition is given by the Mott criterion written as

$$N_{AM}^{1/3} a_h \approx 0.25. \qquad (9)$$

Since in the material under consideration $a_{h2} \approx 2$ nm in view of (5), the concentration $N_A \approx 4 \times 10^{17}$ cm^{-3}, for which the value of a changes drastically in the samples saturated with Te, is five times lower than the critical concentration $N_{AM} \approx 2 \times 10^{18}$ cm^{-3} that corresponds to the Mott transition.

5. CONCLUSION

(i) In undoped p-$Hg_{0.8}Cd_{0.2}Te$ crystals containing the Hg vacancies, hopping conductivity with a variable hopping range dominates over the ε_2 and ε_3 conductivities in a wide range of V_{Hg} concentrations (beginning at least with $N_A \sim 10^{16}$ cm^{-3} and at higher concentrations). Even low concentrations of impurity-related singly charged acceptors can profoundly affect the low-temperature conductivity of undoped p-$Hg_{0.8}Cd_{0.2}Te$ crystals for high concentrations of V_{Hg}. The origin of this phenomenon is related to specific features of the acceptor-band structure for a material in which the acceptor band is formed by a relatively small number of shallow-level, singly charged, impurity-related acceptors and a large number of doubly charged native defects V_{Hg}, whose ionization energy is twice as high.

(ii) The characteristic sizes of the Hg-vacancy neutral state in a p-$Hg_{0.8}Cd_{0.2}Te$ crystal are independent of the native-acceptor concentration, at least for $N_A < 4 \times 10^{17}$ cm^{-3}, which amounts to ~20% of their concentration at the Mott-transition point. At the same time, the radius of the native-acceptor state depends on the conditions of crystal preparation. In the samples saturated with Te, this radius is appreciably smaller, which may be indicative of differences in the microstructure between the Hg- and Te-saturated p-$Hg_{0.8}Cd_{0.2}Te$ crystals.

(iii) Neutral electrically active centers appreciably affect the acceptor-state radius a_l only if their concentration N satisfies the inequality $Na_l^3 > 1$. Such centers virtually do not affect the size a_h.

REFERENCES

1. N. F. Mott and E. A. Davis, *Electronic Processes in Non-Crystalline Materials* (Clarendon Press, Oxford, 1979; Mir, Moscow, 1982).
2. B. I. Shklovskiĭ and A. L. Efros, *Electronic Properties of Doped Semiconductors* (Nauka, Moscow, 1979; Springer-Verlag, New York, 1984).
3. J. M. Ziman, *Models of Disorder: The Theoretical Physics of Homogeneously Disordered Systems* (Cambridge Univ. Press, Cambridge, 1979; Mir, Moscow, 1982).

4. I. M. Tsidil’kovskiĭ, G. I. Kharus, and N. G. Shelushinina, *Impurity States and Transport Phenomena in Zero-Gap Semiconductors* (Sverdlovsk, 1987).
5. A. I. Elizarov and V. I. Ivanov-Omskiĭ, Fiz. Tekh. Poluprovodn. (Leningrad) **15** (5), 927 (1981) [Sov. Phys. Semicond. **15**, 531 (1981)].
6. A. I. Elizarov, V. V. Bogoboyashchiĭ, and N. N. Berchenko, Fiz. Tekh. Poluprovodn. (Leningrad) **18** (3), 455 (1984) [Sov. Phys. Semicond. **18**, 283 (1984)].
7. B. L. Gel’mont, A. R. Gadzhiev, B. L. Shklovskiĭ, *et al.*, Fiz. Tekh. Poluprovodn. (Leningrad) **8** (12), 2377 (1974) [Sov. Phys. Semicond. **8**, 1549 (1974)].
8. V. V. Bogoboyashchiy, Proc. SPIE **3486**, 325 (1997).
9. V. V. Bogoboyashchiĭ, in *Scientific Proceedings of Kremenchug State Polytechnic Institute*, Vol. 1: *Problems in the Developmant of New Machines and Technologies* (Kremenchug. Gos. Univ., Kremenchug, 1999), p. 269.
10. V. V. Bogoboyashchiĭ, S. G. Gasan-zade, and G. A. Shepel’skiĭ, Fiz. Tekh. Poluprovodn. (St. Petersburg) **34** (4), 411 (2000) [Semiconductors **34**, 398 (2000)].

Translated by A. Spitsyn

Semiconductors, Vol. 35, No. 1, 2001, pp. 40–47. Translated from Fizika i Tekhnika Poluprovodnikov, Vol. 35, No. 1, 2001, pp. 40–47.

Original Russian Text Copyright © 2001 by Akhmetov, Fateev.

ELECTRONIC AND OPTICAL PROPERTIES OF SEMICONDUCTORS

Infrared Tomography of the Charge-Carrier Lifetime and Diffusion Length in Semiconductor-Grade Silicon Ingots

V. D. Akhmetov* and N. V. Fateev

Institute of Semiconductor Physics, Siberian Division, Russian Academy of Sciences,
pr. Akademika Lavrent'eva 13, Novosibirsk, 630090 Russia
**e-mail: akhmetov@isp.nsc.ru*

Submitted May 30, 2000; accepted for publication May 31, 2000

Abstract—A nondestructive method for measuring the three-dimensional distribution of the charge-carrier lifetime and diffusion length in silicon ingots with a length of up to 1 m and a diameter as large as 0.3 m is presented. Physically, this method is based on infrared crossed-beam probing of an ingot with polished surface areas. One of the beams is repetitively pulsed, has a wavelength of 1.15–1.28 μm, and generates excess charge carriers in a rodlike zone along the beam trajectory in the ingot. Other beams are continuous and have longer wavelengths; these beams detect the temporal and spatial kinetics of excess charge carriers in a small portion of the rodlike zone and in the vicinity of it (the free-carrier absorption is measured). By virtue of the fact that the investigated zone is at a distance from the ingot surface, there is no need to consider the surface recombination. The capabilities of the method are demonstrated for an ingot with known spatial nonuniformity of the charge-carrier lifetime. Spatial resolution amounting to several millimeters was attained. *© 2001 MAIK "Nauka/Interperiodica".*

INTRODUCTION

The lifetime (τ) and diffusion length (L) of charge carriers characterize the quality of silicon as a semiconductor material. Measurements of τ and L are widely used to analyze silicon wafers and structures. The corresponding diverse methods for measurements have been and are being continually developed and improved. However, as for analysis of silicon ingots as a whole, the approach to the measurements remains the same as it was in the 1950s; namely, two wafers (one wafer from each end of the ingot) are cut, the wafer surfaces are thoroughly treated mechanically and chemically in order to reduce the contribution of the surface recombination, and the measurements are performed by the methods developed for the wafers (e.g., to the ASTM F 1535-94 standard). With this procedure, the distribution of the charge-carrier lifetime along the ingot axis remains unknown. Using the above approach, the whole ingot has to be cut into wafers (i.e., destroyed) in order to determine the lifetime distribution over the ingot.

At the same time, nondestructive measurements of τ in the ingots are of undeniable interest. This is due to the fact that such measurements make it possible, first, to control the quality of ingots as end products, without introducing ambiguities in τ owing to the contribution of the surface recombination. Second, it becomes possible to control the distribution of τ over the ingot while optimizing the growth conditions and refining the conditions of subsequent thermal and irradiation–thermal treatments, for example, when the transmutation doping is used.

The aim of this study was to develop a method for determining the three-dimensional distribution of τ and L as applied to silicon ingots grown both by the Czochralski method and by the crucibleless (floating-zone) method.

Physically, the developed method is based on probing of the ingot by crossed beams. A repetitively pulsed photogeneration of electrons and holes with one of the beams (the pump beam) is used; subsequently, the spatial–temporal evolution of the excess-carrier number is monitored with the second (probe) beam using the free-carrier absorption. Previously, such an approach was used to measure the lifetime in wafers [1] and rectangular bars with millimeter-scale cross-sectional size [2]. In [1, 2], the beam of a pulsed YAG laser with a wavelength of $\lambda = 1.06$ μm whose radiation is absorbed in silicon within a depth of ~1 mm was used to generate the charge carriers. At the same time, the 3.39-μm radiation of a He–Ne laser was employed to detect the decay of the excess-carrier concentration Δn [1, 2]; this radiation is weakly absorbed in moderately doped silicon (the absorption cross section is on the order of 10^{-17} cm^2 [1, 2]). The beams were directed onto the object to be studied in such a way that their axes intersected each other at a certain angle and at a point either at the sample surface or close to it. As a result, the experimentally measured kinetics of the decay of absorption induced at a wavelength of 3.39 μm reproduces the decay of Δn. The volume lifetime τ was determined after certain additional manipulations aimed at taking into account the contribution of the surface recombination. The zone in the sample which is desirable for observation is selected owing to the fact that the detected free-carrier absorption signal is related only to the charge carriers that are located in the vicinity of intersection of the pump beam with the probe beam.

In the method that we suggest and test in this study, radiation with longer wavelength (λ = 1.15–1.28 μm) is used for pulsed photoexcitation. This radiation is weakly absorbed in high-quality silicon; thus, it makes it possible to generate electrons and holes in any zone of the ingot with length as large as ~1 m. In addition to configuration with exact intersection of the beams, we also use the relative position of the beams with the distance between them comparable to the diffusion length of charge carriers. In this configuration, it is possible to (i) perform the tomography of the ingot with spatial resolution of ~1 cm along either of the coordinates, (ii) radically eliminate the unwanted contribution of the surface recombination by increasing the distance between the zone of measurements and the surface, and (iii) additionally measure the diffusion length L.

EXPERIMENT

Transmission spectra of a silicon ingot 125 mm long with polished ends perpendicular to the ingot axis are shown in Fig. 1; the spectra were measured at room temperature and at 80°C using an SF-8 diffraction spectrophotometer for the light propagating along the ingot axis. It can be seen that, at 20 and 80°C and for wavelengths λ < 1.15 μm, silicon is virtually opaque for the thicknesses used, whereas, for λ > 1.28 μm, the material is almost completely transparent (with allowance made for 30% reflectance from the surface). The temperature range T = 20–80°C corresponds to the temperatures conventionally used in the measurements of lifetime in silicon, including also those for detecting the attachment of charge carriers to the traps. Thus, it is necessary to use radiation with wavelengths in the range of 1.15–1.28 μm in order to photogenerate charge carriers in silicon ingots.

On the basis of the measured transmission spectra, we chose a pulsed solid-state LiF laser, whose operation involves the F_2^- centers, as the pump-beam source [3]; such a laser is tunable over the wavelengths in the aforementioned range. The laser emitted the optical pulses with a duration of 30 ns, a repetition rate variable from 20 Hz to 5 kHz, and an energy of 2×10^{-4} J per pulse at a wavelength of λ = 1.17–1.18 μm; the lasing-line width was 0.5 nm. The pump wavelength was first roughly selected on the basis of transmission spectra. For more precise selection, we used the trial-and-error method based on the criterion of signal-amplitude attenuation by two times as the beam-intersection region was shifted from the spot where the pump-beam enters the ingot to the spot where it exits.

As the source of probe radiation, we used the beam of a continuous-wave He–Ne laser with a wavelength of 3.39 μm and power of ~10 mW. The diameters of the beams were varied from 1 to 10 mm using lenses.

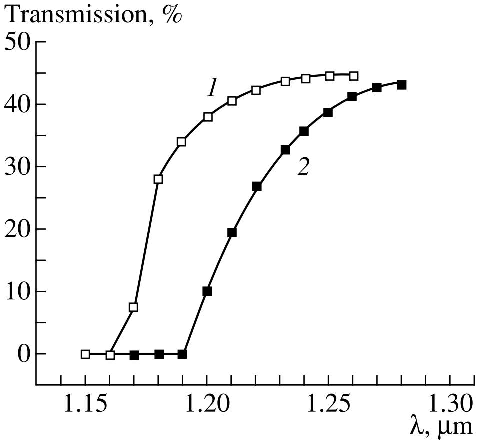

Fig. 1. Transmission spectra in the vicinity of the fundamental-absorption edge for a silicon ingot with a resistivity of 45 Ω cm and a length of 125 mm at temperatures of (*1*) 20 and (*2*) 80°C.

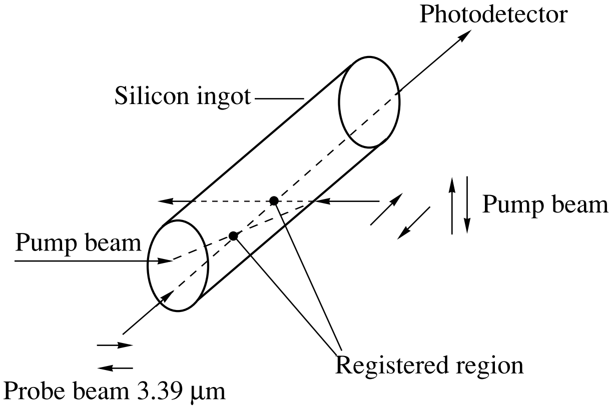

Fig. 2. Schematic representation of measurements of the lifetime and diffusion length of charge carriers in a silicon ingot.

In order to admit the beams into the ingot and ensure their intersection inside the ingot within a desired zone, we used two schemes of the experiment; the beam paths in these schemes are illustrated in Fig. 2.

In the first scheme, henceforth referred to as "perpendicular configuration," the probe beam fell on the flat ingot end at normal incidence and propagated along the ingot axis, whereas the pump beam was directed along the normal to the side surface and propagated perpendicularly to the ingot axis. Preliminarily, two narrow flat faces were formed along the ingot at the quasi-cylindrical side surface of the ingot, with each of the faces formed at the diametrically opposite sides of the "quasi-cylinder." The faces were formed in order to ensure the transmission of the beams without distortion of their shape. The width of the faces was 10–20 mm. The treatment of the surfaces consisted of mechanical cutting, grinding, and polishing; the faces were plane-parallel to within 2°–3°. Chemical treatment of the surfaces was not used. An optical system aligned the beam axes in mutually perpendicular directions and ensured either their precise intersection (for measurements of τ) or imprecise intersection (for measurements of L) with the distance between the beam axes equal to several millimeters. A photodetector cooled with liquid nitrogen and made of Ge:Au was installed at the exit of the probe beam from the ingot. The signal from the photodetector output was fed first to a wideband amplifier and then to a 10-bit digital oscilloscope based on an IBM PC and triggered by the pump-laser pulses. The overall response time of the detection channel was several microseconds. The time required for measurements at a single point ranged from 30 s to 20 min and was governed by the number of scans; the results of these scans were averaged in order to increase the signal-to-noise ratio.

In the second scheme, referred to henceforth as the "Brewster configuration," the side surface of the ingot was not treated, and both beams entered the ingot only through the polished ends prepared in the same way as in the first scheme. The probe beam struck the end at normal incidence and propagated along the ingot axis, whereas the *p*-polarized pump beam was incident on the end (the same or the opposite) at an angle that was nearly equal to the Brewster angle (65°–75°). Otherwise, the configuration was the same as in the first scheme, except for the fact that an additional Ge photodiode was mounted at the side surface of the ingot. This photodiode detected the scattered radiation of the pulsed pump beam; this radiation emerged from the corrugated side surface of the ingot. For this configuration of the beam paths, the angle of incidence of the pump beam on the side surface from within far exceeded the angle of the total internal reflection if the corrugation of the ingot's side surface was disregarded. However, in spite of the large angle of incidence, the signal of the scattered pump-beam radiation emerging from the side surface had so large an amplitude that we had to shadow the entrance window of the supplementary Ge photodiode, lest the latter would operate in the saturation mode. Determining the point of exit of the pump-beam radiation from the ingot made it possible to calculate the pump-beam path inside the ingot more accurately compared to determining the path from the point of entry and the angle of incidence of the pump beam on the ingot end.

We also performed tentative measurements in the configuration where the pump beam propagated along the ingot axis, whereas the probe beam propagated transversely to the axis; in addition, the probe beam was incident on the untreated side surface of the ingot. We found that, in this scheme, the modulated signal of the free-carrier absorption could be detected; however, the signal-to-noise ratio was reduced owing to scattering and distortion of the probe-beam shape at the entry to and exit from the side quasi-cylindrical untreated surface of the grown ingot. This reduced the efficiency of measurements owing to the necessity for long-term accumulation of the signals. In what follows, we report the results obtained only for the "perpendicular" and "Brewster" configurations of the experiment.

We performed the experiments with slabs cut from silicon ingots grown by the Czochralski method (a commercial ingot with a resistivity of 45 Ω cm) and also those obtained by the crucibleless floating-zone method (the experimental ingots were grown using an FZ-20 setup at the Institute of Semiconductor Physics, Siberian Division, Russian Academy of Sciences, Novosibirsk) with a resistivity of 1000 Ω cm. The slabs were 60–80 mm in diameter and 100–250 mm in length. In order to evaluate the spatial resolution of the method, we formed a model object, i.e., a "composite ingot" with known pronounced spatial nonuniformity of τ. To this end, a wafer 15 mm thick was cut from the middle part of the Si ingot grown by the Czochralski method; then this wafer was ground and polished. This wafer was annealed in the atmospheric air at 800°C without any attempts to maintain cleanliness; this annealing was aimed at decreasing τ owing to penetration of rapidly diffusing recombination-active impurities. The ends of two other parts of the ingot were also ground and polished. Afterwards, all three parts of the ingot were combined one after another to form the initial sequence and were measured as a single ingot.

THE RESULTS AND DISCUSSION

The data on the transmittance of silicon ingot in the spectral range of $\lambda = 1.15$–1.30 μm (see Fig. 1) indicate that there is an appreciable near-edge absorption in the grown silicon ingot; this absorption extends to the photon energy of $h\nu \approx 1.01$ eV ($\lambda = 1.23$ μm) if measurements are performed at room temperature, whereas the band gap of silicon is $E_G = 1.126$ eV at room temperature [4]. Apparently, the cause of the observed broadening of the fundamental-absorption edge (which is not observed for the conventionally measured silicon wafers with thickness of ~1 mm) is the absorption due to band-to-band phonon-assisted transitions and also the imperfections of the silicon crystal lattice. Without further specifying the absorption mechanism for $h\nu < E_G$, we point out that the result of optical absorption, as will be clear from the experimental data in what follows, is the generation of the free charge carriers.

Figures 3 and 4 show the families of the curves that represent the relaxation of the signal V with time t after the termination of the pump pulse; the data correspond to measurements at various points along the axis of the "composite ingot." The diameter of both beams (the probe and pump ones) was 2–3 mm. Figure 3 corresponds to the "perpendicular configuration," whereas Fig. 4 corresponds to the "Brewster configuration." For both families of relaxation curves, a drastic increase in the slope of the curves is observed when we examine the middle part of the ingot where the contaminated sil-

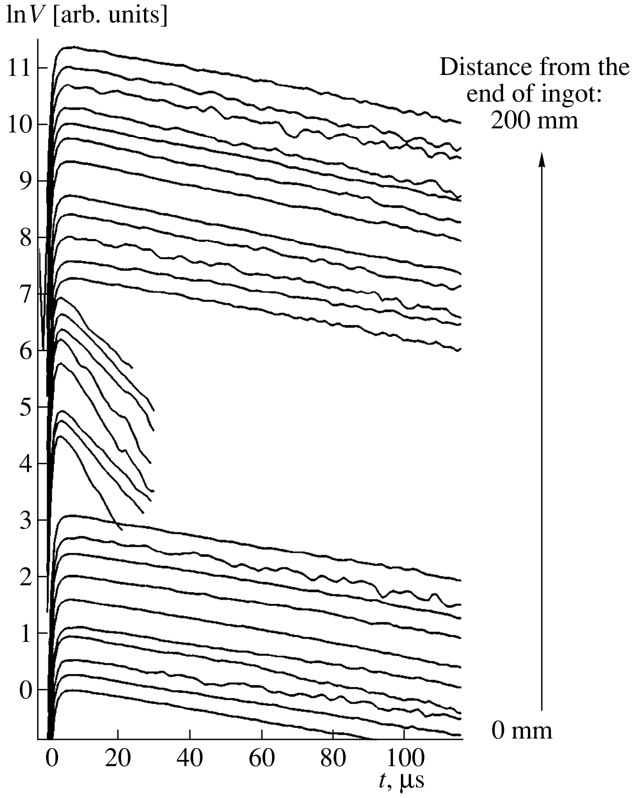

Fig. 3. Relaxation of free-carrier absorption at various distances from the starting point of the composite ingot. The material was crucible-grown silicon with a resistivity of 45 Ω cm. The middle part of the ingot was contaminated owing to annealing in the atmospheric air. The probe beam was incident on the end, and the pump beam was incident on the ingot's side surface (the "perpendicular" configuration).

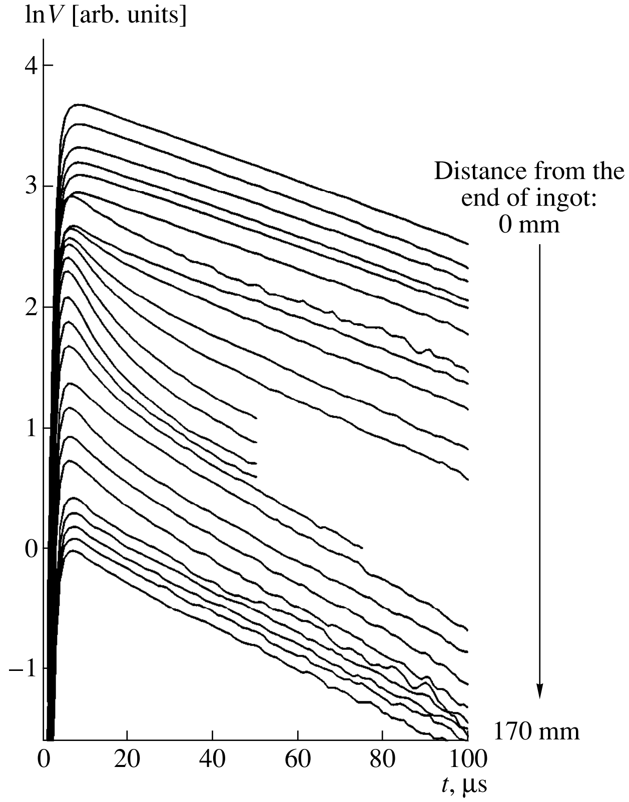

Fig. 4. Relaxation of free-carrier absorption for various distances from the starting end of composite ingot. The ingot is the same as in Fig. 3. The probe and pump beams were admitted to the ingot from the same end and were incident on the end at the angles of 0° and 73°, respectively (the "Brewster configuration").

icon slab is located. However, for "perpendicular" configuration, this specific feature is more pronounced.

Figure 5 shows the dependence of the peak amplitude of the detected signal proportional to the carrier-generation level as the pulsed pump beam is moved along the composite ingot (an ingot ~100 mm long, a wafer 15 mm thick, and an ingot 125 mm long) for injecting the pump beam with a wavelength of 1.17 μm into the ingot from the polished end perpendicular to the ingot axis in the Brewster configuration of measurements. It can be seen from Fig. 5 that the signal corresponding to the intensity modulation of the probe beam at its exit from the ingot is observed the entire distance the pump beam is moved and, in general, decreases steadily with distance from the point of the pump-beam entry. Certain deviations from monotonicity are most likely related to imperfections in the ingot, e.g., to nonideality of the end planes, certain nonparallelity of the ends, inaccuracy in determining the Brewster angle, etc. However, even if these specific features are caused partially by a certain fluctuation of the absorption coefficient (at the pump-beam wavelength) over the ingot volume, the signal level for all studied parts of the composite ingot is found to be sufficient to quantitatively detect the time dependence of the signal with confidence.

It follows from the above that, in single-crystal silicon of semiconductor grade, a rodlike zone of excess charge carriers can be formed in a regular way, without origination of regions where carriers are not generated in the course of the beam motion, and also without origination of regions with enhanced absorption, following which the carrier generation would be reduced appreciably. Physically, this fact signifies that the absorption-edge shape does not significantly change if we choose different ingot portions that differ in structural perfection, impurity type and concentration, and, possibly, the presence of internal electric and deformation fields. Apparently, such a situation favorable for implementation of the suggested measurement technique (namely, for optical generation of charge carriers in the bulk of the ingot) is related to the fact that silicon is an indirect-gap semiconductor (as a result of which the initial portion of fundamental-absorption edge happens to be

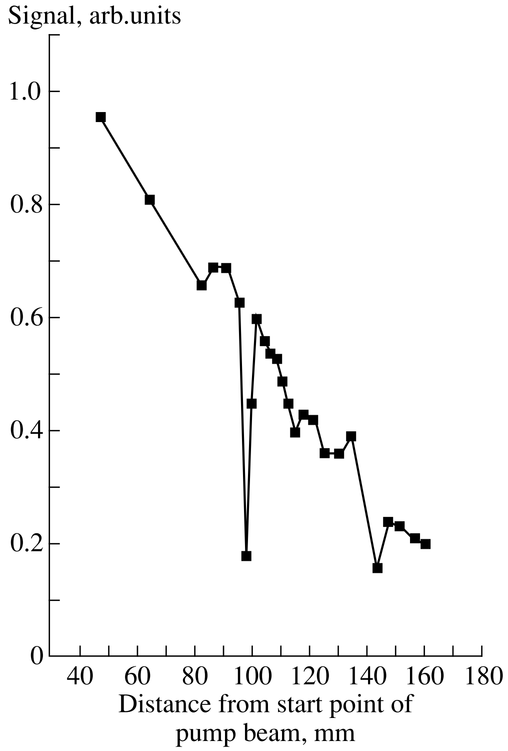

Fig. 5. The amplitude of the peak of the signal corresponding to the free-carrier absorption as a function of the distance between the point of measurement and the point of entry of the pump beam into the ingot. The latter was the same as in Fig. 3. The wavelength of the pump beam was 1.17 μm, and the ingot was at room temperature during measurements.

gently sloping) and also to high quality of crystal structure and high purity of silicon ingots currently grown.

Figure 6 shows the distribution of τ along the ingot axis; the distribution was derived by processing the data shown in Figs. 3 and 4. It can be seen that measurements in the perpendicular configuration faithfully reproduce the geometric position of the nonuniformity of τ (the position of the contaminated silicon wafer is delineated by vertical dashed lines); at the same time, the nonuniformity is greatly expanded for the Brewster configuration. The inferior spatial resolution obtained for the Brewster configuration is probably caused by scattering by irregularities and dust, and also by reflections from internal surfaces of "composite ingot." This parasitic effect was distinct when the Ge photodiode scanned the side surface of the ingot: when the point of the pump-beam exit was within the third portion of the ingot, the intense 1.17-μm radiation emerged from the gaps between the wafer and the adjacent parts of the ingot; this radiation should not exist at all for the Brewster angle of incidence. Apparently, if a genuinely monolithic ingot were used, there would be no parasitic effect, and spatial resolution in the Brewster configuration would correspond to the geometric size of the beam-intersection zone.

Comparing two configurations of measurements, we may conclude that the "perpendicular" configuration features higher spatial resolution but requires certain treatment of the side surface, whereas, in the Brewster configuration, the spatial resolution is lower but

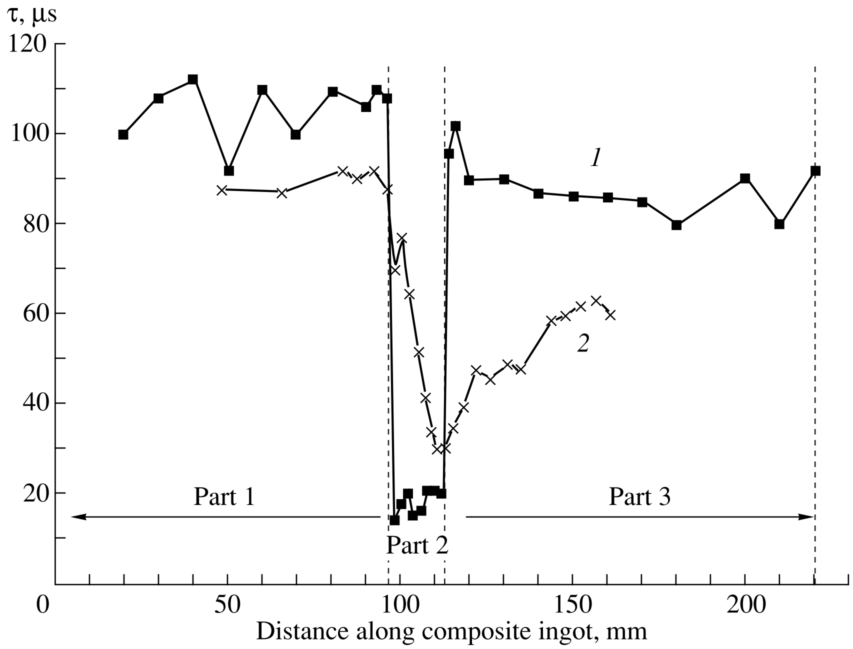

Fig. 6. Distribution of the charge-carrier lifetime along the composite ingot. The data were obtained by analyzing the curves in Figs. 3 and 4. Curve *1* corresponds to perpendicular configuration of the beams in which case the beams are incident on the end and the side surface, whereas curve *2* is for the Brewster configuration, with both beams admitted through the same end.

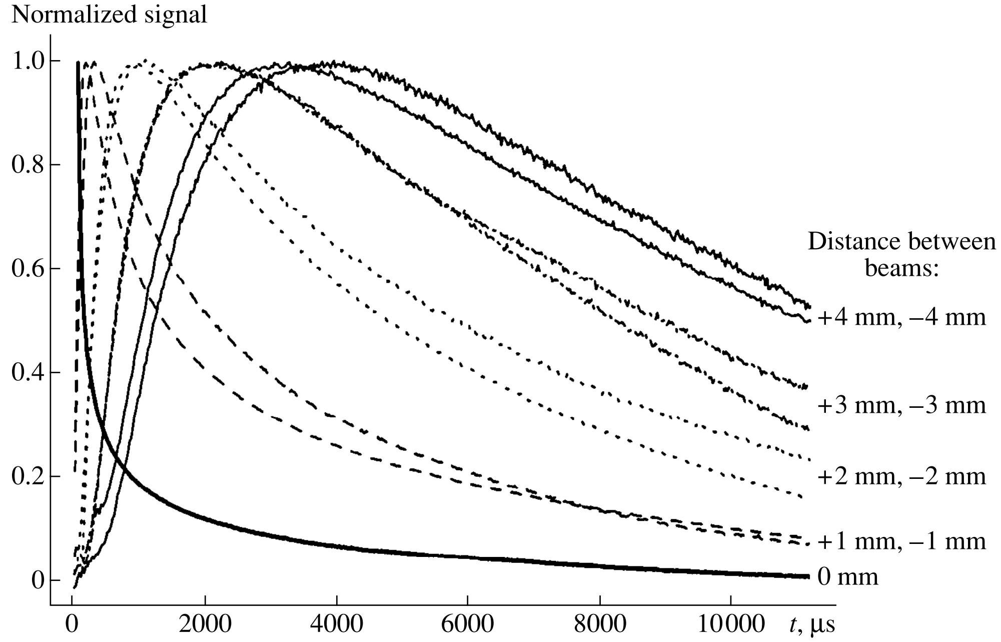

Fig. 7. Time dependences of the signal of induced absorption in a silicon ingot at λ = 3.39 μm along the path of the probe beam in relation to the distance between the axes of the pump and probe beams. The ingot material is silicon grown by the floating-zone method with a resistivity of 1000 Ω cm.

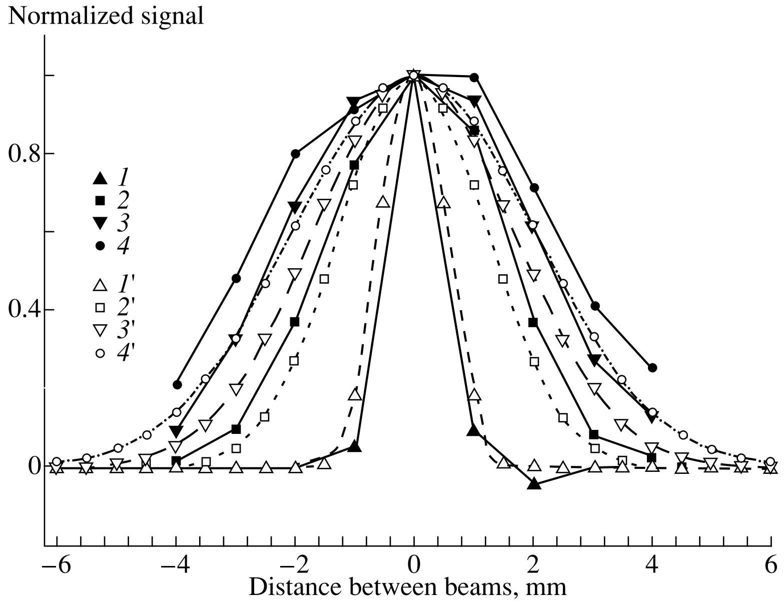

Fig. 8. Spatial distribution of the induced-absorption signal in the ingot for various elapsed times from the pump pulse. The ingot is the same as in Fig. 7. The curves *1–4* are experimental, whereas curves *1'–4'* correspond to the results of calculation based on the diffusion–recombination model. The time elapsed from the photogeneration pulse *t* = (*1*, *1'*) 25, (*2*, *2'*) 500, (*3*, *3'*) 1000, and (*4*, *4'*) 1500 μs.

there is no need for treatment of the ingot’s side surface.

Figure 7 shows the results of measuring the diffusive displacement of charge carriers from the initially excited cylindrical region in *n*-Si ingot grown by the floating-zone method; the measurements were performed in the “perpendicular” configuration. We plot here a family of curves that represent relaxation of the signal of free-carrier absorption. The parameter of the curves is the distance between the axes of the beams; this distance was varied from zero (precise intersection

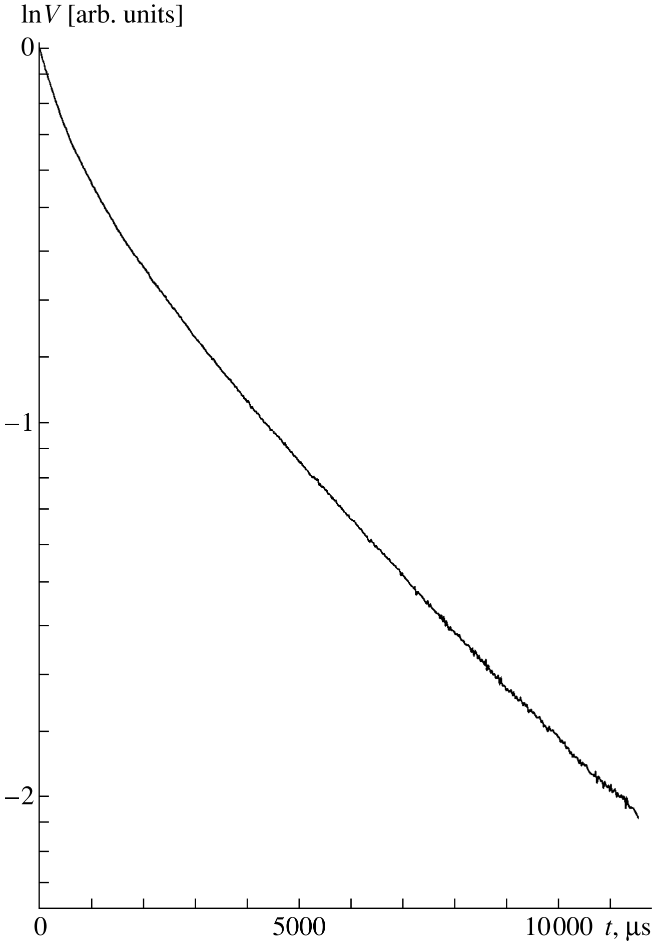

Fig. 9. Kinetics of decay of the signal V corresponding to induced free-carrier absorption in a silicon ingot obtained by the floating-zone method. The charge carriers were generated by a pump beam 10 mm in diameter, with the pump and probe beams intersecting. The ingot is the same as in Fig. 7.

of the beams) to ±4 mm. The beam diameters were 1.2 and 1 mm for the pump and probe beams, respectively. The curves measured for imprecise intersection of the beam axes clearly indicate that there is a time lag in the formation of the signal peak after the pump pulse terminates; this is clearly indicative of the process of motion of charge carriers from the pump beam to the probe beam. On the assumption that there are no internal electric fields in the probed region of the ingot, this motion is governed by ambipolar diffusion. The above assumption is corroborated by the curves shown in Fig. 8, where the results depicted in Fig. 7 are represented as explicit spatial dependences of the signal amplitude on the coordinate; here, time is the parameter of the curves. An almost perfect symmetry of the curves is observed; this symmetry should be distorted if there is a drift of charge carriers.

Distinct spatial redistribution of photogenerated charge carriers (see Fig. 8) indicates that the chosen method for the excitation of the electronic subsystem in silicon (using light with photon energy slightly lower than the band gap) does give rise to free charge carriers.

Dashed lines in Fig. 8 correspond to fitting the results of numerical simulations to the actual time dependences of the measured-signal amplitudes. The temporal–spatial evolution of a photogenerated rodlike packet of charge carriers was simulated. This evolution is caused by diffusion and recombination and is described by the following equation written in cylindrical coordinates:

$$\partial\delta n/\partial t = -\delta n/\tau(\delta n) + D[\partial^2\delta n/\partial r^2 + (\partial\delta n/\partial r)/r].$$

Here, δn is Δn normalized to the corresponding initial value (for $r = 0$ and at $t = 0$); t is the elapsed time from the pump-pulse termination; $\tau(\delta n)$ is the carrier lifetime (generally, dependent on the excitation level); D is the coefficient of ambipolar diffusion; and r is the distance from the pump-beam axis. After this equation had been solved numerically, we calculated the number of charge carriers found at the intersection of the carrier packet (in a circle 20 mm in diameter centered at the pump-beam axis) with the probe beam. The obtained value, equal (to within a factor common to all the family of the curves) to the number of excess charge carriers along the path of the probe beam, was compared to the experimentally measured signal amplitude. Such a comparison, implying that there is a linear relation between the number of the charge carriers and the measured signal, is justifiable because the induced free-carrier absorption is slight under the conditions of our experiments, in which the modulation factor for the probe-beam intensity is no larger than 0.1%.

The results of calculations (see Fig. 8) were obtained for $D = 12$ cm^2/s and $\tau(\delta n) = 0.019/(1 + 154\delta n)$ s. The signal amplitudes represented by experimental (and calculated) curves related to the times of 500, 1000, and 1500 μs elapsed from the termination of the pump pulse are increased in comparison with those observed for the elapsed time of 25 μs by 3.6 (3.4), 5.3 (5.2); and 6.6 (6.7) times, respectively. It can be seen that there is good agreement between the calculated and experimental curves with respect to both the shape and amplitude for the value of the ambipolar-diffusion coefficient typical of lightly doped, defect-free n-Si.

The consistency of experimental data on diffusive spreading of charge carriers with the diffusion coefficient corresponding to the free charge carriers in Si represents additional evidence that the charge carriers generated by photons with energies specified above are actually free.

Introduction of the explicit dependence of τ on the excitation level is justified by the obvious nonexponential shape of the signal in the case of measurements when the pump beam has a large diameter (10 mm) and the diffusive spreading becomes almost negligible (see Fig. 9). For the lower portion of the curve shown in

Fig. 9, the slope corresponds to $\tau = 7$ ms; thus, using the known relation $L = \sqrt{D\tau}$, we obtain $L = 2.9$ mm.

CONCLUSION

Thus, we demonstrated that it is possible to nondestructively measure the three-dimensional distribution of τ and L in silicon ingots by exposing these ingots to the crossed pump and probe beams. Although the largest size of ingots used in the experiments was 250 mm, the suggested method can be extrapolated to larger ingot sizes using the following reasoning. (i) The possibility of measuring τ at a distance of 170 mm from the entry point for the pump beam is demonstrated in Fig. 4 (the lowest curve); thus, using the “perpendicular” configuration, one can easily perform measurements of τ over the cross section of an ingot with a radius of 170 mm. (ii) The largest length of an ingot is limited by attenuation of the probe beam due to free-carrier absorption; for moderately doped ingots with a charge-carrier concentration of $\sim 10^{15}$ cm^{-3}, we use an absorption cross section of 2.5×10^{-17} cm^2 [1, 2] to find that attenuation of the probe-beam intensity due to absorption after passing 1000 mm amounts to ~10 times; the intensity of such a beam can be readily measured. In addition, for a higher level of doping, it is possible to use probe radiation with a shorter wavelength (thus absorbed to a lesser extent) and (or) to use a configuration in which the pump beam propagates along the ingot axis, whereas the probe beam propagates transversely.

The efficiency of the method can be basically enhanced by several orders of magnitude by simultaneously using several probe beams differing in the spectrum and intersecting the pump beam in different zones of the ingot; moreover, several beam groups, each of which consists of a pump beam and several probe beams, can be used.

Thus, the suggested method can be used for rapid nondestructive tomography of silicon ingots of almost any sizes within the range of ingots currently grown.

ACKNOWLEDGMENTS

We thank P.A. Bokhan, V.V. Kalinin, L.S. Smirnov, and S.S. Shaĭmeev for their interest in and encouragement of this study; A.A. Borisov for developing the software for digital oscilloscope; I.I. Ryabtsev for providing a laser for preliminary experiments; and V.A. Tkachenko for valuable comments.

REFERENCES

1. J. Linnros, J. Appl. Phys. **84**, 275 (1998).
2. V. Grivikas, J. Linnros, A. Vigelis, *et al.*, Solid-State Electron. **35**, 299 (1992).
3. Yu. I. Gusev, S. I. Marenikov, and V. P. Chebotaev, Pis’ma Zh. Tekh. Fiz. **3**, 305 (1977) [Sov. Tech. Phys. Lett. **3**, 124 (1977)].
4. *Properties of Silicon* (INSPEC, Inst. of Electrical Engineers, London, 1988), EMIS Datareviews Series, No. 4, p. 171.

Translated by A. Spitsyn

Semiconductors, Vol. 35, No. 1, 2001, pp. 48–53. Translated from Fizika i Tekhnika Poluprovodnikov, Vol. 35, No. 1, 2001, pp. 48–52.
Original Russian Text Copyright © 2001 by Agafonov, Aminov, Georgobiani, Lepnev.

ELECTRONIC AND OPTICAL PROPERTIES OF SEMICONDUCTORS

Observation of Minority-Carrier Traps in Schottky Diodes with a High Barrier and a Compensated Near-Contact Region Using Deep-Level Transient Spectroscopy

E. N. Agafonov, U. A. Aminov, A. N. Georgobiani*, and L. S. Lepnev

Lebedev Institute of Physics, Russian Academy of Sciences, Leninskiĭ pr. 53, Moscow, 117924 Russia

** e-mail: georg@sci.lebedev.ru*

Submitted May 29, 2000; accepted for publication June 1, 2000

Abstract—Schottky diodes based on the single-crystal *n*-ZnSe and fabricated by nitrogen-ion implantation with subsequent postimplantation treatment employing radical-beam epitaxy in atomic oxygen were studied using deep-level transient spectroscopy. On the assumption that the Schottky barrier is high and the near-contact region is compensated, the processes resulting in the occurrence of traps of minority charge carriers under negative biases were analyzed. The procedure for determining the compensated region thickness and the concentration of minority charge carriers in this region is described. The mechanisms of defect formation in zinc selenide crystals under annealing in atomic oxygen are described on the basis of the deep-level transient spectroscopy results. *© 2001 MAIK “Nauka/Interperiodica”.*

One of the promising method for changing the type and concentration of intrinsic defects in II–VI crystals is radical-beam gettering epitaxy based on crystal annealing in previously activated chalcogen vapor [1]. In this case, the type and concentration of defects in the material changes with increasing distance from the treated surface.

We studied the structures obtained by the method considered above and based on zinc selenide by the method of deep-level transient spectroscopy (DLTS). In order to identify the defects formed, we also studied the photoluminescence (PL) spectra.

The initial material of the samples we used was low-resistivity single-crystal *n*-ZnSe annealed in a zinc melt. Wafers 6 × 4 × 1 mm in size were cut from these crystals. After mechanical grinding and polishing, the wafers were etched in a chemical polishing etchant (a solution of bromine in methanol).

Implantation of nitrogen was performed at Lebedev Physical Institute of the Russian Academy of Sciences with ion energies and doses ensuring a uniform impurity concentration of 10^{19}, 10^{20}, and 10^{21} cm^{-3} in layers ~400 nm thick. The postimplantation treatment of crystals was carried out in a flow of oxygen atoms at temperatures ranging from 400 to 700°C by the method of radical-beam gettering epitaxy. The atomic oxygen was produced by a high-frequency discharge under a pressure of 10^{-1}–10^{-3} Torr; the flow intensity was 10^{17} cm^{-2}/s.

The capacitance–voltage (*C*–*V*) characteristics and DLTS spectra of the samples were measured using a setup consisting of a computer and CAMAC blocks connected to a high-frequency capacitance bridge. This setup allowed us to completely automatize the procedure of measuring and processing the experimental dependences and to calculate the distribution of shallow-level impurity, as well as the concentration, energy, capture cross section, and the boundaries of a filling region for deep levels. During measurements, the samples were in a cryostat, in which they were heated from the liquid-nitrogen temperature at a rate lower than 4 K/min. The sensitivity of the capacitance bridge used in the experiment was $\Delta C/C < 10^{-4}$.

The *C*–*V* characteristics for some of the samples studied are shown in Fig. 1; the samples differ in oxygen-treatment temperature (T_O) and in the concentrations of nitrogen [N] introduced. The barrier at the semiconductor–metal boundary turned out to be unusually high: for the majority of the samples its height was 2–2.5 eV. According to the published data [2], the height of the Au–*n*-ZnSe Schottky barrier is 1.4 eV. We discuss this result below. The concentration of shallow-level donors measured in the samples ranged within 10^{17}–10^{18} cm^{-3} at distances from the contact no smaller than 60 nm.

The DLTS spectra of certain samples are shown in Fig. 2. The peaks E_1 (0.2 eV) and E_2 (0.3 eV) were observed in all the samples, both initial and annealed in oxygen without a preliminary implantation. In the spectra of the samples annealed in oxygen at temperatures of 600°C and above, a positive peak H_1 at

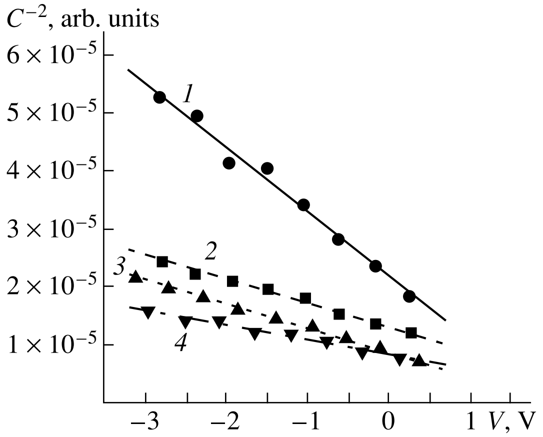

Fig. 1. Capacitance dependence of ZnSe:N samples on the voltage applied. Concentrations of the nitrogen introduced [N] (in cm^{-3}) and the temperatures of the sample treatment in oxygen, T_O (in °C) were (*1*) [N] = 10^{19}, T_O = 700; (*2*) [N] = 10^{20}, T_O = 600; (*3*) [N] = 10^{19}, T_O = 600; and (*4*) [N] = 10^{20}, T_O = 700.

200–250 K is also observed. The measured activation energy corresponding to this peak turned out to be equal to 0.6 eV. The traps E_1 and E_2 have been repeatedly observed and are described elsewhere: the first is related to the complexes involving V_{Se} and Zn_i defects and to impurities [3–5], and the second, as a rule, is attributed to V_{Se} [6–11].

As is known [12], minority-carrier traps can be observed in the DLTS spectra of *p–n* junctions for positive biases due to carrier injection. We used only negative biases in our experiments. Nonetheless, the positive DLTS peaks were observed in all the samples annealed at temperatures of 600°C and above. Consequently, the capacitance relaxation in our samples is not described by the *p–n*-junction model.

The appearance of a peak related to the minority-carrier traps in the DLTS spectrum of a Schottky diode cannot be described by the model of conventional relaxation of its capacitance. In fact, a charge state of such traps in this model does not change when the filling pulse is applied to the barrier and during subsequent relaxation; therefore, they do not contribute to a change in sample capacitance and are not observed in the measurements.

A high series-connected resistance of the material [13] may be one of the reasons for positive peak emergence in the DLTS spectra of Schottky diodes. By measuring the Schottky diode capacitance using a capacitance bridge, its measured (C_m) and a true (C) capacitances are related by the formula

$$\frac{C_m}{C} = \frac{1}{(1 + r/R)^2 + (\omega r C)^2}, \tag{1}$$

where R is the resistance of the Schottky barrier, r is the series resistance (due to the diode material, wires, etc.), and ω is the frequency of the probing signal. Dependence of C_m on C is not monotonic and has a maximum at $\omega rC = 1 + r/R$; i.e., if $\omega rC > 1 + r/R$, the increments

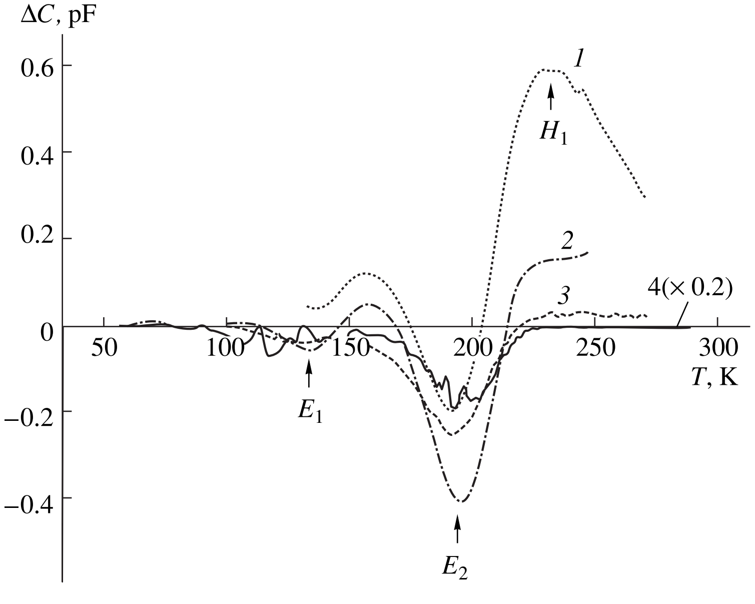

Fig. 2. DLTS spectra of ZnSe:N crystals annealed in the oxygen radicals. Designation of [N] and T_O are the same as in Fig. 1: (*1*) [N] = 10^{19} cm^{-3} and T_O = 600°C; (*2*) [N] = 10^{19} cm^{-3} and T_O = 700°C; (*3*) [N] = 10^{20} cm^{-3} and T_O = 400°C; and (*4*) initial single crystal.

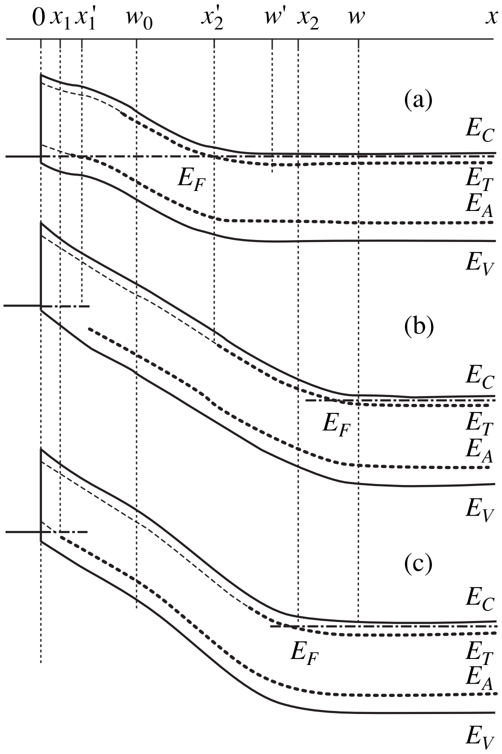

Fig. 3. Energy-band diagram of a Schottky diode with a high barrier, donor E_T and acceptor E_A with deep levels and a compensated near-contact region: (a) is a state for the applied filling pulse, (b) is a state of the subsequent relaxation, (c) is a steady state.

of the values of C_m and C have the opposite signs, which corresponds to the inversion of the peak signs in the DLTS spectra observed. In addition, the decrease in the capacitance C with increasing depletion-region width is accompanied by a reduction in the remaining part of the diode and, therefore, by a decrease in the series resistance r. This can also result in the change of the DLTS signal sign in the observations.

With the aim of checking these conditions of peak inversion, the current–voltage (I–V) and C–V characteristics of all the samples for various temperatures were measured. Analysis of the I–V characteristics showed that the series resistance of the samples annealed at temperatures of 600°C and higher was indeed larger than that of the samples annealed at lower temperatures. However, the values of capacitance and series resistance measured do not correspond to the fulfillment of conditions $\omega rC > 1 + r/R$ for any of the crystals. The change of the value r on filling and depopulating the deep levels also turned out to be rather small and could not result in the DLTS spectrum inversion. Thus, the consideration of a series resistance of the diode does not explain the appearance of the DLTS positive peak in the spectra of our samples.

As was mentioned above, the barrier at the Au–ZnSe contact was anomalously high, which is probably caused by the surface states formed by the treatment [14]. The presence of a high barrier allows us to assume (by analogy with [15]) that the traps of minority charge carriers can manifest themselves in the DLTS spectra of the Schottky diodes under study. At the same time, one should take into account that the structure under study, obtained by the method of radical-beam gettering epitaxy, features a change in the composition of defects upon an increase in the distance from the surface treated in radicals [16]. Resistances of all the diodes measured under a high forward bias significantly exceeded the resistance of an untreated layer near the contact, which indicated that a high-resistance region was present near the contact. This gives grounds to suggest a band diagram of the Schottky barrier with a compensated near-contact region shown in Fig. 3 as a possible basis for analyzing the processes of capacitance relaxation in the structures under study.

Let us divide a near-contact region of a semiconductor into two parts: "compensated" ($0 < x < w_0$) and "uncompensated" ($x > w_0$). The concentration of shallow-level impurity, which does not change its charge state if the bias is varied, is designated as N in the region $0 < x < w_0$ and as N_0 in the region $w_0 < x < w$. The concentration of deep-level acceptor impurities is designated as N_A for $0 < x < w_0$ and N_{A0} for $w_0 < x < w$; the concentration of donor impurities is designated as N_T, and their boundaries for the regions of filling, as x_1 and x_2, respectively (Fig. 3c). Solving the Poisson equation for such a barrier and substituting the values of potentials

$$V|_{x = x_1} = V_1 \quad \text{and} \quad V|_{x = x_2} = V_2,$$

which are determined from the known values of the bias V_b, band gap, and deep-level energies, we obtain

$$V_1 = V_b - \frac{q}{2\varepsilon}\{(N_0 - N_{A0})(w - x_1)^2 + N_T(x_2 - x_1)^2 + [(N - N_A) - (N_0 - N_{A0})](w_0 - x_1)^2\},$$

$$x_2 = w - \sqrt{\frac{2\varepsilon}{q(N_0 - N_{A0})}(V_b - V_2)}, \qquad (2)$$

$$w^2 = \frac{2\varepsilon}{q(N_0 - N_{A0})}V_b - \frac{N_A}{(N_0 - N_{A0})}x_1^2 - \frac{(N - N_A) - (N_0 - N_{A0})}{(N_0 - N_{A0})}w_0^2 - \frac{N_T}{(N_0 - N_{A0})}x_2^2,$$

where q is the elementary charge and ε is the dielectric constant of the semiconductor.

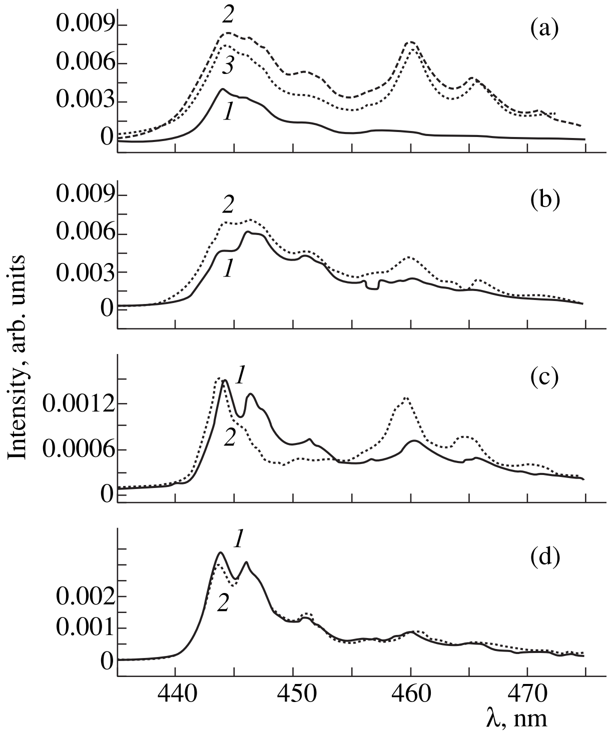

Fig. 4. Photoluminescence spectra for ZnSe:N single crystals annealed in the activated oxygen vapor; the measurements were carried out at a temperature of 4.2 K. Designation of T_O and [N] are the same as in Fig. 1: (a) T_O = 400°C; [N] = (*1*) 10^{19}, (*2*) 10^{20}, and (*3*) 10^{20} cm^{-3}. (b) T_O = 500°C; [N] = (*1*) 10^{19} and (*2*) 10^{21} cm^{-3}. (c) T_O = 600°C; [N] = (*1*) 10^{19} and (*2*) 10^{21} cm^{-3}. (d) T_O = 700°C; [N] = (*1*) 10^{19} and (*2*) 10^{21} cm^{-3}.

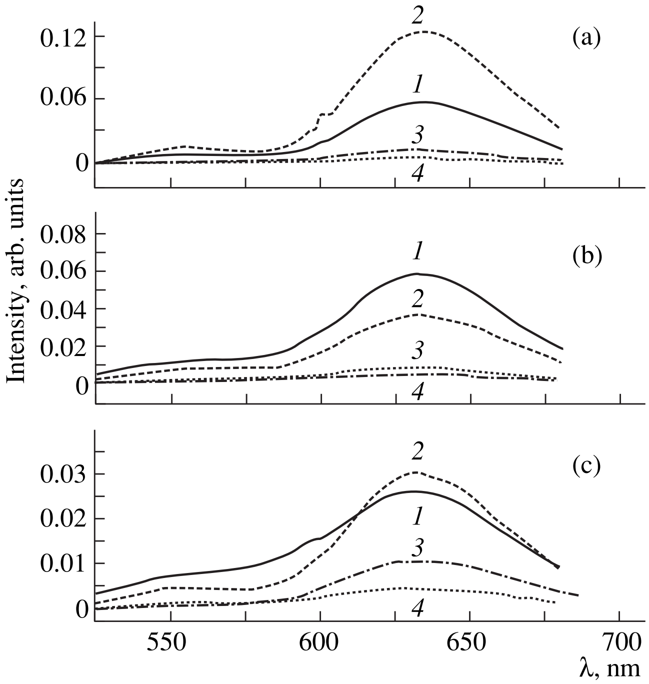

Fig. 5. Photoluminescence spectra of ZnSe:N single crystals annealed in the oxygen vapor; the measurements were carried out at a temperature of 77 K. Designation of [N] and T_O are the same as in Fig. 1: (a) [N] = 10^{19} cm^{-3}; T_O = (*1*) 400, (*2*) 500, (*3*) 600, and (*4*) 700°C. (b) [N] = 10^{20} cm^{-3}; T_O = (*1*) 400, (*2*) 500, (*3*) 600, and (*4*) 700°C. (c) [N] = 10^{21} cm^{-3}; T_O = (*1*) 400, (*2*) 500, (*3*) 600, and (*4*) 700°C.

Dependence of the capacitance relaxation on time has a form

$$\Delta C(t) \approx \frac{\varepsilon}{8\pi w^3(N_0 - N_{A0})}[N_A(x_1'^2 - x_1^2)\exp(-e_p t) - N_T(x_2^2 - x_2'^2)\exp(-e_n t)], \tag{3}$$

where

$$w = \sqrt{2\varepsilon V_b / q(N_0 - N_{A0})},$$

and e_p and e_n are the carrier emission rates from deep acceptor and donor levels. The terms in (3), which correspond to the contribution of deep donor and acceptor states, have different signs. The relaxation of acceptor states leads to a decrease in the diode capacitance, and the relaxation of donor states results in its increase. Depending on the relation between these contributions, the capacitance can increase or decrease in the various time intervals after the change of bias.

We simplify expression (2) by using the approximations $x_1^2 \ll w_0^2$, x_2^2, w^2, and N_T, $N - N_A$, $N_{A0} \ll N_0$, which are justified due to compensation of the near-contact region and the low-resistance of the initial single crystal:

$$x_1 = \frac{\varepsilon}{qN_0}\frac{V_1}{\sqrt{\frac{2\varepsilon}{qN_0}V_b + w_0^2} - w_0},$$

$$x_2 = \sqrt{\frac{2\varepsilon}{qN_0}V_b + w_0^2} - \sqrt{\frac{2\varepsilon}{qN_0}(V_b - V_2)}, \tag{4}$$

$$w = \sqrt{\frac{2\varepsilon}{qN_0}V_b + w_0^2}.$$

Substituting in (4) the value of x_2 determined experimentally from the DLTS peak of the majority-carrier traps, we can calculate w_0, x_1, and x_1'. Now, we take into account that the values of the filling depths and concentration of the acceptor centers are calculated using a program of experimental data processing starting from the capacitance, relaxation amplitude measured, and with the assumption that all the recharging

Table

Level	Energy, eV	The boundaries of filling regions, nm	Concentration, cm^{-3}
E_2	0.36	195–305	9×10^{15}
H_1	0.67	26–15	3×10^{17}

Note: The composition of a shallow impurity is 5×10^{17} cm^{-3}; the length of a compensated region is 130 nm. The region of the space charge is 280 and 390 nm at voltages of 0 and 3 V, respectively.

deep levels in the Schottky diode are traps for majority carriers. Using these values, we can obtain the magnitude of the capacitance relaxation and then, according to formula

$$\Delta C_A(0) = \varepsilon/(8\pi w^3 N_0) N_A(x_1'^2 - x_1^2),$$

determine the correct value of the concentration of acceptor states N_A. The results obtained by the method suggested for the sample annealed in oxygen at a temperature of 700°C after nitrogen implantation at a dose of 10^{20} cm^{-3} are given in the table.

We have also measured the PL spectra at temperatures of 77 and 4.2 K. The PL was excited using a nitrogen laser at a wavelength of 337.1 nm. A distinguishing feature of the samples under consideration is as follows: in a corresponding spectral range of 360–390 nm, the excitonic lines of zinc oxide [17, 18] were not observed; i.e., the layer of zinc oxide at the crystal surface was not formed in the process of treatment in oxygen.

Some of the PL spectra are shown in Figs. 4 and 5. Published data [19–22] allow us to identify the line at 444 nm with emission of an exciton bound at the shallow acceptor level N_{Se}, and the line at 446 nm, with the emission of an exciton bound at the deeper acceptor (zinc vacancy). The band at 460 nm is associated with the emission from donor–acceptor pairs [21–23]. Two emission bands (at 550 nm and 630 nm) are observed in the longer wavelength portion of the spectrum (Fig. 5). The band at 630 nm is associated with a donor–acceptor complex that involves a doubly charged zinc vacancy [19, 24, 25].

The measurements carried our allow us to suggest that a deep acceptor level observed by the DLTS method is associated with a vacancy of zinc. The vacancy formation during a postimplantation annealing in atomic oxygen proceeded according to the gettering mechanism. As shown in [26], the ion implantation can restrict the oxygen diffusion into the sample bulk. The absence of the positive DLTS peak in the spectra of the samples, both initial and annealed in the oxygen without a preliminary implantation, and the appearance of this peak after nitrogen implantation confirms this suggestion. The nitrogen also forms the acceptor centers occupying the site of a selenium in the crystal lattice. The presence of the related PL line and the reduction in the number of the Se vacancies in the implanted samples compared to the unimplanted samples (a decrease of the E_2 peak in the DLTS spectra) supports the explanation presented above.

ACKNOWLEDGMENTS

We are grateful to Z.P. Ilyukhina for etching the initial samples, to V.A. Dravin for ion implantation, to E.G. Chizhevskiĭ for the fabrication of the contacts, and to E.A. Bobrova and N.A. Penin for their productive participation in the discussion of the results.

This work was supported by the Russian Foundation for Basic Research, project no. 00-02-16421; by the Ministry of Science of the Russian Federation, as part of the program “Physics of Solid-State Nanostructures”, project no. 99-1122, and as part of the program “Physics of Quantum and Wave Processes”, sub-program “Fundamental Spectroscopy”, project no. 01.08.02.8-4.

REFERENCES

1. A. N. Georgobiani and M. K. Sheĭkman, *Physics of II–VI Compounds* (Nauka, Moscow, 1986).
2. A. G. Milnes and D. L. Feucht, *Heterojunctions and Metal–Semiconductor Junctions* (Academic, New York, 1972; Mir, Moscow, 1975).
3. T. Ido and M. Okada, J. Cryst. Growth **72**, 170 (1985).
4. M. Karai, K. Kido, H. Naito, *et al.*, Phys. Status Solidi A **117**, 515 (1990).
5. S. Satoh and K. Igaki, Jpn. J. Appl. Phys. **19**, 485 (1980).
6. P. Besomi and B. W. Wessels, J. Appl. Phys. **53**, 3076 (1982).
7. H. G. Grimmeiss and N. Kullendorff, J. Appl. Phys. **51**, 5852 (1980).
8. B. Hu, G. Karczewski, H. Luo, *et al.*, Phys. Rev. B **47**, 9641 (1993).
9. G. Karczewski, W. Hu, A. Yin, *et al.*, J. Appl. Phys. **75**, 7382 (1994).
10. W. B. Leigh and B. W. Wessels, J. Appl. Phys. **55**, 1614 (1984).
11. Y. Shirakawa and H. Kukumoto, J. Appl. Phys. **51**, 5859 (1980).
12. D. V. Lang, J. Appl. Phys. **45**, 3023 (1974).
13. E. V. Astrova, A. A. Lebedev, and A. A. Lebedev, Fiz. Tekh. Poluprovodn. (Leningrad) **19**, 1382 (1985) [Sov. Phys. Semicond. **19**, 850 (1985)].
14. S. Sze, *Physics of Semiconductor Devices* (Wiley, New York, 1981; Mir, Moscow, 1984), Vol. 1.
15. L. Stolt and K. Bohlin, Solid-State Electron. **28**, 1215 (1985).
16. A. N. Georgobiani, M. B. Kotlyarevskiĭ, V. V. Kidalov, *et al.*, Neorg. Mater. **29**, 1399 (1993).

17. I. P. Kuz'mina and V. A. Nikitenko, *Zinc Oxide: Preparation and Optical Properties* (Nauka, Moscow, 1984).
18. S. Miyamoto, Jpn. J. Appl. Phys. **16**, 1129 (1978).
19. D. D. Nedeoglo and A. V. Simashkevich, *The Electric and Luminescent Properties of Zinc Selenide* (Shtiintsa, Kishinev, 1984).
20. J. Gutowski, N. Pressler, and G. Kudlek, Phys. Status Solidi A **120**, 11 (1990).
21. T. Ohkawa, T. Mitsuyu, and O. Yamazaki, J. Cryst. Growth **86**, 329 (1988).
22. J. Qui, J. M. De Puydt, H. Cheng, and M. A. Haasse, Appl. Phys. Lett. **59**, 2992 (1991).
23. I. S. Hauksson, J. Simpson, S. Y. Wang, *et al.*, Appl. Phys. Lett. **61**, 2208 (1992).
24. N. K. Morozova, I. A. Karetnikov, and E. M. Gavrishchuk, Neorg. Mater. **35**, 917 (1999).
25. G. Jones and G. Woods, J. Lumin. **9**, 389 (1974).
26. A. N. Georgobiani, M. B. Kotlyarevskiĭ, I. V. Rogozin, and V. V. Kidalov, Neorg. Mater. **31**, 1357 (1995).

Translated by T. Galkina

Semiconductors, Vol. 35, No. 1, 2001, pp. 54–58. Translated from Fizika i Tekhnika Poluprovodnikov, Vol. 35, No. 1, 2001, pp. 53–57.
Original Russian Text Copyright © 2001 by Bazyk, Kovalenko, Mironchenko, Shutov.

ELECTRONIC AND OPTICAL PROPERTIES OF SEMICONDUCTORS

Effect of the Charge-Carrier Drift in a Built-in Quasi-Electric Field on the Emission Spectrum of the Graded-Gap Semiconductors

A. I. Bazyk, V. F. Kovalenko, A. Yu. Mironchenko, and S. V. Shutov
Institute of Semiconductor Physics, Kherson Division, National Academy of Sciences of Ukraine,
Kherson, 325008 Ukraine

Submitted December 20, 1999; accepted for publication June 9, 2000

Abstract—The shape of the band-to-band photoluminescence spectrum for a graded-gap semiconductor in conditions of nonequilibrium charge-carrier transport affected by a built-in quasi-electric field $E = e^{-1}\nabla E_g$ was calculated. It was demonstrated that the distortion of the short-wavelength region of the emission spectra occurs due to the coordinate dependence on the radiative recombination probability in the wide-gap region of the crystal. The calculations were confirmed by measuring the photoluminescence spectra for the $Al_xGa_{1-x}As$ undoped ($n \leq 10^{16}$ cm^{-3}) graded-gap solid solutions with E varying in the range of 90–650 V/cm at 300 K. *© 2001 MAIK "Nauka/Interperiodica".*

The drift character of the nonequilibrium-charge-carrier transport in a built-in quasi-electric field of the crystal $E = e^{-1}\nabla E_g$ causes variations in the fundamental luminescent properties of graded-gap semiconductors in relation to compositionally uniform ones, more specifically, a variation in the emission spectrum shape occurs. There are many publications devoted to the luminescent properties of graded-gap semiconductors [1–9]. However, the radiative recombination was only investigated in detail for band gaps with a relatively small gradient, i.e., for low velocities of the nonequilibrium-charge-carrier drift in the built-in field. In this case, the emission spectrum shape reproduces the distribution profile for nonequilibrium charge carriers, which is an exponentially decreasing function of the depth.

It was demonstrated [10–14] that for a very large ∇E_g gradient satisfying the condition

$$d \ll e^{-1}\mu\tau|\nabla E_g|,$$

where d is the thickness of the graded-gap crystal and μ and τ are the mobility and lifetime of the nonequilibrium charge carriers (i.e., for very high drift velocities), the residence time of nonequilibrium charge carriers in the graded-gap region is much shorter than their lifetime τ. For this reason, no recombination occurs in this region, and the emission spectrum is absent.

For an intermediate range of ∇E_g variations, i.e., for medium and large ∇E_g, it has been stated elsewhere [6, 15, 16] that radiative recombination is completely or partially absent in the wide-gap region of a graded-gap semiconductor. This manifests itself in the distortion of the short-wavelength region of the emission spectrum and in the shift of the emission peak to longer wavelengths. This special feature of the radiative recombination in graded-gap semiconductors is explained by a decrease in the internal quantum efficiency of emission in the wide-gap region. This decrease is caused by the removal of nonequilibrium charge carriers from this region to narrower-gap regions in the drift times $\tau_{dr} < \tau_r$ (τ_r is the radiative lifetime), which competes with the radiative recombination. This special feature of the radiative recombination in graded-gap semiconductors has not been investigated in detail.

In this paper, the emission spectrum shape for a graded-gap semiconductor was calculated under the assumption that the drift velocity of nonequilibrium charge carriers in the built-in field of the crystal E is high. The result of calculations were compared with the experimental data.

CALCULATION OF THE EMISSION SPECTRUM SHAPE

In order to calculate the band-to-band emission spectrum, we used an approach considered elsewhere [4] for semi-infinite n-type crystals with the band gap E_g linearly decreasing with increasing distance from the illuminated surface (Fig. 1):

$$E_g(z) = E_g(0) - eEz, \tag{1}$$

where $E_g(0)$ is the band gap at $z = 0$. Computations were carried out taking into account that the minority carriers could both recombine within the wide-gap region and leave it without recombining due to the drift in a crystal field. In contrast with this, the effect of this factor on the spectrum shape was not taken into account in computations carried out previously [4].

The analysis of the processes mentioned demonstrates that the minority-carrier drift governs the coordinate dependence of recombination, which can be written as

$$W(z) = \tau^{-1}\exp\left(-\frac{\tau V_{\mathrm{dr}}}{z}\right), \qquad (2)$$

where V_{dr} is the velocity of the minority-carrier drift in the field E. For radiative recombination, the dependence of its probability on the coordinate $W_r(z)$ is similar to the above with the substitution of τ_r for τ in Eq. (2).

For linear recombination, the shape of the band-to-band emission spectrum is described by the following expression:

$$I(z) = W_r(z)\Delta P(z), \qquad (3)$$

where $\Delta P(z)$ is the minority-carrier distribution along the z coordinate in the direction of field E.

In order to calculate $\Delta P(z)$, it is necessary to solve the continuity equation. It is noteworthy that the classical continuity equation [17] is written as

$$D\frac{d^2}{dz^2}\Delta P(z) - \mu E\frac{d}{dz}\Delta P(z) - \frac{\Delta P(z)}{\tau} + G(z) = 0, \qquad (4)$$

where D is the minority-carrier diffusivity, and $G(z)$ is the generation function of the minority charge carriers. This equation was used to compute $\Delta P(z)$ elsewhere [4], and is inadequate for the case under consideration, since, although Eq. (4) implies simultaneous diffusion, drift in the E field, and minority-carrier recombination in the graded-gap semiconductor, it does not account for the probability of the minority charge carriers' removal from the wide-gap region of the crystal without recombination. In order to take into account this probability, we replaced the recombination probability $W = 1/\tau$ in Eq. (4) by a recombination probability with allowance made for its coordinate dependence $W(z)$. In this case, the continuity equation takes the form

$$D\frac{d^2}{dz^2}\Delta P(z) - \mu E\frac{d}{dz}\Delta P(z) - \frac{\Delta P(z)}{\tau} \times \exp\left(-\frac{\tau V_{\mathrm{dr}}}{z}\right) + G(z) = 0. \qquad (5)$$

In order to simplify the solution of Eq. (5), we consider the ∇E_g values, for which the diffusion flux is negligible in comparison to the drift flux. In this case, $L/l_+ \ll 1$, where L and l_+ are the diffusion length and diffusion–drift length for minority charge carriers, respectively. For 300 K and diffusion length $L = 5 \times 10^{-4}$ cm, the above inequality is valid even for $\nabla E_g > 50$ eV/cm. In this case, Eq. (5) can be rewritten as

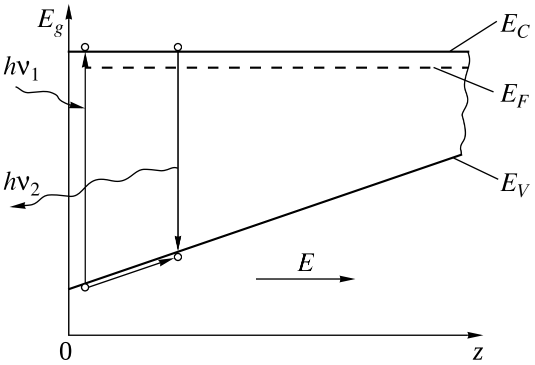

Fig. 1. Energy-band diagram for a graded-gap semiconductor.

$$-V_{\mathrm{dr}}\frac{d}{dz}\Delta P(z) - \frac{\Delta P(z)}{\tau}\exp\left(-\frac{\tau V_{\mathrm{dr}}}{z}\right) + G(z) = 0. \qquad (6)$$

For a direct-gap semiconductor [18] and the exciting photon energy $h\nu > E_{g0}$ (where E_{g0} is the band gap for the illuminated surface), the generation function for the fields $E < e^{-1}\alpha(h\nu - E_{g0})$ can be written as

$$G(z, h\nu) = \alpha\beta J_0\exp(-\alpha z), \qquad (7)$$

where β is the quantum efficiency for the internal photoeffect, α is the exciting radiation absorbance, which can be expressed by the step function [2]

$$\alpha(z) = \begin{cases} \alpha_0 & \text{for } h\nu \ge E_g(z), \\ 0 & \text{for } h\nu < E_g(z); \end{cases} \qquad (8)$$

and J_0 is the excitation intensity.

The general solution to Eq. (6) for the boundary conditions

$$V_{\mathrm{dr}}\Delta P(0) + S_0\Delta P(0) = \beta J_0, \quad \Delta P(z)|_{z\to\infty} = 0, \qquad (9)$$

where S_0 is the surface-recombination rate for minority charge carriers, is given by

$$\Delta P(y) = e^{-F(y)}[C + C_0\int\exp(F(y) - \delta y)dy], \qquad (10)$$

where

$$y = \frac{z}{l_+}, \quad \delta = \alpha l_+, \quad G_0 = \beta\alpha J_0\tau,$$

$$C = \mathrm{const}, \quad F(y) = \int e^{-\frac{1}{y}}dy.$$

An investigation of the $F(y)$ dependence demonstrated that, for the range $0 < y \le 10$, this dependence can be adequately approximated by the continuous sequence of line segments $F_i(y) = b_i y - q_i$ (b_i and q_i are the con-

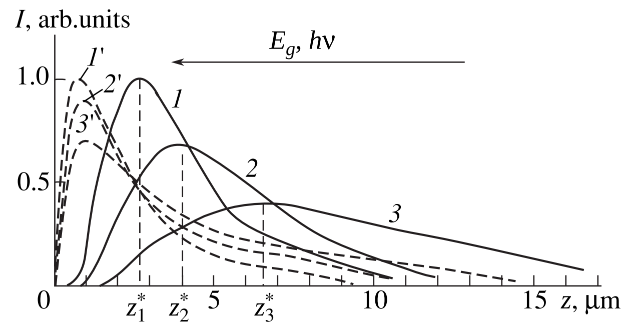

Fig. 2. Calculated emission spectra for graded-gap semiconductors: (*1–3*) from formula (14) with allowance made for the coordinate dependence for radiative-recombination probability, and (*1'–3'*) from formula (16) with the coordinate dependence disregarded. The band-gap gradient ∇E_g = (*1, 1'*) 200, (*2, 2'*) 300, and (*3, 3'*) 500 eV/cm.

stants for each segment). In this case, solution (10) is transformable to the form

$$\Delta P(y) = e^{q-by}\left[C + G_0\int e^{by-q-\delta y}dy\right] = Ce^{q-by} + \frac{G_0}{b-\delta}e^{-\delta y}. \tag{11}$$

Determining C from boundary conditions (9)

$$C = \frac{\beta J_0}{e^q(V_{\mathrm{dr}} + S_0)} + \frac{G_0}{e^q(\alpha l_+ - b)}$$

and passing on to the z variable, we can write solution (11) as

$$\Delta P(z) = \left[\frac{\beta J_0}{V_{\mathrm{dr}} + S_0} + \frac{G_0}{\alpha l_+ - b}\right] \times \exp\left(-\frac{bz}{l_+}\right) + \frac{G_0}{b - \alpha l_+}\exp(-\alpha z). \tag{12}$$

Taking into account that $b = F'(y)$ (b is the slope of $F(y)$ for a given line segment), we obtain the following expression for the shape of the band-to-band emission spectrum:

$$I(z) = \frac{1}{\tau_r}\exp\left(-\frac{\tau_r V_{\mathrm{dr}}}{z}\right)\left\{\left[\frac{\beta J_0}{V_{\mathrm{dr}} + S_0} + \frac{\beta J_0 \alpha\tau}{\alpha l_+ - \exp\left(-\frac{l_+}{z}\right)}\right] \times \exp\left[-\frac{z}{l_+}\exp\left(-\frac{l_+}{z}\right)\right] + \frac{\beta J_0 \alpha\tau\exp(-\alpha z)}{\exp\left(-\frac{l_+}{z}\right) - \alpha l_+}\right\}. \tag{13}$$

In the case of the strongly absorbing exciting radiation (for $\alpha z \gg 1$), we have

$$I(z) = \frac{1}{\tau_r}\exp\left(-\frac{\tau_r V_{\mathrm{dr}}}{z}\right) \times \left\{\left[\frac{\beta J_0}{V_{\mathrm{dr}} + S_0} + \frac{\beta J_0 \alpha\tau}{\alpha l_+ - \exp\left(-\frac{l_+}{z}\right)}\right]\exp\left[-\frac{z}{l_+}\exp\left(-\frac{l_+}{z}\right)\right]\right\}. \tag{14}$$

Within the crystal bulk at the distances $z > l_+$ and $z > \tau_r V_{\mathrm{dr}}$ from the illuminated surface,[1] expression (14) takes the form

$$I(z) = \frac{1}{\tau_r}\left(\frac{J_0\beta}{V_{\mathrm{dr}} + S_0} + \frac{J_0\beta\alpha\tau}{\alpha l_+}\right)\exp\left(-\frac{z}{l_+}\right) \tag{15}$$

and coincides with the expression

$$I(z) = C'\exp\left(-\frac{z}{l_+}\right), \tag{16}$$

which is valid for the emission-spectrum shape if the coordinate dependence of the radiative recombination probability is disregarded [4].

The theoretical dependence of the emission-spectrum shape for epilayers on the built-in E, which was calculated from formulas (14) and (16), is shown in Fig. 2 (curves *1–3* and *1'–3'*, respectively). The following parameters, which approximately corresponded to those for the $\mathrm{Al}_x\mathrm{Ga}_{1-x}\mathrm{As}$ graded-gap solid solutions, were adopted in computations:

$$T = 77\ \mathrm{K},\quad \alpha = 2.72\times10^4\ \mathrm{cm}^{-1},\quad D_p = 5\ \mathrm{cm}^2\ \mathrm{s}^{-1},$$

$$\tau = 10^{-9}\ \mathrm{s},\quad \beta = 1,\quad \tau_i = 2.5\times10^{-9}\ \mathrm{s},$$

$$S_0 = 10^5\ \mathrm{cm/s},\quad J_0 = 10^{20}\ \mathrm{cm}^{-2}\ \mathrm{s}^{-1}.$$

As can be seen from curves *1–3* shown in Fig. 2, consideration of the coordinate dependence for the radiative recombination probability leads to a spectral peak shift to longer wavelengths. The shift increases with increasing E. If this dependence is neglected, no shift of the peak is observed with an increase in the built-in field E (curves *1'–3'*).

COMPARISON WITH THE EXPERIMENT

In order to experimentally verify the validity of the theoretical conclusions derived above, we measured the photoluminescence (PL) spectra for epilayers of the $\mathrm{Al}_x\mathrm{Ga}_{1-x}\mathrm{As}$ undoped ($n \le 10^{16}\ \mathrm{cm}^{-3}$) graded-gap solid solutions. The layers were grown from the limited solution–melt volume with the largest content of AlAs at the layer–substrate interface ($x \cong 0.37$), which decreased almost linearly (approximately by 80% of the thickness) from the substrate to the layer surface ($x = 0$). The ∇E_g and d values for various structures varied within the ranges of $90 \le \nabla E_g \le 650$ eV/cm and $16 \le d \le 70$ μm, respectively.

---

[1] For actual crystals, the thickness d is usually no more than several l_+ and, invariably, $d < 10l_+$.

PL was excited at 300 K both at the narrow-gap (at deceleration by the field E) and wide-gap (at acceleration by the field E) side of the layers on the forward and reverse angle laps with an angle of inclination of 5′–40′ [19]. The exciting radiation source was an Ar laser with $\lambda = 0.488$–0.514 μm and excitation intensity $J = 2 \times 10^{20}$ cm^{-2} s^{-1}. The optical probe diameter was about 30 μm. The PL spectra were detected using a Ge photodiode according to conventional procedure.

In forward angle laps, the epilayers were partially removed from the narrow-gap ($E_g^{\min}$) side, and in the reverse angle laps, the substrate and epilayers were partially removed from the wide-gap ($E_g^{\max}$) side. By scanning the surfaces of these angle laps with an optical probe, PL was excited in various regions over the layer surface at the narrow-gap and wide-gap side, respectively.[2]

The PL spectra for epilayers with various E measured at both the wide-gap (curves *1–3*) and narrow-gap (curve *4*) sides are shown in Fig. 3. The solid solution composition at both the illuminated surfaces is identical and corresponds to the band gap E_{g0}, as it is shown in the inset in Fig. 3.[3] If PL was excited from the narrow-gap side, the emission-spectrum energy peak $h\nu_{m4}$ was independent of E. In this case, the decelerating field E forced the minority charge carriers to the illuminated surface, and the generation region coincided with the radiative recombination region.

If PL was excited from the side with $E_g^{\max}$, the short-wavelength peak of the emission spectra $h\nu_{m1-3}$ was shifted to lower energies in comparison to E_{g0} for the illuminated surface (curves *1–3*). The shift increased with increasing E.[4] The shift corresponded to the spatial offset of $E_g(z) = h\nu_{m1-3}$ to the narrow-gap region of the crystal for a distance $z^* = z' - z_0$ (z' is the peak energy $h\nu_{m1-3} = E_g(z')$, see inset in Fig. 3) from the illuminated surface. This is a consequence of the coordinate dependence for the radiative-recombination probability under the accelerating effect of the E field. For a wide-gap region of the crystal, which is extended to z^*, this probability is significantly lower in comparison to the narrow-gap region (at $z \ge z'$, see inset in Fig. 3). Because of this, it is conceivable that the generation and radiative recombination regions for minority charge carriers are spatially separated by a distance of about z^*. The dependences of the spatial displacement of a peak energy for experimental and calculated emis-

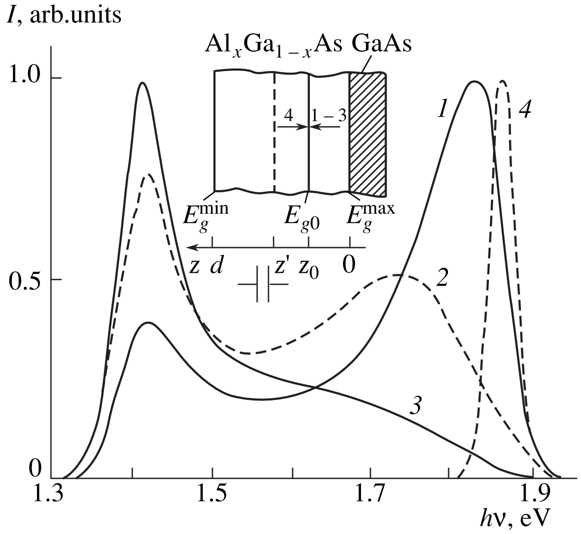

Fig. 3. Photoluminescence spectra for n-Al$_x$Ga$_{1-x}$As graded-gap solid solutions with various E_g gradients for the accelerating (*1–3*) and decelerating (*4*) built-in field E. T = 300 K, ∇E_g = (*1, 4*) 160, (*2, 4*) 372, and (*3, 4*) 645 eV/cm. The schematic layout of the experiment is shown in inset: arrows indicate the excitation directions. The numbers of the arrows in the inset correspond to those of the PL spectra.

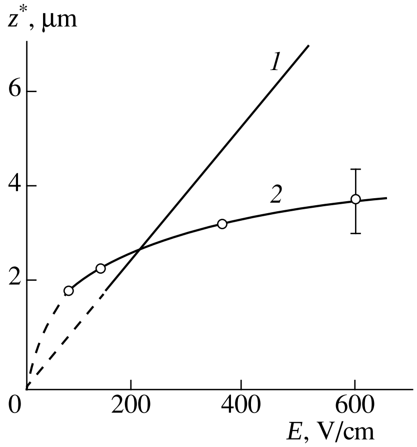

Fig. 4. Spatial displacement z^* for (*1*) the calculated spectra shifts and (*2*) measured PL spectra for the Al$_x$Ga$_{1-x}$As solid solutions to the narrow-gap region in relation to the built-in field E.

---

[2] The procedure of recording the PL spectra for graded-gap semiconductors using the angle laps is given in detail elsewhere [19].

[3] If PL was excited from the side with $E_g^{\min}$, E_{g0} for layers with various E was determined from the PL band peak energy $h\nu_{m4} \cong E_{g0}$ (Fig. 3, curve *4*). If PL was excited from the side with $E_g^{\max}$, the coordinate on the illuminated surface of the reverse lap, which corresponds to the E_{g0} value, was set by the precise displacement of the sample at a distance of $z_0 = (E_f(0) - h\nu_{m4})/eE$ from the layer–substrate interface. The latter was determined from the jump of the PL spectral features and intensity while scanning the lap surface with an optical probe.

[4] The additional long-wavelength peak in the PL spectra measured is related to an accumulation of minority charge carriers at the narrow-gap rear surface [5].

sion spectra to the narrow-gap region z^* on the accelerating field strength E are shown in Fig. 4. For experimental PL spectra, the values of z^* were determined from formula (1) under the assumption that $E_g(z) = h\nu_{m1-3}$ and $E_g(0) = E_{g0} = h\nu_{m4}$. The values of z^* for the spectra calculated were taken directly on the abscissa in Fig. 2.

It can be seen that the experimental dependence $z^*(E)$, which is similar to the theoretical one, exhibits its own specific features. Thus, the shift of the emission spectra peak at $E < 200$ V/cm for actual crystals is larger than the calculated one. This is related to the fact that the values of recombination parameters (L and τ) for the solid solutions investigated with $\nabla E_g <$ 200 V/cm are larger than those used in calculations [20]. The values of z^* for actual crystals are smaller than theoretical ones for $\nabla E_g > 200$ V/cm. The $z^*(E)$ dependence for the crystals studied weakens with an increase in E. The behavior of the $z^*(E)$ dependence is determined by a decrease in the recombination parameters upon an increase in the composition gradient, which is caused by degradation of the crystal structure [20, 21].

Thus, the experimental data obtained confirm the validity of the above theoretical consideration. For medium and high strengths of the built-in field, the short-wavelength region of the emission spectra for the graded-gap semiconductors is governed by the coordinate dependence of the radiative-recombination probability.

REFERENCES

1. Zh. I. Alferov, V. M. Andreev, V. I. Korol'kov, *et al.*, Fiz. Tekh. Poluprovodn. (Leningrad) **3** (2), 541 (1969) [Sov. Phys. Semicond. **3**, 460 (1969)].
2. G. V. Tsarenkov, Fiz. Tekh. Poluprovodn. (Leningrad) **13** (6), 1095 (1979) [Sov. Phys. Semicond. **13**, 641 (1979)].
3. R. G. Roedel and V. G. Keramidas, J. Appl. Phys. **50** (10), 6353 (1979).
4. V. F. Kovalenko, G. P. Peka, and L. G. Shepel', Fiz. Tekh. Poluprovodn. (Leningrad) **11**, 208 (1977) [Sov. Phys. Semicond. **11**, 1224 (1977)].
5. V. F. Kovalenko, G. P. Peka, and L. G. Shepel', Fiz. Tekh. Poluprovodn. (Leningrad) **12** (12), 1421 (1978) [Sov. Phys. Semicond. **12**, 839 (1978)].
6. V. F. Kovalenko, G. P. Peka, and L. G. Shepel', Fiz. Tekh. Poluprovodn. (Leningrad) **12** (9), 1851 (1978) [Sov. Phys. Semicond. **12**, 1099 (1978)].
7. A. I. Bazyk, V. F. Kovalenko, and G. P. Peka, Ukr. Fiz. Zh. **27** (11), 1728 (1982).
8. A. I. Bazyk, V. F. Kovalenko, G. P. Peka, *et al.*, Zh. Prikl. Spektrosk. **42** (10), 441 (1985).
9. A. I. Bazyk, V. F. Kovalenko, and G. P. Peka, Ukr. Fiz. Zh. **27** (7), 1007 (1982).
10. V. V. Gutov, A. N. Imenkov, R. F. Kazarinov, *et al.*, Pis'ma Zh. Tekh. Fiz. **1**, 386 (1975) [Sov. Tech. Phys. Lett. **1**, 184 (1975)].
11. V. V. Gutov, A. N. Imenkov, B. S. Kondrat'ev, *et al.*, Fiz. Tekh. Poluprovodn. (Leningrad) **13** (9), 1336 (1979) [Sov. Phys. Semicond. **13**, 782 (1979)].
12. R. F. Kazarinov and R. A. Suris, Fiz. Tekh. Poluprovodn. (Leningrad) **9** (1), 12 (1975) [Sov. Phys. Semicond. **9**, 6 (1975)].
13. R. F. Kazarinov and G. V. Tsarenkov, Fiz. Tekh. Poluprovodn. (Leningrad) **10** (2), 297 (1976) [Sov. Phys. Semicond. **10**, 178 (1976)].
14. O. V. Konstantinov and G. V. Tsarenkov, Fiz. Tekh. Poluprovodn. (Leningrad) **10** (4), 720 (1976) [Sov. Phys. Semicond. **10**, 427 (1976)].
15. V. F. Kovalenko, Avtometriya, No. 6, 54 (1980).
16. A. I. Bazyk, V. F. Kovalenko, A. I. Kurbangaleev, and G. P. Peka, Optoélektron. Poluprovodn. Tekh., No. 15, 42 (1989).
17. S. M. Ryvkin, *Photoelectric Effects in Semiconductors* (Fizmatgiz, Leningrad, 1963; Consultants Bureau, New York, 1964).
18. M. Konagai and K. Takahashi, Solid-State Electron. **19**, 259 (1976).
19. V. F. Kovalenko, G. P. Peka, and L. G. Shepel', Fiz. Tekh. Poluprovodn. (Leningrad) **14** (7), 1350 (1980) [Sov. Phys. Semicond. **14**, 798 (1980)].
20. F. P. Kesamanly, V. F. Kovalenko, I. E. Maronchuk, *et al.*, Fiz. Tekh. Poluprovodn. (Leningrad) **12** (7), 1318 (1978) [Sov. Phys. Semicond. **12**, 780 (1978)].
21. O. K. Gorodnichenko, N. K. Dryapiko, V. F. Kovalenko, and G. P. Peka, Ukr. Fiz. Zh. **27** (2), 267 (1982).

Translated by N. Korovin

Semiconductors, Vol. 35, No. 1, 2001, pp. 59–66. Translated from Fizika i Tekhnika Poluprovodnikov, Vol. 35, No. 1, 2001, pp. 58–64.
Original Russian Text Copyright © 2001 by Daunov, Kamilov, Gabibov.

ELECTRONIC AND OPTICAL PROPERTIES OF SEMICONDUCTORS

The Electronic Spectrum and Electrical Properties of Germanium with a Doubly Charged Gold Impurity on Both Sides of the $L_1 \rightleftarrows \Delta_1$ Intervalley Transition for Uniform Pressures of up to 7 GPa

M. I. Daunov, I. K. Kamilov*, and S. F. Gabibov

Institute of Physics, Dagestan Scientific Center, Russian Academy of Sciences, ul. 26 Bakinskikh Komissarov 94, Makhachkala, 367003 Russia

**e-mail: kamilov@datacom.ru*

Submitted June 8, 2000; accepted for publication June 16, 2000

Abstract—The dependences of resistivity ρ and the Hall coefficient $R < 0$ on hydrostatic pressure P ($P \le 7$ GPa) were studied at room temperature in Ge:(Au, Sb) with a partially populated (at 0 K) doubly charged Au level E_{Au}^{2-} on both sides of the intervalley transition that occurred for $P \cong 2.8$ GPa. In terms of the two-band model, the baric dependences ρ(P) and R(P) and also the similar dependence of the Hall mobility with allowance made for interband scattering were calculated; the results agree satisfactorily with the experimental data. Characteristic parameters of the charge carriers and the baric coefficients for energy gaps between the edges of the L_1 and Δ_1 subbands in the conduction band and the E_{Au}^{2-} level were determined. It was ascertained that the position of the energy level for a doubly charged gold impurity in germanium is fixed with respect to the valence-band top. The density-of-state effective mass of electrons in the (100) minimum of the conduction band of germanium was determined experimentally (and using the known values of the band parameters) and was found to be $m_{d\Delta} = 6^{2/3}(m_{\|} m_{\perp}^2)^{1/3} = 1.05m_0$. It is shown that Ge:Au^{2-} can be used to check the uniformity of pressure of up to 10 GPa. © *2001 MAIK "Nauka/Interperiodica".*

1. INTRODUCTION

In contrast to the theory of hydrogen-like impurities, the theory of deep-level impurity centers (regardless of their origin) is still in the initial stage of development [1–4]. Furthermore the rough approximations used and the suggested models "are rather far from reality" (quoted from [3]). It is known that, in a number of cases, the deep energy levels of certain centers are located near the edges of the allowed bands; because of this, it is difficult to discriminate between the deep- and shallow-level centers merely on the basis of their phenomenological description including the ionization energy, capture cross section, etc. under atmospheric pressure. Therefore, studies of changes in the energy spectrum of charge carriers in semiconductors exposed to an effective perturbing effect of uniform pressure (especially for the well studied model of Ge and Si monatomic semiconductors with multiply charged centers) are very topical.

However, baric dependences of the energy spectrum even in Ge and Si with deep-level centers have, nevertheless, been studied inadequately. Thus, for example, studies of Ge:Au [5] and Si:Au [6] were restricted to mere measurements of resistivity for pressures of up to 0.7 and 3 GPa, respectively. The values of the baric coefficients $d(E_{\mathrm{Au}}^{3-} - E_V)/dP = 29$ meV/GPa and $d(E_{\mathrm{Au}}^{2-} - E_V)/dP = 21$ meV/GPa for Ge:Au [5] and $d(E_{\mathrm{Cu}}^{3-} - E_V)/dP = 23$ meV/GPa and $d(E_{\mathrm{Cu}}^{2-} - E_V)/dP = 19$ meV/GPa for Ge:Cu [7] are seemingly indicative of the reduction of coupling to the valence band and, correspondingly, of an increase in the effect of the conduction band as the level approaches the conduction-band bottom (E_{Au}^{1-}, E_{Au}^{2-}, E_{Au}^{3-}, E_{Cu}^{2-}, and E_{Cu}^{3-} are the energy levels corresponding to singly, doubly, and triply charged Au impurity ions, and to doubly and triply charged Cu impurity ions; and E_V is the energy corresponding to the valence-band top). However, this inference (see, e.g., [7]) contradicts the data on the stabilization of the energy position for the deep-level acceptor with reference to the valence-band top in Si:Au^{1-} [6],

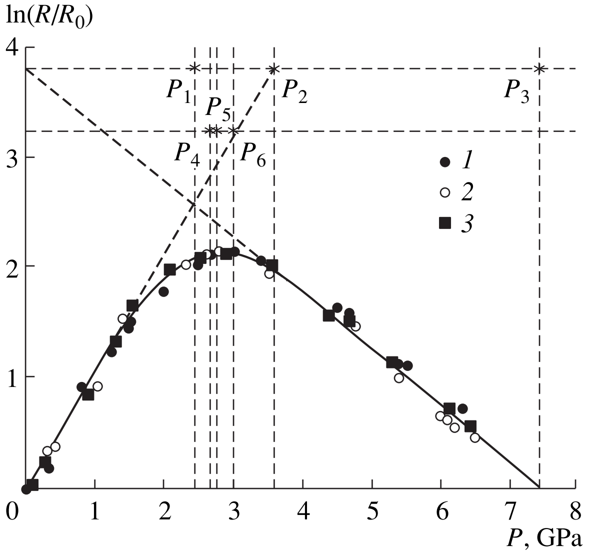

Fig. 1. The pressure dependence of the Hall coefficient (normalized to atmospheric pressure) at 295 K for samples *1–3*. The significance of the pressures $P_1 = L\beta^{*-1}$, $P_2 = L\beta^{*-1}_{Li}$, $P_3 = L\beta^{*-1}_{\Delta i}$, $P_4(n_{\min})$, $P_5(\Delta = 0)$, and $P_6(c = b)$ is clarified in Section 4.

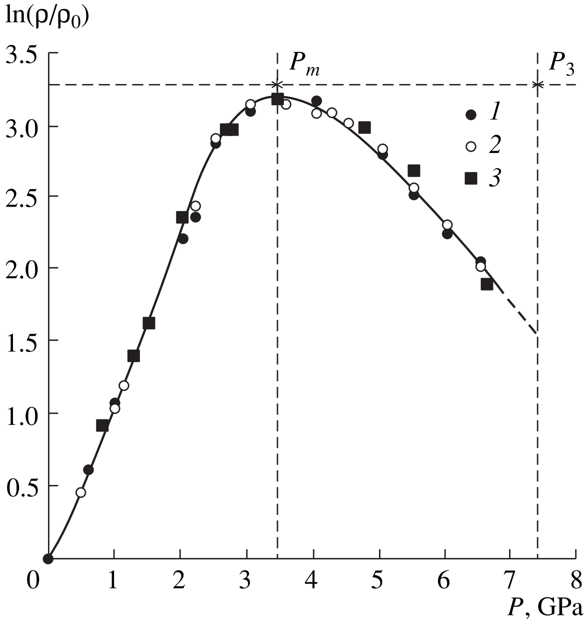

Fig. 2. The pressure dependence of resistivity (normalized to atmospheric pressure) at 295 K for samples *1–3*. The significance of pressures P_3 and $P_m(\rho)$ is clarified in Section 4.

InSb:Cr [8], *p*-InAs [9], InAs:Cr [10], $CdSnAs_2$:Cu [11–14], although, in the above-listed semiconductors (except for Si), the energies of the deep-level acceptor at atmospheric pressure are located in the vicinity of the conduction-band bottom. Studies of radiation defects which, as a rule, give rise to deep-level centers with small radius have shown that, under hydrostatic compression, the levels of these defects “respond” to valence bands in GaAS, InP, GaSb, $CdSnP_2$, and $ZnGeP_2$ [15].

It has been pointed out previously [13, 14] that it is important to study electron transport and the energy spectrum of charge carriers in Ge:(Au, Sb) subjected to a high pressure. It has been suggested [13, 14] that the influence of a large-scale fluctuation potential on the kinetic properties of Ge:(Au, Sb) at low temperatures under the conditions of hydrostatic compression is profound.

In this paper, we report the results of experimental studies of resistivity $\rho(P)$ and the Hall coefficient $R(P)$ measured at 295 K in Ge:(Au, Sb) crystals with the relation between the impurity concentrations $N(\mathrm{Au}) < N(\mathrm{Sb}) < 2N(\mathrm{Au})$ in the range of uniform pressures of up to $P = 7$ GPa (Figs. 1–3).

2. SAMPLES AND METHODS

The single-crystal Ge:(Au, Sb) ingot was grown by the Czochralski method and was doped simultaneously with two impurities of different types. There were two stages. In the first stage, the initial material was synthesized by fusing the weighed samples of dopants with germanium in the operating chamber of the Czochralski grower under excess argon pressure. In the second stage, the Ge:(Au, Sb) was grown in vacuum with a rate of 5 mm/h using a single-crystal seed oriented in the $\langle 111 \rangle$ direction.

Studies of electrical and optical properties under atmospheric pressure (see Fig. 4 and table) showed that we obtained an ingot with *n*-type conduction and that the relation between the impurity concentrations was $N(\mathrm{Au}) < N(\mathrm{Sb}) < 2N(\mathrm{Au})$; i.e., for this ingot, the Au level is partially occupied in the vicinity of 0 K and is located at a distance of $E^{2-}_{\mathrm{Au}} = 0.20 \pm 0.01$ eV from the bottom of the L_1 subband in the Ge conduction band. The obtained value of E^{2-}_{Au} is consistent with published data [5].

In order to produce pressure, we used a high-pressure setup comprising a flat anvil with a hole and toroidal support. The method for producing and varying the uniform pressure has been described previously [16]. A Teflon cell that contained the sample was filled with liquid and was then inserted into the opening of a catlinite gasket and was pressed with two hard-alloy plunger dies. As the pressure-transferring medium, we used the known 4 : 1 methanol–ethanol mixture [17] that was satisfactorily hydrostatic up to $P = 10$ GPa (see, e.g., [16]). However, in a recently published review devoted to experiments involving high pressure [18], it is pointed out that, at room temperature and pressures above 3 GPa, the commonly used organic liquids solidify.

In order to check the uniformity of the pressure, we measured $\rho(P)$ for pressures as high as 9 GPa for two identical single-crystal n-Ge samples with $\rho = 1.75\ \Omega$ cm at 300 K; the samples were positioned in a mutually perpendicular configuration in the measurement cell. Coincidence of the measured values of resistivity for a fixed pressure in both samples when the pressure was increased and decreased was indicative of the absence of uniaxial stresses observed previously in the range of 4–5 GPa when n-pentanisoamyl alcohol was used as the pressure-transferring medium [19]. In addition, the obtained data on the dependence $R(P)$ in Ge:Au with level E_{Au}^{2-} confirm the conclusion that the degree of uniformity of the pressure is satisfactory (see Section 4).

The high-pressure setup was installed inside a multiple-turn solenoid that generated magnetic fields as high as 5 kOe. In view of the fact that the solenoid was outside the high-pressure zone, the volume of 60 mm^3 of the measurement cell made it possible to use samples of optimal geometrical dimensions and employ the conventional methods for measuring R and ρ. The samples were treated by the known methods before measurements [5].

For studies under high pressures, we selected samples uniform in their electrical properties. The quantities R and ρ were measured using two pairs of probes (a pair for each quantity); the samples were in the shape of a rectangular parallelepiped with the ratio between the edge sizes being 1 : 2 : 5. The limiting relative errors in the measurements of electrical conductivity, the Hall coefficient, and the Hall mobility were 4, 2, and 5%, respectively. A maximum possible relative error in the measurements of resistivity and of the Hall coefficient at uniform pressure was no larger than 5%. The accuracy of measuring the relative variations in the kinetic coefficients with pressure was higher by more than an order of magnitude.

It is worth noting that the pressure coefficients β_{Li}, $\beta_{\Delta i}$, $m_{d\Delta}$, and other parameters were calculated from relative variations in kinetic coefficients in relation to pressure, which, obviously, significantly enhances the reliability of the estimates for these coefficients.

3. RESULTS

The results of measuring the uniform-pressure dependences of resistivity and the Hall coefficient in Ge:(Au^{2-}, Sb) are shown in Figs. 1 and 2. The following characteristic features are observed. First, the dependences $R(P)$ and $\rho(P)$ are exponential on both sides of the intervalley transition for $P_L < 1.5$ GPa and $P_\Delta > 4.5$ GPa; it is notable that $\Delta\ln((\rho/\rho_0)/\Delta P) \approx \Delta\ln((R/R_0)/\Delta P)$. Second, the maximum value of $\rho_m/\rho_0 \approx 25$ far exceeds the value $R_m/R_0 \approx 8.5$ at the extremum. Third, the pressure for which the maximum resistivity is observed $P_m(\rho)$ exceeds the value $P_m(R)$ for the Hall coefficient.

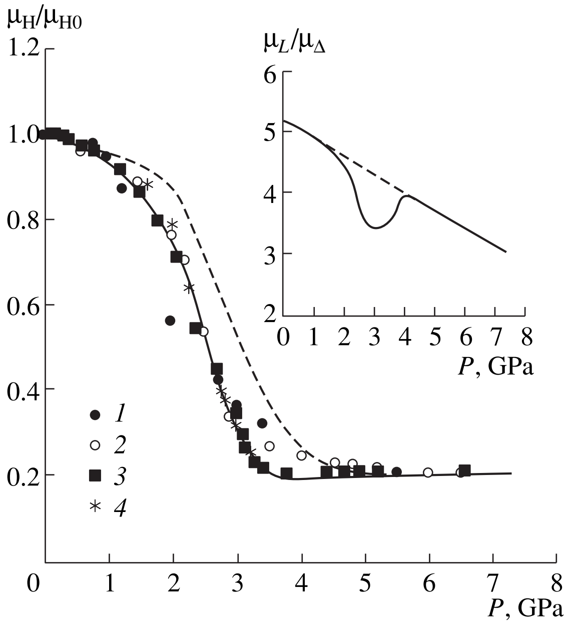

Fig. 3. The pressure dependences of the Hall mobility (normalized to atmospheric pressure) at 295 K for samples *1–3*. The calculated mobility ratio $b = \mu_L/\mu_\Delta$ as a function of pressure with (the solid line) and without consideration for interband scattering is shown in the inset. The dashed line is plotted for the case where the interband scattering is disregarded. The symbols ∗ (*4*) correspond to the results of calculations based on the theory [25] that accounts for the interband scattering.

The shapes of curves $\rho(P)$ and $R(P)$ are similar to those in n-Ge [19, 20]; for the pressures $P_L < 1.5$ GPa and $P_\Delta > 4.5$ GPa, the relative variations in ρ and R coincide. However, the extreme values of R and ρ are appreciably smaller for n-Ge: $R_m/R_0 = 1.5 \pm 0.1$ for $P_m(R) = (3 \pm 0.1)$ GPa and $\rho_m/\rho_0 = 5.3 \pm 0.1$ for $P_m(\rho) = (3.4 \pm 0.1)$ GPa in n-Ge with $\rho_0 = 1.5$–$12\ \Omega$ cm and electron concentration $n = 10^{14}$–10^{15} cm^{-3} at room temperature and under normal pressure.

Relative variations in the Hall mobility $\mu_{\mathrm{H}}(P)/\mu_{\mathrm{H}0}$ in n-Ge [20] and in Ge:Au^{2-} (Fig. 3) coincide. In the pressure range of 0–4 GPa, $\mu_{\mathrm{H}}/\mu_{\mathrm{H}0}$ decreases by a factor of 5; the rate of decrease is 4% per gigapascal for $P \le 1$ GPa and is 50% per gigapascal for $P = 2$–3 GPa. For $P > 4$ GPa, $\mu_{\mathrm{H}}/\mu_{\mathrm{H}0}$ increases with P only slightly; the rate is 0.6% per gigapascal.

4. DISCUSSION OF THE EXPERIMENTAL DATA

Obviously, the aforementioned special features of the baric dependences of kinetic coefficients are induced, on the one hand, by the intervalley transition at $P_5 = 2.8$ GPa (see below) and, on the other hand, by

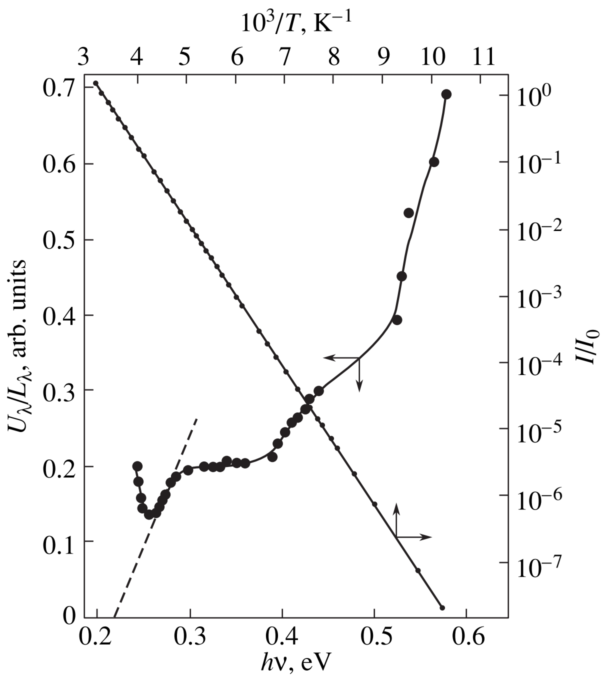

Fig. 4. Spectral distribution of photosensitivity at 90 K and the temperature dependence of the dark current (normalized to room temperature) at the atmospheric pressure for sample *3*.

the presence of the E^{2-}_{Au} Au energy level that is partially occupied at 0 K. In view of the latter fact and in contrast with *n*-Ge, the total concentration of electrons in the conduction band is not constant; rather, it first decreases with pressure up to $P_4 = 2.7$ GPa and then increases (Fig. 5). In addition, the interband scattering significantly affects the dependences $\rho(P)$ and $\mu_{\mathrm{H}}(P)$ in the vicinity of the intervalley transition (Fig. 3).

In order to determine the main parameters of charge carriers in terms of a two-band model, we calculated the baric dependences of kinetic coefficients using the following known formulas written as

$$\frac{R}{R_0} = \frac{R_n}{R_0}\frac{(b^2+c)(1+c)}{(b+c)^2}, \tag{1}$$

$$\frac{\rho}{\rho_0} = \frac{R_n}{R_0}\frac{1+c}{b+c}\frac{\mu_{L0}}{\mu_\Delta}, \tag{2}$$

$$\frac{\mu_{\mathrm{H}}}{\mu_{\mathrm{H0}}} = \frac{b^2+c}{b+c}\frac{\mu_\Delta}{\mu_{L0}}, \tag{3}$$

where $b = \mu_L/\mu_\Delta$, $c = n_L/n_\Delta$ (n_L and n_Δ are the electron concentrations in the valleys L_1 and Δ_1, and μ_L and μ_Δ are the corresponding mobilities), $R_n = [(n_L + n_\Delta)e]^{-1}$, and e is the elementary charge. The subscript “0” indicates that a parameter is measured at atmospheric pressure. It was assumed that the ratio of Hall factors $r/r_0 = 1$.

We use the Gibbs distribution as applied to Ge:Au^{2-}. We have

$$n_L = n_{L0}\exp(-\beta^*_{Li}P)\frac{k}{k_0},$$
$$n_\Delta = n_{\Delta 0}\exp(\beta^*_{\Delta i}P)\frac{k}{k_0}, \tag{4}$$
$$k = \frac{N(\mathrm{Sb}) - N(\mathrm{Au}) - n}{2N(\mathrm{Au}) - N(\mathrm{Sb}) + n} = \frac{N^{2-}_{\mathrm{Au}}}{N^{1-}_{\mathrm{Au}}}.$$

Here, $\beta^*_{Li} = \beta_{Li}/k_{\mathrm{B}}T = \partial(E_{CL} - E^{2-}_{\mathrm{Au}})/\partial P$ and $\beta^*_{\Delta i} = \beta_{\Delta i}/k_{\mathrm{B}}T = |\partial(E_{C\Delta} - E^{2-}_{\mathrm{Au}})|/\partial P$ are the reduced baric coefficients for the edges of L_1 and Δ_1 bands with respect to the level E^{2-}_{Au}, k_{B} is the Boltzmann constant, T is the absolute temperature, and $n = n_L + n_\Delta$.

It was found (Figs. 1, 2) that, for pressures of $P_L < 1.5$ GPa and $P_\Delta > 4$ GPa, electrical conductivity is controlled by electrons from the L_1 and Δ_1 bands, respectively. Therefore, for $R_L = R_\Delta$, it follows from (1) and (4) that

$$P_\Delta = L/\beta^*_{\Delta i} - (\beta_{Li}/\beta_{\Delta i})P_L = 7.45 - 2.1P_L. \tag{5}$$

Here, $L = \Delta^*_0 = \ln(N_{C\Delta}/N_{CL})$, where Δ_0 is the intervalley energy gap, and $N_{C\Delta}$ and N_{CL} are the effective density of states in the corresponding valleys. It follows from (5) and experimental data (Fig. 1) that $P_1 = L/\beta^* = 2.4$ GPa ($\beta^* = \beta^*_{Li} + \beta^*_{\Delta i} = \partial(\Delta_0/k_{\mathrm{B}}T)/\partial P$), $P_2 = L/\beta^*_{Li} = 3.55$ GPa, and $P_3 = L/\beta^*_{\Delta i} = 7.45$ GPa. We now use the known values $\Delta_0 = 0.18$ eV and $\beta = 65$ meV/GPa [3, 19]. As a result, we obtain $\beta_{Li} = 44$ meV/GPa, $\beta_{\Delta i} = 21$ meV/GPa, $c = \exp[\beta^*(P - L/\beta^*)] = \exp[2.55(P - 2.4)]$ (at $T = 295$ K and for P expressed in gigapascals), and $N_{C\Delta}/N_{CL} = 2.65$. Using the known density-of-state effective mass of electrons in the L_1 band $m^*_{dL} = 4^{2/3}(m_\parallel m^2_\perp)^{1/3} = 0.55m_0$ [22] and the obtained value of the ratio $N_{C\Delta}/N_{CL}$, we determine the density-of-state effective mass in the Δ_1 band as $m_{d\Delta} = 6^{2/3}(m_\parallel m^2_\perp)^{1/3} = 1.05m_0$. The value of $m_{d\Delta}$ obtained for the first time experimentally is consistent with the value calculated by Cardona and Pollak [23] and with the density-of-state effective mass of electrons in Si [24].

In order to estimate $N(\mathrm{Au})$ and $N(\mathrm{Sb})$, we used the linearizing transformation

$$\frac{(k/k_0)(n/n_0)-1}{(k/k_0)-1} = \frac{1}{k_0}\frac{1-(n/n_0)}{(k/k_0)-1} - \frac{2N(\mathrm{Au})-N(\mathrm{Sb})}{n_0} \qquad (6)$$

in combination with the method of least squares. In this manner, we determined the parameters k_0^{-1} and $[2N(\mathrm{Au}) - N(\mathrm{Sb})/n_0^{-1}$. For the samples studied, we obtained $N(\mathrm{Sb}) = (8 \pm 0.5) \times 10^{15}$ cm^{-3}, $N(\mathrm{Au}) = (4.2 \pm 0.4) \times 10^{15}$ cm^{-3}, and the occupancy of the E_{Au}^{2-} level $[N(\mathrm{Sb}) - N(\mathrm{Au})]/N(\mathrm{Au}) \cong 0.9$ at $T \longrightarrow 0$.

Figures 3 and 5 show the result of estimations of $b(P)$, $n(P)$, and $k(P)$.

In addition to P_1, P_2, and P_3 (Fig. 1), critical points also include the pressure $P_4 = 2.7$ GPa where n is at a minimum and, correspondingly, k is maximal (Fig. 5); the pressure corresponding to the intervalley transition $P_5 = \Delta_0/\beta = 2.8$ GPa, which coincides with $P_m(R)$; the pressure $P_6 \cong 3$ GPa where $c = b$ and R/R_n is at the extremum; and, finally, the pressure $P_m(\rho) = 3.3$–3.4 GPa where the resistivity attains a maximum (Fig. 2). The pressure P_4 was determined from the value of the ratio between concentrations $n_\Delta/n_L = \beta_L/\beta_\Delta = 2.1$ (5), where $\partial n/\partial P = \partial k/\partial P = 0$.

It is known [25] that in Ge, under the conditions of energetic proximity of the (111) and (100) minimums, the interband mechanism of electron scattering related to the exchange of charge carriers between nonequivalent minimums is important. Following Nathan *et al.* [25], we obtain the following expression for the pressure that corresponds to the intervalley transition:

$$1 + S = \frac{(\mu_L^*/\mu_{L0}^*)}{(\mu_{\mathrm{H}}/\mu_{\mathrm{H}0})}\frac{b^2+c}{b(b+c)} = \frac{(\mu_L^*/\mu_{L0}^*)(\rho/\rho_0)}{(R_n/R_0)}\frac{(b+c)}{(1+c)b}, \qquad (7)$$

$$(1 + S') = \frac{(\mu_\Delta^*/\mu_{\Delta 0})}{(\mu_{\mathrm{H}}/\mu_{\mathrm{H}0})}\frac{(b^2+c)}{b_0(b+c)} = \frac{(\mu_\Delta^*/\mu_{\Delta 0})(\rho/\rho_0)}{(R_n/R_0)}\frac{(b+c)}{b_0(1+c)}. \qquad (8)$$

The parameters S and S' define the relative intensity of intervalley scattering compared to the intraband scattering for the bands L_1 and Δ_1, respectively. The quantities μ_L^*/μ_{L0}^* and $\mu_\Delta^*/\mu_{\Delta 0}^*$ define the contribution of mechanisms that are unrelated to interband scattering to the pressure dependences of μ_L/μ_{L0} and $\mu_\Delta/\mu_{\Delta 0}$. According to [25], $\mu_L^*/\mu_{L0}^* = 1$–$4 \times 10^{-2} P$ (in GPa). In accordance with obtained data (Fig. 3) and with the pressure dependence of $\mu_\Delta/\mu_{\Delta 0}$ in n-Si as reported previously [26], we have $\mu_\Delta^*/\mu_{\Delta 0}^* = 1 + 3 \times 10^{-2} P$ (in GPa). It was mentioned above that the baric dependences of normalized Hall mobility are the same in n-Ge [20] and Ge:Au^{2-}.

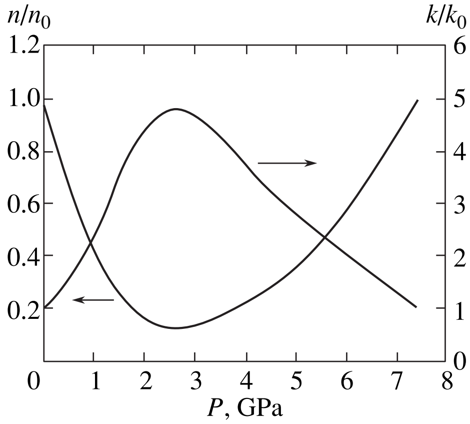

Fig. 5. The calculated pressure dependences of the parameters $n = n_L + n_\Delta$ and $k = N_{\mathrm{Au}}^{2-}/N_{\mathrm{Au}}^{1-}$ (normalized to the atmospheric pressure) for sample 3 at 295 K.

The value of $c(P)$ is known; thus, we used (7) and (8) and the above reasoning to determine the parameters b at the point of intervalley transition, b_0, S, and S'. Almost the same value of the mobility ratio b was obtained at the extreme point of the dependence $R(P)$ in n-Ge [18]. The data on $b(P)$ are shown in Fig. 3. For the parameters S and S', we have $S = 0.53$ and $S' = 0.26$, which corresponds to a decrease in μ_L by a factor of 1.53 and in μ_Δ by a factor of 1.26 due to interband scattering in the energetic vicinity of the minimums (111) and (100).

The dependence $\rho(P)$ in n-Ge has been used previously [19] to obtain $S = 3.8$ and $S' = 0.24$, which implies a decrease in μ_L by about a factor of 5 as the pressure varies from atmospheric pressure to that corresponding to the intervalley-transition point. In this case, according to (7), the ratio of mobilities is $b \cong 1$. This result is inconsistent with profound dependence $R(P)$ in n-Ge. As mentioned above, an extremum is observed in n-Ge [20] in the vicinity of 3 GPa, so that $R_m = R_0 \cong 1.5$, rather than $R_m = R_0 \cong 1$ (for $b \cong 1$). The fallacy of the results of the qualitative analysis [19] was caused by the fact that the pressure corresponding to the extre-

Parameters of the studied Ge:(Au, Sb) samples with Au^{2-} at $T = 295$ K and atmospheric pressure

Sample no.	$-R$, cm^3/C	ρ, Ω cm	$\lvert R\rvert/\rho$, cm^2/(V s)
1	4198	4.94	850
2	4009	4.40	912
3	3800	3.90	974

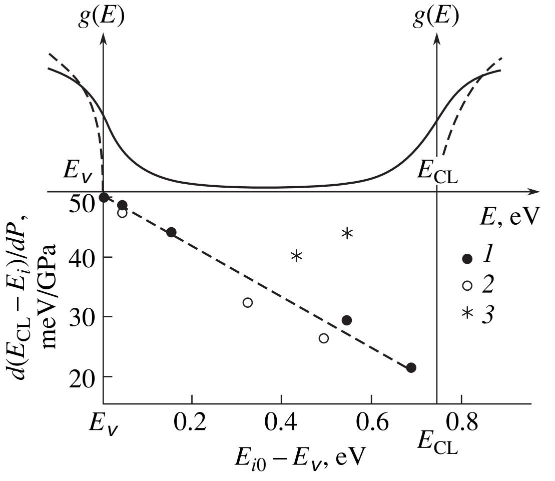

Fig. 6. A schematic representation of the density of states $g(E)$ in heavily doped compensated germanium [27] and the baric coefficient for Au levels according to (*1*) [5] and (*3*) the results of this study and (*2*) for Cu levels according to [7].

mum $P_m(\rho)$ in the dependence $\rho/\rho_0(P)$ was identified with that corresponding to the intervalley transition; i.e., an increase in the factor $(1 + c)/(b + c)$ with increasing pressure in (2) and the transfer of electrons from the L_1 to Δ_1 minimums were ignored. Thus, the role of interband scattering of the L_1 band electrons was overestimated. Cardona and Pollak [25] quantitatively analyzed the dependence $\rho(P, T)$ in *n*-Ge and concluded that the parameter S in *n*-Ge decreases with decreasing temperature, and agreement between theory and experiment was observed for $S < 1$ at 295 K.

In conclusion, we discuss a basic problem concerning the mechanism of the effect of uniform pressure on the level E^{2-}_{Au}. The obtained values of baric coefficients β_{Li} = 44 meV/GPa and $\beta_{\Delta i}$ = 21 meV/GPa almost coincide with the corresponding values of baric coefficients for the band gap both in Ge [21] and in Si [26]; it is worth noting that the coefficient $\beta_{\Delta i}$ for Ge:Au^{2-} is determined in this study for the first time.

However, the published data on baric coefficients β_{Li} for the energy levels of multiple-charged centers of gold [5] and copper [7] in Ge:Au^{2-} (Fig. 6) seem to indicate that these coefficients decrease as the level moves away from the valence-band top; i.e., this indicates that coupling to the valence band weakens.

There are two factors leading to an underestimation of the value of the above coefficients determined from the baric dependence of the charge-carrier concentration. First of all, this is related to the necessity of using the Gibbs statistics. In the expression for the charge-carrier concentration, there appears a multiplier (k in (4) for the doubly charged Au level in Ge) dependent on the level occupancy. The value of this multiplier increases with increasing P for fixed temperature and pressure lower than that corresponding to the intervalley transition $P_5 \cong 2.8$ GPa, whereas the electron concentration decreases (Fig. 5). Typically, it is assumed [7] that, if, in the approximation $n \sim \exp(-E_i/kT)$, the value of E_i obtained from the slope of the dependence $\ln n(10^3/T)$ is approximately equal to the activation energy for the impurity center, the parameter k may be considered constant. However, we also have $n_L \sim T^{3/2}$, so that an increase in temperature is compensated by a decrease in $k(T)$. For a fixed temperature, an increase in k with pressure weakens appreciably the dependence $n_L(P)$. Quantitative analysis of the obtained experimental data (Figs. 1, 4) and the data reported elsewhere [7] showed that the error arising in this case (the underestimation of the baric coefficient) is comparable to the corresponding value.

The above reasoning was taken into account in [5], and the baric measurements were carried out at low temperatures in order to obtain reliable results for Ge:Au. However, in doped and compensated germanium, the low-solubility impurities (such as Au, Hg, and Cu) form clusters with a high degree of probability. The same effect is observed if *n*-Ge is compensated as a result of irradiation with fast neutrons [27]. As a result of compensation, a large-scale potential relief is formed at low temperatures for low concentrations of charge carriers. Precisely this reasoning was used to interpret the observed anomalies in the temperature dependences $R(T)$ and $\rho(T)$ in *n*-Ge:Au with a triple-charged Au level at low temperatures [28] and in $\mu_L(T)$ in *n*-Ge:Cu with a triple-charged Cu level at $T \le 290$ K [7]. For a fixed low temperature, as the pressure increases, the charge-carrier concentration decreases, the effect of screening the random potential by free charge carriers becomes less profound, and, correspondingly, increases the amplitude of the random potential. As a result, a pronounced fluctuational bending of the bands appears, which increases with pressure, for the limiting density of states illustrated in Fig. 6. If there is a deep level of impurity center in the band gap, a transition to the state of heavily doped and completely compensated semiconductor [11–14] would be observed, in which case the random variations in potential energy attain values comparable to the activation energy of charge carriers at the impurity centers. This inevitably leads to an underestimation of the baric coefficients for energy gaps determined from the baric dependences of electron concentration as in [5]. In this study, due to the attainment of sufficiently high pressures that made it possible to measure the kinetic coefficients on both sides of the intervalley transition and to a high fixed temperature (295 K), we managed to avoid the errors caused by the effects of the occupancy of the deep level and the random potential.

5. CONCLUSION

(i) According to the aforementioned results and the published data [6–11, 15, 21, 29–32] related to the values of baric coefficients for energy gaps between the deep levels of acceptor and donor impurity centers and the band edges in semiconductors, the absolute values of energies of these states with respect to the vacuum depend only slightly on pressure. These energies are fixed relative to the edges of the bands whose position under the effect of pressure also varies only slightly with respect to a vacuum. This is due to the fact that the effect of hydrostatic compression on the energy of deep-level impurity states depends on the pressure-induced shift of the entire structure of the energy spectrum, rather than of a small portion of it. Therefore, it is necessary to take into account the contribution of not only the nearest bands to the formation of the wave function of a deep-level impurity center but also the effect of remote energy bands.

(ii) The Ge:Au^{2-} crystals can be used to check the degree of uniformity of the pressure up to 10 GPa. Linear extrapolations of $\ln R(P)$ from the regions of low and high pressures on both sides of the intervalley transition $L_1 \rightleftarrows \Delta_1$ for satisfactory degree of the pressure uniformity should intersect at the pressure of $P_1 = L/\beta^* = 2.3$ GPa defined by the known values of $N_{C\Delta}/N_{CL}$, Δ_0, and β^*. Thus, the study of germanium, a model material in semiconductor physics, shows that the current level of the high-pressure methods makes it possible to perform precise measurements of kinetic characteristics of semiconductor crystals in relation to uniform pressure as high as 10 GPa in a magnetic field and use the obtained data for not only qualitative inferences but also for estimations of characteristic and energy-band parameters.

Some of the results of this study were presented at conferences [33, 34].

ACKNOWLEDGMENTS

We are grateful to R.K. Arslanov for his participation in the measurements and to R.Kh. Akchurin for the preparation of the single-crystal Ge:(Au, Sb) ingot.

This study was supported by the Russian Foundation for Basic Research, project nos. 97-02-16545 and 99-02-17280.

REFERENCES

1. L. V. Keldysh, Zh. Éksp. Teor. Fiz. **45**, 364 (1963) [Sov. Phys. JETP **18**, 253 (1963)].
2. K. B. Tolpygo, Fiz. Tverd. Tela (Leningrad) **11**, 2846 (1969) [Sov. Phys. Solid State **11**, 2304 (1970)].
3. V. A. Telezhkin and K. B. Tolpygo, Fiz. Tekh. Poluprovodn. (Leningrad) **16**, 1337 (1982) [Sov. Phys. Semicond. **16**, 857 (1982)].
4. I. M. Tsidil'kovskiĭ, *The Concept of Effective Mass* (Ural. Otd. Ross. Akad. Nauk, Yekaterinburg, 1999).
5. M. G. Holland and W. Paul, Phys. Rev. **128**, 43 (1962).
6. M. I. Nathan and W. Paul, Phys. Rev. **128**, 38 (1962).
7. É. G. Pel', V. I. Fistul', A. Yagshygel'dyev, and A. G. Yakovenko, Fiz. Tekh. Poluprovodn. (Leningrad) **14** (6), 1220 (1980) [Sov. Phys. Semicond. **14**, 721 (1980)].
8. V. V. Popov, M. L. Shubnikov, S. S. Shalyt, and V. V. Kosarev, Fiz. Tekh. Poluprovodn. (Leningrad) **11**, 1914 (1977) [Sov. Phys. Semicond. **11**, 1120 (1977)].
9. M. I. Daunov, I. K. Kamilov, A. B. Magomedov, and A. Sh. Kirakosyan, Fiz. Tekh. Poluprovodn. (St. Petersburg) **33** (1), 36 (1999) [Semiconductors **33**, 31 (1999)].
10. A. Plitnikas, A. Krotkus, L. A. Balagurov, and É. M. Omel'yanovskiĭ, Fiz. Tekh. Poluprovodn. (Leningrad) **14**, 2123 (1980) [Sov. Phys. Semicond. **14**, 1262 (1980)].
11. M. I. Daunov, A. B. Magomedov, and V. I. Danilov, Fiz. Tekh. Poluprovodn. (Leningrad) **25** (3), 467 (1991) [Sov. Phys. Semicond. **25**, 282 (1991)].
12. I. K. Kamilov, M. I. Daunov, V. A. Elizarov, and A. B. Magomedov, Zh. Éksp. Teor. Fiz. **104** (1), 2436 (1993) [JETP **77**, 92 (1993)].
13. M. I. Daunov, I. K. Kamilov, and A. B. Magomedov, Zh. Éksp. Teor. Fiz. **111** (2), 562 (1997) [JETP **84**, 309 (1997)].
14. M. I. Daunov, I. K. Kamilov, V. A. Elizarov, *et al.*, Dokl. Akad. Nauk **357** (5), 612 (1997) [Phys. Dokl. **42**, 657 (1997)].
15. V. N. Brudnyĭ, Izv. Vyssh. Uchebn. Zaved., Fiz. **29** (8), 84 (1986).
16. L. G. Khvostantsev and V. A. Sidorov, Phys. Status Solidi A **46**, 305 (1978).
17. G. J. Piermani, S. Block, and J. D. Barnett, J. Appl. Phys. **44** (12), 5377 (1973).
18. E. S. Itskevich, Prib. Tekh. Éksp., No. 3, 6 (1999).
19. A. Dzhaĭyaraman and B. Kositskiĭ, in *Proceedings of the IX International Conference on Semiconductors, Moscow, 1968*, Vol. 1, p. 51.
20. M. I. Daunov, A. Yu. Mollaev, R. K. Arslanov, *et al.*, in *Abstracts of VIII International Conference on High Pressure Semiconductor Physics, Thessaloniki, Greece, 1998*, p. 97.
21. *Solids Under Pressure*, Ed. by W. Paul and D. Warschauer (McGraw-Hill, New York, 1963; Mir, Moscow, 1966), Chap. 8.
22. B. Levinger and L. Frankl, J. Phys. Chem. Solids **20**, 281 (1961).
23. F. Pollak and M. Cardona, Phys. Rev. **142**, 530 (1966).
24. M. R. Samuelsen, Phys. Status Solidi B **43**, K83 (1971).
25. M. I. Nathan, W. Paul, and H. Brooks, Phys. Rev. **124**, 391 (1961).
26. M. J. Holland and W. Paul, Phys. Rev. **128** (1), 30 (1962).

27. A. R. Gadzhiev, S. M. Ryvkin, and I. S. Shlimak, Pis'ma Zh. Éksp. Teor. Fiz. **15**, 605 (1972) [JETP Lett. **15**, 428 (1972)].
28. V. S. Vavilov, A. M. Idalbaev, I. A. Kurova, and A. Enrikes, Fiz. Tekh. Poluprovodn. (Leningrad) **2**, 407 (1980) [Sov. Phys. Semicond. **14**, 239 (1980)].
29. M. I. Daunov, A. Yu. Mollaev, R. K. Arslanov, *et al.*, Available from VNITI, No. 2038.V.96 (1996); Izv. Vyssh. Uchebn. Zaved. Fiz., No. 12, 128 (1996).
30. M. I. Daunov, A. Yu. Mollaev, R. K. Arslanov, and L. A. Saypulaeva, in *Proceedings of 7th International Conference on High Pressure Semiconductor Physics, Gemany, 1996*, p. 23.
31. E. P. Skipetrov, B. B. Kovalev, L. A. Skipetrova, and E. A. Zvereva, Phys. Status Solidi B **211**, 539 (1999).
32. I. M. Tsidil'kovskiĭ, in *Electron Spectrum of Zero-Gap Semiconductors* (Ural. Otd. Ross. Akad. Nauk, Sverdlovsk, 1991).
33. R. K. Arslanov, S. F. Gabibov, M. I. Daunov, *et al.*, in *Proceedings of XXXVII of the European High Pressure Research Group Meeting, Monpellier, France, 1999*, P1–04.
34. M. I. Daunov, I. K. Kamilov, R. Kh. Akchurin, *et al.*, in *Proceedings of the IV Russian Conference on Physics of Semiconductors, Novosibirsk, 1999*, p. 84.

Translated by A. Spitsyn

Semiconductors, Vol. 35, No. 1, 2001, pp. 67–71. Translated from Fizika i Tekhnika Poluprovodnikov, Vol. 35, No. 1, 2001, pp. 65–69.
Original Russian Text Copyright © 2001 by Ageeva, Bronevoĭ, Krivonosov.

ELECTRONIC AND OPTICAL PROPERTIES OF SEMICONDUCTORS

Distribution of Electrons between Valleys and Band-Gap Narrowing at Picosecond Superluminescence in GaAs

N. N. Ageeva, I. L. Bronevoĭ*, and A. N. Krivonosov

Institute of Radio Engineering and Electronics, Russian Academy of Sciences, ul. Mokhovaya 18, Moscow, 103907 Russia
** e-mail: bil@mail.cplire.ru*

Submitted June 13, 2000; accepted for publication June 16, 2000

Abstract—Band-gap narrowing due to photogeneration of dense hot electron–hole plasma in GaAs was studied. Plasma was generated by picosecond light pulses, and picosecond superluminescence was observed. In this case, the total concentration of photogenerated electron–hole pairs was experimentally proved to be the sole parameter controlling the electron distribution between Γ_6 and L_6 valleys and the corresponding band-gap narrowing. This was explained by the fact that the carrier temperature and concentration are correlated in the presence of superluminescence. *© 2001 MAIK "Nauka/Interperiodica".*

This study is dedicated to band-gap E_g variation with the concentration ($>10^{18}$ cm^{-3}) and temperature ($\geq$300 K) of electron–hole plasma (EHP). The EHP was produced by interband absorption of a high-power 14-ps pulse of excitation light in a thin GaAs layer. This investigation continues the study [1, 2] of integral (over time) spectra of picosecond superluminescence. By this is meant enhanced spontaneous emission in an active GaAs medium without a resonator, with this emission arising during dense EHP generation and quenching with a characteristic time of about 10 ps as the exciting pulse decays.

The dependence of E_g on carrier concentration appeared too weak at high concentrations. We relate this to the EHP temperature growth with concentration under the superluminescence condition. An increasing fraction of electrons appears in the L_6 valley, whereas band-gap narrowing is controlled mainly by electrons of the Γ_6 valley. Comparison of experimental and calculated data confirms this assumption.

Another consequence of the electron redistribution between valleys is related to features in the dependence of the superluminescence integral energy on the exciting photon energy (see [3]). These special features were interpreted as recombination-superluminescence enhancement due to stimulated Raman scattering of the exciting light by coupled plasmon–phonon oscillations. Emission of a quantum of these oscillations enhances the probability of electron transition from a state before excitation to a state corresponding to superluminescence. The energy of a plasmon–phonon oscillation quantum determined on this assumption conforms to electron redistribution between valleys during superluminescence.

Variations in the GaAs band gap E_g were reported in many publications (see, for example [4–10]), where the carrier temperature did not exceed 300 K, and conduction-band electrons were considered as concentrated in the Γ_6 valley. To our knowledge, the problem has not been studied previously.

In this study, experiments were carried out at room temperature. The sample was an $Al_{0.22}Ga_{0.78}As$–GaAs–$Al_{0.4}Ga_{0.6}As$ heterostructure with layer thicknesses 1.3–1.5–1.2 μm, respectively, grown by the molecular-beam epitaxy on a (100) GaAs substrate. The background impurity concentration in the heterostructure was lower than 10^{15} cm^{-3}. The substrate was etched off at an area of 4 × 4 mm^2. The $Al_xGa_{1-x}As$ layers intended to stabilize surface recombination and mechanical strength did not absorb light with $\hbar\omega <$ 1.7 eV, which was used in the experiment. A two-layer SiO_2/Si_3N_4 antireflective coating was applied to the sample, due to which reflection of light incident normally to the surfaces did not exceed 2% under the experimental conditions. The sample was irradiated with high-power exciting pulses 14 ps long, incident at an angle of 10° to the normal. The light intensity distribution over the exciting beam cross section was approximately Gaussian. Interband absorption of exciting light and corresponding EHP generation proceeded only in the GaAs layer. Superluminescence spectra (integrated over time) of emission radiating inside a solid angle of about 4° were measured according to the technique described in [11]. The angle axis coincided with the normal to epitaxial layers, drawn from the excited region. Such a technique allows measurement of a superluminescence-emission fraction outgoing from the sample due to imperfection in its waveguide properties [1, 2].

The GaAs emission spectra were measured at exciting pulse parameters varied in the following ranges: the photon energy $\hbar\omega_{ex}$ = 1.423–1.528 eV; the beam diameter (at half-maximum) F = 0.2–0.7 mm; and the density of pulse integral energy, averaged over the irradi-

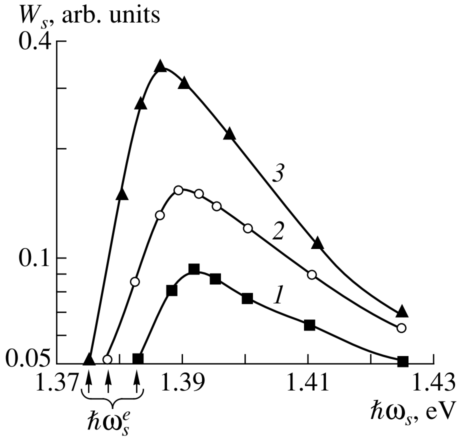

Fig. 1. GaAs emission spectra for the excitation-beam diameter $F = 0.35$ mm and the pulse energy density (averaged over the beam cross section) $D_{\text{ex}} = 2.5$, 2.5, and 7.4 arb. units and $\hbar\omega_{\text{ex}} = 1.455$, 1.485, and 1.455 eV (*1–3*, respectively). Arrows indicate the long-wavelength edge position $\hbar\omega_s^e$.

ated GaAs layer area, $D_{\text{ex}} = 1$–25 rel. units. Variation in excition-pulse parameters was obviously accompanied by variations in the EHP concentration and temperature. According to the estimates [12], the superluminescence intensity can be as high as ~10^8 W/cm^2, while lattice heating can be neglected at the experimental conditions used.

The typical time-integrated spectra $W_s = f(\hbar\omega_s)$ of GaAs emission are shown in Fig. 1 on the semilogarithmic scale, where W_s is the time-integrated energy of light with photon energy $\hbar\omega_s$. It is evident that the spectrum long-wavelength falloff and peak are shifted to the longer wavelength as the area under the curve increases, i.e., as the integral (over the spectrum) energy grows. This was also observed previously [1, 2].

This shift reflects the band gap E_g narrowing. The long-wavelength spectrum slope and its edge position can be approximated by an exponential and by the photon energy $\hbar\omega_s^e$, respectively. For this photon energy, the exponential crosses a fixed energy level somewhat exceeding zero (by 0.05 arb. units in Fig. 1). This level in various spectra was chosen so that it corresponded to the same emission-energy density averaged over a GaAs layer area irradiated with exciting light. Below this level, as the emission energy approached zero, the long-wavelength slope deviation from the exponential increased, which is conventionally explained by the impact of impurities. An analogous method for determining the spectrum edge $\hbar\omega_s^e$ was employed in [6, 9].

It was found that, as excitation-pulse parameters (see table in Fig. 2) were varied, the photon energy $\hbar\omega_s^e$ varied approximately as a unified function of the energy density D_s integrated over the emission spectrum and averaged over the irradiated GaAs layer area (see Fig. 2). To explain the observed dependence $\hbar\omega_s^e(D_s)$, we reasonably assume the emission density D_s to be approximately proportional to the concentration of photogenerated electron–hole pairs,

$$D_s \sim p = n = n_\Gamma + n_L, \tag{1}$$

where p is the total concentration of heavy and light holes; n, n_Γ, and n_L are the total electron concentration and the concentration in valleys Γ_6 and L_6, respectively. Then the dependence $\hbar\omega_s^e(D_s)$ can be assumed to reflect the long-wavelength edge shift caused by the band gap E_g narrowing as the EHP concentration grows.

Usually, electrons can be heated to various temperatures at a fixed total concentration n. The EHP temperature and the carrier concentration are related in the presence of superluminescence. In this case, the carrier energy distribution is close to the threshold one [13, 14], at which the distance between the electron and hole quasi-Fermi levels μ_e and μ_h is equal to the band gap:

$$\mu_e - \mu_h = E_g. \tag{2}$$

In this approximation, the electroneutrality condition $n_\Gamma + n_L = p$ and the temperature dependence of the electron distribution between the Γ_6 and L_6 valleys [15] allow the electron concentrations n and n_Γ to be determined in relation to the EHP temperature (Fig. 3).

The band-gap narrowing ΔE_g proceeds due to the Coulomb interaction between carriers [9, 16]. Estimations by formulas [17] showed the contribution of the correlation energy to the band-gap narrowing to be small in the range shown in Fig. 2. Then, taking into account only the exchange energy,

$$\Delta E_g = 4/3(E_{\text{ex}}^e + E_{\text{ex}}^h), \tag{3}$$

where E_{ex}^e and E_{ex}^h are the electron (e) and hole (h) exchange energies, we obtain

$$\begin{aligned} E_{\text{ex}}^e &= -3e^2(3\pi^2 n_\Gamma)^{1/3}/4\pi\varepsilon, \\ E_{\text{ex}}^h &= -3e^2\eta(3\pi^2 p)^{1/3}/4\pi\varepsilon. \end{aligned} \tag{4}$$

Here, e is the elementary charge, $\varepsilon = 12.85$ is the static dielectric constant, and $\eta = 0.73$ is the coefficient accounting for “attachment” of light and heavy holes [18].

The dependence $E_g = E_{g0} + \Delta E_g(n)$ calculated by formulas (3) and (4) and relied on an insignificant contribution of the correlation energy approximately coincided with the dependence $\hbar\omega_s^e(D_s)$ (see Fig. 2), thus confirming the above interpretation of the latter. To fit the calculated dependence to the experimental one, it was assumed that $E_g = \hbar\omega_s^e = 1.382$ eV for $n \approx 1.32 \times 10^{18}$ cm^{-3}. Then $E_g = 1.407$ eV, which conforms to the photon energy of the long-wavelength edge of the emission spectrum for “unexcited” GaAs [15, 19]. The agreement between calculation and experiment was achieved without considering the exchange energy variation with temperature, as in [4, 9]. This seemingly does not introduce substantial errors under the given conditions when electrons are degenerate and the hole state is intermediate between the degenerate state and that defined by the Boltzmann statistics.

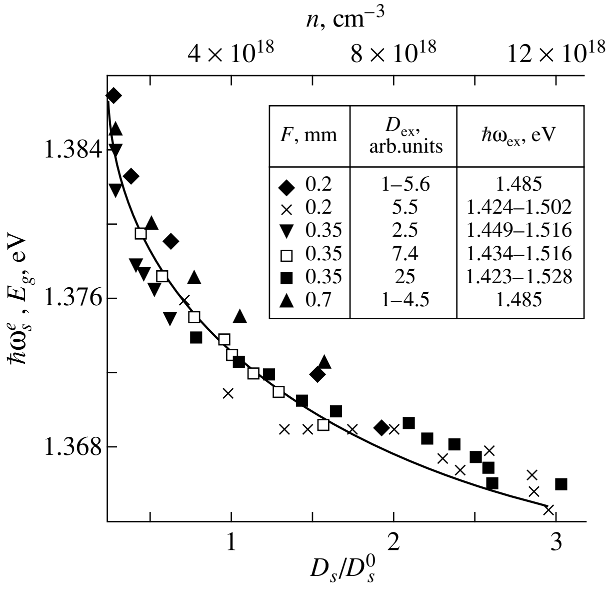

F, mm	D_{ex}, arb.units	$\hbar\omega_{ex}$, eV
◆ 0.2	1–5.6	1.485
× 0.2	5.5	1.424–1.502
▼ 0.35	2.5	1.449–1.516
□ 0.35	7.4	1.434–1.516
■ 0.35	25	1.423–1.528
▲ 0.7	1–4.5	1.485

Fig. 2. Dependence of the photon energy $\hbar\omega_s^e$ on the emission energy density D_s. The normalized energy density D_s^0 is equal to the energy D_s measured at $\hbar\omega_{ex} = 1.475$ eV, $F = 0.35$ mm, and $D_{ex} = 7.4$ arb. units. The inset lists the excitation-pulse parameters: beam diameter F, energy density D_{ex} averaged over the beam section, and the photon energy $\hbar\omega_{ex}$. The solid line is the calculated dependence of the band gap E_g on the total concentration n of electron–hole pairs.

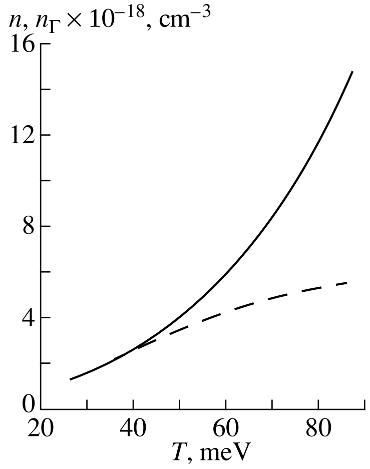

Fig. 3. Temperature dependences of the total electron concentration n (solid line) and n_Γ (dashed line) in the valley Γ_6.

Figure 2 demonstrates the applicability of the EHP threshold-state approximation to the case of superluminescence, at which the concentration, temperature, and electron distribution over valleys become unambiguously interrelated. However, after increasing the exciting spot diameter to $F > 0.5$ mm, the experimental curve systematically deviated from the calculated dependence $E_g(n)$. This disagreement calls for additional study.

Applicability of the EHP “threshold”-state approximation to superluminescence was also confirmed in this study in another way. As was indicated in the Introduction, we previously detected special features in the dependence of the superluminescence energy on the pumping photon energy [3]. These features were interpreted as a consequence of superluminescence enhancement by plasmon-assisted stimulated Raman scattering of exciting light. From the condition $\hbar\omega_s^e \approx E_g(n)$, we determined the concentration n at the excitation-photon energy at which these features arose. The optical plasmon energies $\hbar\omega_{op}$ experimentally determined in [3] for the found values of n are consistent with the calculated dependences $\hbar\omega_{op}(n)$.

The Raman scattering was represented in [3] as a direct electron transition from the valence-band top to a virtual state of the conduction band on pump-photon absorption, transition of this electron to the conduction band bottom with a plasmon emission, and electron transition into the valence band with a photon emission. The first transition into just the virtual state is explained by the need to satisfy the wave-vector conservation law. Figure 4 (taken from [3]) shows the energy W_s^M at the superluminescence spectrum peak versus the photon energy $\hbar\omega_{ex}$ in an exciting pulse of length 14 ps. The data of [3] (also shown in Fig. 2) were obtained at the beam diameter $F = 0.35$ mm and various (constant for each curve) energy densities D_{ex} of an exciting pulse. Local convexities in curves $W_s^M(\hbar\omega_{ex})$ (correspondingly, in curves $D_s(\hbar\omega_{ex})$) reflect additional superluminescence enhancement when Raman scattering of exciting light is initiated. The peaks of this amplification (indicated by arrows in Fig. 4) were determined by positions of local curvature maximums in curves $W_s^M(\hbar\omega_{ex})$ using the dependence $d^2 W_s^M/d(\hbar\omega_{ex})^2 = f(\hbar\omega_{ex})$.

Figure 5 displays the difference $\hbar\omega_{ex} - \hbar\omega_{ex}^m$ versus the concentration n, where $\hbar\omega_s^m$ is the photon energy corresponding to the superluminescence spectrum

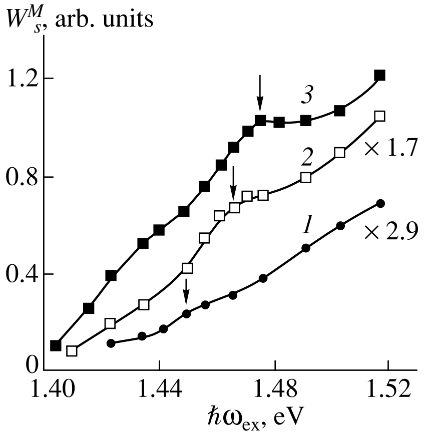

Fig. 4. Dependence of the energy W_s^M at the emission spectrum peak on the excitation-pulse photon energy $\hbar\omega_{ex}$ at the excition-beam diameter $F = 0.35$ mm and the total pulse energy density D_{ex} = (*1*) 2.5, (*2*) 7.4, and (*3*) 25 arb. units. Arrows indicate peaks of superluminescence amplification due to Raman scattering of exciting light.

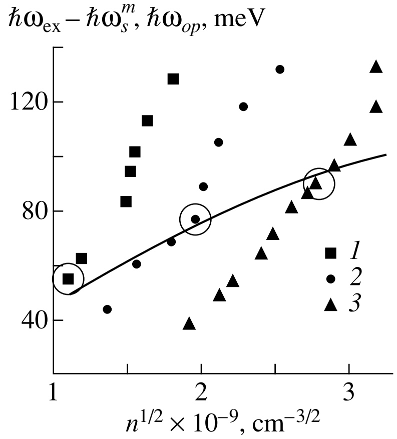

Fig. 5. Dependence of the difference $\hbar\omega_{ex} - \hbar\omega_s^m$ on the total concentration of electron–hole pairs at the diameter $F = 0.35$ mm and the excition-pulse energy density D_{ex} = (*1*) 2.5, (*2*) 7.4, and (*3*) 25 arb. units. Here, $\hbar\omega_s^m$ is the photon energy corresponding to the superluminescence spectrum peak. Open circles indicate points with maximum superluminescence amplification caused by Raman scattering of exciting light (corresponding points in Fig. 4 are indicated by arrows). The solid line corresponds to the calculated dependence of a quantum with energy $\hbar\omega_{op}$ of coupled oscillations of an optical plasmon and an *LO*-phonon on concentration *n*.

peak, while the concentration *n* was determined from the condition $\hbar\omega_s^e = E_g(n)$ in Fig. 2. The experimental points where the superluminescence amplification caused by Raman scattering was at a maximum are indicated by open circles (corresponding points in Fig. 4 are indicated by arrows). Figure 5 also shows the dependence of the optical plasmon energy $\hbar\omega_{op}$ on concentration *n*, calculated by formula (5). Deviation of the indicated experimental points from this calculated dependence is insignificant, which also justifies the above-described determination of the concentration *n* and, hence, applicability of the threshold-state approximation to a multicomponent EHP at superluminescence.

To calculate the frequency ω_{op} of coupled oscillations of the optical plasmon and LO-phonon (these oscillations were referred to above as simply the optical plasmon), we used the following expressions (see, for example, [20])

$$\begin{aligned} \omega_{op}^2 &= (\omega_L^2 + \omega_p^2)/2 + [(\omega_L^2 + \omega_p^2)^2 - 4\omega_p^2\omega_T^2]^{1/2}/2, \\ \omega_p^2 &= 4\pi e^2(n_\Gamma/m_e^\Gamma + n_L/m_e^L + p_h/m_{hh} + p_l/m_{lh})/\varepsilon \end{aligned} \qquad (5)$$

(where m_e^L, $m_e^L = 0.4m_0$, $m_{hh} = 0.62m_0$, and $m_{lh} = 0.075m_0$ are, respectively, effective masses of electrons in the Γ_6 (see below) and L_6 valleys, heavy, and light holes; m_0 is the electron rest mass; and $\omega_L = 292$ cm^{-1} and $\omega_T = 269$ cm^{-1} are frequencies of optical longitudinal and transverse phonons, respectively). The change of mass $m_e^\Gamma = 0.074–0.088m_0$ as *n* and *T* vary was taken into account by formula (74) from [21]. The given effective masses of electrons and holes are realistic; however, their accurate determination is complicated due to disagreement of various experimental data (caused by mass anisotropy, especially in the subband of heavy holes and in the L_6 valley), nonparabolicity and corrugation of energy bands, and the "apparent" change of mass due to the exchange interaction [15, 22–24]. The mass anisotropy should be taken into account according to the anisotropic wave vector of plasmons emitted during Raman scattering. This wave vector is equal to the difference between the exciting photon wave vector approximately orthogonal to the GaAs layer (i.e., to the (100) plane) and the superluminescence photon wave vector predominantly parallel to the GaAs layer surface (i.e., lying in the (100) plane). The value of m_e^L for the L_6 valley was chosen with approximate consideration for the above anisotropy. We proceeded from the Ge cyclotron mass data [25], since ellipsoidal isoenergetic surfaces in *L* valleys are similar in GaAs and Ge.

Thus, our studies of integral spectra of picosecond superluminescence, including analyzing them under plasmon-assisted Raman scattering, experimentally substantiate the following. The approximation of the threshold state of multicomponent EHP can be applied to the case of picosecond superluminescence in GaAs. The total concentration of electron–hole pairs, carrier temperature, and the distribution of electrons over valleys in this approximation become unambiguously interrelated. Correspondingly, the band-gap narrowing due to the Coulomb interaction of carriers is uniquely controlled by the total concentration of electron–hole pairs.

ACKNOWLEDGMENTS

This study was supported by the Russian Foundation for Basic Research, project no. 98-02-17377, as well as by the Ministry of Science and Technical Policy of the Russian Federation.

The authors are grateful to V. I. Perel for important suggestions and to Yu. D. Kalafati and G. N. Shkerdin for their fruitful participation in discussions.

REFERENCES

1. N. N. Ageeva, I. L. Bronevoĭ, E. G. Dyadyushkin, and B. S. Yavich, Pis'ma Zh. Éksp. Teor. Fiz. **48**, 252 (1988) [JETP Lett. **48**, 276 (1988)].
2. I. L. Bronevoĭ and A. N. Krivonosov, Fiz. Tekh. Poluprovodn. (St. Petersburg) **32**, 537 (1998) [Semiconductors **32**, 479 (1998)].
3. I. L. Bronevoi, A. N. Krivonosov, and V. I. Perel, Solid State Commun. **94**, 363 (1995).
4. H. C. Casey and F. Stern, J. Appl. Phys. **47**, 631 (1976).
5. B. E. Sernelius, Phys. Rev. B **33**, 8582 (1986); H. S. Bennet and J. R. Lowney, J. Appl. Phys. **62**, 521 (1987); H. Yao and A. Compaan, Appl. Phys. Lett. **57**, 147 (1990).
6. D. Olego and M. Cardona, Phys. Rev. B **22**, 886 (1980).
7. J. Shah, R. F. Leheny, and C. Lin, Solid State Commun. **18**, 1035 (1976).
8. J. Camassel, D. Auvergne, and H. Mathieu, J. Appl. Phys. **46**, 2683 (1975).
9. S. Tarucha, H. Kobayashi, Y. Horikoshi, and H. Okamoto, Jpn. J. Appl. Phys. **23**, 874 (1984).
10. A. Tomita and A. Suzuki, IEEE J. Quantum Electron. **QE-23**, 1155 (1987).
11. I. L. Bronevoi, A. N. Krivonosov, and V. I. Perel, Solid State Commun. **94**, 805 (1995).
12. I. L. Bronevoi, Yu. D. Kalafati, and A. N. Krivonosov, in *Proceedings of 24th International Conference on the Physics of Semiconductors, Jerusalem, 1998*, ISBN: 981-02-4030-9 (CD), 0051.pdf.
13. I. L. Bronevoi, A. N. Krivonosov, and T. A. Nalet, Solid State Commun. **98**, 903 (1996).
14. I. L. Bronevoĭ, S. E. Kumekov, and V. I. Perel', Pis'ma Zh. Éksp. Teor. Fiz. **43**, 368 (1986) [JETP Lett. **43**, 473 (1986)]; N. N. Ageeva, I. L. Bronevoi, E. G. Dyadyushkin, *et al.*, Solid State Commun. **72**, 625 (1989); N. N. Ageeva, I. L. Bronevoi, V. I. Mironov, *et al.*, in *Mode-Locked Lasers and Ultrafast Phenomena*, Ed. by G. B. Altshuler (SPIE, Bellingham, 1992); Proc. SPIE **1842**, 70 (1992).
15. J. S. Blakemore, J. Appl. Phys. **53**, R123 (1982).
16. T. Rice, J. Hensel, T. Phillips, and G. Thomas, Solid State Phys. **32**, 1 (1977); *The Electron–Hole Liquid in Semiconductors: Theoretical Aspects. Experimental Aspects* (Mir, Moscow, 1980).
17. *Theory of the Inhomogeneous Electron Gas*, Ed. by S. Lundqvist and N. H. March (Plenum, New York, 1983; Mir, Moscow, 1987).
18. M. Combescot and P. J. Noziers, J. Phys. C **5**, 2369 (1972).
19. N. C. Casey, Jr. and M. B. Panish, *Heterostructure Lasers* (Academic, New York, 1978; Mir, Moscow, 1981).
20. P. M. Platzman and P. A. Wolff, in *Solid State Physics*, Suppl. 13 (Academic, New York, 1973); *Waves and Interactions in Solid State Plasmas* (Mir, Moscow, 1975).
21. G. Skerdin, J. Stiens, and R. Vounckx, J. Appl. Phys. **85**, 3792 (1999).
22. W. F. Brinkman and T. M. Rice, Phys. Rev. B **7**, 1508 (1973).
23. O. Madelung, *Introduction to Solid State Theory* (Springer-Verlag, Berlin, 1978; Nauka, Moscow, 1980).
24. S. Adachi, J. Appl. Phys. **58**, R1 (1985); *Landolt-Bornstein Numerical Data and Functional Relationships in Science and Technology*, Vol. 17a: *Physics of Group IV Elements and III–V Compounds*, Ed. by O. Madelung (Springer-Verlag, Berlin, 1982).
25. G. Dreselhaus, A. F. Kip, and C. Kittel, Phys. Rev. **98**, 368 (1955).

Translated by A. Kazantsev

Semiconductors, Vol. 35, No. 1, 2001, pp. 72–76. Translated from Fizika i Tekhnika Poluprovodnikov, Vol. 35, No. 1, 2001, pp. 70–74.
Original Russian Text Copyright © 2001 by Gerasimov, Chiradze, Kutivadze.

ELECTRONIC AND OPTICAL PROPERTIES OF SEMICONDUCTORS

On the Physical Nature of a Photomechanical Effect

A. B. Gerasimov, G. D. Chiradze, and N. G. Kutivadze
Tsereteli State University of Kutaisi, Kutaisi, 384000 Georgia
e-mail: irpdd@sanetk.net.ge

Submitted March 20, 2000; accepted for publication June 29, 2000

Abstract—A photomechanical effect was studied in single-crystal Si by a unified method. The dependences of the photomechanical effect on the spectrum and intensity of light, the residual photomechanical effect (the persistence of crystal softening for some time after the termination of indention), the effect of illumination on microhardness anisotropy, and the temperature dependence of the photomechanical effect were studied. Based on the experimental results and on the analysis of relevant published data, the correlation between the photomechanical effect and the corresponding density of photogenerated nonequilibrium carriers (so-called antibonding quasiparticles) is determined. This correlation suggests a mechanism according to which, in covalent crystals, microhardness decreases mostly owing to chemical bond weakening and isotropization caused by the photogenerated antibonding quasiparticles. *© 2001 MAIK “Nauka/Interperiodica”.*

1. INTRODUCTION

The photomechanical effect (PME) [1], which is actually a photoinduced change in material microhardness (MH), has been studied previously [1–8]. However, no explanation of the physical nature of this effect has been offered. This is probably due to a discrepancy in the experimental data obtained by different techniques under different conditions. In this paper, we report the results of studying the PME in Si by a single method, which gives an insight into the physical nature of the effect of illumination on microhardness.

The MH measurement is known to involve material damage leading to a displacement of a certain amount of the studied material under the indentor pressure. By producing a decrease in MH, light facilitates the material displacement, which means an increase in the mobility of atoms relative to each other, i.e., a change in atomic interaction. The origin of the photoinduced increase in the atomic mobility is clarified by a new concept of atom displacement in solids proposed in [9, 10]. The main idea of this concept is outlined below.

The method of linear combination of atomic orbitals (LCAO) applied to electronic states in semiconductors in a tight binding approximation yields two energy values [11]: the lower energy corresponds to bonding states and the higher, to antibonding states. The top of the valence band, which consists of bonding orbitals, corresponds to electronic P states, while the conduction band bottom, to electronic S states (Fig. 1). Consequently, each electron transition from the valence to the conduction band, i.e., a transition from a bonding to an antibonding state, involves a corresponding change in the electron quantum state. In other words, the binding energy decreases, and the distribution of negative charge changes around the atoms adjacent to a free electron or to a hole involved in thermal motion. Since the S orbital exhibits spherical symmetry and the P orbital has an oriented dumb-bell-like electron cloud, an electron transition from the P state increases the specific weight of the S state in the vicinity of an atom (Fig. 1). Therefore, the more conduction electrons and holes are induced in crystal, the larger is the decrease in the binding energy and in the fraction of the fixed-orientation P bonds. Consequently, the atoms acquire an additional degree of freedom, and their mobility relative to each other becomes higher [10]. It is worth noting that the local energy levels introduced by defects within the band gap are actually bonding and antibonding orbitals for acceptor and donor levels, respectively. Hence, the electrons in the conduction band, at donor levels and holes in the valence band, and at acceptor levels appear to be antibonding quasiparticles. The experimental data presented below illustrate the crucial role of antibonding quasiparticles in PME.

2. EXPERIMENTAL

We used dislocation-free single-crystal n-Si samples, with resistivity $\rho = 200\ \Omega$ cm, Sb-doped to a concentration of $N_d = 2.3 \times 10^{13}$ cm^{-3}. The samples were cut in the (100) surface plane with a disorientation no larger than 0.3°. The microhardness was measured using a Durimet indenter equipped with a standard tetrahedral Knoop pyramid. Before indentation, the sample surfaces were chemically and mechanically treated with subsequent vacuum annealing. The sample was unloaded some time after the light has been switched off. In all the experiments, the large diagonal of the Knoop pyramid coincided with the $\langle 100 \rangle$ direction of the studied (100) plane. The necessity of the last two conditions will be clarified in Sections 4 and 5. The thickness of SiO_2 film on the studied Si surface was measured by an ellipsometer to be about 30 Å. In preliminary testing, the SiO_2 layers less than 60 Å thick were shown to produce no effect on the MH load curve. Nonmonochromatic light was produced by tungsten-filament lamps of type K21-150. The lamps were regularly arranged, at an 8-cm distance from the studied sample. The luminous flux made an angle of 60° with the normal to the sample surface. To obtain light with photon energy $h\nu < \Delta E_g$ if required, where ΔE_g is the band gap in Si, 300-μm-thick silicon wafers ($\rho \simeq 150\ \Omega$ cm) were placed in front of the lamps at a 2-cm distance in a normal-incidence position. To produce light with photon energy $h\nu > \Delta E_g$, we employed a monochromatic light source, an LGN-404V He–Ne laser operating at a ~0.64 μm wavelength. To vary the intensity of light, we used neutral filters and varied the number of lamps. To eliminate thermal effects, the lamps, filters, and the studied sample were cooled with blowing air. The temperatures of the illuminated surface were measured, and the testing of samples in the dark at the same temperatures demonstrated that the additional heating does not effect MH, thus indicating a nonthermal origin of the observed PME.

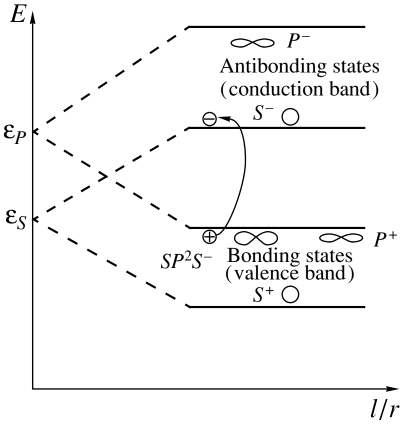

Fig. 1. Energy bands of approaching atoms (r is the internuclear separation) and the change in the energy and electron density distribution of a chemical bond as a result of electron transition from a bonding to an antibonding state.

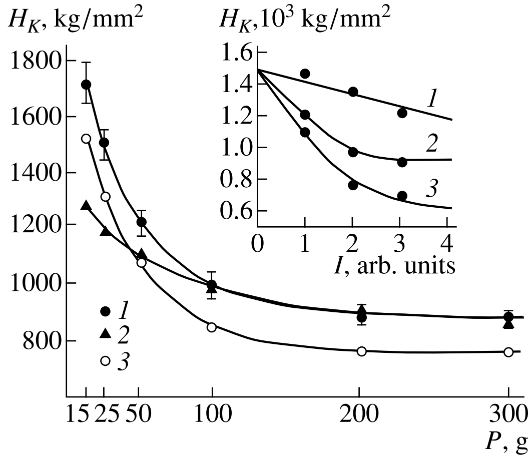

Fig. 2. Microhardness vs. load curve in Si (P is the indenter pressure) (*1*) in the dark, under irradiation with photons (*2*) with $h\nu > \Delta E_g$ and (*3*) with $h\nu < \Delta E_g$. The accuracy is the same for all the curves. Inset: microhardness H_K versus intensity of light in the case of irradiation with (*1*) photons with $h\nu < \Delta E_g$, (*2*) photons with $h\nu > \Delta E_g$, and (*3*) white light. I is intensity in arbitrary units corresponding to the number of light sources, $I = 0$ corresponds to darkness.

3. DEPENDENCE OF PME ON THE SPECTRUM AND INTENSITY OF LIGHT

Figure 2 shows the results of measuring PME as a function of light spectrum. Curve *2* in Fig. 2 corresponds to the action the of laser irradiation on the studied crystal. It is obvious from the plot that PME exists in a certain region of the load ($P < 100$ g), while, as the load increases, the curves obtained during irradiation and in the dark merge together. The photoinduced decrease in MH is noticeable if the indentor penetrates into the surface layer to a depth comparable with inverse absorption coefficient $1/\alpha$, since most of the antibonding quasiparticles are produced within this layer (farther on, their concentration drops exponentially with the depth). The dependence of silicon MH on the radiation intensity for $h\nu > E_g$ is plotted at the inset in Fig. 2 (curve *2*). Here, the linear drop gives way to saturation. This behavior can be explained by the following considerations. After a certain intensity of light is exceeded, the photogenerated quasiparticles soften the thin surface layer to the extent that it does not contribute to the material MH that, in this case, is defined by the deeper layers where quasiparticles are practically absent. We have also observed PME in the crystals irradiated with light with photon energy $h\nu < \Delta E_g$ (Fig. 2, curve *3*). In this case, the irradiation of Si results in a decrease in MH within the entire range of the loads used in the experiment. Indeed, the decrease in MH with increasing intensity of light with photon energy $h\nu < \Delta E_g$ is nearly linear (inset in Fig. 2, curve *1*). Therefore, in this case, PME is independent of the indentor penetration depth. This fact can be attributed to the following. Since the studied crystal is transparent to radiation with $h\nu < \Delta E_g$, the observed PME is due to the absorption of light by defects produced by the indentor. Because of a low absorption, the radiation penetrates into the entire damaged region, no matter how deep the indentor may penetrate during the experiment. As a result of indentation, a considerable crystal disordering occurs: a defect layer forms around the indentor and extends deep into the crystal. As is known [12], the band gap of a highly disordered semiconductor contains the tails of the density of states, which in their turn lead to a change in the optical absorption of the damaged region compared to an undamaged crystal. The tails of the valence and conduction bands consist of

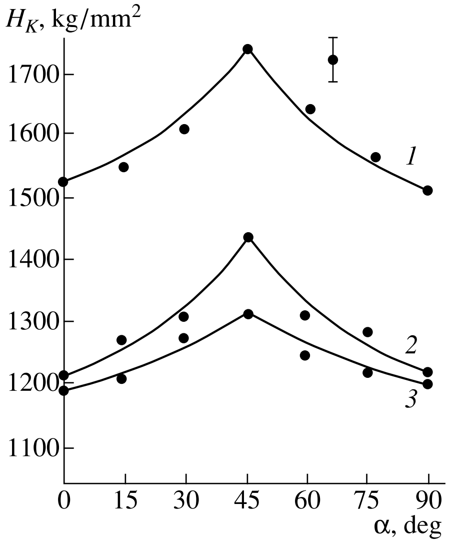

Fig. 3. Microhardness H_K measured for the Si (100) face versus the angle between the Knoop pyramid large diagonal and direction ⟨110⟩ (*1*) in the dark and under irradiation with photons of energy (*2*) $h\nu < \Delta E_g$ and (*3*) $h\nu > \Delta E_g$.

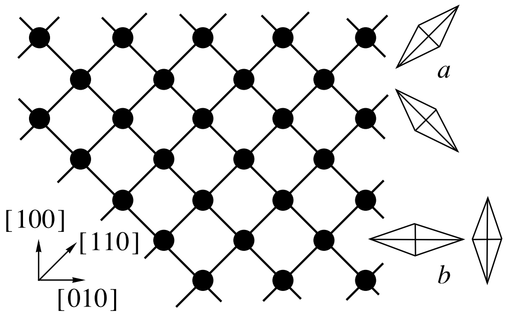

Fig. 4. Arrangement of atoms and chemical bonds in the (100) plane of a Si single crystal and the indenter orientations corresponding to (*a*) minimum and (*b*) maximum microhardness.

bonding and antibonding orbitals, respectively. The radiation with photon energy $h\nu < \Delta E_g$ induces a redistribution of electrons over the tails and increases the density of antibonding quasiparticles in the damaged region thus promoting its softening.

4. RESIDUAL PME AS A RESIDUAL SOFTENING OF THE SURFACE LAYER AFTER EXPOSURE TO LIGHT

After the light has been switched off, the MH of a sample starts to increase and with time reaches the value that it had before irradiation [13]. We studied the time and the temperature dependences of MH and propose a mechanism of this relaxation[1] [14, 15]. In accordance with this mechanism, the residual softening of the material is a result of electron and hole capture into the minimums of the distorted energy band in the damaged surface region [16]. The increase in temperature facilitates the surmounting of the barrier and, consequently, enhances recombination, which reduces the lifetime of the residual PME.

The extent of the near-surface energy-band bending to the crystal depth is governed by surface-treatment technology and the impurity concentration [16]. These factors influence the load curve of the residual PME (i.e., the dependence of the PME on the indentation depth).

5. PME ANISOTROPY

The MH value is defined by both the crystallographic orientation of the studied surface (type I anisotropy) and the indentor orientation relative to the crystallographic directions of the studied surface (type II anisotropy). When the large diagonal of the Knoop pyramid is perpendicular to direction ⟨100⟩ (the “hard” direction) in the (100) plane of a Si single crystal, MH is larger than when the large diagonal of the Knoop pyramid is perpendicular to direction ⟨110⟩ (the “soft” direction). The anisotropy of MH on a crystal face is defined as the difference between its maximum and minimum values [17]. When the crystal position is changed relative to a fixed indentor, MH varies periodically from its minimum to maximum values (Fig. 3, curve *1*). This behavior can be explained by the following considerations: during microhardness indentation in a covalent crystal, the indentor can produce bond breakage, contraction, stretching, and rotation. A two-dimensional schematic representation of atom and chemical-bond arrangements in the studied (100) plane of a Si single crystal is shown in Fig. 4. As can be seen, an indentation with the large diagonal of Knoop pyramid being parallel to the bond projection on the (100) plane (*a* position in Fig. 4), mainly causes a stretching and rotation of bonds, thus promoting their breakage and minimizing the MH value. In contrast, when the large diagonal forms an angle of 45° with the bond projection on the (100) plane (*b* position in Fig. 4), a contraction of bonds prevails, and MH is at a maximum. The study of MH anisotropy as a function of spectral features of light irradiating the (100) plane of a Si single crystal shows the following. First, the radiation with photon energy $h\nu < \Delta E_g$ is mainly absorbed in the damaged region that is isotropic and induces an identical decrease in MH in all directions; thus, the initial anisotropy is preserved (Fig. 3, curve *2*). In contrast, radiation with the photon energy $h\nu > \Delta E_g$ is absorbed in an undamaged region of the crystal, and the MH decrease in the “hard” direction is more pronounced than in the “soft” one (Fig. 3, curve *3*). The above data suggest that the light with $h\nu > \Delta E_g$ reduces the MH anisotropy, because it is the undamaged region that governs anisotropy, and, since bond compression prevails at the MH maximum over the given face, the photoinduced electron excitations cause the isotropization of highly directional bonds (Fig. 1). Therefore, the MH load curve measured during irradiation is smoother than that measured in the dark.

---

[1] We note that similar results were obtained in [6] for GaAs and GaP, but were not interpreted.

6. TEMPERATURE DEPENDENCE OF THE PME

From the above experimental data one can infer that, during heating, a decrease in MH should be mainly attributed to the thermal generation of antibonding particles. In order to verify this conjecture, we studied experimentally the temperature dependence of MH in a Si single crystal both in the dark and using white light of various intensities. The MH-temperature curve appears to depend on the conditions under which the indenter is lifted and the indentation measured. For example, cooling a sample to 50°C after indentation without lifting the indenter and the subsequent measurement of MH after lifting the indenter yields the data shown in Fig. 5 (curve *1*). If the indenter has been removed before cooling, the indentation is smaller than in the previous case, which indicates the elastic recovery of a sample. Consequently, in this case MH is overestimated, and the leveling off of the MH temperature dependence is only apparent (Fig. 5, curve *2*). The plot (Fig. 5, curves *1*, *2*) indicates that, as for illumination, the thermally induced increase in the antibonding quasiparticle density leads to a decrease in MH with temperature and to the mechanical destabilization of the indentation contour, which manifests itself in an enhanced elastic recovery of the indentation size. To obtain the temperature dependence of the PME, we first measured the temperature of the irradiated sample, and then the indentation was measured after the sample was cooled without lifting the indenter. It can be seen from Fig. 5 (curves *3*, *4*) that, at low temperatures, MH is nearly constant. When the temperature increases and attains a value specific for every intensity of light, the MH of the irradiated sample becomes temperature-dependent. The further temperature growth leads to the disappearance of the PME. We note that, with an increase in the intensity of light, the point of merging for the MH-temperature curves obtained in the dark and under illumination shifts towards higher temperatures.

Comparing the densities of thermally induced and photogenerated antibonding quasiparticles, n_d and n_{ill}, respectively, one may conclude that, in the temperature region where the photoinduced density exceeds the thermally induced one, i.e., $n_{ill} > n_d$, the decrease in MH is governed by illumination and is nearly constant. With a further increase in temperature, when n_d becomes comparable with n_{ill}, the MH measured under illumination becomes temperature-dependent. Finally, when $n_{ill} < n_d$, the PME vanishes, and MH depends on temperature only.

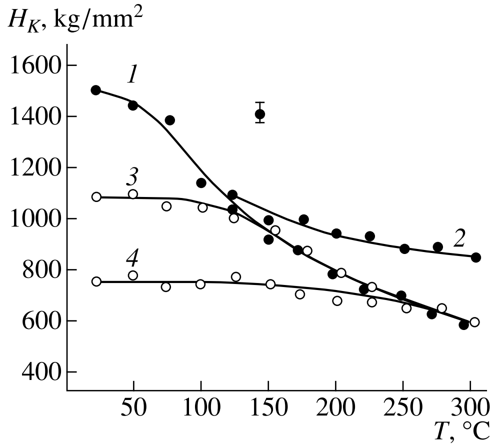

Fig. 5. Temperature dependences of Si microhardness measured (*1*, *2*) in the dark and (*3*, *4*) under irradiation. Indentation conditions: (*1*, *3*, *4*) cooling without lifting the indenter; (*2*) cooling with lifted indenter. White light intensity: (*3*) I_1, (*4*) $I_2 > I_1$.

7. PME IN Ge AND SiC CRYSTALS

We should note that, using the above described technique, qualitatively the same results were obtained with Ge (n-Ge:Sb, $\rho \simeq 40\ \Omega$ cm) [18] and hexagonal 6*H*-SiC with surface orientation (0001) doped with nitrogen to the concentration of $N_D - N_A = 3 \times 10^{18}$ cm^{-3} [19].

8. CONCLUSION

The distinct correlation between a decrease in MH and an increase in antibonding quasiparticle density clearly indicates that, in crystals with mostly covalent bonds, the main reason for photoinduced MH change is the chemical bond weakening and isotropization due to antibonding quasiparticles, which are excited electrons and holes.

REFERENCES

1. G. C. Kuczynsky and R. H. Hochman, Phys. Rev. **108**, 946 (1957).
2. P. P. Kuz'menko, N. N. Novikov, and N. Ya. Gorid'ko, Fiz. Tverd. Tela (Leningrad) **4**, 2656 (1962) [Sov. Phys. Solid State **4**, 1950 (1963)].
3. V. M. Beĭlin and Yu. Kh. Vekilov, Fiz. Tverd. Tela (Leningrad) **5**, 2372 (1963) [Sov. Phys. Solid State **5**, 1727 (1964)].
4. P. P. Kuz'menko, N. N. Novikov, N. Ya. Gorid'ko, and K. I. Fedoren'ko, Fiz. Tverd. Tela (Leningrad) **8**, 1732 (1966) [Sov. Phys. Solid State **8**, 1381 (1966)].
5. V. A. Drozdov, L. A. Mozgovaya, and A. L. Rvachev, Dokl. Akad. Nauk SSSR **177**, 168 (1967).
6. I. A. Domoryad, *Radiation Physics of Non-metallic Crystals* (Nauka i Tekhnika, Minsk, 1970), p. 131.
7. N. Ya. Gorid'ko and N. N. Novikov, Ukr. Fiz. Zh. **9**, 1550 (1972).

8. V. I. Kruglov, Uch. Zap.-Leningr. Gos. Univ. im A. A. Zhdanova **386**, 119 (1976).
9. A. B. Gerasimov, V. B. Golubkov, É. R. Kuteliya, *et al.*, Pis'ma Zh. Tekh. Fiz. **6**, 58 (1980) [Sov. Tech. Phys. Lett. **6**, 25 (1980)].
10. A. B. Gerasimov, Mater. Sci. Forum **65–66**, 47 (1990).
11. W. A. Harrison, *Electronic Structure and the Properties of Solids: The Physics of the Chemical Bond* (Freeman, San Francisco, 1980; Mir, Moscow, 1983), Vol. 1.
12. N. F. Mott and E. A. Davis, *Electronic Processes in Non-Crystalline Materials* (Clarendon Press, Oxford, 1979; Mir, Moscow, 1982), Vol. 1.
13. A. B. Gerasimov, Z. V. Dzhibuti, and G. D. Chiradze, Soobshch. Akad. Nauk Gruz. **142**, 53 (1991).
14. A. B. Gerasimov, G. D. Chiradze, N. G. Kutivadze, *et al.*, Fiz. Tverd. Tela (St. Petersburg) **40**, 503 (1998) [Phys. Solid State **40**, 462 (1998)].
15. A. B. Gerasimov, G. D. Chiradze, N. G. Kutivadze, *et al.*, Fiz. Tverd. Tela (St. Petersburg) **42** (4), 683 (2000) [Phys. Solid State **42**, 701 (2000)].
16. *Problems in Radiation Technology of Semiconductors*, Ed. by L. S. Smirnov (Nauka, Novosibirsk, 1980), p. 149.
17. P. D. Warren, S. G. Roberts, and P. B. Hirsch, Izv. Akad. Nauk SSSR, Ser. Fiz. **51**, 812 (1987).
18. G. D. Chiradze, Author's Abstract of Candidate's Dissertation (Tbilisi, 1992).
19. A. B. Gerasimov, G. D. Chiradze, N. G. Kutivadze, *et al.*, Bull. Georg. Acad. Sci. **156**, 391 (1997).

Translated by A. Sidorova-Biryukova

Semiconductors, Vol. 35, No. 1, 2001, pp. 77–79. Translated from Fizika i Tekhnika Poluprovodnikov, Vol. 35, No. 1, 2001, pp. 75–77.
Original Russian Text Copyright © 2001 by Karazhanov, Atabaev, Saliev, Kanaki, Dzhaksimov.

SEMICONDUCTOR STRUCTURES, INTERFACES, AND SURFACES

Excess Tunneling Currents in *p*-Si–*n*-3*C*-SiC Heterostructures

S. Zh. Karazhanov*, I. G. Atabaev, T. M. Saliev, É. V. Kanaki, and E. Dzhaksimov
Physicotechnical Institute, Academy of Sciences of Uzbekistan, Tashkent, 700084 Uzbekistan
** e-mail: atvi@physic.uzsci.net*

Submitted May 31, 2000; accepted for publication June 9, 2000

Abstract—An attempt is made to interpret the current–voltage characteristic of a *p*-Si–*n*-3*C*-SiC heterostructure in terms of the excess-tunneling mechanism. The space charge region width W and tunneling length λ are estimated. It is shown that $W \gg \lambda$ and, despite this, that the current transport through the heterostructure obeys the tunneling mechanism. The characteristic tunneling energy $\varepsilon = 57$ meV, temperature coefficient of the saturation current, and the barrier thinness factor are found. © *2001 MAIK "Nauka/Interperiodica".*

Silicon carbide is a material possessing an extremely broad set of useful properties: electrotechnical, anticorrosive, strength-related, etc. Recently, interest in this material and structures based on it has been aroused owing to its capacity to emit in the excitonic spectral range [1–3] under illumination or during the passage of current.

This study is concerned with the mechanism of current transport through *p*-Si–*n*-3*C*-SiC heterostructures. 3*C*-SiC films were grown using CVD epitaxy by the thermal decomposition of trimethylchlorosilane. Heterostructures grown by this method are known to have abrupt boundaries [4].

To study the current–voltage (I–V) characteristics of *p*-Si–*n*-3*C*-SiC heterojunctions, KDB-20 (*p*-Si, $\rho = 20\ \Omega$ cm) (111) silicon wafers were taken as substrates, and SiC layers 5–15 μm thick were deposited. The capacitance–voltage characteristic of such a structure, measured at 10 kHz under reverse biases of up to 1.5 V, is linear in the coordinates $C^{-2} = f(V)$, with the slope of this straight line corresponding to the uncompensated impurity concentration $N = 10^{15}$ cm^{-3}. This is in agreement with the nominal acceptor concentrations in the silicon substrate $N = 7 \times 10^{14}$ cm^{-3}.

I–V characteristics of *p*-Si–*n*-3*C*-SiC heterostructures were measured under forward and reverse biases (see figure). Analysis of the figure readily shows that the forward I–V characteristics are linear in a wide range of currents, voltages, and temperatures, which points to the tunneling nature of the charge transport. Previously, we related the tunneling nature of the charge transport to the presence of a thin silicon oxide layer at the heteroboundary, whose traces were detected by secondary-ion mass spectrometry (SIMS) [5]. However, the presence of a very thin continuous layer of silicon oxide is required, which is highly improbable in the case of growth in a chlorine-containing gas medium. It should be recalled that the films were grown by the thermal decomposition of trimethylchlorosilane.

The mechanism of charge transport in Si–3*C*–SiC structures similar to those used in this study was studied in detail previously [6]. It was assumed that the most probable nature of the forward currents is the carrier recombination in the space charge region (SCR) via trap levels shifted by more than $10kT$ away from the midgap, in accordance with the model proposed by Dolega [7]. Also, we estimated the surface density of these traps at $N_t = 10^{11}$–10^{12} cm^{-2} ($N_t = 10^{16}$–10^{18} cm^{-3} in terms of the "bulk" concentration). At the same time, it was mentioned [7] that an attempt to detect deep levels in the SCR of heterostructures by DLTS failed. Thus, the conclusion about the recombination nature of forward currents seems to be not quite convincing.

To study a similar I–V characteristic, an excess tunneling-current mechanism has been proposed [8–14] and validated for a great number of homostructures, heterostructures, and metal–semiconductor structures (for more detail, see [8]). According to this mechanism, a broad spectrum of energy levels enabling multistep tunneling is present in the energy gap at the interface.

We have shown previously [4] that SiC films grown on Si substrates include a transition SiC region with a high concentration of structural defects appearing as a result of a large lattice mismatch between Si and SiC. It is in view of the aforesaid that an attempt is made here to interpret the I–V characteristics of *p*-Si–*n*-3*C*-SiC in terms of the excess tunneling-current mechanism [8–14] according to which the dependence of the current (I) on voltage (V) can be described by

$$I = I_0 \exp(qV/\varepsilon), \tag{1}$$

where the pre-exponential factor I_0 changes with temperature following the law

$$I_0 = I_{00} \exp(aT). \tag{2}$$

Here q is the elementary charge, and a is a proportionality factor of dimension [K^{-1}]. The characteristic tunneling energy ε, found from the figure using formula

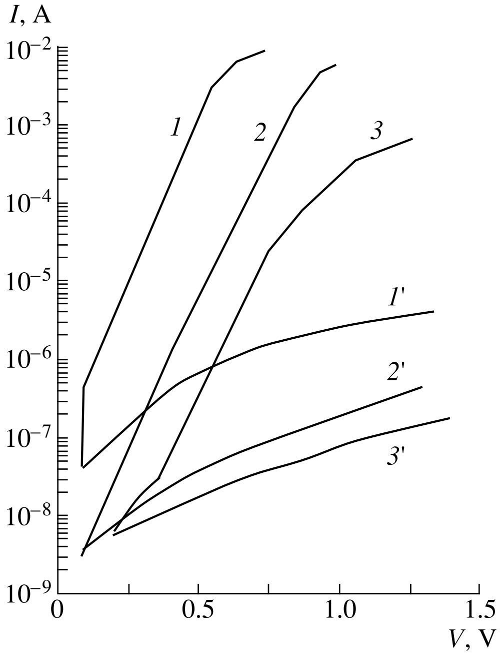

Forward (*1*, *2*, and *3*) and reverse (*1*', *2*', and *3*') *I–V* characteristics of *p*-Si–*n*-3*C*-SiC structures at T = (*1*, *1*') 15, (*2*, *2*') 130, and (*3*, *3*') 196°C.

(1), is 57 meV. We note that the value ε lies within the limits indicated in [8].

Also, the temperature coefficient a of the saturation current I_0 and the pre-exponential factor I_{00} are found from the *I–V* characteristics to be $a = 0.05\ \mathrm{K}^{-1}$ and $I_{00} = 2 \times 10^{-9}$ A, respectively. Further, we estimated the SCR width W as

$$W = \left[\frac{2\kappa_0(\kappa/N)_{\mathrm{eff}}(U_s - U)}{q}\right]^{1/2}, \qquad (3)$$

according to which W = 1.05 μm, in good agreement with the data of [8]. Here, κ is the dielectric constant: $\kappa_p = 11.2$ for silicon and $\kappa_n = 10.2$ [15] for SiC. The ratio $(\kappa/N)_{\mathrm{eff}}$ is evaluated by the formula [8]

$$(\kappa/N)_{\mathrm{eff}} = \frac{\kappa_n\kappa_p(n_n + p_p)^2}{n_n p_p(n_n\kappa_n + p_p\kappa_p)}, \qquad (4)$$

where n_n and p_p are the majority carrier concentrations in *n*-SiC and *p*-Si and are equal to 10^{17} and $7 \times 10^{14}\ \mathrm{cm}^{-3}$, respectively. The quantity qU_s is evaluated by the formula

$$qU_s = E_g^{\mathrm{Si}} - \mu_p^{\mathrm{Si}} - \mu_n^{\mathrm{SiC}}, \qquad (5)$$

where E_g^{Si} is the band gap of silicon; $\mu_p^{\mathrm{Si}} = kT\ln(N_c/p_p)$ and $\mu_n^{\mathrm{SiC}} = kT\ln(N_V/n_n)$ are the chemical potentials in silicon and silicon carbide, respectively; $N_c = 2 \times 10^{19}(T/300)^{3/2}$ is the density of quantum states in the conduction band of silicon carbide; and $N_V = 3.4 \times 10^{19}(T/300)^{3/2}$ is the density of hole states in the valence band. The expression for N_0 was obtained with the effective masses of electrons, m_n^*, and holes, m_p^*, taken to be $0.6m_0$ and $1.2m_0$ [15], respectively, where m_0 is the electron mass at rest. Further, we evaluate the tunneling distance λ [8]

$$\lambda = h(2m_n^*q(U_s - U))^{1/2}, \qquad (6)$$

which yields λ = 2.6 nm. Comparison of the W and λ values shows that $W \gg \lambda$. This means that the assumed tunneling through the heterojunction has an enhanced probability. In the band gap, there is a broad spectrum of energy levels,

$$\varepsilon_t = \frac{hq}{2}\left[\frac{(\kappa/N)_{\mathrm{eff}}}{\kappa_0 m_n^*}\right]^{1/2},$$

ensuring multistep tunneling. According to [8], such a tunneling process can be described using a scaling thinness factor r for the barrier, making the tunneling distance λ longer and the characteristic tunneling energy ε higher compared with the theoretical value ε_t.

The ε_t value is estimated at 1.16 meV, which is 49–50 times smaller than ε. Thus, the phenomenological thinness factor of the barrier $r = \varepsilon/\varepsilon_i$ = 49–50, and the probability of tunneling becomes higher by the same factor.

CONCLUSION

The *I–V* characteristic of a *p*-Si–*n*-3*C*-SiC heterostructure was studied. The SCR width W and the tunneling distance were evaluated. It is shown that $W \gg \lambda$ and, despite this fact, the charge transport through the heterostructure under study obeys the tunneling mechanism modified in [8]. The characteristic tunneling energy ε = 57 meV, temperature coefficient of saturation current, and barrier thinness factor were found.

REFERENCES

1. M. A. Kadyrov, N. V. Kunina, Kh. A. Shamuratov, *et al.*, Fiz. Tekh. Poluprovodn. (Leningrad) **14** (8), 1591 (1980) [Sov. Phys. Semicond. **14**, 942 (1980)].
2. L. I. Berezhinskiĭ, S. I. Vlaskina, Yu. V. Kalinichenko, *et al.*, Ukr. Fiz. Zh. **30**, 513 (1991).
3. L. I. Berezhinskiĭ, S. I. Vlaskina, F. K. Dzhaparova, *et al.*, Ukr. Fiz. Zh. **37**, 565 (1992).
4. Kh. A. Shamuratov and T. M. Saliev, Ukr. Fiz. Zh. **36** (3), 92 (1991).
5. T. M. Saliev, Author’s Abstract of Candidate’s Dissertation (Tashkent, 1994).
6. A. S. Zubrilov, Fiz. Tekh. Poluprovodn. (St. Petersburg) **28** (10), 1742 (1994) [Semiconductors **28**, 967 (1994)].
7. U. Dolega, Z. Naturforsch. A **18**, 653 (1963).

8. V. V. Evstropov, Yu. V. Zhilyaev, M. Dzhumaev, and N. Nazarov, Fiz. Tekh. Poluprovodn. (St. Petersburg) **31** (2), 115 (1997) [Semiconductors **31**, 115 (1997)].
9. V. V. Evstropov, Yu. V. Zhilyaev, N. Nazarov, *et al.*, Pis'ma Zh. Tekh. Fiz. **19** (15), 61 (1993) [Tech. Phys. Lett. **19**, 496 (1993)].
10. V. V. Evstropov, Yu. V. Zhilyaev, N. Nazarov, *et al.*, Zh. Tekh. Fiz. **63** (12), 41 (1993) [Tech. Phys. **38**, 1057 (1993)].
11. V. V. Evstropov, Yu. V. Zhilyaev, N. Nazarov, *et al.*, Fiz. Tekh. Poluprovodn. (St. Petersburg) **27**, 1319 (1993) [Semiconductors **27**, 729 (1993)].
12. V. V. Evstropov, Yu. V. Zhilyaev, N. Nazarov, *et al.*, Fiz. Tekh. Poluprovodn. (St. Petersburg) **27**, 688 (1993) [Semiconductors **27**, 369 (1993)].
13. V. V. Evstropov, Yu. V. Zhilyaev, N. Nazarov, *et al.*, Fiz. Tekh. Poluprovodn. (St. Petersburg) **29**, 385 (1995) [Semiconductors **29**, 195 (1995)].
14. A. V. Bobrov, V. V. Evstropov, Yu. V. Zhilyaev, *et al.*, Pis'ma Zh. Tekh. Fiz. **19**, 30 (1993) [Tech. Phys. Lett. **19**, 378 (1993)].
15. S. A. Dobrolezh, S. M. Zubkova, V. A. Kravets, V. Z. Smushkevich, K. B. Tolpygo, and I. N. Frantsevich, *Silicon Carbide* (Gos. Izd. Tekh. Lit. USSR, Kiev, 1963), p. 316.

Translated by M. Tagirdzhanov

Semiconductors, Vol. 35, No. 1, 2001, pp. 80–85. Translated from Fizika i Tekhnika Poluprovodnikov, Vol. 35, No. 1, 2001, pp. 78–83.
Original Russian Text Copyright © 2001 by Panin, Shugurov, Kalygina.

SEMICONDUCTOR STRUCTURES, INTERFACES, AND SURFACES

Effect of Sulfur and Selenium on the Surface Relief of Insulating Films and Electrical Characteristics of Metal–Insulator–*p*-GaAs Structures

A. V. Panin*, A. R. Shugurov*, and V. M. Kalygina**

* *Institute of Strength Physics and Materials Science, Siberian Division, Russian Academy of Sciences,*
Akademicheskiĭ pr. 2/1, Tomsk, 634055 Russia

e-mail: pav@ispms.tsc.ru

** *Kuznetsov Physicotechnical Institute, pl. Revolyutsii 1, Tomsk, 634050 Russia*

Submitted June 13, 2000; accepted for publication June 16, 2000

Abstract—The effect of S and Se atoms on the surface relief of insulating layers deposited on the GaAs substrate was investigated. It was demonstrated that the incorporation of chalcogens in the surface region of a semiconductor leads to smoothing of the surface relief of insulating films. Simultaneous decrease in the density of surface states at the insulator–*p*-GaAs interface was observed. The resulting effect of the S and Se atoms depends on the insulating material. © *2001 MAIK “Nauka/Interperiodica”.*

1. INTRODUCTION

It is known that passivation of the GaAs surface by chalcogens leads to an increase in the photoluminescence (PL) intensity [1], a stronger dependence of the metal–GaAs potential barrier on the electron work function of the metal [2], a weakening of the frequency dependence of electrical characteristics [3], etc. The effects mentioned are caused by a decrease in the density of surface states and depinning of the Fermi level on the GaAs surface.

However, if the insulating layer is deposited on the GaAs passivated surface, the density of surface states (N_{ts}) at the insulator–GaAs interface increases again. The resulting N_{ts} value depends on the insulator material, its thickness, and the deposition temperature of the insulating coating [3]. An increase in the density of surface states can be related to stresses at the GaAs–insulator interface, which determine the surface relief of insulating films.

In this study, we attempted to establish a link between the insulating material, the relief of insulating coatings, and electrical characteristics of the metal–insulator–GaAs structures.

2. EXPERIMENTAL

The studied samples were formed on the *p*-GaAs(100) epitaxial layers with $N_a = 10^{15}$–10^{16} cm^{-3}, which were grown on the p^+-type substrates by a gaseous-phase epitaxy. Prior to the deposition of insulating layers, the GaAs substrates were treated according to conventional procedure, which involved degreasing and subsequent etching in a $C_2H_5OH : H_2SO_4 = 10 : 1$ solution in order to remove the native oxide film.

Chalcogen (S and Se) atoms were incorporated into the GaAs near-surface region by the growth of an anodic oxide film with an addition of the chalcogen salt to the electrolyte. Anodic oxidation was carried out using an electrolyte composed of an aqueous solution of ammonium citrate (2.5 g/l) and ethylene glycol in a ratio of 1 : 1 [4]. The anodic oxide thickness for all samples was identical (100 nm). It was assumed that the S and Se atoms diffuse from the anodic oxide into the near-surface semiconductor region. Subsequent to anodization, the oxide was removed by etching. The etchant composition and etching conditions were identical to those used for native oxide removal. The presence of chalcogens in GaAs was verified using Auger spectroscopy.

The surface of S(Se)-doped GaAs was covered with the working insulator, namely SiO_2, BN, $Si_xN_yO_z$, or their binary compounds. The films were deposited by a plasma-enhanced chemical deposition [5] at $T = 500°C$. The data on insulating film thickness (d) are given in the table.

The surface relief of GaAs and the insulating films was investigated using an SMM-2000TA scanning multimicroscope (ZAO “KPD,” Moscow Institute of Electronic Engineering, Moscow, Russia). Surface images for the semiconductor and insulating films were obtained in an atomic force microscope (AFM) mode at room temperature in air. The cantilever was scanned

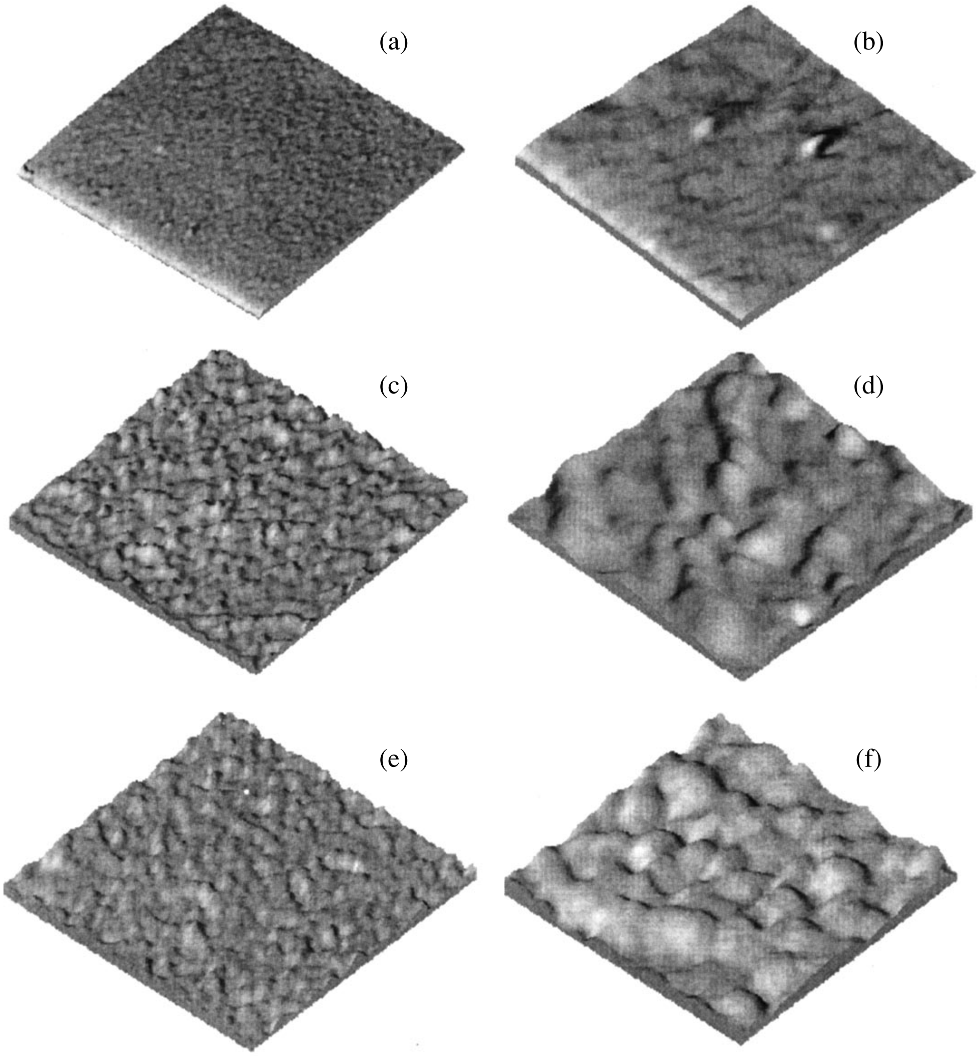

Fig. 1. (a, b) AFM images of the surfaces of the initial semiconductor substrate and SiO_2 layers (c, d) 10 nm or (e, f) 170 nm thick. Image size along the x and y axes is (a, c, e) 4.0 × 4.0 μm and (b, d, f) 1.0 × 1.0 μm.

over the surface with the photodiode current maintained constant using a feedback. This corresponds to scanning in a mode with a constant probe–substrate interaction force.

Investigations of the elemental composition of insulating layers that revealed the S and Se atoms in the layers were carried out using secondary-ion mass spectrometry on an MS-7021M device with a layer-by-layer resolution of 3–5 nm and sensitivity of 10^{-3}–10^{-4} at. %.

Metal electrodes for measurements of electrical characteristics were fabricated by vacuum deposition on both the insulator and p^+-GaAs sides. The control electrode of a fixed area $S = (1.6–2.3) \times 10^{-3}$ cm^{-2} was fabricated by vacuum evaporation of the Ni–Cr alloy through corresponding masks at a residual pressure of 6.6×10^{-3} Pa.

The capacitance–voltage (C–V) and conductance–voltage (G–V) characteristics for metal–insulator–semiconductor (MIS) structures were measured in the frequency range of $f = 10^3$–10^6 Hz at room temperature.

3. DATA

3.1. Results of AFM Investigations

Figure 1 demonstrates the surface images of the GaAs substrate without the insulating film (Figs. 1a, 1b) after deposition of the 10 and 170 nm thick SiO_2 layers (Figs. 1c, 1d and Figs. 1e, 1f, respectively). As can be seen from Figs. 1a and 1b, the surface of the GaAs substrate is the least developed and no clearly distinguishable relief is observed on it. However, island mesas appear on the surface of the insulating layer during its deposition. The analysis of the surface images

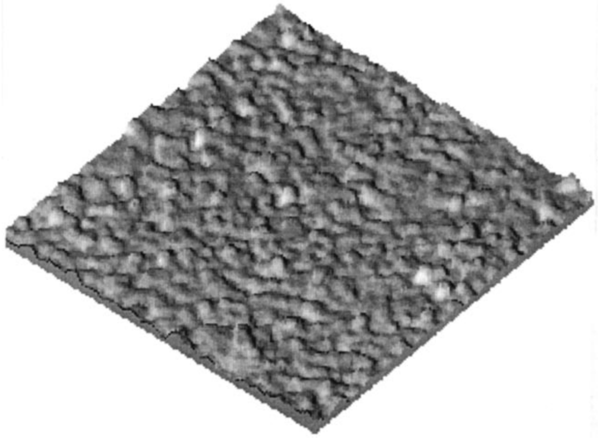

Fig. 2. AFM image of the surface of the $Si_xN_yO_z$–BN film. Layer thicknesses are $d_{Si_xN_yO_z} = 68$ nm and $d_{BN} = 128$ nm. Image size is 4.0 × 4.0 µm.

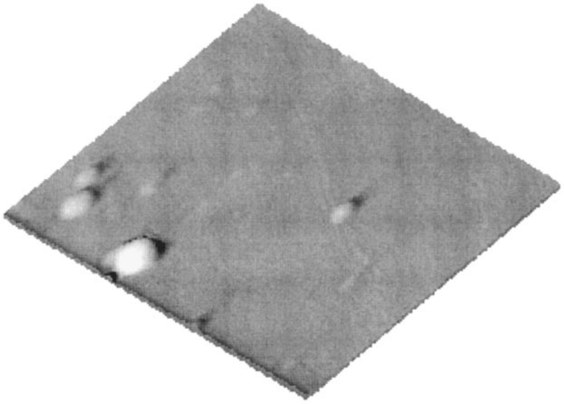

Fig. 3. AFM image of the surface of the $Si_xN_yO_z$–SiO_2(Se) film. Layer thicknesses are $d_{Si_xN_yO_z} = 45$ nm and $d_{SiO_2} = 105.5$ nm. Image size is 4.0 × 4.0 µm.

for SiO_2 films 10–250 nm thick demonstrated that they have a quasi-periodic undulating relief with a period of 200–300 nm and a height of 4–8 nm regardless of the thickness of the layer deposited [6]. In some cases, more developed separate features 200–500 nm in diameter and 10–30 nm in height were observed on the surface. The lateral (*L*) and vertical (*h*) oscillations for insulating layers investigated are given in the table. The period and height of the oscillations observed are determined by *L* and *h*, respectively.

Similar defect mesas were also formed on the surface of the BN and $Si_xN_yO_z$ films, as well as on the surface of their multilayer compositions. The AFM surface image for the $Si_xN_yO_z$ bilayer film deposited on the GaAs substrate is shown in Fig. 2. It is seen from Fig. 2 that the quasi-periodic oscillations are also present on the surface of the $Si_xN_yO_z$ bilayer insulator. Their period and height are similar to those for SiO_2 films (see table).

Incorporation of the S and Se atoms into the surface region of the semiconductor causes the complete disappearance of quasi-periodic oscillations. The SiO_2 and $Si_xN_yO_z$–SiO_2 films become smooth, and individual hillocks remain on their surface (Fig. 3).

The effect of the S and Se atoms on the surface relief of the insulating layer is identical, but, depends on the type of insulating material. Thus, in the case of BN, the incorporation of chalcogens in the GaAs surface region does not cause any smoothing of the insulator film (Fig. 4). The surface relief of the $Si_xN_yO_z$–BN insulator, which is deposited on the Se-doped GaAs substrate, is similar to that in the image shown in Fig. 2.

3.2. Capacitance–Voltage and Conductance–Voltage Characteristics for the Metal–Insulator–p-GaAs Structures

The *C–V* and *G–V* characteristics for the NiCr–$Si_xN_yO_z$–*p*-GaAs structure are characterized by

Insulator thickness, surface relief of insulating films deposited on the GaAs substrate, and density of surface states at the insulator–GaAs interface

Sample no.	Insulator	*d*, nm	Relief	*L*, nm	*h*, nm	N_{ts}, eV^{-1} cm^{-2}
1	BN	140	Oscillatory	200–300	3–8	–
2	$Si_xN_yO_z$	120	Oscillatory	–	–	3.0×10^{13}
3	$Si_xN_yO_z$–BN	196	Oscillatory	150–250	4–8	–
4	$Si_xN_yO_z$–BN–Se	180	Oscillatory	100–200	5–9	2.1×10^{13}
5	SiO_2–Se	185	Smooth			2.3×10^{12}
6	$Si_xN_yO_z$–SiO_2–Se	150	Smooth			–
7	$Si_xN_yO_z$–BN–S	190	Oscillatory	80–130	4–14	9.9×10^{12}
8	SiO_2–S	170	Smooth			2.5×10^{12}

the shift to higher negative voltages and strong frequency dispersion (Fig. 5). The capacitance modulation portion in the *C–V* characteristic is observed in the voltage regions of $|U| \geq 11$ and 20 V at frequencies of $f = 10^3$ Hz and 10^6 Hz, respectively (Fig. 5, curves *1* and *2*). The largest conductance in the *G–V* curves was attained for $U_{max} = -16$ V ($f = 10^3$ Hz) and –32 V ($f = 10^6$ Hz) (Fig. 5, curves *1*' and *2*').

The use of the BN, SiO_2–BN, and $Si_xN_yO_z$–BN films as the insulating material causes a slight shift of the *C–V* and *G–V* curves to lower negative voltages. An appreciable shift of the *C–V* and *G–V* curves to low negative voltages was only observed for the GaAs-based MIS structures with S and Se atoms contained in the surface region of the semiconductor (Fig. 5, curves *3–5* and *3*'*–5*'). The largest shift of the *C–V* and *G–V* curves to $U = 0$, as well as the lowest frequency dispersion of these curves, were observed for the samples in which the insulator did not contain BN layers (Fig. 6). The largest conductance was independent of the test signal frequency for $U_{max} = 0$ V (Fig. 6, curves *1*'*–3*').

The density of surface states at the insulator–*p*-GaAs interface was calculated according to [7]. The computed N_{ts} values are given in the table. The lowest density of the surface states ($N_{ts} = (2.3–2.5) \times 10^{12}$ eV^{-1} cm^{-2}) was observed for the structure with the S or Se sublayers and insulating films containing no BN (samples 5 and 8). Periodic oscillations were absent on the insulator layer surface in these structures and the surface relief was less pronounced (Fig. 3). If BN was involved in the insulating composition, the incorporation of S or Se in the GaAs surface region did not cause a decrease in the density of surface states. The fragmentary corrugated mesa were formed on the exterior insulator surface (Fig. 4) and the density of surface states increased to 9.9×10^{12}–2.1×10^{13} eV^{-1} cm^{-2} (see table, samples 4 and 7).

Thus, the results of passivating the GaAs surface with S and Se atoms are largely governed by the material of insulating layers deposited on the semiconductor surface.

3.3. Investigations of the Elemental Composition of Insulating Films

The time dependences of intensity of the secondary-ion current for samples 3, 5, and 8 are shown in Fig. 7. The special feature of the secondary-ion emission spectra for the SiO_2–S(Se)–*p*-GaAs structures is the presence of S^+ (Se^+) ions not only at the insulator–GaAs interface, but also in the SiO_2 film (Figs. 7a, 7b). The S^+ ions were observed in the spectra of the $Si_xN_yO_z$–BN–S–*p*-GaAs structures at the BN–GaAs interface only, and were absent in the $Si_xN_yO_z$ film (Fig. 7c).

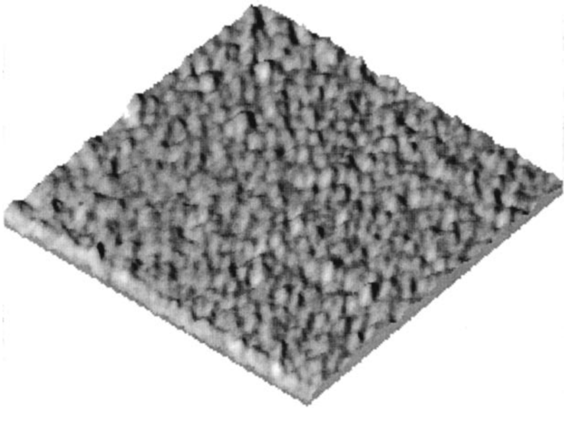

Fig. 4. AFM image of the surface of the $Si_xN_yO_z$–BN(Se) film. Layer thicknesses are $d_{Si_xN_yO_z} = 68$ nm and $d_{BN} = 128$ nm. Image size is 4.0×4.0 μm.

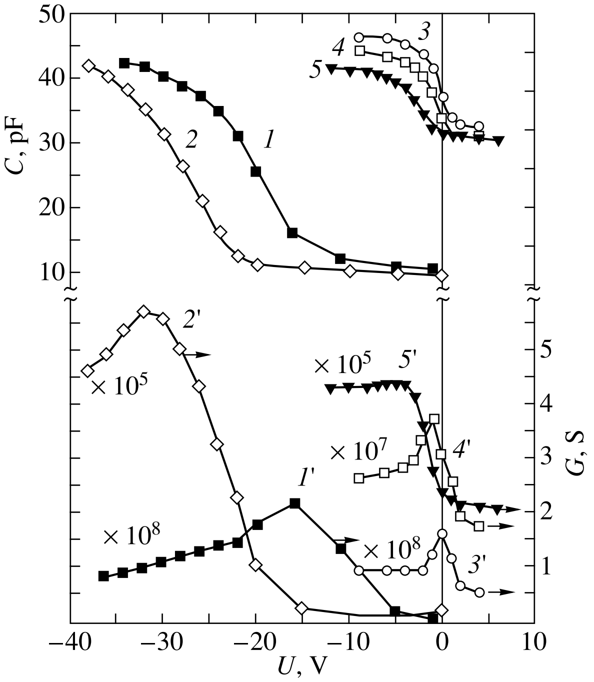

Fig. 5. Capacitance–voltage and conductance–voltage characteristics for the (*1*, *2*) NiCr–$Si_xN_yO_z$–*p*-GaAs and (*3*, *4*, *5*) NiCr–$Si_xN_yO_z$–BN–Se–*p*-GaAs structures at the frequencies f = (*1*, *1*', *3*, *3*') 10^3, (*4*, *4*') 2×10^4, and (*2*, *2*', *5*, *5*') 10^6 Hz.

4. DISCUSSION

The presence of the fragmented mesas on the surface of insulating films is caused by strong stresses that appear in the local flexure regions of the crystal lattice. Thus, the deposition and subsequent etching of the Si_3N_4 film on the surface of the SiO_2–Si structure caused a reversible variation in the density of surface states at the insulator–Si interface [8].

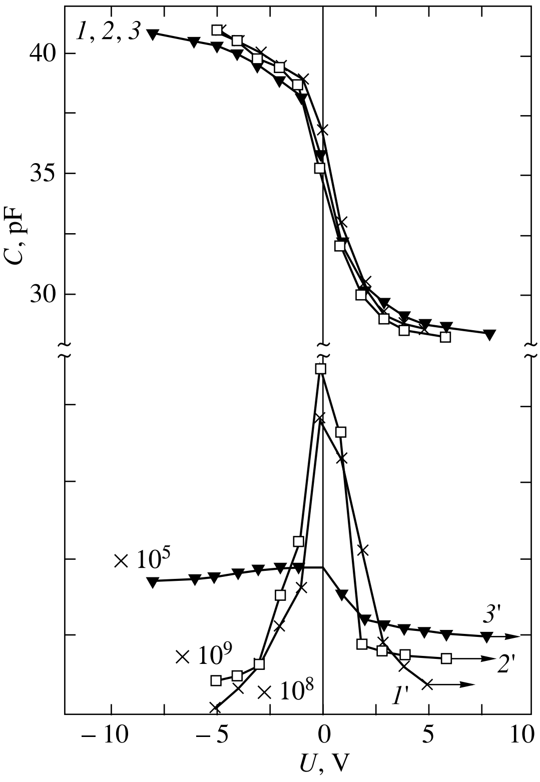

Fig. 6. Capacitance–voltage and conductance–voltage characteristics of the NiCr–SiO_2–Se–*p*-GaAs structures at frequencies f = (*1*, *1*') 10^3, (*2*, *2*') 2×10^4, and (*3*, *3*') 10^6 Hz.

The dependence of the density of surface states on the stresses was observed when the control-electrode thickness in Si-based MIS structures was varied [9].

A similar effect of stresses on the density of surface states was observed for the insulator–GaAs interface. As follows from the data listed in the table, a high density of surface states was obtained for the structures with a quasi-periodic surface relief.

Smoothing of the surface relief for the S- and Se-doped samples (samples 5, 6, and 8) can be explained if we assume that the chalcogen atoms play the role of surfactants. During growth of the SiO_2 or $Si_xN_yO_z$ films, the S(Se) atoms emerge above the surface of the growing film due to the vertical exchange, while the atoms of the substance deposited immediately sink below the surfactant layer. As a result, the lateral diffusion length for insulator atoms is decreased and the growth of three-dimensional islands is suppressed. The presence of chalcogens in the insulating films is confirmed by the secondary-ion mass spectroscopy data (Figs. 7a, 7b).

The BN layer apparently constitutes the barrier for diffusion of chalcogen atoms, and S and Se atoms do not penetrate into the insulating coating film (Fig. 7c). In this case, the insulating layer is strained, which manifests itself in periodic oscillations on the layer surface and high density of surface states on the insulator–GaAs interface.

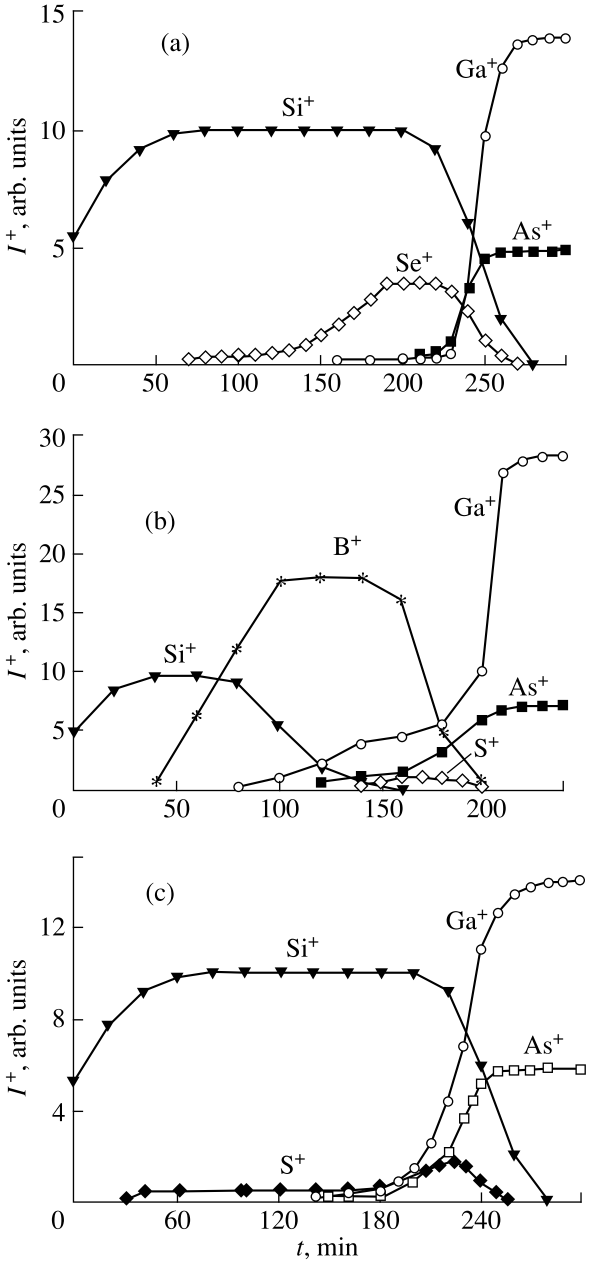

Fig. 7. Concentration profiles of positive ions in the (a) SiO_2–S–*p*-GaAs, (b) SiO_2–Se–*p*-GaAs, and (c) $Si_xN_yO_z$–BN–S–*p*-GaAs structures.

5. CONCLUSION

These investigations demonstrate that the periodic island mesas appear as corrugations on the surface of the thin insulating films deposited on the GaAs substrate. The existence of local flexure zones in the crystal lattice of the insulator induces strong stresses that give rise to a high density of surface states in the band gap of the semiconductor. Incorporation of S and Se atoms in the GaAs surface region smooths the surface relief of the SiO_2 and $Si_xN_yO_z$–SiO_2 films and lowers the density of surface states at the semiconductor–insulator interface.

ACKNOWLEDGMENTS

We thank L.N. Puchkareva for analysis of the elemental composition of insulating films.

REFERENCES

1. V. N. Bessolov and M. V. Lebedev, Fiz. Tekh. Poluprovodn. (St. Petersburg) **32** (11), 1281 (1998) [Semiconductors **32**, 1141 (1998)].
2. B. I. Bednyĭ, Soros. Obraz. Zh. **7**, 141 (1998).
3. V. I. Gaman, V. M. Kalygina, and A. V. Panin, Solid-State Electron. **43**, 583 (1999).
4. É. V. Buts, L. N. Vozmilova, V. I. Mitin, *et al.*, Élektron. Tekh., Ser. Mater. **9**, 46 (1982).
5. L. V. Khramova, T. P. Smirnova, and E. G. Eremina, Neorg. Mater. **28**, 1662 (1992).
6. A. V. Panin and N. A. Torkhov, Fiz. Tekh. Poluprovodn. (St. Petersburg) **34**, 698 (2000) [Semiconductors **34**, 671 (2000)].
7. V. I. Gaman, N. N. Ivanova, V. M. Kalygina, and E. B. Sudakova, Izv. Vyssh. Uchebn. Zaved., Fiz. **11**, 99 (1992).
8. E. D. Vasil'eva, M. N. Kolotov, V. I. Sokolov, *et al.*, Mikroélektronika **21**, 74 (1992).
9. V. A. Brazhnik, T. A. Dolgova, and A. B. Spiridonov, Élektron. Tekh., Ser. Mikroélektron. Ustroĭstva **1**, 48 (1990).

Translated by N. Korovin

Semiconductors, Vol. 35, No. 1, 2001, pp. 86–90. Translated from Fizika i Tekhnika Poluprovodnikov, Vol. 35, No. 1, 2001, pp. 84–88.
Original Russian Text Copyright © 2001 by Grinyaev, Chaldyshev.

Deep Levels Related to Gallium Atom Clusters in GaAs

S. N. Grinyaev* and V. A. Chaldyshev
Tomsk State University, Tomsk, 634050 Russia
**e-mail: gsn@phys.tsu.ru*

Submitted May 22, 2000; accepted for publication May 25, 2000

Abstract—The pseudopotential method and supercell ($8 \times 8 \times 8$) approach were used to study localized electron states introduced by tetrahedral clusters of gallium atoms into the band gap of GaAs. With increasing cluster size, the Fermi energy (E_F) rapidly reaches its limiting value close to the Schottky barrier height at the planar metal–semiconductor interface. The gap between the completely filled and empty size-quantization levels is 0.06 eV for the largest cluster of 159 gallium atoms. The energy position and "tails" of metal-induced gap states in the vicinity of E_F are governed by the outermost layers of Ga_{As} antisite defects. © *2001 MAIK "Nauka/Interperiodica".*

1. INTRODUCTION

Clusters of various defects modify the properties of semiconducting materials, frequently opening up new possibilities of their use in electronics. In recent years, the development of technologies allowing control over cluster growth has stimulated an upsurge of interest in materials of this kind. A prominent example is gallium arsenide with clusters of intrinsic defects, giving rise to a number of unique properties [1]. The properties of an imperfect crystal are largely determined by specific features of its electronic spectrum and the nature of interfacial states at the cluster–matrix heteroboundary. Actual materials contain various polyatomic clusters with symmetry depending on their size and growth conditions. A logical description of the electronic states in such crystals in terms of self-consistent methods taking into account the relaxation of the atomic structure, as it has been done for small clusters [2], seems to be impossible for the time being. At the same time, simple models of the jellium type [3] and the effective mass method [4] have limited applicability to semiconducting materials, being only valid at sufficiently homogeneous electron density and large clusters, when bulk band structure states are already formed. Therefore, semiempirical approaches remain the most efficient for describing spectra of complex semiconductor nanostructures. Consideration of the microscopic potential in terms of the tight binding [5], molecular orbital [6], empirical pseudopotential [7], and *k–p* [8] methods allows rather successful interpretation of size-quantization effects in spectra of free semiconducting clusters and quantum dots. We previously used an approach based on the supercell and model pseudopotential methods [9]. Taking explicit account of the point symmetry of an imperfect material, we managed to consider clusters containing hundreds of atoms. This method was applied to study localized states related to small tetrahedral clusters of arsenic in GaAs; the cubic symmetry of these clusters has been confirmed by structural studies of GaAs epitaxial films grown at low temperature.

This study is concerned with deep levels related to gallium clusters formed via substitution of arsenic atoms by those of gallium in the nearest coordination shells of GaAs. Of particular interest was to clarify the nature of states responsible for the Schottky barrier at the cluster–semiconductor heteroboundary. In contrast to [9], a much larger supercell ($8 \times 8 \times 8$) was used in this study, which furnished an opportunity to determine the limiting characteristics of the electronic spectrum in relation to the cluster size. To reveal the effect exerted by the shape of the heteroboundary between a metal inclusion and the surrounding matrix, electron states of $(GaAs)_n(Ga)_n$ superlattices modeling the planar metal–semiconductor interface were also considered.

2. CALCULATION PROCEDURE

The electronic energy spectrum of gallium arsenide with cluster defects was calculated by the local model pseudopotential method [9]. The ($8 \times 8 \times 8$) supercell contains 1024 atoms of which only a minor part (~10%) were replaced by atoms belonging to the cluster. This made it possible to neglect the overlapping of wave functions from neighboring cells and to obtain a band of deep levels with relatively small variance. In calculating the spectrum, 15 lower bands of the ideal GaAs were taken into account in the expansion of the wave function; the potentials of gallium atoms in inner layers were shielded by the electron density of the metal; other details of the method were described elsewhere [9]. The deep levels related to the cluster were identified with the states of a superlattice composed of periodically arranged clusters at the zero wave vector of the superlattice. Clusters were considered including up to 11 coordination shells and centered at the anion site of the GaAs lattice. Correspondingly, 5, 29, 47, 87, 123, and 159 atoms are contained in such clusters if all inner As atoms are replaced, and the boundary layer of Ga atoms in the embedding GaAs matrix is included into the cluster. The diameter of the largest cluster is ~17 Å. Defect-induced relaxation and distortion of the lattice were not taken into account. The rearrangement of the atomic structure changes positions of separate levels and, to a lesser extent, affects such integrated characteristics of the spectrum as the density of states and Schottky barrier height [10]. A calculated energy spectrum of GaAs with a single Ga_{As} antisite defect contains one level t_2 in the energy gap (this level is located at 0.28 eV above the top of the valence band), which, corrected for the spin–orbit splitting, is in agreement with experiment [11] and our previous calculation [12] for a (4 × 4 × 4) supercell. The charge density of states for this level is less localized compared with the density of the deeper state A_1 related to a single As_{Ga} defect [9], which leads to a more pronounced hybridization of the wave functions of neighboring Ga_{As} defects in the clusters.

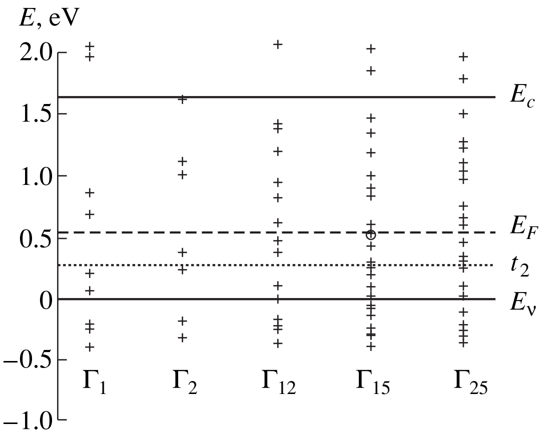

Fig. 1. Levels in GaAs with clusters composed of 159 gallium atoms. The positions of the t_2 level related to a single Ga_{As} antisite defect, Fermi level and conduction and valence band edges of the ideal GaAs crystal, E_c and E_v, are shown. The highest occupied level is circled.

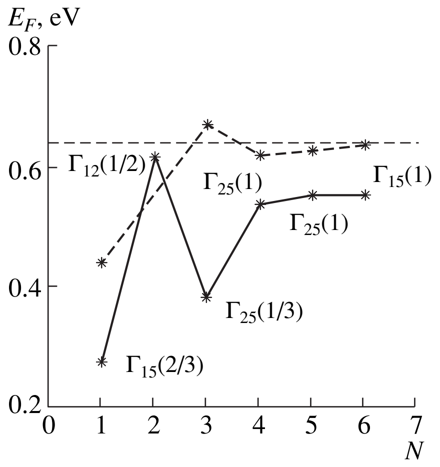

Fig. 2. Position of the Fermi level E_F vs. the number N of antisite defect layers in tetrahedral clusters of gallium atoms (solid line) and in $(GaAs)_n(Ga)_n$ superlattice (dashed line). Clusters composed of 5, 29, 47, 87, 123, and 159 atoms and superlattices with $n = N$ monolayers correspond to N = 1, …, 6. The symmetry of the highest occupied state and its occupancy (in parentheses) are given for the cluster material.

3. RESULTS OF CALCULATION AND DISCUSSION

Deep levels in GaAs with gallium clusters are formed from the localized states t_2 and resonance states of single Ga_{As} antisite defects. It follows from an expansion of a degenerate state of noninteracting defects in irreducible representations of the point symmetry group T_d of the cluster that most of cluster-related levels have symmetries Γ_{15} and Γ_{25}. Figure 1 presents an energy diagram of deep levels in GaAs with the largest cluster formed of 159 atoms, with the energies reckoned from the top of the valence band of the ideal crystal. The gap between the lowest unoccupied (Γ_{25}) and highest occupied (Γ_{15}) states is 0.06 eV. Analysis of the wave functions of the deep levels shows that they mainly originate from valence band states, with the contribution from conduction band states increasing to only ~10% for levels lying close to the conduction band bottom. The energy, symmetry, and occupancy of the highest occupied state depend on the cluster size. In clusters composed of 87 and 123 atoms, this state has the Γ_{25} symmetry and is completely filled. Figure 2 illustrates the variation in the Fermi level (E_F) with the number N of coordination shells containing defects in a cluster. Its position is defined as the midgap between the highest occupied and lowest unoccupied states. For small clusters (N = 1, 2, 3), the energy E_F varies nonmonotonically; with N growing further, it rapidly approaches the limiting value of ~0.55 eV.

To analyze the nature of deep levels, the charge density distribution was calculated for different states. Figure 3 presents a charge density map in the (111) plane within the periodicity unit of the supercell for one of the states of the degenerate Γ_{15} level associated with a cluster of 159 atoms. The density maps for other states of this level are obtained by rotation through 120° and 240°. The peaks of total density are mainly localized near the heteroboundary. Figure 4 shows the charge $\partial Z(r)/\partial r$ inside the sphere versus its radius r for the highest occupied states of different symmetries, related to the same cluster. States with the symmetry Γ_1 are inside the cluster with the highest probability, and those characterized by the symmetry Γ_2, with the lowest. For degenerate states (Γ_{12}, Γ_{15}, Γ_{25}), the derivative $\partial Z(r)/\partial r$, describing the radial density distribution, is the largest at the heteroboundary. Figure 5 shows the radial density per unit sphere surface area S_r for the states with

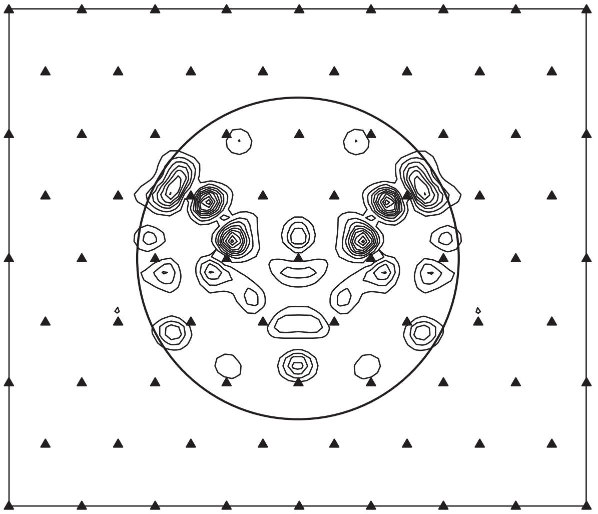

Fig. 3. Charge density of a state of the highest occupied level with Γ_{15} symmetry in GaAs with clusters composed of 159 gallium atoms in the (111) plane within the cross-section of a supercell. Density contours with the same charge are given in e/Ω units (Ω is the supercell volume), the minimum contour and the step between the contours is 4. The circle radius corresponds to the position of defects in the 10th coordination shell. Triangles show positions of atoms, with Ga atoms inside, and As atoms outside the sphere (in the given section).

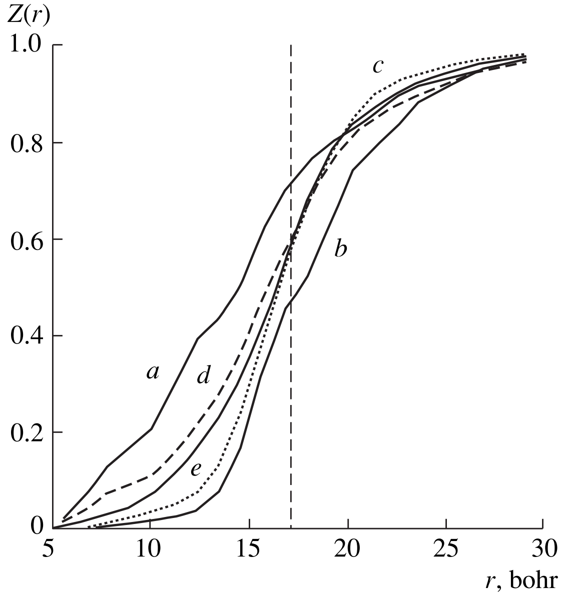

Fig. 4. Charge Z (in $e \cdot m$ units, where m is the degeneracy multiplicity for the level) inside the sphere vs. its radius r for upper occupied states with different symmetries related to a cluster composed of 159 gallium atoms: (*a*) Γ_1, (*b*) Γ_2, (*c*) Γ_{12}, (*d*) Γ_{15}, and (*e*) Γ_{25}. The vertical dashed line corresponds to the outer radius of the 10th coordination shell.

symmetry Γ_{12} and Γ_{15}, which characterizes the average density per unit volume at a distance r from the cluster center. Inside the cluster, this density oscillates, with its peaks somewhat shifted away from the coordination shells, owing to the overlapping of defect potential tails. The decrement of density into the GaAs region (~3.5 Å) is determined by the mean imaginary component of the wave vector of the smallest loop in the complex band structure of GaAs at an energy equal to that of the deep level.

To clarify the origin of localized states lying near the Fermi level, deep levels were calculated for a cluster in which Ga atoms were replaced by As only in the 10th coordination shell (24 defects). The highest occupied state of this cluster is transformed with respect to representation Γ_{12} and has an energy nearly coinciding with the energy of the Γ_{15} state for a cluster of 159 atoms. The Fermi levels of these two clusters are also close, and the averaged charge densities for the states of the same symmetry are similar in the vicinity of the heteroboundary (Fig. 5). Some discrepancies between the energies of the corresponding cluster-related levels lead to correlated shifts of their charge densities. For the states with the Γ_{12} symmetry, the main charge resides near the metal–semiconductor interface. Thus, deep levels forming the Schottky barrier are related to states originating from the outer layer of $\mathrm{Ga_{As}}$ antisite defects. The Fermi level pinning by ultrathin planar metal layers (about one monolayer thick) has been established previously [13]. Owing to the interaction of states related to the 10th coordination shell with the states associated with the cluster of 123 atoms, the levels are shifted, and the symmetry of the highest occupied state changes. However, the difference between the numbers of states pushed above, and sinking below, the E_F level coincides with the deficit of valence electrons in the last imperfect layer, and, therefore, the position of the Fermi level remains unchanged. We note that the charge densities of cluster states related to the outer imperfect layer have the highest symmetry with respect to the heteroboundary and the smallest dipole moment, which was reflected (albeit in a somewhat different interpretation) in Tersoff's zero-dipole model [14] used to determine the Schottky barrier height.

Obviously, with growing cluster size and for a sufficiently large supercell, the Fermi level must tend to a certain limiting value corresponding to a metal–semiconductor contact with the planar interface. A surface with infinite Miller indices corresponds to this limit for tetrahedral clusters. For the well-understood (001) and (110) interfaces, the Schottky barrier heights for GaAs are almost identical [15, 16], which also would be expected for interfaces with other orientations. The dependence of the energy E_F on the metal layer thickness was studied in $(\mathrm{GaAs})_n(\mathrm{Ga})_n$ (001) superlattices, where n is the number of monolayers ($n = 1,\ldots, 6$). Metal layers were considered as having a zinc-blende

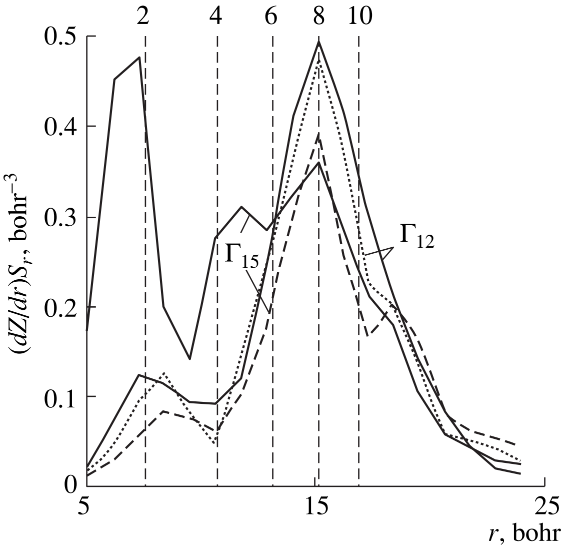

Fig. 5. Radial charge density for outer occupied states of a cluster containing 159 gallium atoms (solid line) and 24 antisite Ga_{As} defects within the 10th coordination shell (dashed line). The vertical dashed lines correspond to the outer radii of the coordination spheres (2, 4, 6, 8, 10) with defects.

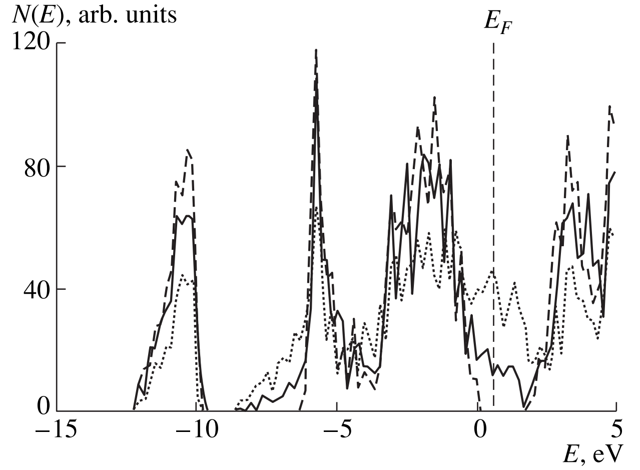

Fig. 6. Electron state density of an ideal GaAs crystal (long dashes), $(GaAs)_6(Ga)_6$ superlattice (short dashes), and gallium arsenide with clusters composed of 159 gallium atoms (solid line).

structure and were obtained by adding the planes of Ga_{As} antisite defects to GaAs. A calculated dependence of the energy of the highest occupied state on the superlattice layer thickness is shown in Fig. 1. E_F mainly changes over the first 2–3 monolayers, when the interaction between states related to defects at opposite boundaries is still significant. For $n = 6$, the Fermi energy is 0.64 eV, which, with correction made for the spin–orbit splitting of the valence band of GaAs, is in good agreement with the experimental Schottky barrier heights for the planar GaAs–Ga(110) interface, which are 0.56(0.59) eV for $p(n)$-type GaAs [16]. We note that the pinning of the Fermi level in GaAs with tetrahedral clusters and metal layers is achieved at approximately the same number of Ga_{As} antisite-defect layers (planar or spherical), when the interaction of states related to outer layers becomes negligible. The fact that the values of E_F are somewhat different for these two cases can be attributed to the effect of surface deformation and to the increasing role of hybridization of states related to large clusters from neighboring cells. Figure 6 presents density-of-state histograms for a cluster composed of 159 atoms and a superlattice with an $n = 6$, plotted with an energy step of 0.15 eV. It can be seen that, despite the different shapes of metal inclusions, their densities of states are in many respects similar, with the difference mainly accounted for by a multiplier proportional to the ratio of defect densities in the two materials.

Thus, gallium arsenide with small clusters containing gallium atoms is a narrow-gap semiconductor with an effective band gap < 0.1 eV, which allows the use of this material in IR devices if the density of such clusters is sufficiently high. Gallium clusters act as quantum wells for electrons and holes. Similar results would also be expected for other microscopic metal inclusions (e.g., Al or In) whose atomic potentials and Schottky barrier heights are close.

It is demonstrated that pinning of the Fermi level and formation of the Schottky barrier at the planar metal–semiconductor and metallic cluster–semiconductor interfaces is due to states originating from Ga_{As} antisite defects in the interfacial layers. These states act simultaneously as metal-induced gap states and deep levels related to single Ga_{As} defects, “renormalized” due to interaction. From this standpoint, the Heine [17] and Spicer et al. [18] models are not alternatives, as is commonly believed [14–16, 19], but closely related and complementary.

ACKNOWLEDGMENTS

This study was performed in the framework of the Program “Fullerenes and Atomic Clusters” and was supported by the Russian Foundation for Basic Research.

REFERENCES

1. M. G. Mil’vidskiĭ and V. V. Chaldyshev, Fiz. Tekh. Poluprovodn. (St. Petersburg) **32**, 513 (1998) [Semiconductors **32**, 457 (1998)].
2. J.-Y. Yi, Phys. Rev. B **61**, 7277 (2000); I. Vasiliev, S. Ogut, and J. R. Chelikowsky, Phys. Rev. B **60**, R8477 (1999); A. Rubio, J. A. Alonso, X. Blase, *et al.*, Phys. Rev. Lett. **77**, 247 (1996); D. Nehete, V. Shah, and D. G. Kanhere, Phys. Rev. B **53**, 2126 (1996); U. Rothlisberger, W. Andreoni, and M. Parrinello, Phys. Rev.

Lett. **72**, 665 (1994); J.-Y. Yi, D. J. Oh, and J. Bernholc, Phys. Rev. Lett. **67**, 1594 (1991).
3. E. Koch, Phys. Rev. Lett. **76**, 2678 (1996); W. Ekardt, Phys. Rev. B **31**, 6360 (1985).
4. Y. Wang and N. Herron, Phys. Rev. B **42**, 7253 (1990).
5. P. E. Lippens and M. Lannoo, Phys. Rev. B **39**, 10935 (1989).
6. A. M. Mazzone, Phys. Rev. B **54**, 5970 (1996).
7. M. V. Rama Krishna and R. A. Friesner, Phys. Rev. Lett. **67**, 629 (1991).
8. L. W. Wang and A. Zunger, Phys. Rev. B **54**, 11417 (1996).
9. S. N. Grinyaev and V. A. Chaldyshev, Fiz. Tekh. Poluprovodn. (St. Petersburg) **30**, 2195 (1996) [Semiconductors **30**, 1144 (1996)]; Fiz. Tekh. Poluprovodn. (St. Petersburg) **32**, 1094 (1998) [Semiconductors **32**, 980 (1998)].
10. C. Berthod, N. Binggeeli, and A. Baldereschi, Phys. Rev. B **57**, 9757 (1998).
11. C. Corbel, F. Pierre, K. Saarinen, and P. Hautojarvi, Phys. Rev. B **45**, 3386 (1992).
12. S. N. Grinyaev and V. A. Chaldyshev, Izv. Vyssh. Uchebn. Zaved., Fiz. **39**, 13 (1996).
13. P. R. Skeath, I. Lindau, P. Pianetta, *et al.*, J. Electron Spectrosc. Relat. Phenom. **17**, 259 (1979).
14. J. Tersoff, Phys. Rev. B **30**, 4874 (1984).
15. T. Bechshtedt and R. Enderlein, *Semiconductor Surfaces and Interfaces. Their Atomic and Electronic Structures* (Akademie-Verlag, Berlin, 1988; Mir, Moscow, 1990).
16. F. Flórez and C. Tejedor, J. Phys. C **20**, 145 (1987).
17. V. Heine, Phys. Rev. **138**, 1689 (1965).
18. W. E. Spicer, P. W. Chye, P. R. Skeatch, *et al.*, J. Vac. Sci. Technol. **16**, 1422 (1979).
19. P. Phatak, N. Newman, P. Dreszer, and E. R. Weber, Phys. Rev. B **51**, 18003 (1995).

Translated by M. Tagirdzhanov

Semiconductors, Vol. 35, No. 1, 2001, pp. 91–92. Translated from Fizika i Tekhnika Poluprovodnikov, Vol. 35, No. 1, 2001, pp. 89–91.
Original Russian Text Copyright © 2001 by Prykina, Polygalov, Kopytov.

LOW-DIMENSIONAL SYSTEMS

Vibrational Spectra of Strained (001) ZnSe/ZnS, ZnSe/ZnTe, and ZnS/ZnTe Superlattices in Terms of the Keating Model

E. N. Prykina*, Yu. I. Polygalov, and A. V. Kopytov
Kemerovo State University, ul. Krasnaya 6, Kemerovo, 650043 Russia
** e-mail: lena@asdul.kuzbe.elektra.ru*

Submitted January 24, 2000; accepted for publication June 16, 2000

Abstract—The dynamics of strained (001) ZnSe/ZnS, ZnSe/ZnTe, and ZnS/ZnTe superlattices is calculated in terms of the Keating model, taking into account the long-range Coulomb force. The effect of a plane deformation on the phonon spectra of bulk materials and superlattices is studied. The dependence of a strain-induced shift of the studied modes on the number of monolayers and relative thickness of constituents is analyzed. *© 2001 MAIK "Nauka/Interperiodica".*

We studied the semiconductor isocation strained superlattices (SL), ZnS/ZnSe (lattice constant mismatch is ~4.5%), ZnSe/ZnTe (~7.7%), and ZnS/ZnTe (~12.7%), formed by sphalerite-structure crystals. Along with the size effects, strain also considerably affects the properties of these superlattices. For example, the strain produced as a result of accommodation of different layers leads to a considerable change in the energy band structure (splitting in the Brillouin zone, shift of energy band edges), the optical phonon shift relative to the modes of the bulk materials. We also studied the effect of biaxial deformation (which is a result of accommodation of composite layers to each other and to the substrate) on the phonon spectra of ZnSe/ZnS, ZnSe/ZnTe, and ZnS/ZnTe superlattices. Both short-period SLs and those with a period comparable to or exceeding the critical value of layer thickness [1, 2] were considered.

We calculated the phonon spectra in ZnS/ZnSe, ZnSe/ZnTe, and ZnS/ZnTe superlattices using the Keating model [3] that provides a qualitative explanation for the main features of phonon spectra in ionic–covalent crystals. The model also facilitates an interpretation of the results from the chemical-bond theoretical standpoint (in terms of effective charge, force constant, and contribution of covalent and ionic bondings). We have already successfully used the Keating model to study the vibrational properties of matched SLs [4] and low-strained SLs with low ionicity [5]. In the optical range, the Keating model yields a quantitative agreement with experimental data within 10% [3–5], whereas, in the low-frequency region, the discrepancy between the experiment and theoretical calculations is noticeably larger. For example, the discrepancy between the predicted and experimental transverse acoustic modes of bulk compounds is about 40% at point *X*, which is typical of the Keating model applied to III–V compounds [4, 5]. For II–VI compounds, with ionicity higher than that in III–V compounds, the Keating model yields a result that deviates still more from the experiment [3]. It should be mentioned however that the qualitative description of phonon spectrum was in line with predictions of the more elaborate theoretical models [6].

The short-range interaction taken into account by the Keating model up to the second coordination shell can be described by force constants of two types: α (central interaction) and β (noncentral interaction). The Coulomb part of the dynamic matrix was constructed in the rigid point-ion approximation. The parameters of the model (see table) were determined by fitting the long-wavelength longitudinal ω_{LO} and transverse ω_{TO} optical frequencies and elastic constants C_{11} and C_{12} of bulk crystals to experimental values. We took β at the interface as an average of the corresponding parameters of bulk compounds. As can be seen from the table, the chemical bond ionicity (effective charge *Z*) increases in the direction from sulfide to telluride. The strain effect on SL dynamics was taken into account geometrically, in terms of Poisson displacement of atom in the direction of growth. We consider the two cases: first, when the lattice constant parallel to the interface is equal to the lattice constant of a substrate and, second, the "free position" of SL, when the mismatch of lattice constants is accommodated by extension and contraction of the layers close to the interphase, thus providing for an equillibrium $a_{\parallel}$ [7].

Force constants in II–VI compounds (α and β are given in 10^3 dyne/cm, *Z* is given in units of electron charge)

Compound	α	β	*Z*
ZnS	41.38	4.83	0.902
ZnSe	32.50	4.23	0.837
ZnTe	28.50	4.43	0.745

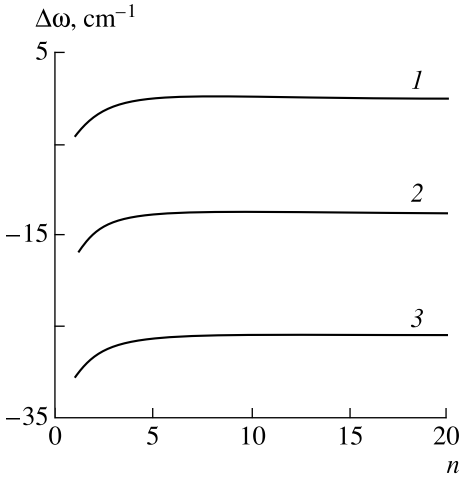

Fig. 1. Frequency shift of ZnS-like LO-modes in $(ZnS)_n(ZnSe)_n$ $\Delta\omega = \omega(CP) - \omega(ZnS)$ versus the number of monolayers n for (*1*) ZnS substrate, (*2*) free position of SL, and (*3*) ZnSe substrate.

We have calculated the frequency shifts $\Delta\omega = \omega(CP) - \omega(ZnS(Se))$ of ZnS-like LO-phonons in $(ZnS)_n(ZnSe)_n$ and $(ZnS)_n(ZnTe)_n$ SLs relative to LO-mode of bulk ZnS and ZnSe-like LO-phonons in $(ZnSe)_n(ZnTe)_n$ SL relative to LO-mode of bulk ZnSe. In ZnS/ZnSe SL, for both the ZnSe substrate and the free position of SL, the frequency of ZnS-like LO-modes decreases compared to the LO-mode in the bulk ZnS (Fig. 1). When a ZnSe substrate is used, the frequency shift obtained for $n = 1$ is $\Delta\omega = 41$ cm^{-1} (which amounts to 10% of the calculated frequency in the bulk ZnS); for $n = 20$, we have $\Delta\omega \approx 24$ cm^{-1} (6%). When SL is in the free position, $\Delta\omega \approx 28$ cm^{-1} (7%) for $n = 1$, and $\Delta\omega \approx 11$ cm^{-1} (2%) for $n = 20$. As evident from Fig. 1, the maximum shift of ZnS-like LO-modes in $(ZnS)_n(ZnSe)_n$ SL occurs in monolayer SLs. Similar trends are observed for the frequency shift of ZnS- and ZnSe-like modes in ZnS/ZnTe and ZnSe/ZnTe SLs.

We used the technique described elsewhere [4] to evaluate the percent contribution of the bulk modes into the vibrational states of the studied SLs. Thus, the main contribution to the upper ZnS-like LO-mode is made by the center of the Brillouin zone of sphalerite. In ZnS/ZnSe SL (free position of SL), for $n = 1$ and $n = 5$, the contribution of phonon states of the bulk zinc sulfide to the vibrational state of the studied mode is 75% and 50%, respectively. Hence, an increase in the number of monolayers enhances the contribution of the peripheral parts of the sphalerite Brillouin zone.

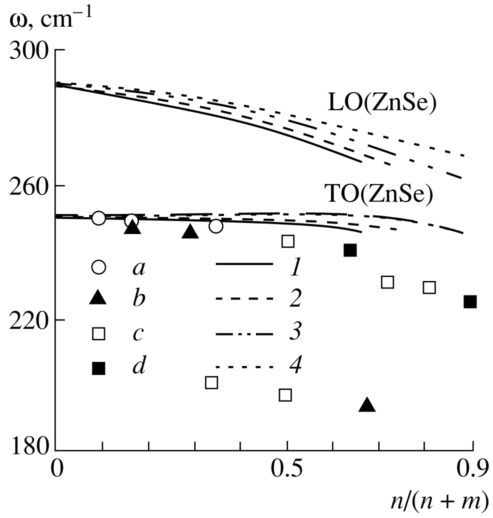

Fig. 2. Frequencies of ZnSe-like LO- and TO-modes in $SL(ZnSe)_m(ZnTe)_n$ versus the layer thickness ratio $n/(n + m)$, where n is the number of monolayers in ZnTe and m is the number of monolayers in ZnSe. Keating model prediction for (*1*) $n = 2$, (*2*) $n = 3$, (*3*) $n = 8$, and (*4*) $n = 16$. Experimental data according to [8] with (*a*) $n = 2$, (*b*) $n = 3$, (*c*) $n = 8$, and (*d*) $n = 16$.

We also calculated the frequencies of ZnS-like modes in $(ZnS)_n(ZnSe)_m$, $(ZnS)_n(ZnTe)_m$ SL and ZnSe-like modes in $(ZnS)_n(ZnTe)_m$ SL in relation to the thickness ratio $n/(n + m)$. The corresponding curves for ZnSe/ZnTe SL are shown in Fig. 2. Here, geometrical symbols stand for the experimental results [8], and the solid curve is derived in the Keating approximation. It is evident from Fig. 2 that the calculation of LO- and TO-phonons is in qualitative agreement with the experiment. Thus, with an increase in $n/(n + m)$ (n and m denote the number of monolayers in the compounds), the frequencies of the studied modes become lower. It should be noted that, for constant $n/(n + m)$ and unequal n and m, the frequencies of the studied modes are different due to an increase in the ZnTe fraction in ZnSe/ZnTe, ZnS/ZnTe SL as well as the ZnSe fraction in ZnS/ZnSe. For example, in a ZnSe/ZnTe SL with $n = m = 2$, the frequency of ZnSe-like LO-mode amounts to $\omega \approx 275$ cm^{-1}, while, for $n = m = 16$, we have $\omega \approx 279$ cm^{-1} (in both cases, $n/(n + m) = 0.5$).

REFERENCES

1. L. H. Shon, K. Inoe, O. Matsuda, and K. Murase, Solid State Commun. **67**, 779 (1988).
2. L. H. Shon, K. Inoe, and K. Murase, Solid State Commun. **62**, 621 (1987).
3. R. Martin, Phys. Rev. B **1**, 4005 (1970).
4. E. N. Prykina, Yu. I. Polygalov, and A. V. Kopytov, Available from VINITI, No. 3643-V98 (1998).
5. E. N. Prykina, Yu. I. Polygalov, and A. V. Kopytov, Available from VINITI, No. 3961-V98 (1998).
6. K. Kunc, M. Balkanski, and M. Nusimovici, Phys. Status Solidi B **72**, 229 (1975).
7. M. Herman, *Semiconductor Superlattices* (Akademie-Verlag, Berlin, 1986; Mir, Moscow, 1989).
8. S. Nakashima, Y. Nakakura, H. Fujiyasu, and K. Mochizuki, Appl. Phys. Lett. **48**, 236 (1986).

Translated by A. Sidorova-Biryukova

Semiconductors, Vol. 35, No. 1, 2001, pp. 93–98. Translated from Fizika i Tekhnika Poluprovodnikov, Vol. 35, No. 1, 2001, pp. 92–97.
Original Russian Text Copyright © 2001 by Zvonkov, Karpovich, Baĭdus’, Filatov, Morozov.

LOW-DIMENSIONAL SYSTEMS

Influence of Bismuth Doping of InAs Quantum-Dot Layer on the Morphology and Photoelectronic Properties of Gas/InAs Heterostructures Grown by Metal-Organic Chemical Vapor Deposition

B. N. Zvonkov*, I. A. Karpovich, N. V. Baĭdus’, D. O. Filatov, and S. V. Morozov
Lobachevskii Nizhni Novgorod State University, pr. Gagarina 23, Nizhni Novgorod, 603600 Russia
** e-mail: get@phys.unn.runnet.ru*

Submitted April 24, 2000; accepted for publication June 16, 2000

Abstract—GaAs/InAs quantum dot (QD) heterostructures prepared by metalloorganic chemical vapor deposition (MOCVD) are investigated. It is established that the introduction of isovalent bismuth doping during the growth of InAs QD layer results in the suppression of the nanocluster coalescence and favors the formation of more uniform QDs. Bismuth itself is virtually not incorporated into the dots, its role being mainly in limiting the migration mobility of atoms at the surface of the growing layer. A method for investigating the morphology of buried layers of InAs QDs in GaAs matrix by atomic-force microscopy is developed; it relies on the removal of the cap layer by selective chemical etching. The photoluminescence (PL) and photoelectric sensitivity spectra of the fabricated heterostructures and their relation to the morphology of the QD layer are studied. In doped structures, PL and selective photosensitivity owing to the QDs are observed at a wavelength of 1.41 μm with the linewidth of 43 meV at room temperature. Some of the morphological features and photoelectronic properties of the MOCVD-grown heterostructures are related to the formation of a transitional layer at the GaAs/InAs QD interface due to the diffusion-induced mixing of the components. © *2001 MAIK “Nauka/Interperiodica”.*

Investigations of heterostructures with self-organized GaAs/InAs quantum dots (QDs) attract much attention due to the broad prospects for their use in optoelectronics, in particular for the development of high-efficiency injection lasers [1]. QD heterostructures are mainly fabricated by molecular-beam epitaxy (MBE) technique. The technique of chemical-vapor deposition from metalloorganic compounds (MOCVD), which is employed successfully to produce heterostructures with quantum wells (QWs), is much less commonly used, because of the difficulties in controlling the growth and self-assembly of the QDs, as well as some other drawbacks of this method. However, the relative simplicity and commercial advantages of the MOCVD technique motivate the efforts to overcome its drawbacks.

The morphology and photoelectronic properties of InAs QD layers grown by MBE and MOCVD can differ significantly due to the influence of a chemically active atmosphere and, usually, higher QD-heterostructure growth temperatures typical of the latter technique on the QD layer self-organization processes. One of the serious problems related to the growth of QDs by MOCVD is ensuring the suppression of the nanocluster coalescence at the growth temperatures optimal for the optical properties of the fabricated QD heterostructures. Coalescence results in enhanced variation in the QD sizes, reduced surface density of the QDs, as well as in the formation of a significant number of relatively large relaxed clusters in the QD layer, which adversely affect its morphology and photoelectronic characteristics [2]. In this study, we examine the possibility of coalescence suppression by doping the growing InAs QD layer with isovalent Bi impurity. It was assumed (and confirmed experimentally) that the emergence of heavier and larger Bi atoms at the growth surface should limit the migration mobility of In and As atoms and prevent their coalescence.

1. EXPERIMENTAL

GaAs/InAs QD heterostructures were grown by atmospheric pressure MOCVD on the surface of semi-insulating GaAs substrates disoriented from the (100) plane by 3° in the [110] direction. A *n*-GaAs 0.8-μm-thick buffer layer was grown at 600°C; the temperature was then reduced to 530–510°C and the InAs QD layer was deposited. Trimethylindium and arsine were alternately fed to the reactor during intervals of six and two seconds, respectively, separated by a 4-s interval, and the number of cycles was up to 10. The estimated nominal thickness of the InAs layer is ~1.5 nm (about 5 monolayers). Doping with bismuth in the course of the QD layer deposition was performed by sputtering a target, installed at 12 cm from the substrate in the cold reactor zone, with the beam of a *Q*-switched YAG:Nd

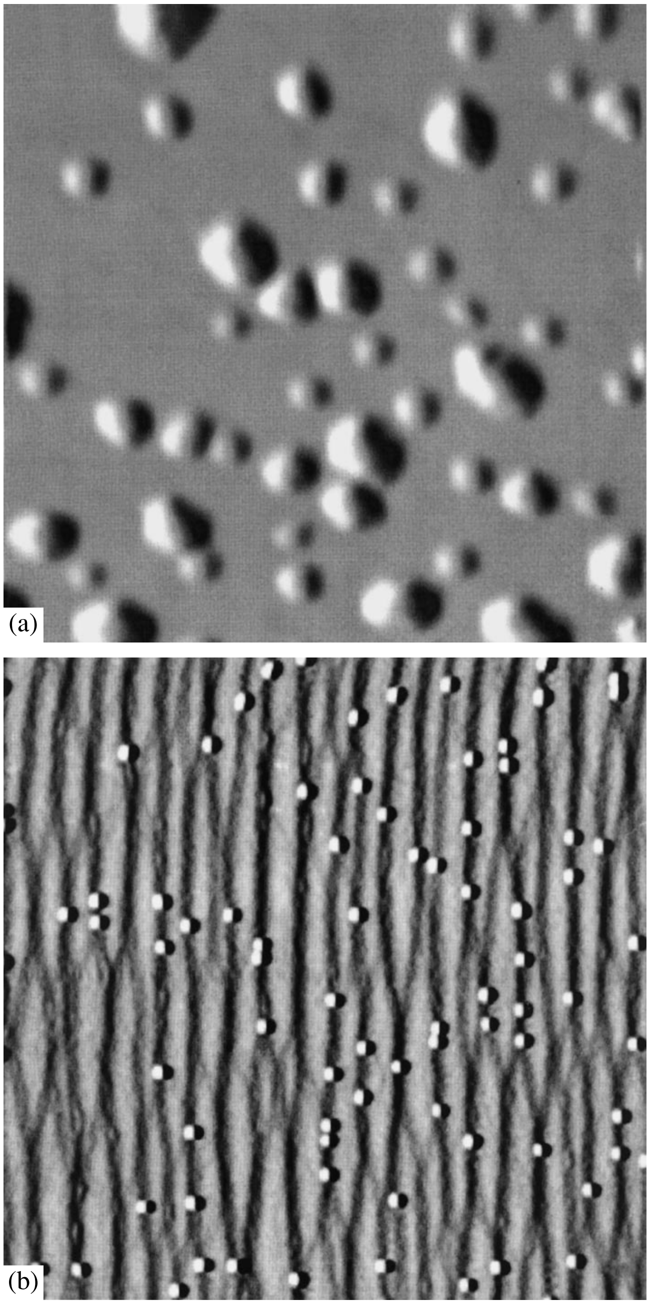

Fig. 1. AFM images of (a) undoped and (b) Bi-doped uncapped QD layers; area scanned is 1 × 1 μm^2.

laser. The density of the deposited Bi atoms was estimated at ~10^{14} cm^{-2}.

The structures without a capping layer and with a ~15-nm-thick GaAs capping layer were grown. Morphology of the QD layer was studied by atomic-force microscopy (AFM) using an Accures TMX-2100 microscope in the contact mode. The spectra of the QD-heterostructure photoluminescence (PL) at 77 and 300 K and of capacitor photovoltage (CPV) at 300 K were investigated as well. The techniques used in optical and photoelectric measurements are described elsewhere [3].

2. DISCUSSION

2.1. Morphology of the QD Layer

AFM studies demonstrated that doping with bismuth during the growth and self-organization of the InAs QD layer suppresses coalescence and favors the formation of clusters (QDs) with a more uniform size distribution. This is especially evident when the indium concentration is moderate. Figure 1 shows AFM images of uncapped QD layers grown at 530°C without doping (a) and with bismuth doping (b). In the first case, a significant spread in the cluster lateral sizes and heights is observed, and a considerable number of large, obviously relaxed clusters, whose lateral dimensions and heights are as large as 200 and 50 nm, respectively, are present. In the second case, large clusters are virtually absent, and pseudomorphous clusters are highly uniform both in lateral size (~40 nm) and height (~6 nm). However, surface density of the dots is not high ($N_s^{QD} \approx 4 \times 10^9$ cm^{-2}).

It has been previously established [2] that deposition of a thin (~15 nm) cap layer immediately after growing the QD layer also leads to the suppression of coalescence and to the dissolution of the relaxed clusters that are not very large, with the formation of craters in place of them; the pseudomorphous clusters, however, are not dissolved. Total suppression of the formation of large clusters during the growth of a QD layer by conventional MOCVD technique is not achieved. Large clusters extend beyond the thin cap layer, which impairs its morphology and particularly hinders the formation of high-quality multilayer QD arrays.

When a Bi-doped QD layer is capped in a similar way, the AFM image of the structure surface usually has the same appearance as the image obtained without the QD layer: only terraces with a step height of about 2 nm can be seen. Using a slow selective etchant that is characterized by low InAs etch rate on this surface reveals the buried QD layer and its morphology. We note that this is especially important for MOCVD-grown QD heterostructures, since the morphology of buried QD layers may differ significantly from the morphology of the surface ones, which are commonly the subject of the AFM studies [2].

In Fig. 2, we show an AFM image of a doped QD layer taken after etching off the 15-nm-thick cap layer. Although partial etching of the clusters is possible, such an image gives an idea of the size and surface density of the QDs. One can see that two cluster types exist. The lateral size and height of larger clusters are close to those characteristic of the uncapped QD layers; the density of this type of QDs in the sample under study equals $N_s^{QD} \approx 1.6 \times 10^{10}$ cm^{-2}. Smaller clusters, whose density is of the same order of magnitude, are less uni-

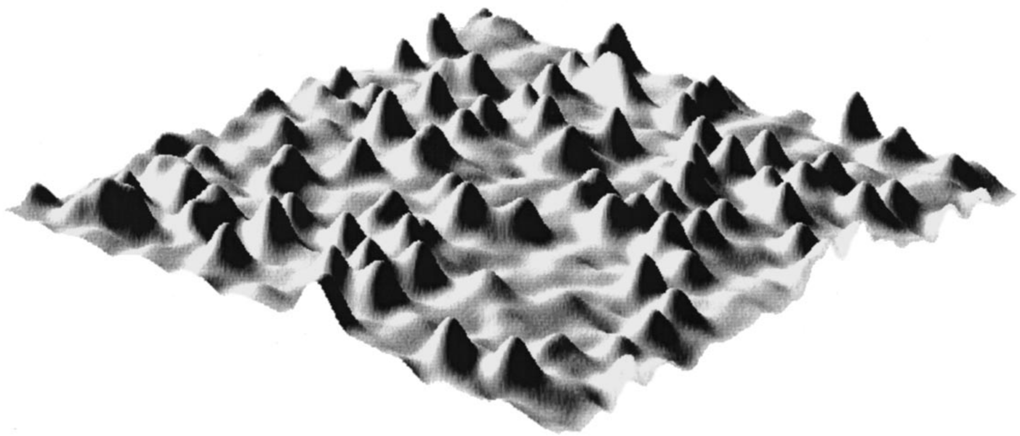

Fig. 2. AFM image of a QD layer opened by etching off of a 15-nm-thick cap layer; area scanned is 0.75 × 0.75 μm^2.

form in their size, probably due to the stronger etching effect. Their average lateral size and height equal ~30 nm and ~1.6 nm, respectively. It should be noted that such clusters are not observed in the uncapped QD layers. Thus, we may assume that they either disappear at a free surface due to coalescence or are formed only after the deposition of the cap layer as a result of wetting layer reconstruction. Reconstruction may be caused by an increase in the elastic strain in a relatively thick wetting layer that originally formed at the free surface. A simple calculation indicates that changing the wetting layer thickness by one monolayer is sufficient for the formation of clusters with the sizes and density given above. Since other explanations of the origin of these nanorelief features observed at the etched surface also exist (remnants of the etched-off large clusters, nonuniform etching, etc.), additional arguments corroborating the real existence of the small clusters (QDs) will be presented below.

Increasing In content in the QD layer results in an increased surface density of the QDs, but, with an unchanged supply of Bi, the effectiveness of coalescence suppression is reduced, and large clusters appear. However, the uniformity of pseudomorphous clusters (QDs) remains significantly higher than that in the undoped QD layers, which is evidenced by the PL and CPV spectra (see below). It is possible that after the corresponding optimization of In and Bi fluxes, one can achieve an increase in the QD density, avoiding at the same time the large cluster formation, which impairs the layer morphology.

2.2. Photoluminescence of Quantum-Dot Heterostructures

Figure 3 illustrates the effect of the Bi-doped QD layer deposition temperature T_d on the QD-heterostructure PL spectra recorded at 77 K. For T_d = 550°C, the QD emission band is broadened considerably and shifted to higher energies, its peak being at $h\nu_m$ = 1.185 eV. For lower deposition temperatures, narrower PL peaks, which shift to lower energies with decreasing T_d, are observed; however, the PL intensity is reduced. Optimal temperatures, corresponding to the smallest PL-band width at half-maximum Γ^{QD} (equal to 35–40 meV) and sufficiently high PL intensity, range from 510 to 530°C. In addition to the ground-state optical transition, transition to the first excited state of the QD becomes clearly resolved as well in the structures grown at these temperatures (curve *3*). It is separated by ~85 meV from the ground-state transition, which provides for good QD properties at room temperature. In undoped QD heterostructures, the smallest Γ^{QD} value is about 55 meV. It should be mentioned that, in some of the doped QD heterostructures, anomalously broad PL bands (Γ^{QD} up to 200 or even 300 meV) were observed. Their structure indicates that QDs of several characteristic sizes are formed. Nonuniformities of this kind are

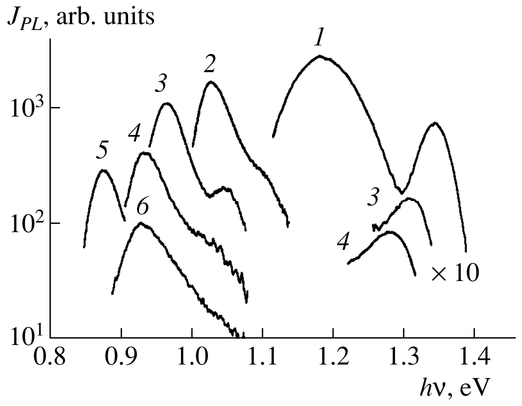

Fig. 3. PL spectra (recorded at 77 K) for QD layer deposition temperature T_d equal to (*1*) 550, (*2*) 530, (*3*) 510, (*4*) 490, (*5*) 490 (the spectrum taken at room temperature), and (*6*) 470°C.

probably related to some particular uncontrolled properties of the substrates, but the immediate cause of appearance of these anomalously broad PL bands is not yet established.

As Fig. 3 demonstrates, QD heterostructures with a PL peak energy $h\nu_m$ as low as 0.93 eV at 77 K (curves *4*, *6*) can be obtained by the MOCVD technique. This energy falls in the wavelength region around 1.3 μm, important for applications in optoelectronics; in MBE-grown QD heterostructures, such low values of $h\nu_m$ are usually obtained only at 300 K in the samples where QDs are covered by an external QW [4, 5] layer. In doped QD heterostructures, the PL intensity at room temperature was only 2–3 times lower than that at 77 K. The lowest $h\nu_m$ obtained equals 0.87 eV (1.41 μm), and the band width was 43 meV (curve *5*).

Some of the specific morphological and photoelectronic properties of the QD heterostructures under study, such as low ground-state transition energies, fairly high structural quality, and manifestation of quantum properties at 300 K for nanoclusters of sufficiently large size (as evidenced by AFM), which contradicts some estimates [1], can be explained assuming that, due to the diffusion-induced mixing at the GaAs/InAs QD interface during the MOCVD process, a transitional solid-solution layer is formed, which acts as a covering QW. Its presence leads to the redistribution and partial relaxation of the elastic stresses and to a change in the shape of the QD potential, which results in a corresponding change in the QD energy spectrum. We note that low PL peak energies cannot be attributed to incorporation of Bi in the QDs themselves, since similar values of $h\nu_m$ were obtained for undoped QD heterostructures [6]. Owing to the large size of the Bi atoms, they are most likely driven away to the QD-heterostructure surface rather than being incorporated into the QDs in noticeable amounts. This is evidenced by the formation of a thin layer, which diffusely reflects the light (and is, apparently, composed of bismuth or its alloy), at the surface of multilayer doped QD heterostructures. Possibly, Bi is also partially adsorbed at the boundaries of the growing clusters (QDs), which can affect the surface elastic energy of a cluster array. Under certain conditions, this can favor the formation of more uniform clusters [7].

Along with the main PL band related to the QDs, a short-wavelength band with lower intensity was observed in the spectra of almost all of the structures. It appears in the region 1.35–1.28 eV at 77 K (see Fig. 3). With decreasing T_d, it shifts to lower energies, like the main peak, and its intensity decreases. Apparently, this emission originates from the array of small clusters (QDs) discussed above, rather than from the wetting layer (as one might expect). The band has a spectral width typical of the QD emission, ~60 meV, and its energy is lower than the energy of a common wetting-layer PL peak ($h\nu_m > 1.4$ eV). To emit in the spectral region around 1.28 eV, the wetting layer must be 2.5- to 3-monolayer-thick. It may grow to this thickness at the free surface prior to its assumed reconstruction after the capping layer deposition. We note that, in the spectra of certain samples, two separate PL peaks are observed at ~1.3 and 1.4–1.45 eV. On increasing the deposition temperature to higher than 600°C and decreasing the nominal width of the InAs layer to ~2 monolayers, only small clusters (QDs) of this type are formed. Photoelectronic spectra of such QD heterostructures were previously investigated [3].

2.3. Photoelectric Spectroscopy of QD Heterostructures

Photoelectric spectroscopy techniques proved to be effective in the studies of the QW heterostructures (see, e.g., [8]). However, their application to the QD-heterostructure studies is relatively uncommon, which is probably related to some difficulties encountered in this case. Photoelectric sensitivity of a QD layer is usually much lower than that of a QW: in the former case the absorption coefficient (proportional to the QD surface density) is lower, and the barrier that photogenerated charge carriers have to overcome to be emitted from a QD into the matrix is higher. For this reason, it is common that, in the QD-heterostructure photoelectric spectra (unlike the PL spectra), the band related to the wetting layer QW is readily observed, while the photosensitivity band of the QDs themselves is difficult to observe against the background of the impurity photoresponse that originates from deep-level states in the substrate. Photosensitivity related to the QDs is usually observed only in the QD heterostructures with a fairly thin cap layer (~15 nm) and thick buffer layer (~0.5 μm), in which case the QD layer is located within the high-field region near the surface barrier; in addition, the QD density needs to be on the order of 10^{10} cm^{-2}. However, if the QD layer is located immediately at the surface, its photosensitivity (and the PL) is often also undetectable owing to the high surface recombination rate.

Figure 4 shows the CPV spectra of a number of QD heterostructures at 300 K. For some of them, the PL spectra are shown in Fig. 3. The photoelectric spectra of undoped QD heterostructures (see curve *1*) usually feature only the QD photosensitivity threshold related to the ground-state transition (at ~1 eV for this sample), while the spectral features related to the excited states are poorly resolved or unresolved. In Bi-doped QD heterostructures, owing to higher QD uniformity, both ground- and excited-state optical transitions are resolved in the CPV spectra, as in the PL spectra, and even transitions to the second excited state are distinguishable (curves *2*–*4*). The structure of the photoelectric spectra and energy positions of the peaks agree well with the PL spectra recorded at 77 K, with allowance made for an ~80-meV temperature shift. In some of the doped structures, even photosensitivity related to the uncapped QDs was observed (curve *5*).

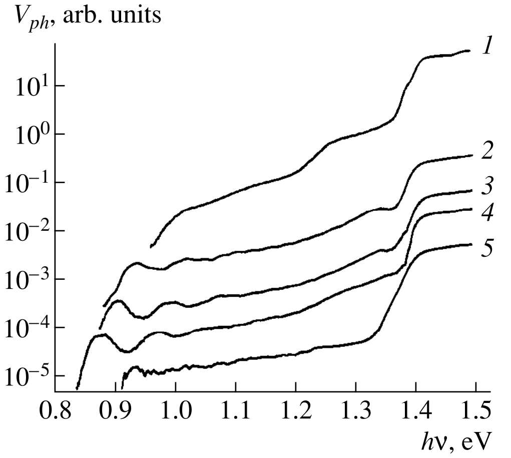

Fig. 4. CPV spectra of QD heterostructures for different conditions of the QD layer deposition: (*1*) undoped QD layer, T_d = 530°C; (*2*) doped QD layer, T_d = 530°C; (*3*) the same, T_d = 510°C; (*4*) the same, T_d = 490°C; (*5*) the same, T_d = 530°C, no capping layer (all other structures have a 15-nm-thick capping layer). For the samples represented by curves *2*–*4*, the PL spectra are given in Fig. 3 under the same numbers.

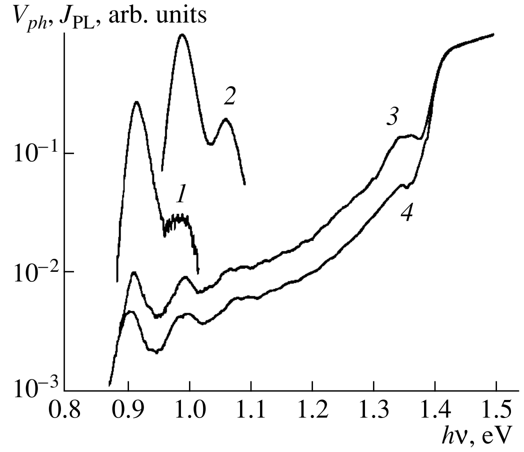

Fig. 5. Spectra of a structure with three QD layers: PL recorded at (*1*) 300 and (*2*) 77 K and (*3*) CPV measured at 300 K. Curve *4* represents the CPV spectrum of a structure with a single QD layer.

It is typical of the structures with the cap layer that the photosensitivity band originating from the wetting layer is clearly observed (a step at $h\nu \approx 1.33$ eV), and the band with the threshold at 1.2–1.27 eV, corresponding to the PL peak in the region ~1.3 eV, is weakly pronounced (as a rise of the curves at $h\nu \gtrsim 1.2$ eV) or is not present at all. This agrees with the assignment of this peak to small QDs. In the spectrum of the structure with an uncapped QD layer (curve *5*), the wetting layer does not manifest itself due to its oxidation.

The CPV spectra of two QD heterostructures grown under the same conditions and containing either one or three QD layers are shown in Fig. 5 (curves *3* and *4*, respectively). Spacers in the three-layer structure, as well as cap layers in both structures, have a thickness of 15 nm. The curves are normalized to unity in the region of intrinsic absorption. If the QD density and photoelectric quantum yield are equal in all layers, it should be expected that the normalized photosensitivity of the two structures in the region corresponding to the QD and wetting layer absorption differ by a factor of three. The actual ratio is nearly 2.5, which is indicative of the reproducibility of the QD layer parameters. PL spectra of the multilayer structure recorded at 300 and 77 K are also shown in Fig. 5 (curves *1* and *2*, respectively). Energy positions of the corresponding peaks in the PL and CPV spectra virtually coincide, and the main peaks in both have nearly the same width, equal to 33 meV.

The coexistence of QDs and a wetting-layer QW (which clearly manifests itself in the CPV spectra with a threshold at ~1.33 eV) in the same structure, makes it possible to estimate the surface QD density from photoelectric spectra using the QW as an optical absorption reference [3]. Since the photosensitivity of the QD layer is nearly 15 times lower than that of the QW, the same ratio should also hold for the corresponding optical absorption coefficients β^{QD} and β^{QW}, provided the quantum yield for the absorbed radiation in both cases is close to unity. The latter assumption is reasonable, because both quantum systems are located in the region of a strong surface-barrier field (~10^4 V/cm). The absorption coefficient of an $In_xGa_{1-x}As$ QW depends weakly on the In content and the well width and amounts to ≈7×10^{-3} [3]. Consequently, at the maximum of photosensitivity, $\beta_m^{QD} \sim 5 \times 10^{-4}$ for a single QD layer. Taking into account the values of β_m^{QD} and the photoresponse peak width $\Gamma^{QD} \sim 0.033$ eV obtained from the photoelectric spectrum, we can estimate the QD surface density by the following formula [3]:

$$N_s^{QD} = \frac{c m_e \sqrt{\varepsilon}}{2\sqrt{\pi \ln 2}\, h e^2 |X|^2} \beta_m^{QD} \Gamma^{QD}.$$

Here, c is the speed of light, m_e is the electron effective mass in GaAs, ε is the GaAs permittivity, h is the Plank constant, e is the elementary charge, and $|X|^2$ is the overlap integral of the electron and hole wave-function envelopes. For $m_e = 0.07m_0$ and $|X|^2 \sim 1$ $N_s^{QD} \approx 2 \times 10^{15} \beta_m^{QD} \Gamma^{QD}$ [$\text{cm}^{-2}\,\text{eV}^{-1}$], and the above estimation, the yields are $N_s^{QD} \approx 3 \times 10^{10}$ cm^{-2}. This satisfactorily agrees with the value of 1.6×10^{10} cm^{-2} obtained for this sample from the AFM image taken over an etch-opened QD layer (Fig. 2).

CONCLUSION

The results reported in this paper demonstrate that isovalent Bi doping of an InAs layer during its growth provides an effective means for the improvement of morphological and photoelectronic properties of heterostructures with GaAs/InAs quantum dots obtained by gaseous-phase epitaxy. Heterostructures whose emission and photosensitivity spectra extend to 1.41 μm at room temperature were obtained by this technique.

ACKNOWLEDGMENTS

This study was supported by the Russian Foundation for Basic Research, project nos. 98-02-16688 and 00-02-17598, the Ministry of Science of the Russian Federation under the Interdisciplinary Science and Technology Program “Physics of the Solid-State Nanostructures” (project no. 99-1141), Ministry of Education of the Russian Federation (grant no. 97-7.1-204 and the Program “Universities of Russia”), and CRDF (BRHE Program, REC-001).

REFERENCES

1. N. N. Ledentsov, V. M. Ustinov, V. A. Shchukin, *et al.*, Fiz. Tekh. Poluprovodn. (St. Petersburg) **32**, 385 (1998) [Semiconductors **32**, 343 (1998)].
2. N. V. Baĭdus’, B. N. Zvonkov, D. O. Filatov, *et al.*, in *Proceedings of the All-Russia Conference “Microprobe Microscopy-99,” Nizhni Novgorod, 1999*, p. 164; Poverkhnost’ (in press).
3. B. N. Zvonkov, I. G. Malkina, E. R. Lin’kova, *et al.*, Fiz. Tekh. Poluprovodn. (St. Petersburg) **31**, 1100 (1997) [Semiconductors **31**, 941 (1997)].
4. H. Saito, K. Nishi, and S. Sugou, Appl. Phys. Lett. **73**, 2742 (1998).
5. B. V. Volovik, A. F. Tsatsul’nikov, D. A. Bedarev, *et al.*, Fiz. Tekh. Poluprovodn. (St. Petersburg) **33**, 990 (1999) [Semiconductors **33**, 901 (1999)].
6. I. A. Karpovich, D. O. Filatov, S. V. Morozov, *et al.*, Izv. Akad. Nauk, Ser. Fiz. **63** (2), 313 (2000).
7. V. A. Shchukin, A. I. Borovkov, N. N. Ledentsov, *et al.*, Phys. Low-Dimens. Struct. **12**, 43 (1995).
8. I. A. Karpovich and D. O. Filatov, Fiz. Tekh. Poluprovodn. (St. Petersburg) **30**, 1745 (1996) [Semiconductors **30**, 913 (1996)].

Translated by M. Skorikov

Semiconductors, Vol. 35, No. 1, 2001, pp. 99–105. Translated from Fizika i Tekhnika Poluprovodnikov, Vol. 35, No. 1, 2001, pp. 98–104.
Original Russian Text Copyright © 2001 by Dorozhkin, Timofeev, Hvam.

LOW-DIMENSIONAL SYSTEMS

Persistent Photoeffects in *p–i–n* GaAs/AlGaAs Heterostructures with Double Quantum Wells

S. I. Dorozhkin*, V. B. Timofeev*, and J. Hvam**
** Institute of Solid-State Physics, Russian Academy of Sciences, Chernogolovka, Moscow oblast, 142432 Russia*
e-mail: dorozh@issp.ac.ru
*** Danmarks Tekniske Universitet, Microelectronics Center, III–V Nanolab, 2800 Lyngby, Denmark*

Submitted June 13, 2000; accepted for publication June 16, 2000

Abstract—Abrupt changes in the capacitance between the *p* and *n* regions were observed in a planar *p–i–n* GaAs/AlGaAs heterostructure with two tunneling-coupled quantum wells exposed to laser irradiation (λ = 633 nm). These changes can be caused by variations in both temperature (in the vicinity of $T \sim 2$ K) and the dc voltage applied to the structure. A memory effect was detected; this effect manifested itself in the long lifetime of anomalies observed after the illumination had been turned off. Self-consistent calculations of distributions of charge and electric field were performed for the structures that contained a donor impurity in AlGaAs layers; this impurity is responsible for origination of *DX* centers that give rise to persistent photoconductivity. It is demonstrated that abrupt changes in capacitance can occur in such a structure, and the values of the parameters required for origination of these jumps are determined. *© 2001 MAIK “Nauka/Interperiodica”.*

Considerable interest in optical properties of semiconductor heterostructures with double quantum wells (QWs) [1–7] is caused by the hope that, in such structures, the collective effects in a system of spatially indirect excitons can be observed; first of all, these effects include the theoretically predicted [8] phenomenon of condensation of these excitons when critical conditions are attained (see also [9–13]). This hope is based on the long lifetime of indirect excitons formed by a hole and electron in spatially separated QWs and on the related possibility of obtaining a high-density system of excitons at fairly low temperatures. For attainable densities of excitons, their condensation is expected to occur at liquid-helium temperatures and should show evidence of a phase transition. Experimentally, large changes in optical spectra of a number of semiconductor heterostructures with double QWs have indeed been observed [5–7]; these changes occurred within narrow temperature ranges. In this paper, we report the results of observing abrupt changes in the dependences of low-frequency impedance of previously used samples [6, 7] on temperature and electric field applied along the growth direction of the structures. These abrupt changes occur reversibly under conditions of continuous illumination and can also be observed in the previously illuminated samples after illumination has been turned off. Thus, changes in the sample caused by illumination at liquid-helium temperature are persistent. We analyze plausible interpretations of the observed special features of the low-frequency impedance as evidenced by the existence of persistent photoeffects.

The cross section of the heterostructure obtained by the molecular-beam epitaxy is schematically illustrated in the inset in Fig. 1. The structure includes two GaAs QWs (the layers *3* and *5*) 8 nm wide each separated by an AlGaAs barrier (layer *4*) 5 nm wide. The QWs are located within a *p–n* junction formed by the layers of *n*-GaAs (layer *1*) and *p*-GaAs (layer *7*), which ensures the presence of appreciable internal electric field perpendicular to the layers, even in the absence of external voltage applied to the structure. The *n*- and *p*-GaAs layers are doped with Si and Be, respectively, with concentrations of 2×10^{18} and 1×10^{18} cm^{-3}. When preparing the samples, layers *1–7* (and, partially, the substrate *0*) were etched off from most of the area of the wafer; a pedestal (mesa) 1.6×1.7 mm^2 in area was preserved from epitaxially grown layers. Contacts to the substrate and *p*-GaAs layer were formed using a Ge–Ni–Au alloy. The metal contact pad to *p*-GaAs layer *7* had the form of a frame with an area of 0.96 mm^2 and covered only a fraction of the mesa area. In order to measure the low-frequency impedance of the sample, we applied alternating voltage (from a audio-frequency oscillator) to the junction of the substrate and the frame; two components of the current flowing through the structure [the active component (in-phase with the applied voltage) and reactive component (shifted in phase with respect to applied voltage by 90°)] were measured using an ac phase-sensitive amplifier. In this paper, we report the results obtained only at low frequencies (about 10 Hz) and under conditions where the capacitive component far exceeds the active component. In order to vary the electric field in the sample, we can apply additional dc voltage of both polarities between the substrate and the frame. The samples exhibit the following specific features: (i) In the absence of illumination and in the region of temperatures below 10 K, the freezing-out of conduction over the *p*-GaAs layer

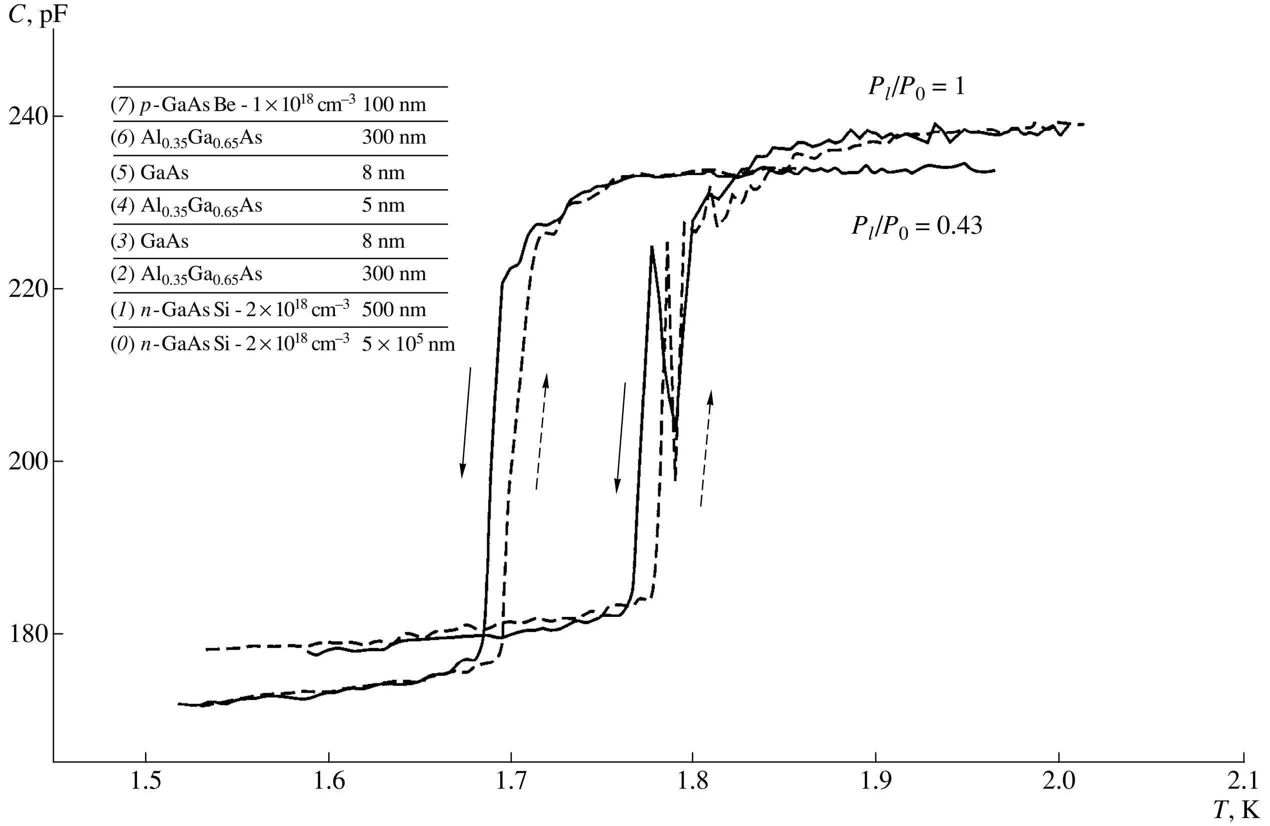

(*7*) p-GaAs Be - 1×10^{18} cm^{-3}	100 nm
(*6*) $Al_{0.35}Ga_{0.65}As$	300 nm
(*5*) GaAs	8 nm
(*4*) $Al_{0.35}Ga_{0.65}As$	5 nm
(*3*) GaAs	8 nm
(*2*) $Al_{0.35}Ga_{0.65}As$	300 nm
(*1*) n-GaAs Si - 2×10^{18} cm^{-3}	500 nm
(*0*) n-GaAs Si - 2×10^{18} cm^{-3}	5×10^5 nm

Fig. 1. Temperature dependences of the capacitance C measured between the substrate and metal frame for two values of relative illumination intensities P_l/P_0 indicated at the curves. The solid (dashed) lines were measured under conditions of decreasing (increasing) temperature. The inset shows the sequence and width of the studied-heterostructure layers.

(layer *7*) occurs [14]; i.e., the conductivity of this layer decreases exponentially as the temperature is lowered. Thus, under the conditions where most of the measurements were performed ($T \approx 2$ K), the effective area of plates of the studied plane capacitor is close to the metal-frame area. (ii) The metal frame virtually does not transmit the light of the visible region of the spectrum; therefore, photogenerated charge carriers can appear beneath the frame, either owing to scattered light incident obliquely on the heterostructure plane or owing to diffusion of charge carriers from other regions of the sample. The sample was illuminated using a light waveguide connected to a He–Ne laser with a photon energy of 1.95 eV, which exceeds the band gap of all semiconductor materials used in the studied heterostructure. The relative value of intensity of the optical beam P_l/P_0 incident on the mesa was checked using direct measurements performed outside the cryostat. Here, P_0 is the largest absolute value of intensity used, which according to estimations, amounted to 100 μW. A typical temperature dependence of capacitance between the metal frame and the conducting substrate under the conditions of continuous illumination is shown in Fig. 1; an abrupt change in capacitance occurring in a narrow temperature range of several hundredths of kelvin is observed. For this abrupt change in capacitance, the presence of slight hysteresis is typical on cooling and heating the sample; also, there are instabilities manifesting themselves in the high noise level (these instabilities can be clearly perceived from the shape of the curves measured for $P_l/P_0 = 1$). The temperature at which the drastic change in capacitance is observed increases as the illumination power increases. This fact is directly indicative of the secondary role of thermal effects related to illumination of the sample, if these effects are important at all. The magnitude of the abrupt change in capacitance depends on the dc voltage between the substrate and the frame, as it is demonstrated in Fig. 2. The corresponding dependence of the abrupt-change magnitude on the voltage also features a distinct discontinuity as demonstrated in Fig. 3. It follows from Fig. 3 that there are evidently two different magnitudes of abrupt changes in the temperature dependence of capacitance: $\Delta C \approx 20$ pF for $V < 0.1$ V and $\Delta C \approx 70$ pF for $0.15\text{ V} < V \leq 0.4$ V. It is noteworthy that we will not discuss the effects occurring for larger values of forward voltage $V > 0.5$ V, in which case the dissipative current increases rapidly and ultimately exceeds the capacitive current. In addition, it was ascertained in experiments performed under constant illumination that an abrupt change in capacitance occurs

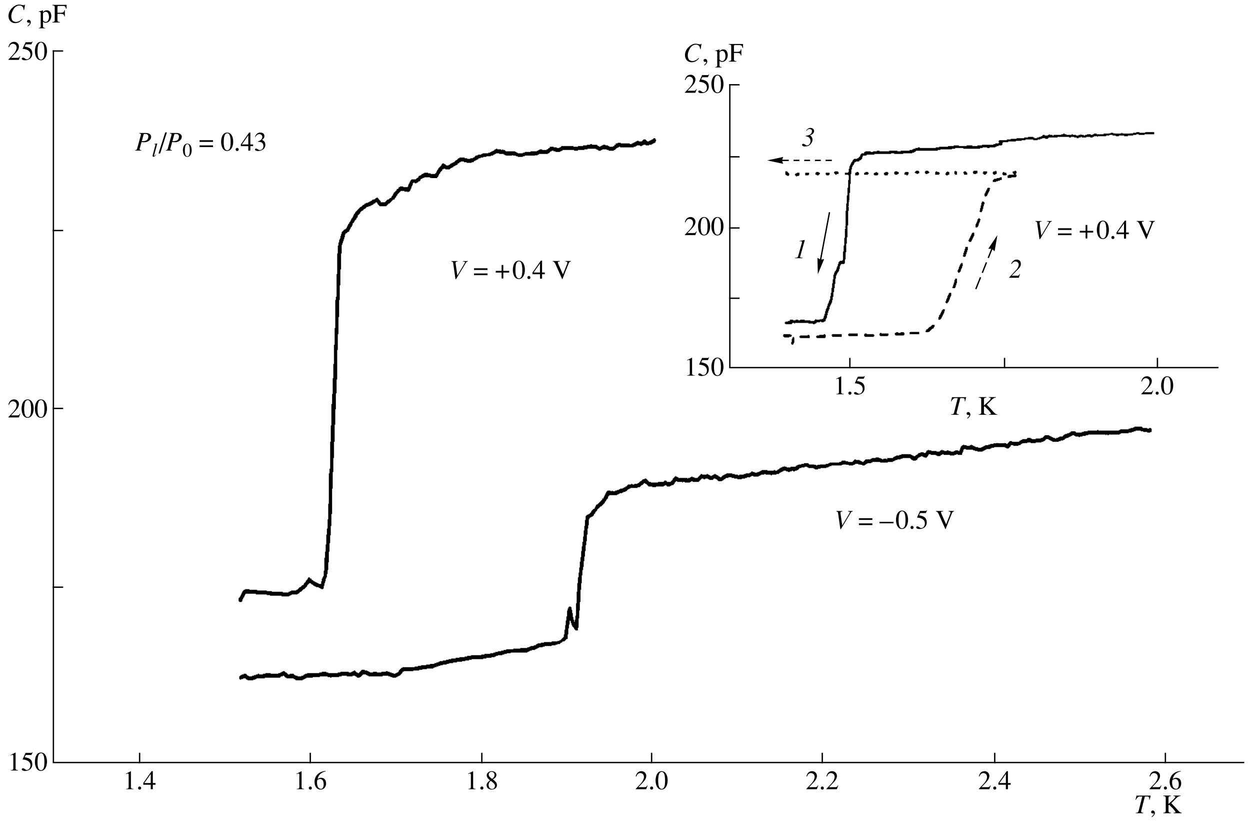

Fig. 2. Temperature dependences of capacitance measured for $P_l/P_0 = 0.43$ and two values of voltages applied to the structure and indicated at the curves. The dependences measured (*1*) under continuous illumination and (*2*, *3*) also after switching off the illumination at the lowest temperature point are shown in the inset; the arrows at the curves indicate the direction of variations in the temperature ($V = 0.4$ V).

simultaneously with modifying the luminescence spectrum of the sample.

The above results were obtained under conditions of continuous illumination. We now dwell on the results obtained without illumination, in which case the use of capacitance measurements made it possible to detect the memory effects in the phenomenon under study; these effects were observed after a one-time illumination of the sample at liquid-helium temperature (the corresponding data are shown in the insets in Figs. 2 and 3). First of all, we note that, without even a one-time illumination of the sample after it has been cooled from room temperature to liquid-helium temperature, we fail to observe any abrupt changes in capacitance. An example of the memory effect is demonstrated by the data shown in the inset in Fig. 2 (curve *2*). It can be seen that an abrupt change in capacitance when temperature is raised can also be observed in the dark, if the sample has been preliminarily cooled (under conditions of continuous illumination) to a temperature lower than that corresponding to an abrupt change in capacitance (curve *1*) and if the illumination has been switched off in this low-temperature state. However, under such conditions of the absence of illumination, the temperature width of the abrupt change in capacitance was smaller than that under continuous illumination. In addition, without illumination, this abrupt change is irreversible, because the abrupt changes in the temperature dependences of the illuminated-sample capacitance measured in the dark at the temperatures from 4.2 to 1.4 K are not observed (curve *3*). The second type of the memory effects consists in the emergence of abrupt low-temperature changes in capacitance after the sample has been illuminated; these changes occur reversibly when the voltage at the structure is varied (see the inset in Fig. 3). The lifetime of the latter effect amounts, at least, to hours.

Before proceeding to discussion of possible origins of the observed effects, we would like to note that, under the experimental conditions used, the measured value of capacitance is directly proportional to the area of the upper conducting plate of the capacitor and is inversely proportional to the thickness of the insulating region between the substrate and the frame; it is in this region that the drop of electrochemical potential occurs. Taking into account the aforementioned effect of freezing-out of conduction in the *p*-GaAs layer, we cannot at present unambiguously posit whether the observed abrupt changes in capacitance are related to variation in the effective area of the capacitor plates or

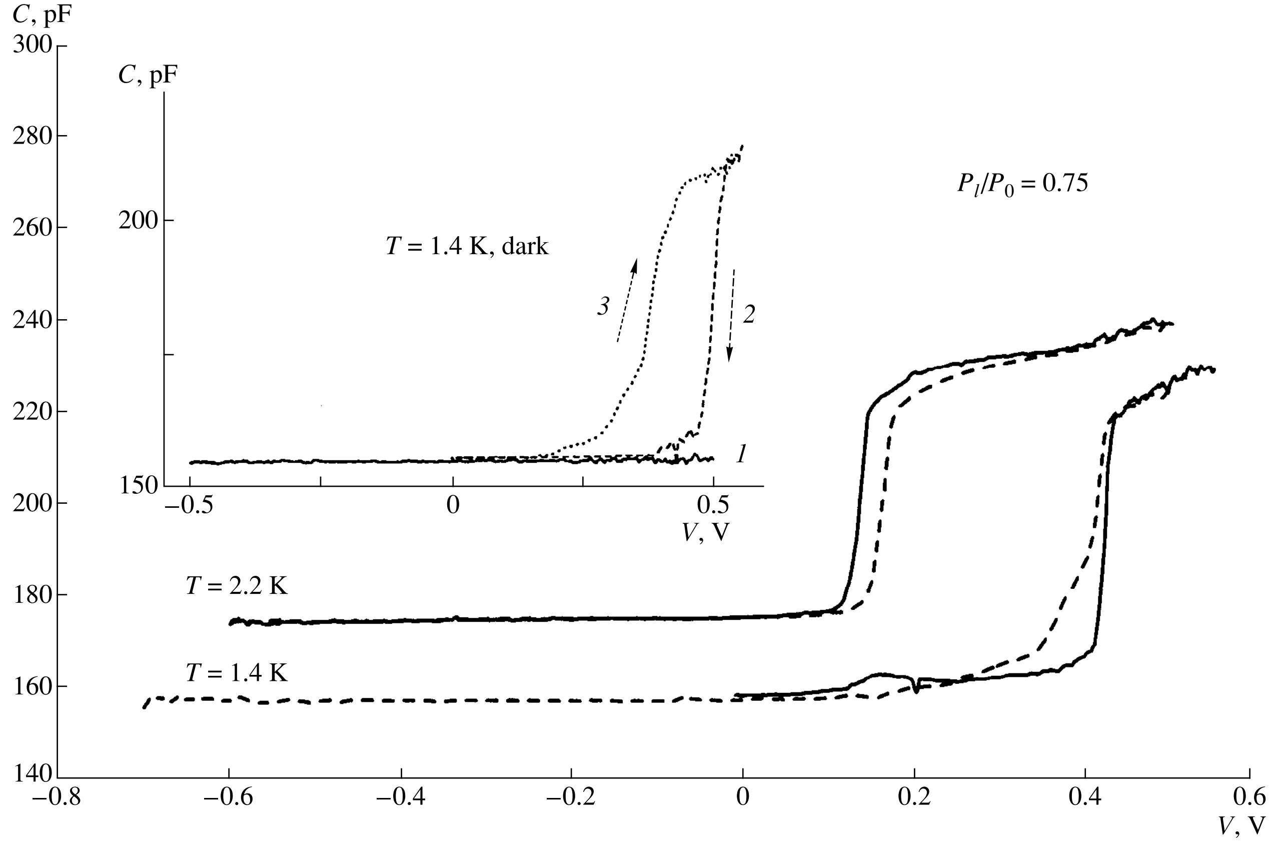

Fig. 3. Dependences of capacitance on the voltage V applied to the structure. The dependences were measured at $P_l/P_0 = 0.75$ and two different temperatures: $T = 1.4$ and 2.2 K. The solid (dashed) lines correspond to the scan of V in the positive (negative) directions. The inset shows the dependences $C(V)$ measured in the dark before the first illumination (solid line *1*) and after the illumination was turned off (the dashed and dotted lines *2* and *3*). $T = 1.4$ K.

in the insulator-layer thickness. However, it is obvious that, in any case, these abrupt changes are related to variations in the electric field (perpendicular to the structure layers) in a large fraction of volume of the sample.

We begin the discussion of the experimental results with the issue concerning the mechanism of persistent photoeffect in the sample capacitance; we will try to analyze the possibilities that arise for abrupt changes in capacitance in connection with this effect in the samples we studied. The existence of this effect can be most reasonably related to the well-known effect of optical excitation of persistent photoconductivity in AlGaAs doped with a donor impurity that gives rise to the so-called *DX* centers. The latter effect consists in excitation of the electron to the conduction band and in transformation of the *DX* center into a state such that the return of the electron to the center requires penetration of a fairly high potential barrier. In the presence of electric fields in the structure, the photoexcited electrons move under the effect of these fields and arrive at potential wells if the latter are available [15]. In order to calculate the distribution of such electrons in inhomogeneous semiconductors to the first approximation, we may consider the illuminated AlGaAs layers as layers containing a donor impurity with a very shallow level. Under this assumption, we self-consistently calculated the electron distribution and electric field for GaAs/AlGaAs structures with the layer sequence corresponding to the samples under investigation. The calculation is aimed at determining the distributions of charge and potential, taking into account the variation in the position of the conduction-band bottom in the electric field and the occupancy of all electron states below the electrochemical-potential level ξ in the sample. In the calculation, we took into account the size-quantization effects in the motion of electrons in QWs and also the finite value of the density of states in each of the subbands in the QWs; this density of states is equal to $m^*/\pi\hbar^2$, where $m^* \approx 0.17m_e$ is the effective electron mass in GaAs. We assumed that the distance between the QW bottom and the bottom of the lowest subband was 34 meV, which corresponded to a QW with the width of 8 nm and the height of the walls of 0.3 eV; tunneling coupling between the QWs was disregarded. The calculation presents no problems for the equilibrium state, in which case there is no voltage applied between the *n*-GaAs and *p*-GaAs layers, while the elec-

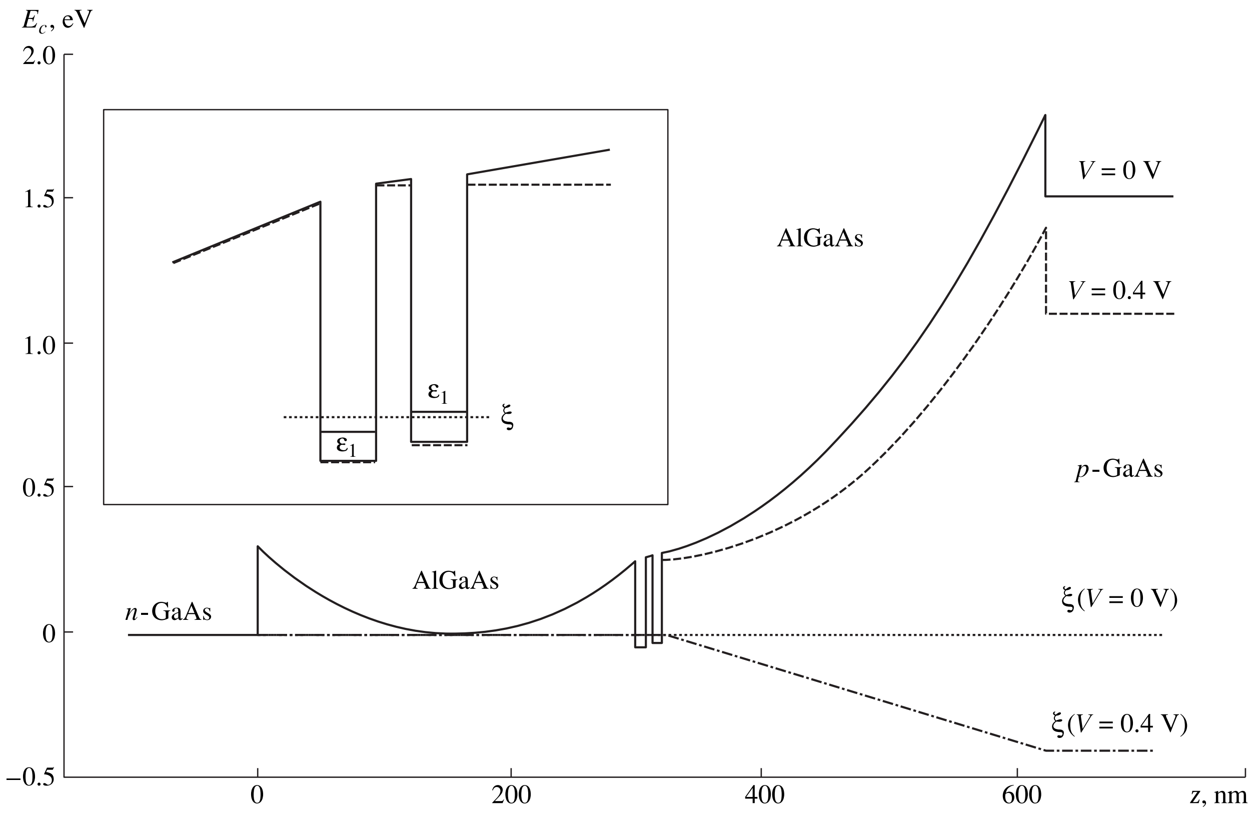

Fig. 4. Calculated dependences of the position of the conduction-band bottom E_c in the studied structures on the coordinate z in the direction perpendicular to the layers for $V = 0$ (solid line) and $V = 0.4$ V (dashed line). The value $z = 0$ corresponds to the boundary between the n-GaAs and AlGaAs layers. The region of the structures in the vicinity of quantum wells is shown on an enlarged scale in the inset; the positions ε_1 of bottoms of the lower size-quantization subbands in both wells are also shown. The coordinate dependence of electrochemical potential ξ is shown by the dotted and dash-and-dot lines. In calculation, we assumed that the DX-center concentration was $N_d = 1.6 \times 10^{16}$ cm^{-3}; the conduction-band offset at the GaAs/AlGaAs interface was taken equal to 0.3 eV, and the band gap of GaAs was assumed to be 1.5 eV.

trochemical potential is constant over the entire sample and coincides with the conduction-band bottom in the n-GaAs layer and the valence-band top in the p-GaAs layer (i.e., it is assumed that the density of electron states is high in these layers). The result of such a calculation is shown in Fig. 4 by solid line for the case where the concentration of DX centers in AlGaAs is equal to $N_d = 1.6 \times 10^{16}$ cm^{-3}. This result demonstrates that three effects can exist in the structures of this type: occupation of one or both GaAs QWs by long-lifetime photoexcited electrons and also the origination of the region where the conduction band of AlGaAs is filled with electrons. For the chosen values of parameters and $V = 0$, the left-hand QW is found to be filled to the surface electron density equal to $n_{s1}(V = 0\text{ V}) = 18.9 \times 10^{10}$ cm^{-2}, whereas the right-hand QW is empty, and the AlGaAs conduction band is filled with electrons for 150 nm < z < 165 nm. It is easy to calculate the values of the DX-center concentration for which the occupation of the corresponding regions sets in. The results of calculations are listed in the table for $V = 0$ and several values of the AlGaAs-layer thickness.

In the nonequilibrium situation that arises when there is a voltage applied between the n- and p-GaAs layers, additional information is required about conductivity occurring in the samples and defining the electrochemical-potential distribution across the layers. In order to semiqualitatively demonstrate the phenomena occurring in this situation, we assumed that electrons filling the QWs and conduction band in AlGaAs are always in equilibrium with electrons in the n-GaAs layer. The changes occurring in this case in the structure subjected to a voltage of $V = 0.4$ V are demonstrated by the dashed line in Fig. 4. The electron densities corresponding to this dependence in the left- and right-hand QWs are $n_{s1}(V = 0.4\text{ V}) = 21.2 \times 10^{10}$ cm^{-2} and $n_{s2}(V = 0.4\text{ V}) = 5.4 \times 10^{10}$ cm^{-2}, respectively. For $N_d = 1.6 \times 10^{16}$ cm^{-3}, Fig. 5a shows the voltage (V) dependences of the surface electron density in both QWs and the width of the region where occupation of the AlGaAs conduction band occurs. Vanishing of any of the above quantities induces changes in the effective thickness of insulating layer in the structure and initiates a corresponding abrupt change (see Fig. 5b) in the

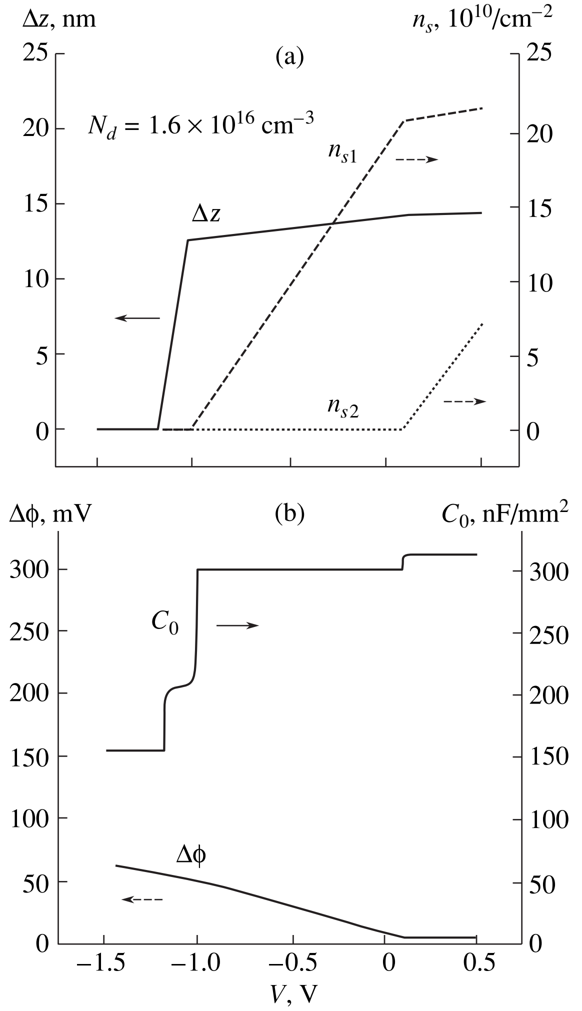

Fig. 5. (a) Calculated dependences of the surface density of electrons in the left-hand (n_{s1}) and the right-hand (n_{s2}) wells, and the width (Δz) of the AlGaAs layer filled with electrons on the voltage V applied to the structure for $N_d = 1.6 \times 10^{16}$ cm^{-3}. (b) Calculated dependences of capacitance per unit surface area of the sample C_0 and the potential difference between the wells Δφ on V. The data shown here were obtained under the same assumptions and for the same choice of parameters as those shown in Fig. 4.

The *DX*-center concentrations for which (for $V = 0$) the left-hand well (N_{d1}), right-hand well (N_{d2}), and the conduction band (N_{d3}) of ALGaAs sets in for various values of thickness d of AlGaAs layers, which were assumed equal to the left and right of the wells

N_{d1}, 10^{16} cm^{-3}	N_{d2}, 10^{16} cm^{-3}	N_{d3}, 10^{16} cm^{-3}	d, nm
1.0	1.7	1.5	300
2.1	3.7	3.2	200
7.3	13.5	12.3	100

capacitance $C \equiv dQ/dV$ (Q is the charge of the p-GaAs layer) measured between the n- and p-GaAs layers. Variation in the potential difference between the QWs Δφ is also shown in Fig. 5. This dependence demonstrates that an electric field between the QWs is low if both QWs are filled with electrons. This physically evident result is a consequence of a fairly high density of states in QWs and is independent of a specific model as long as the permeability of the barrier layer (separating the QWs) for electrons is much larger than the permeability of at least one of two lateral AlGaAs layers (layers *2* and *6* in Fig. 1). Thus, the considered model demonstrates that abrupt capacitance changes can occur when voltage applied to the structure varies; these changes may have various magnitudes. Obviously, the distribution of the abrupt electrochemical-potential change different from what is expected will change only the magnitude and position of changes in capacitance, without affecting the qualitative result. The presence of continuous low-intensity illumination could also hardly affect the considered pattern. It is very likely that the presence of nonequilibrium charge carriers under continuous illumination is conducive to the establishment of quasi-equilibrium between various reservoirs with charge.

It should be mentioned that it is very difficult to explain the abrupt changes in capacitance in terms of the model under consideration, because, in this model, there are no characteristic energies that are related to the temperatures at which these abrupt changes are observed. Nevertheless, we can explain these phenomena if we consider the following additional effect: As is evident from the data listed in the table, a variation in the insulator-layer thickness should result in depopulation (population) of the wells and the conduction band in AlGaAs; this is accompanied by abrupt changes in capacitance, which was demonstrated above. If we now take into account the effect that exists in the samples studied and consists in the freezing-out of electrical conductivity in a p-GaAs layer, we may assume that the abrupt change in capacitance observed on varying the temperature occurs as a result of temperature-induced variation in the effective thickness of an insulator layer above the QWs. The estimates we made assuming that electric field penetrated into the p-GaAs layer in the case of its dielectrization showed that, for $N_d \sim 1 \times 10^{16}$ cm^{-3}, dielectrization of the p-GaAs layer may well result in an onset of occupation of the right-hand GaAs QW (layer *5*), which was previously unoccupied for $V = 0$.

In conclusion, we should mention another effect that requires additional assumptions to be made in order to be explained in terms of the model under consideration. These assumptions include the irreversibility of the abrupt capacitance change observed when temperature is varied, with continuous illumination being absent (see the inset in Fig. 2). It might be expected that the model based on consideration of only the stationary states and used by us cannot explain this effect.

In order to decide whether the above-considered model can at least qualitatively explain the observed abrupt changes in capacitance, we consider the most critical issue of whether there is a donor impurity in an amount sufficient for occupation of QWs with electrons in nominally undoped AlGaAs layers (i.e., $N_d > 1 \times 10^{16}$ cm^{-3}). At present, we cannot settle this question, although, in our opinion, the persistent photoeffects observed in the measured capacitance are conclusively indicative of the presence of donor impurity in AlGaAs layers. The origin of hystereses observed in the absence of continuous illumination may present another object of investigation.

ACKNOWLEDGMENTS

We thank the Russian Foundation for Basic Research, INTAS, and the State Scientific and Technological Program “The Physics of Solid-State Structures” for support of this study.

REFERENCES

1. Y. J. Chen, E. S. Koteles, B. S. Elman, and C. A. Armieto, Phys. Rev. B **36**, 4562 (1987).
2. J. E. Golub, K. Kash, J. P. Harbison, and L. T. Flores, Phys. Rev. B **41**, 8564 (1990).
3. T. Fukuzawa, E. E. Mendes, and J. M. Hong, Phys. Rev. Lett. **64**, 3066 (1990).
4. J. A. Kash, M. Zachau, E. E. Mendes, *et al.*, Phys. Rev. Lett. **66**, 2247 (1991).
5. L. V. Butov, A. Zrenner, G. Abstreiter, *et al.*, Phys. Rev. Lett. **73**, 304 (1994).
6. V. B. Timofeev, A. V. Larionov, A. S. Ioselevich, *et al.*, Pis’ma Zh. Éksp. Teor. Fiz. **67**, 630 (1998) [JETP Lett. **67**, 613 (1998)].
7. V. B. Timofeev, A. V. Larionov, M. Grassi Alessi, and M. Capizzi, Phys. Rev. B **60**, 8897 (1999); Phys. Rev. B **61**, 8420 (2000).
8. Yu. E. Lozovik and V. I. Yudson, Zh. Éksp. Teor. Fiz. **71**, 738 (1976) [Sov. Phys. JETP **44**, 389 (1976)].
9. D. Yoshioka and A. H. MacDonald, J. Phys. Soc. Jpn. **59**, 4211 (1990).
10. X. M. Chen and J. J. Quinn, Phys. Rev. Lett. **67**, 895 (1991).
11. Xuejun Zhu, P. B. Littlewood, M. S. Hybersen, and T. Rice, Phys. Rev. Lett. **74**, 1633 (1995).
12. J. Fernández-Rossier and C. Tejedor, Phys. Rev. Lett. **78**, 4809 (1997).
13. Lerwen Liu, L. Swierkowski, and D. Neilson, Physica B (Amsterdam) **249–251**, 594 (1998).
14. P. S. Dorozhkin, Degree Work (Mosk. Fiz.-Tekh. Inst., Moscow, 1999).
15. M. I. Nathan, Solid-State Electron. **29**, 167 (1986).

Translated by A. Spitsyn